

Development of a new visual prosthesis for preclinical studies on artificial vision

Présentée le 29 mai 2020

à la Faculté des sciences et techniques de l'ingénieur
Chaire Medtronic en Neuroingénierie
Programme doctoral en microsystemes et microélectronique

pour l'obtention du grade de Docteur ès Sciences

par

Marta Jole Ildelfonsa AIRAGHI LECCARDI

Acceptée sur proposition du jury

Prof. S. Lacour, présidente du jury
Prof. D. Ghezzi, directeur de thèse
Prof. T. Stieglitz, rapporteur
Prof. G. Lanzani, rapporteur
Prof. Ph. Renaud, rapporteur

*To Nature, for Its variety of wonders, beautiful inspirations, and essential perseverance;
to Chaos, for creating the opportunities;
and to Time, for allowing everything to exist.*

Acknowledgements

The adventures of my Ph.D. thesis started about five years ago when I was looking for an inspiring project within the EPFL walls. At that time, in May 2015, I met Professor Diego Ghezzi, and I somehow convinced him to share his plans with me. I remember that one of my spontaneous comments on the project he proposed was “fico” (which means “cool” in a quite plebeian Italian way). Ever since, he has been the railways of my thesis, guiding me towards smarter decisions, supporting my suggestions, and trusting my opinions. Indeed, regularly double-checking that we were on the same page, after all. I sincerely thank him for all the great opportunities I received and the knowledge I learned along with the experience of a young dynamism in setting up a growing research group. This has been my most incredible professional journey so far; and Diego has always been there, with his never-ending energy, day and night, workweek or holiday, in person or by phone, text, email, Skype, Zoom, WhatsApp, Asana, Slack, and other ways that I might have forgotten.

A Ph.D. thesis, however, cannot be completed with only two people: many souls have crossed paths with me, either for a short time, or for the duration of this thesis, or from way before the start. I take this opportunity to thank them all, as they have contributed, in one way or another, to the success of this thesis.

I would like to start my list with the jury members: Professor Stéphanie Lacour, Professor Philippe Renaud, Professor Guglielmo Lanzani, and Professor Thomas Stieglitz. They agreed to participate in the evaluation of the work, offering their availability, precious time, and priceless opinions and corrections, which led to a fruitful discussion and a more valuable dissertation. I was honored to “meet” them via Zoom (during the COVID-19 isolation), and I hope to have other occasions to meet them again, hopefully in person.

A crucial role in this thesis has been personified by Professor Thomas J. Wolfensberger, from Hôpital ophtalmique Jules-Gonin, who actively participated from the beginning of the project in developing various aspects of the prosthesis, and he performed (and still will perform) all the arduous surgeries. We couldn't get this far without his precious and essential contributions. A big thank also to Anisoara Nicastro (Annie), Sylvie Roulet, and Jean-Pierre Giliberto for their professionalism and efficiency in assisting the surgeries, and particularly for their patience and fondness when dealing with us trying to help them without messing up nor panicking. Another important figure has been Professor Kevin Sivula and his group LIMNO at EPFL, who helped us with theory, fabrications, measurements, and discussions about anything related to organic photovoltaics, including

strange effects and incomprehensible results. I would also like to thank Maciej Kawecki, from EMPA, who performed ToF-SIMS measurements and tedious analysis.

During the entire duration of my thesis, I operated in cleanroom facilities for the manufacturing of the samples. Big thanks to all the members of the EPFL Center of MicroNanoTechnology (CMi) for their massive support during fabrication processes, as well as their professionalism, patience, kindness, and congeniality. In particular, I would like to thank Patrick, Giovanni, Gatera, Cyrille, Joffrey, Rémy, Niccolò, Julien, Kaspar, Zdenek, Guy, Giancarlo, and Jérémy for fixing everything and debugging the RiteTrack, MLA, SPTS, SPIDER, and DP650 issues even during out-of-office hours or lunchtimes; for supporting PDMS etching in CMi-1; for the immediate delivery of forgotten wafers and photoresist bottles; for the improbable dicing “not-all-the-way-through” of glass wafers; for delicate “please-don’t-break-my-stencil” grinding; and for the random discussions and laughs in the open space, changing rooms, and along the corridors. I am so proud that I could be part of this great facility.

And yet, I could enjoy the benefit from a second cleanroom at Campus Biotech in Geneva, managed by the Wyss Neural Microsystems Platform and inaugurated after the beginning of the thesis. There, I could run the necessary processes that would be forbidden elsewhere due to the less standardized materials involved. Only three people were managing the platform, namely Michael Stoeckel, Anthony Guillet, and Valerian Ruhaut. I would like to thank them for their infinite patience with me and my strange processes, for the precious help during the development of these procedures, for fixing all the machines I needed, for sometimes cleaning up after me, for their creative solutions like nothing could stop them, and for not kicking me out of the cleanroom. ☺ Many thanks also to the Wyss Preclinical Neuroscience Platform for their support with histological analyses and all sorts of bio-imaging.

The great EPFL environment offers amazing services among the various facilities. I would like to thank the staff from the Atelier de l’Institut des Matériaux for their fantastic work in producing the divers high-quality PMMA molding parts and from the Interdisciplinary Center for Electron Microscopy for the laborious TEM-EDX analyses.

A thesis could not be carried out without the administrative and social support from the lab and EDMi secretaries. For this, I thank Nadia Macor, Manuela Da Silva, Frédérique Toulet Rapaccioli, and Lucie Auberson for their marvelous job in taking care of the paper works, controlling that finances match, and reminding us (sometimes forcing us) to take holidays.

I could use tens of pages to thank each member of the LNE group for the impressive quantity and quality of work that I had the chance to use during my thesis. They have contributed profoundly to this work, and they should be dutifully acknowledged. I thank all of them for professionally having taken part in this thesis, but most of all, I thank them for sentimentally having taken part as well. For more than four years, I have been “obliged” to share offices, labs, cleanrooms, projects, group meetings, conferences, cafeterias, and coffee breaks with the group members. Only, this did not feel like an obligation: on the contrary, it has been a real pleasure; so much that I could also share fitness centers, climbing and jogging sessions, skiing, bars and restaurants, BBQs, game nights, holidays, rabbits-sitting, and I don’t know how many WhatsApp groups. In the order of appearance and trying to be concise... Thank you, Paola, for experiencing this journey with me from the first to the last month, for answering all of my random biology-related questions, and for your high spirit and irony lighting up the moments, even if you don’t believe it (and also with the general tonality of your

clothes). Thank you, Laura, for your constant guidance, patience, and many good laughs when doing something stupid together (like taking a picture of us through the reflection of a silicon stencil). Thank you, Naïg, for all the publications we co-authored, for sharing a different perspective of basically everything, and for explaining plenty of words I didn't know (it wouldn't surprise me if you start doing it in Italian as well). Thank you, Vivien, for being such a kind, respectful, and resourceful guy, and for instilling in us your passion for good art, good food, good coffee, good drinks, good social games, and... strange facts (which I totally get). Thank you, Eleonora, for being the key component of LNE social life, for your strength in facing the challenges that the OSTE and the nanowires might serve you, and for being such a good friend (and stylish too!). Thank you, Charles, for your never-ending enthusiasm, for your crazy ideas and ingenious solutions, and for all the hours (and overtime) spent together to prepare for the surgeries (with occasionally pushed panic buttons). Thank you, Elodie, for taking such good care of the entire LNE, for your extraordinary energy, and for the immediate trust and affection you kicked off in us (don't worry, not just because you brought good food to us). Thank you, Adele, for being such a sensitive and kind person, for your positivism and friendship, and for always being there when I needed your help and never complaining (even when you were picking up rabbits excrements, without me asking). Thank you, Enrico, for your delightful presence, for your enthusiasm in initiating us to Dungeons & Dragons, and for the amount of knowledge you manage to store in your head (which always comes useful; but seriously, how do you do that?). Thank you, Jake, for showing to the world the importance of POLYRETINA's visual field, and for filling up our days with jokes, but more importantly for always getting mine when no one else does (sometimes I can't believe it myself). Thank you, Golnaz, for recently joining our lab and ensuring the continuity of the projects, for your patience in understanding my instructions and especially in understanding them remotely (even with my rattling voice due to poor internet connection). Thank you all for your friendship and huge moral support. I will miss you as soon as I step foot out of LNE...

Teaching and supervising are part of the thesis educational path. During the four years, I had the chance to supervise a bunch of great students, which contributed to the projects in many ways. Thank you Loïc Sottas, Adrien Boissenin, Elsa Genzoni, Matteo Salari, Bastien Duckert, Carlos Nunez, Eleonora Borda (here again), Florian Köhler, Michele Bevilacqua, Amanda Kläger, Ludovica Romanin, Samuel Gilliéron, Giammarco Pacifico, Ricardo Moreira, Alice Juanico, and Christian Vivori. Thank you all for your patience, for your input, for believing in it, and for your moral support. I would also like to thank Giulia Mongardi, Marina Liberti, and Danashi Medagoda for their transferable social skills.

The admirable spirit of sharing and helping each other among labs came out essential for both theoretical and practical aspects. I would like to thank the colleagues at LSBI, LMIS4, HEPIA in Campus Biotech, Neurosoft, and cleanroom fellows from other groups, for the knowledge, tools, time, and wafers they shared with me. As a matter of fact, some of these folks shared more than professional cordiality: they have been amazing friends, spending time together at wine tastings, dinners, weddings, laser games, hiking, and ski weekends. Special thanks go to Yoram and Veronika, Florent, Damien, Soumya, Kaitlin, Laurent, Stefano, and Valentin for all the moments we spent either eating pizza late in the office or drinking good wine after work, complaining about life and about people sabotaging our wafers. An exceptional thank goes to Matthias and Léa, for never giving up on our friendship and for even cooking for us when we were too tired or busy. And also for complaining about people sabotaging our wafers. Besides the EPFL and cleanroom entourage, I would

like to thank all the people that accompanied me during this journey, even if for a brief period. Thanks to my friends from ETHZ, Joni, Iacopo, and Diamante, for being such great friends on which I can always count. An enormous thank to the Italian group of friends “Monsters”, with Giacomo, Barbara, Deborah, Davide, Rosanna, Giovanni, Marcella, Giuseppe, Gianni, Dino, Alberto, and Samuele, for the exceptional memories among which enlarged BBQs, dangerous river ridings, hilarious mime games, surfing holidays, celebrated Christmas and birthday parties, and 24h of swimming. I would also like to thank Cami, Dimi, Sam, and Lore for the limitless resources and imagination in organizing surprising birthday parties and unique events. And then, among those high-school friendships that could never end, I thank you, Daniele, for the time we spent together down-playing mathematical problems, laughing at funny photos, looking for vipers, driving through Estonia, and running from drunk strangers. Thank you for being such a great and funny person, always happy to talk and meet. And I thank you, Alice, for your kindness and altruism, for your support and advice, and for your beautiful laughs. Thank you for suddenly entering my life and hopefully never going out, for your precious friendship without time nor boundaries, for always believing in me, and for being my treasure chest of memories.

And finally, my deepest gratitude goes to my whole family. I take this opportunity to thank the people in my family that left in me memories and pieces of themselves, helping me become the person I am now. I wish to sincerely thank my mother, Cristina, for her innumerable sacrifices that allowed me to achieve plenty of goals in my life, including this one. Thank you, Ma, for your serenity, energy, kindness, and immense love; for always doing what is best for us with altruism and modesty; for your constant and silent desire to help us, even if it means to break your own back; for encouraging me to never give up on education and training, teaching me that we need to work hard to achieve our ambitions; and for facing life with immeasurable strength and courage, which made you an exceptional model to get inspired from. I also wish to thank Sergio for becoming part of our family and decorating our days with a shining personality and funny humor. Special big thanks to my siblings, Pietro, Maria, and Cesare, for the irreplaceable experiences as partners “in crime” and escaping adventures, and for completing my life with tenderness, fun, and a comforting sense of belonging. Thank you, Pié, for your fascinating enthusiasm and creativity, for your hilarious attitude and unceasing support, which allowed me to move forward with more serenity. Thank you, Mary, for your kindness, sensitivity, and humanity, for all the fooleries and laughs we experienced together, making me forget about stressful periods. And thank you, Cesare, for your playfulness, your energetic spirit, and for our rediscovered brotherhood. My gratitude also goes to my dad, Massimo. I would have loved to share this achievement with you, and I hope I could make you proud. I’ll always carry with me your (sadly too few) valuable teachings and good memories.

Furthermore, I would like to express my thanks for the rest of the family, which always got our backs, no matter what. I thank my grandparents, Jole and Gianmaria, as well as Paola, for their unconditional support and love. Many thanks also to my aunts and uncles, Gianluca, Andrea, Renata, Stefania, Mario, Dani, Lorenzo, Dado, Anca, Matteo, and Giulia, for their generosity, their enthusiasm, their trust, and encouragements. And thanks to my cousins, Vale, Franci, Kikka, Tommy, Elisa, Claudia, Pietrino, Paola, Carlotta, Mattia, and Matilde, for the many past and many more future beloved moments together.

Many people would agree with me if I’d say “the more, the better”, especially when it’s about family. I got the immense chance to get warmly welcomed into a special French family, which immediately treated me like one of their own, with great kindness and affection. I would like to deeply thank

Georges and Isabelle for their extraordinary hospitality, their generous attentions, and their sincere and constant interest. I also truly thank Olivia for being an incredibly kind and big-hearted person, always treating me and believing in me like a sister. In addition, I thank Emilio for his great generosity and altruism. Many thanks also to Marguerite, William and Chantal, Claude and Bernadette, Maryline and Mickaël, Christelle and Lionel, Hervé and Christelle, Marlène and Matthieu, Sylvain and Marine, Martin, and their respective kids, for their infinite cordiality and wonderful time spent together. And finally, a special place in our hearts is filled for the little Méline and her highly contagious and beautiful smiles.

Moreover, I would like to share the countless laughs and incredible comfort that Gaston, Mignolo, and Pepito made me experience, particularly during the hard times preparing the manuscript and the defense. The people aware of those furry, long-eared, and unique four-legged companions (two of them extra-large) shouldn't be surprised that I decided to mention them here. As a message to the reader, never underestimate the benefits of such reciprocal affections!

At last, but definitely not least, I want to sincerely thank Benoît. As the perfect soul mate, you've filled my days with love, support, joy, care, adventures, laughs, sweetness, music, and colors (and not just figuratively). You made me evolve towards a better person and made me discover that our hearts can be bigger than what I thought. You are my strength when I'm weak, my voice when I cannot speak, and my eyes when I cannot see (and Céline Dion would agree on that). Thank you for this and everything you've done for me. Thank you for all the hours you spent assisting me in figuring out work problems, surprising me with thoughtful dinners, taking care of me when I was sick or tired, supporting every single decision and guiding me to make finer ones, alleviating difficult and stressful moments, and sharing with me your day as if you've been waiting so long to do so. I'm struggling to express how important you are to me and how much of what you've done has helped me during this thesis. It seems like words would never be enough. Anyway, I'm so thankful, and I'm looking forward to seeing where our future will bring us, personally and professionally.

Thank you all.

Lausanne, April 2020

Marta Airaghi Leccardi (MAL)



Abstract

The technological evolution in materials science and microengineering favored the production of advanced visual prostheses useful for fighting blindness and to improve patients' quality of life. Visual prostheses aim at replacing lost visual functions by artificial (electrical) stimulation of the remaining circuitry with microfabricated electrodes inducing phosphene appearance in blind people. In particular, for people affected by retinal degenerative diseases such as retinitis pigmentosa and age-related macular degeneration, retinal prostheses offer a valuable treatment option thanks to several advantages: among them, the retinotopic organization, the large surface area available for stimulation, and the straightforward surgical and optical access. The latter becomes very convenient for photovoltaic implants, in which amplified light entering the pupil is exploited as wireless source of power and visual information, allowing the implant to lay freestanding and the placement of a large number of stimulating pixels without the inconvenience of electrical connections. However, although all these advancements, there is nowadays no visual implant suited for artificial vision with both high spatial resolution and large visual field coverage.

In this thesis, we developed a photovoltaic and foldable wide-field epiretinal prosthesis with a high density of stimulating pixels (more than 10^4 and 18^6 pixels with a density of 79 and 141 pixels/mm², respectively) distributed over a very large surface area, covering 46 ° of visual field, greatly improved with respect to state-of-the-art implants. The large size of the implant imposes two major challenges: the necessity of a good contact between the implant and the retina and of a safe implantation procedure. To address these challenges, the photovoltaic interface is placed on a curved and stretchable substrate, able to be folded, injected into the eye through a small scleral cut, and self-unfold to recover the curvature matching the one of the eyes. Consequently, the rigid pixels were mechanically engineered to withstand the required deformation.

We investigated the use of organic optoelectronic materials, such as P3HT:PCBM and PCPDTBT:PCBM, to manufacture photovoltaic pixels able to induce retinal ganglion cells activity upon illumination with short pulses of light. For both systems, light pulses of irradiances within the safety limits allowed the photogeneration of currents and voltages suitable for a stimulation frequency up to 20 Hz with green (565 nm) and near-infrared (730 nm) light, respectively. The conjugated polymer PEDOT:PSS and sputtered Ti (with TiN coating) were used for the anodic and cathodic ends correspondingly, with only the Ti-TiN surface exposed to the electrolytic solution. *Ex vivo* evaluation with blind mice retinas demonstrated that the photovoltaic pixels could induce, together with direct electrical short-latency stimulation, medium-latency spiking activity of retinal ganglion cells as evidence of prosthetic-induced network-mediated responses.

Investigations and optimizations about functional, mechanical, thermal, optical, and stability properties of the prosthesis were carried out in vision of *in vivo* experiments with blind miniature pigs. Blinded by IAA treatment, the miniature pigs recovered light sensitivity when implanted with the prosthesis. This preliminary result motivates further preclinical inquiries with the prosthesis towards clinical applications.

Keywords

POLYRETINA, artificial vision, retinal prosthesis, photovoltaic stimulation, curved injectable implant, organic optoelectronic materials, OSTEmer, retinal ganglion cells, miniature pigs.

Sommario

Lo sviluppo tecnologico nel campo della microingegneria e delle scienze dei materiali ha favorito la produzione di protesi visive innovative, utili a combattere la cecità e a migliorare la qualità di vita dei pazienti. Le protesi visive mirano a rimpiazzare le funzioni della vista stimolando artificialmente (elettricamente) i circuiti restanti della retina con l'aiuto di elettrodi microfabricati, i quali possono indurre l'apparizione di fosfeni nelle persone cieche. Le protesi retiniche offrono un trattamento promettente per le persone affette da malattie degenerative della retina grazie a svariati vantaggi, tra cui l'organizzazione retinotopica, un'ampia superficie disponibile alla stimolazione, e un diretto accesso chirurgico nonché ottico. Quest'ultima caratteristica risulta conveniente per le protesi fotovoltaiche, in cui le informazioni visive e l'energia necessaria per attivare gli elettrodi sono trasmesse wireless da luce intensificata attraverso la pupilla. Dal momento che le connessioni elettriche non sono necessarie, è possibile situare un gran numero di pixels stimolanti in uno spazio ristretto. Tuttavia, nonostante i progressi, attualmente non esiste una protesi retinica che possa provvedere ad un'elevata risoluzione e ampia copertura del campo visivo.

In questa tesi viene illustrato lo sviluppo di una protesi epiretinica fotovoltaica e pieghevole, con un'elevata densità di pixels (fino a 18'600 pixels con una densità 141 pixels/mm²) distribuiti su un'ampia superficie capace di coprire 46° di campo visivo, notevolmente superiore rispetto alle attuali protesi. La vasta superficie, tuttavia, impone due sfide principali: la necessità di un buon contatto tra protesi e retina e di una procedura di impianto sicura. Per affrontare queste sfide, l'interfaccia fotovoltaica è posizionata su un substrato estensibile con una curvatura adattata a quella oculare, in grado di essere arrotolato e iniettato nell'occhio attraverso un piccolo taglio sclerale e di riaprirsi per recuperare la curvatura iniziale. Di conseguenza, i pixels rigidi sono stati meccanicamente concepiti per resistere alla deformazione necessaria.

Per produrre pixels fotovoltaici in grado di stimolare le cellule gangliari della retina con brevi impulsi di luce, abbiamo esplorato l'uso di materiali organici optoelettronici, come P3HT:PCBM e PCPDTBT:PCBM. Per entrambi i sistemi, gli impulsi luminosi hanno permesso la fotogenerazione di correnti adatte ad una frequenza di stimolazione fino a 20 Hz con luce rispettivamente verde (565 nm) e vicino infrarosso (730 nm). Il polimero coniugato PEDOT:PSS e Ti applicato in sputtering (con rivestimento in TiN) sono stati usati per l'estremità anodica e catodica, con la superficie di TiN esposta alla soluzione elettrolitica. I test *ex vivo* su retine di topi ciechi hanno dimostrato che i pixels fotovoltaici inducono, insieme alla stimolazione elettrica diretta, attività di spiking a media latenza delle cellule gangliari. Questo risultato è la prova di una risposta indotta dalla protesi e mediata dal circuito retinico.

Inoltre, abbiamo condotto analisi e ottimizzazioni riguardanti le proprietà funzionali, meccaniche, termiche, ottiche e di stabilità della protesi in vista di esperimenti *in vivo* con maiali con cecità indotta da IAA. Gli animali hanno recuperato la sensibilità alla luce una volta impiantati con la protesi. Questo risultato preliminare motiva ulteriori sforzi verso indagini precliniche e future applicazioni cliniche.

Parole chiavi

POLYRETINA, visione artificiale, protesi retinica, stimolazione fotovoltaica, impianto sferico e iniettabile, materiali organici optoelettronici, OSTEmer, cellule gangliari della retina, minipig.

Contents

Acknowledgements	v
Abstract	xi
Sommario	xiii
List of Figures	xix
List of Tables	xxiii
List of Equations	xxv
Symbols and variables	xxvii
Nomenclature and abbreviations	xxix
Chapter 1 Introduction	1
1.1 The human visual system.....	4
1.2 Vision impairments.....	6
1.3 Approaches for vision restoration.....	7
1.3.1 LGN and cortical visual prostheses	8
1.3.2 Optic nerve prostheses	9
1.3.3 Retinal prostheses	9
1.4 Photovoltaic stimulation of the retina.....	15
1.5 Thesis strategy	17
1.5.1 Motivation and open challenges	17
1.5.2 Objectives and thesis structure	18
Chapter 2 Development and validation of a wide-field and photovoltaic epiretinal prosthesis	21
2.1 Introduction	23
2.2 Results	23
2.2.1 Design and fabrication.....	23
2.2.2 Optimization of the photovoltaic pixel	27

2.2.3	Validation <i>ex vivo</i> with explanted retinas from blind mice.....	32
2.2.4	Spatial selectivity	36
2.2.5	Cytotoxicity and long-term functioning.....	37
2.2.6	Thermal and optical safety.....	39
2.3	Discussion.....	42
2.4	Methods	44
2.4.1	Prosthesis microfabrication.....	44
2.4.2	Chips microfabrication.....	45
2.4.3	Ti electrochemical characterization	46
2.4.4	pH measurements	46
2.4.5	Kelvin probe force microscopy.....	46
2.4.6	Accelerated ageing tests.....	46
2.4.7	Measure of PV and PC.....	47
2.4.8	Electrophysiology	47
2.4.9	Spatial selectivity measures and modeling	48
2.4.10	Optical safety	48
2.4.11	Thermal measurements	49
2.4.12	Thermal modeling.....	49
2.4.13	<i>In vitro</i> cytotoxicity test	50
2.4.14	Surgical implantation	51
2.4.15	Statistical analysis and graphical representation.....	51
2.5	Acknowledgements.....	51
Chapter 3	Optimization of the POLYRETINA pixel	53
3.1	Introduction.....	55
3.2	Results.....	56
3.2.1	Impact of the pixels density	56
3.2.2	Spatial selectivity of stimulation.....	59
3.2.3	Single pixel electrophysiology.....	60
3.3	Discussion.....	63
3.4	Methods	64
3.4.1	Prostheses and chip microfabrication	64
3.4.2	Mechanical FEA simulations	64
3.4.3	Voltage spreading	65
3.4.4	KPFM.....	65
3.4.5	PC and PV measurements.....	66
3.4.6	Electrophysiology	66
3.4.7	Statistical analysis and graphical representation.....	66

3.5	Acknowledgements.....	66
Chapter 4	POLYRETINA for <i>in vivo</i> experiments in miniature pigs	67
4.1	Introduction	69
4.2	Results	70
4.2.1	Improving mechanical stability.....	70
4.2.2	OSTEmer encapsulation	73
4.2.3	Black POLYRETINA.....	75
4.2.4	POLYRETINA injector	77
4.2.5	Preliminary <i>in vivo</i> results	79
4.3	Discussion.....	83
4.4	Methods	84
4.4.1	Prostheses microfabrication.....	84
4.4.2	AFM and roughness measurements	86
4.4.3	Ti and TiN electrochemical characterization.....	86
4.4.4	Transmittance measurements.....	86
4.4.5	Mechanical characterizations.....	86
4.4.6	Sterilization procedures	87
4.4.7	Animals and anesthesia.....	87
4.4.8	IAA injection	87
4.4.9	Spectral domain-OCT	88
4.4.10	Immunohistochemistry	88
4.4.11	Hematoxylin and Eosin staining	88
4.4.12	Electrode implantation and electrophysiological recordings	88
4.4.13	Surgical procedure and POLYRETINA implantation.....	89
4.4.14	Statistical analysis and graphical representation.....	89
4.5	Acknowledgments	90
Chapter 5	Toward a NIR-responsive POLYRETINA.....	91
5.1	Introduction	93
5.2	Results	94
5.2.1	Optimization of the bulk heterojunction	94
5.2.2	Optoelectronic optimization of the anodic layer.....	96
5.2.3	Optimization of the anodic layer adhesion	97
5.2.4	Thermal management	102
5.2.5	Functional validation of the NIR-responsive photovoltaic prosthesis	103
5.3	Discussion.....	105
5.4	Methods	106

5.4.1	Chip microfabrication	106
5.4.2	Measure of photo-voltage and photo-current.....	106
5.4.3	Spectral absorbance	106
5.4.4	Resistance measurements.....	107
5.4.5	Thickness measurements	107
5.4.6	Time-of-flight secondary ion mass spectrometry measurements.....	107
5.4.7	Fabrication of nir-POLYRETINA prostheses	107
5.4.8	Cytotoxicity test.....	107
5.4.9	Electrophysiology <i>ex vivo</i>	108
5.4.10	Optical safety	108
5.4.11	Thermal model.....	108
5.4.12	Statistical analysis and graphical representation.....	110
5.5	Acknowledgments	110
Chapter 6	Conclusions and Outlook.....	111
6.1	Summary of performed research.....	113
6.2	Limitations.....	114
6.3	Future perspectives	115
Appendices	119
References	127
List of publications	141
Curriculum Vitae	143

List of Figures

Figure 1.1 The human visual system.....	4
Figure 1.2 Visual acuity and visual field.	5
Figure 1.3 Occurrence of vision impairments and outer retinal degenerations.....	6
Figure 1.4 Visual prostheses.	8
Figure 1.5 Three examples of retinal prostheses.....	11
Figure 1.6 Electrical stimulation of RGCs.....	13
Figure 1.7 Materials and structures for photovoltaic stimulation of retinas.	16
Figure 1.8 The concept of POLYRETINA.....	19
Figure 2.1 Design and materials of POLYRETINA.....	24
Figure 2.2 Evaluation of Ti-electrolyte charge injection mechanism.	25
Figure 2.3 Foldable and wide-field retinal prosthesis.....	26
Figure 2.4 Simulated surgical implantation.	27
Figure 2.5 Optimization of the photovoltaic pixel.....	28
Figure 2.6 Characterization of the photo-current and photo-voltage.....	30
Figure 2.7 High-frequency train stimulation.....	31
Figure 2.8 Evaluation <i>ex vivo</i> with retinal explants.....	32
Figure 2.9 Further evaluation <i>ex vivo</i> with retinal explants.....	34
Figure 2.10 Recordings of Rd10 retinas <i>ex vivo</i>	35
Figure 2.11 Pharmacological blockage of network activity.....	36
Figure 2.12 Spatial confinement of the prosthetic stimulation.....	37
Figure 2.13 Lifetime of the retinal prosthesis.....	38
Figure 2.14 Temperature variation during operation.....	39
Figure 2.15 Optical absorption of POLYRETINA.....	40
Figure 2.16 FEA simulation of thermal effects.....	41
Figure 2.17 FEA simulation of thermal effects with POLYRETINA.....	42
Figure 2.18 Microfabrication process flow of POLYRETINA photovoltaic interface. ..	45
Figure 2.19 Aggregated model of POLYRETINA.....	50
Figure 3.1 Capacitive-like (photovoltaic) vs rectangular monopolar stimulation of RGCs.....	55
Figure 3.2 Improved designs for a high-density POLYRETINA.....	57

Figure 3.3	Fabrication of patterned pixels with the four layouts.	58
Figure 3.4	Mechanical validation of the new POLYRETINA layouts.	59
Figure 3.5	Evaluation of the electrical crosstalk of the photovoltaic pixels.	60
Figure 3.6	Characterization of the photovoltaic pixels with Ti-TiN electrodes.....	61
Figure 3.7	Responses of RGCs stimulated upon illumination of photovoltaic pixels with Ti and Ti-TiN electrodes.....	62
Figure 3.8	Thicknesses and sizes used for construction of the deformable membrane in Abaqus.	65
Figure 4.1	Parylene-C for improved mechanical stability.	71
Figure 4.2	Increased roughness of Ti and Ti-TiN electrodes.....	72
Figure 4.3	OSTEmer material.	74
Figure 4.4	The POLYRETINA version with improved stability for preclinical trials with minipigs.....	75
Figure 4.5	Development of black POLYRETINA.	76
Figure 4.6	Characterization of the black OSTE coating.	77
Figure 4.7	POLYRETINA injection.	78
Figure 4.8	Göttingen minipig model of IAA-induced photoreceptor degeneration. ...	80
Figure 4.9	Surgical implantation of POLYRETINA in Göttingen minipig eyes.....	81
Figure 4.10	Prosthetic-evoked recordings in minipigs primary visual cortex.....	82
Figure 4.11	Microfabrication process flow of the second-generation POLYRETINA photovoltaic interface.....	86
Figure 5.1	Relevance of NIR illumination for organic photovoltaic retinal prostheses.....	94
Figure 5.2	Optimization of the bulk heterojunction.....	95
Figure 5.3	Optimization of the anodic layer.....	97
Figure 5.4	Optoelectronic responses with GOPS.....	98
Figure 5.5	Electrical tuning with the GOPS concentration.....	99
Figure 5.6	Adhesion of the interface.....	100
Figure 5.7	Redistribution of molecules as a function of the GOPS concentration....	101
Figure 5.8	Thermal simulations.	103
Figure 5.9	Functional validation <i>in vitro</i> and <i>ex vivo</i>	104
Appendix Figure 1	Microfabrication process flow of the Si stencils.....	119
Appendix Figure 2	Photographs of Si stencils and application.....	120

Appendix Figure 3 ISO certificate for *in vitro* cytotoxicity of POLYRETINA. 120

Appendix Figure 4 Simulation with virtual reality of phosphenes appearance from POLYRETINA stimulation. 121

Appendix Figure 5 Dependence of von Mises tensile stress from Ti thickness..... 121

Appendix Figure 6 Details about the PDMS domes, molding, and bonding. 122

Appendix Figure 7 Materials for nir-POLYRETINA..... 124

Appendix Figure 8 Possible molecular interactions between the organic layers of nir-POLYRETINA. 124

List of Tables

Table 1.1 Pros and cons of epiretinal and subretinal prostheses.	10
Table 1.2 List of the principal retinal prostheses	12
Table 2.1 FEA simulation of thermal effects.	49
Table 2.2 FEA model of POLYRETINA.	50
Table 3.1 Calculated visual field and theoretical acuity for the four POLYRETINA designs	57
Table 3.2 Materials parameters used for the mechanical simulations in Abaqus.....	65
Table 4.1 Characterization of electrode-electrolyte interface with different materials and surface roughness.	73
Table 5.1 Eye parameters for the FEM model.	109
Table 5.2 Aggregated parameters for nir-POLYRETINA.....	109
Appendix Table 1 Microfabrication details for POLYRETINA presented in Ch 4.....	123

List of Equations

Equation 2.1 Calculation of visual field coverage.....	26
Equation 2.2 Acceleration factor for accelerated ageing tests.....	46
Equation 2.3 MPE_T calculation for optical safety.....	48
Equation 2.4 MPE_C calculation for optical safety	49
Appendix Equation 1 Equivalent model of electrode-electrolyte impedance.....	119
Appendix Equation 2 Calculation of equivalent absorption coefficients	125
Appendix Equation 3 Calculation of equivalent specific heat capacity	125
Appendix Equation 4 Calculation of equivalent thermal conductivity.....	125
Appendix Equation 5 Calculation of equivalent density	125

Symbols and variables

α	Visual field	[°]
α''	Visual angle (also used for visual acuity)	[°]
C_{DL}	Double layer capacitance	[F]
C_j	Junction capacitance	[F]
d	Pixel diameter	[m]
D	Implant diameter or diagonal	[m]
i	Current	[A]
I_D	Diode current	[A]
I_{pv}	Photovoltaic current	[A]
j	Imaginary unit ($j^2 = -1$)	[-]
λ	Wavelength	[m]
n	Constant phase element's empirical factor	[-]
n	Number of measurements	[-]
N	Number of animals or chips/prostheses	[-]
ω	Angular frequency	[rad s ⁻¹]
p	Pitch size	[m]
PC	Photocurrent	[A]
PCD	Photocurrent density	[A m ⁻²]
PV	Photovoltage	[V]
r	Radius of curvature	[m]
R^2	Coefficient of determination (statistics)	[-]
R_{CT}	Charge transfer resistance	[Ohm]
R_s	Series resistance	[Ohm]
R_{sh}	Shunt resistance	[Ohm]
R_{spread}	Spreading resistance	[Ohm]
$\tau_{fast(slow)}$	Time constants of (bi)exponential decay	[s]
V_{app}	Applied voltage	[V]

Nomenclature and abbreviations

3D	Three-dimensional	IrOx	Iridium oxide
AFM	Atomic force microscopy	ITO	Indium tin oxide
Ag/AgCl	Silver/silver chloride	KPFM	Kelvin probe force microscopy
Al	Aluminum	L-cone	Long-wavelength sensitive cone
AMD	Age-related macular degeneration	LED	Light emitting diode
Ar	Argon	LGN	Lateral geniculate nucleus
ASIC	Application specific integrated circuit	LIFE	Longitudinal intrafascicular electrodes
BHJ	Bulk heterojunction	LL	Long latency
CB	Carbon black	LUMO	Lowest unoccupied molecular orbital
CE	Certification Europe	M-cone	Medium-wavelength sensitive cone
Cl ₂	Chlorine gas	MAR	Minimum angle of resolution
CNS	Central nervous system	MEA	Multielectrode array
CO ₂	Carbon dioxide	ML	Medium latency
CPE	Constant phase element	MPE	Maximum permissible exposure
CSC	Charge storage capacity	N ₂	Nitrogen gas
CV	Cyclic voltammetry	NaCl	Sodium chloride
CVD	Chemical vapor deposition	NIR	Near-infrared
CW	Continuous wave	O ₂	Oxygen gas
DC	Direct current	OCT	Optical coherence tomography
DI	Deionized	ONL	Outer nuclear layer
ED50	50% probability of retinal damage	OSTE	Off-stoichiometry thiol-ene-epoxy
EIS	Electrochemical impedance spectroscopy	P3HT	Poly(3-hexylthiophene-2,5-diyl)
ERG	Electroretinography	PBS	Phosphate-buffered saline
FDA	Food and Drug Administration	PC	Photo-current
FEA/M	Finite element analysis/method	PCBM	Phenyl-C ₆₁ -butyric acid methyl ester
FWHM	Full width at half maximum	PCD	Photo-current density
GOPS	(3-glycidyloxypropyl)trimethoxysilane	PCPDTBT	Poly[2,6-(4,4-bis-(2-ethylhexyl)-4H-cyclopenta [2,1-b;3,4-b']dithiophene)-alt-4,7(2,1,3-benzothiadiazole)]
He	Helium	PDE	Partial differential equation
H&E	Haematoxylin and Eosin (staining)	PDMS	Polydimethylsiloxane
HOMO	Highest occupied molecular orbital	PEDOT	Poly(3,4-ethylenedioxythiophene)
HTL	HTL PEDOT:PSS	PES	Polyethersulfone
IAA	Iodoacetic acid	PH1000	PH1000 PEDOT:PSS
ICP	Inductively coupled plasma	PI	Polyimide
IHC	Immunohistochemistry	PMMA	Poly(methyl methacrylate)
INL	Inner nuclear layer	PNS	Peripheral nervous system
IPA	Isopropyl alcohol	PSS	Poly(styrene sulfonate)
IR	Infrared		

Nomenclature and abbreviations

PSTH	Peri-stimulus time histogram	Si	Silicon
Pt	Platinum	SiO ₂	Silicon dioxide
PTFE	Polytetrafluoroethylene	SL	Short latency
PV	Photo-voltage	Ti	Titanium
Rd10	Retinal degeneration 10	TiO _x	Titanium oxide
RF	Radio frequency	TIME	Transverse intrafascicular multichannel electrodes
RGC	Retinal ganglion cell	TiN	Titanium nitride
RMS	Root mean square	ToF-SIMS	Time-of-Flight Secondary Ion Mass Spectrometry
RP	Retinitis pigmentosa	UV	Ultra-violet
RPE	Retinal pigmented epithelium	V1	Primary visual cortex
S-cone	Short-wavelength sensitive cone	VEP	Visually evoked potential
s.d.	Standard deviation	VPU	Visual processing unit
SELINE	Self-opening intraneural electrodes		
SEM	Scanning electron microscopy		
s.e.m.	Standard error of the mean		

Chapter 1 Introduction



Eyes of a mantis shrimp (Source: Michael Bok)

NOTE to the reader:

At the beginning of each chapter, I decided to share photographs of spectacular eyes found in the animal kingdom. I hope you will appreciate the beauty and complexity of these nature's works of art.

The technological evolution achieved over the years by the congregation of human brains favored the enhancement of our lives. We live safer, better, and thus longer than our ancestors; and we are blessed with successful medical treatments for diseases that some time ago people would have classified as lethal. Although these achievements surely warm our hearts and lift our spirits, a growing burden appears on the other side of the coin carrying, among other issues related to the population increase, those modern health problems that are inevitably related to ageing (in addition to genetic and environmental conditions)¹ and to a confused natural selection. However, humanity's ambition, curiosity, and stubbornness will always try to advance science and technology to solve those consecutive health problems related to the previous scientific and technological advancements. In certain fields, a never-ending, exciting dance battle between technology and biology has started. Moreover, we are quick learners; natural materials and their architectures, and the biology and the physics of nature's phenomena are a source of inspiration for artificially constructed compounds and machines to be used for our benefit. Bio-inspiration is a bold move; but, will technology ever outsmart nature? I doubt it. Nature has countless and extraordinary resources, which often operate and dovetail unpredictably.

To narrow the subject (and for the sake of this thesis), understanding the brain, its functions, and its diseases has motivated researchers in the 20th Century to cross new biomedical frontiers and develop advanced neurotechnologies to help the hundreds of million people worldwide that suffer from neurological and mental disorders.² Neuroengineering might nowadays offer potential solutions for neurological afflictions based on prosthetic devices, which establish bidirectional communication between electronic machines and neurons.³⁻⁵ Neuromodulation, for instance, is a technique that allows influencing the activity of neurons via their excitation or inhibition.⁶ Consequently, the modulation of the central and peripheral nervous system (CNS and PNS, respectively) allows to induce sensory perception (e.g., blindness⁷, deafness⁸, and amputation⁹), control movement disorders (e.g., Parkinson's disease¹⁰ and spinal cord injury¹¹), improve memory deficits (e.g., Alzheimer's disease¹²), alleviate behavioral disorders (e.g. obsessive-compulsive disorder¹³ and addiction¹⁴), and reduce pain (e.g., phantom limb pain¹⁵). One approach to stimulate and record neuronal activity is using implantable neural interfaces, which offer an intimate connection with the nervous tissue. Pertinently, the progresses in materials science and micro-/nanofabrication techniques permitted the miniaturization of imaging and communication systems down to cellular, molecular, and even single photon resolutions.^{16,17}

It is the dawn of neuroprosthetics, that is, the repair or substitution of impaired sensory, motor, and cognitive functions by means of prostheses. One of the first neuroprosthetic devices was a cochlear implant developed in 1957 by André Djourno and Charles Eyriès.¹⁸ After that, numerous other pioneering works were carried out based on the discovery of electrophysiology and the electrical stimulation of human tissue in the 18th Century.¹⁹⁻²¹ To mention another example, in the late 1960s efforts were made to produce vision sensations in blind patients.²²

Among human senses, vision is probably the most appreciated one and the most missed in case of loss. Ambitious research and developments in order to restore sight originated about 50 years ago and progresses never stopped ever since. In this regard, the proposed thesis is about novel technologies and materials suitable for improving the state of the art in artificial vision. The work focuses on enhancing important aspects of modern retinal prostheses to obtain a safer and more useful form of artificial vision for people blinded by retinal degeneration diseases. The interdisciplinary nature of this work required, in addition to my expertise in materials science, the synergy from various

researchers including bioengineers, neurobiologists, and ophthalmologists. In the following paragraphs, relevant aspects related to the thesis will be introduced; namely, the human visual system, the typologies of pertinent vision impairments, some modern strategies for the restoration of sight (with emphasis on retinal prostheses), and the possibility to exploit light as a mean for electrical stimulation of retinal neurons, which is the working principle of the developed implants in this thesis.

1.1 The human visual system

One of the most impressive and complex visual systems in the animal kingdom is the one of the mantis shrimp (*Neogonodactylus Oerstedii*), displayed in the photograph at the beginning of this chapter. This crustacean, apart from having the fastest punch on Earth, has 12 classes of color photoreceptor, and hence, it is able to detect a light wavelength range much wider than humans²³, which only have three type of color photoreceptors (cones). However, although very interesting, we are not going to talk about the mantis shrimp any further, but we will focus on the human visual system, which is an example of nature's piece of art as well.

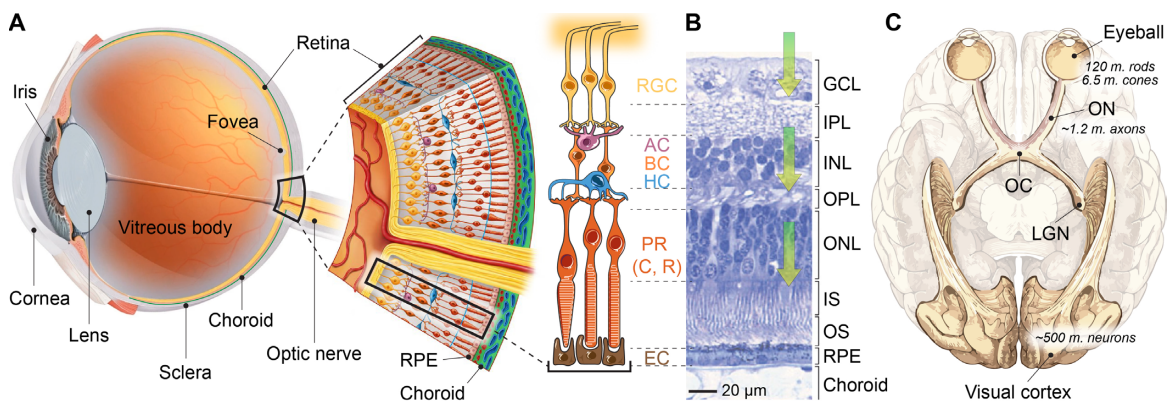


Figure 1.1 The human visual system. **A)** Components and organization of the eye and the retina. RPE: retinal pigmented epithelium, RGC: retinal ganglion cells, AC: amacrine cells, BC: bipolar cells, HC: horizontal cells, PR: photoreceptors, C: cones, R: rods, EC: epithelial cells. Müller cells are here omitted. **B)** Micrograph of an H&E-stained transverse section of a human retina.²⁴ GCL: ganglion cell layer, IPL: inner plexiform layer, INL: inner nuclear layer, OPL: outer plexiform layer, ONL: outer nuclear layer, IS: photoreceptor's inner segment, OS: photoreceptor's outer segment, RPE: retinal pigmented epithelium. Arrows indicate the path of the light reaching the IS and OS absorbing layers. **C)** Schematics of the horizontal cut view of a human brain with the visual path highlighted.²⁵ 120 million rods and 6.5 million cones converge into 1.2 million axons, which then branch out to 500 million neurons at the visual cortex.²⁶ ON: optic nerve, OC: optic chiasm, LGN: lateral geniculate nucleus.

The journey of visual information starts from the eye (**Figure 1.1A**), which can be represented as a sphere of about 12 mm in radius filled with the gelly vitreous body.²⁷ The light passes through the cornea, enters the pupil surrounded by the iris, and is focused by the lens onto the retina, the nervous tissue that conveys extraordinary image processing.²⁴ The first cells touched by the projected light are not the photosensors; light has to travel through the entire thickness of the retina until reaching the outer nuclear layer (ONL), where photoreceptors (rods and cones) are vertically oriented and accommodated on the retinal pigmented epithelium (RPE). **Figure 1.1B** shows a micrograph of a human retina transversal section, where different cells layers and cells nuclei are easily recognizable.²⁴ The total thickness of a human healthy retina (choroid excluded) is about 220 μm. The arrows in the picture indicate the path of the light from the surface of the retina to the photoreceptors' inner

and outer segments, where the light is absorbed. Cone photoreceptors are responsible for high-acuity and color vision, while rod photoreceptors allow us to see at low light intensity levels (scotopic vision). All photoreceptors communicate back to horizontal and bipolar cells in the inner nuclear layer (INL), which signal to amacrine cells and finally to retinal ganglion cells (RGCs). The axons of each RGC extend from the location of the cell body to the optic disc, where they are collected and directed out of the eyeball to form the optic nerve (**Figure 1.1A** and C). At the optic chiasm, the two optic nerves are split roughly in half and recollected to have the same visual field side bundle together. The axons finally arrive at the lateral geniculate nucleus (LGN) of the thalamus, where the visual input is sent to the occipital lobe at the primary visual cortex (V1) for information integration and generation of visual experiences.

Visual acuity is a measure of the clarity and sharpness of vision, and it can be influenced by refractive errors (such as the cornea and lens focusing) or neurological issues (such as a malfunctioning somewhere along the visual path from the retina to the brain cortex). A healthy human visual system is able to recognize letters and symbols rated 20/20 or better on the Snellen chart (**Figure 1.2A**), which means that its minimum angle of resolution (MAR) measures 1 minute of arc ($1/60^\circ$). A person with 20/200 vision, for instance, can see objects at 20 feet that a person with normal vision manages to see at 200 feet. High visual acuity vision is found in the fovea (central point on the retina) and is very important for reading and faces recognition.²⁸ Peripheral vision, however, is characterized by a lower concentration of cone photoreceptors compared to the fovea. **Figure 1.2B** shows how the density of cones exponentially decays with retinal eccentricity.²⁹ The effect of such distribution is represented in **Figure 1.2C** with an example of reading. The reading of the entire music sheet can be obtained through scanning, but if we fix our gaze to the center (note colored in red) we would not be able to read what is outside the delimitation of 10° field (how it is represented on the right). Nevertheless, although peripheral vision has a lower resolution, it is just as much valuable as the macular high visual acuity. In fact, humans can get information about the location of objects, their overall shape and size, their color, and their movements from a field of view much wider than 10° (see **Figure 1.2D**). The extent of a normal visual field is up to about 200° horizontally (with 120° binocular) and 130° vertically.³⁰ Vision is essential up to the far periphery, even if with poor resolution, in order for us to move in the environment, avoid obstacles, and react to incoming dangers such as cars, flying axes, and running bears.

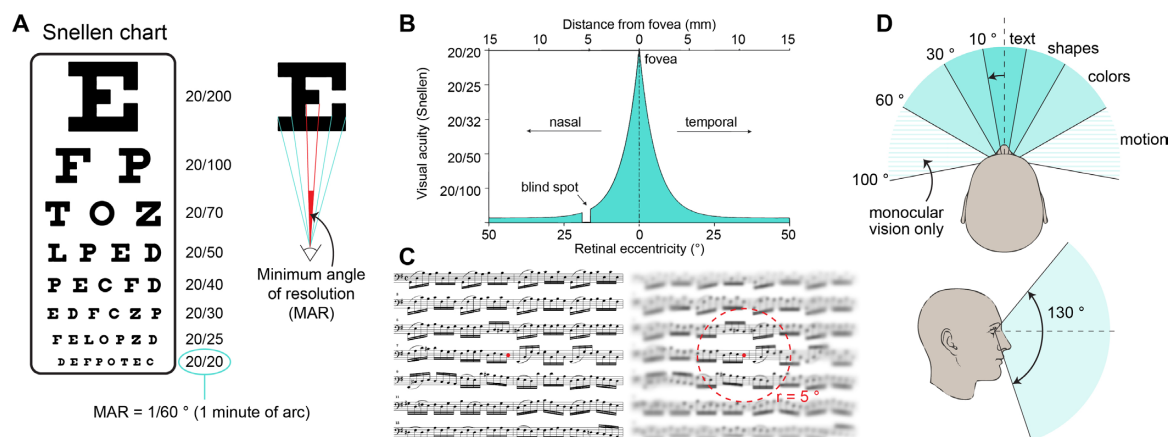


Figure 1.2 Visual acuity and visual field. **A)** Assessment of visual acuity with a Snellen chart. The minimum angle of resolution (MAR) is defined as the corresponding angle of the minimal recognizable feature size. In

normal vision (20/20), the MAR equals 1 minute of arc. **B**) Graphical representation of the relative cone density (expressed in visual acuity) depending on retinal eccentricity (or distance from the fovea). The blind spot delineates the location of the optic disc, where no photoreceptors are present. Adapted from Lambertus *et al.* 2017.²⁹ **C**) Likeness of real vision: the image on the right depicts the plausible visual acuity when fixing the note marked in red. **D**) Extent of human's horizontal (top image) and vertical (bottom image) visual fields.³⁰

1.2 Vision impairments

Vision disorders, especially among an ageing population, are a major health issue for society and for the individual's quality of life. The discomfort caused by these afflictions is immense and it can lead to anxiety and depression.³¹ It hinders or completely eliminates the possibility to perform the majority of professions and routine activities, sustain independency, and experience everyday-life visual emotions (like seeing someone's face and expressions). Blindness is defined as visual acuity of less than 20/400 or a corresponding visual field loss to less than 10 °, in the better eye with the best possible correction.³² In North America and most of European countries, legal blindness is defined as visual acuity worse than 20/200 or visual field no greater than 20 °. This burden affects more than 38 million people worldwide and it is estimated that there will be 115 million blind people by 2050.³³ Additionally, this is only a portion of the persons with vision impairments, as more than 230 million people worldwide have today moderate to severe vision loss (estimated 587 million in 2050), which corresponds – together with the blind – roughly to 4-5% of the world population (see **Figure 1.3A**). The most common causes of vision impairments and blindness are cataract, glaucoma, macular degeneration, diabetic retinopathy, trachoma, and uncorrected refractive errors, which all situate at the level of the eye.³⁴ However, an impairment can occur along the entire visual path (**Figure 1.3B**, blue dots) and can be due to genetic, environmental, or traumatic reasons.

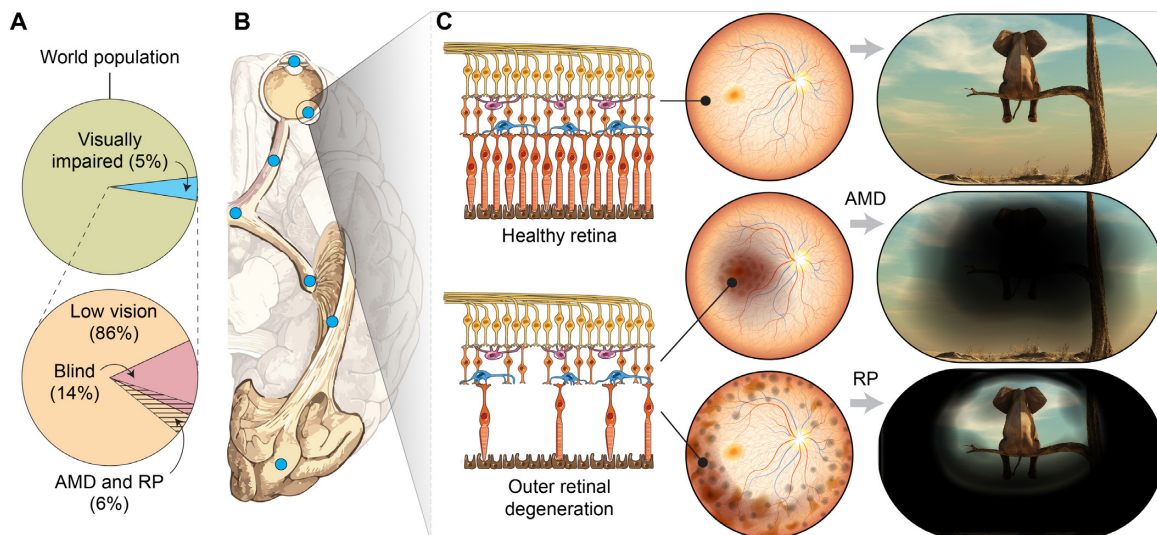


Figure 1.3 Occurrence of vision impairments and outer retinal degenerations. **A**) Pie charts depicting the abundance of visually impaired people worldwide (moderate to severe vision loss and blindness).³³ AMD and RP account for over 6% of such group. **B**) Approximate regions of impairment origin (from top to bottom): optical components of the eye, retina, optic nerve, optic chiasm, LGN, optic radiations, V1.²⁵ **C**) Illustration of retinal cell layers, fundus, and vision of a healthy retina and a retina affected by photoreceptors degeneration (AMD and RP). People affected by these visual disorders might as well interpret the world in completely different ways.

Vision loss can occur because of the progressive degeneration of photoreceptors, resulting in dysfunctional light detection, transduction, and transmission. Among these chronic degenerative diseases, retinitis pigmentosa (RP) is the most common form of inherited retinal dystrophies. RP is characterized by a continuous death of rods, resulting in loss of night vision at first, followed by a loss of peripheral vision, to culminate in loss of central vision due to implication of cones. The age of affected people can vary from children to elderly.³⁵ Another brutal degenerative disease of the retina is the age-related macular degeneration (AMD), which afflicts photoreceptors in the central (macula) vision first. AMD has a smaller hereditary component, but is the leading cause of blindness worldwide for people over 60 years old.³⁶ **Figure 1.3C** illustrates the two mentioned examples of photoreceptors progressive deterioration. When looking at the eye fundus and compared to a healthy retina, the outer retinal degeneration in AMD and RP leads to the appearance of stains in the macular or peripheral regions of the retina, respectively. Consequently, the image perceived by the patients is affected in the center for AMD or on the sides for RP, which develops the so-called “tunnel” vision before complete blindness.

1.3 Approaches for vision restoration

Nowadays, there is no cure for blindness and conditions like AMD and RP but to prevent or mitigate the disease advancement, which is often detected too late. Moreover, in the late stages of photoreceptors degeneration, certain therapeutic approaches such as pharmacotherapy, gene replacement therapy, and neuroprotection are not suitable anymore, leaving to other strategies like optogenetics, stem cells therapy, and visual prostheses the ambition to achieve some sort of artificial vision.³⁷ Although the development of efficient biomedical and engineering concepts is promisingly advancing, for some of the emerging treatments the path for clinical and commercial applications remains delayed. However, visual prostheses, more precisely retinal prostheses, have finally received regulatory market approval in Europe and United States, becoming a valuable option to artificially induce visual perceptions in blind patients.

The long journey of visual prostheses started in 1755 with Charles LeRoy, who could evoke visual disturbances in a blind volunteer with a wire conducting electricity wrapped around the head (**Figure 1.4A**).^{20,38} Since then, 265 years of scientific and technological discoveries lead to the development of more advanced visual implants, which can be classified according to their implantation location (**Figure 1.4**): at the retina (B), along the optic nerve (C), in the deep brain (D), and at the brain cortex (E). Generally, in addition to the implanted interface, visual prostheses are combined with a system to capture the information from the environment (a camera) and a computing unit for encoding stimulation protocols to deliver the artificial input to the targeted neurons. Currently and independently from the implant location, most of the developed prostheses stimulate neuronal cells using electrical fields (voltage perturbations) based on the Hodgkin–Huxley model of excitable tissue.³⁹

The artificial vision created by the stimulation is defined by the appearance of bright spots and lines within the darkness of a blind patient. These bright spots are called phosphenes and can have various brightness, shape, size, and blurring depending on the stimulating electrodes (size, shape, pitch, and field lines distribution), stimulation parameters (current pulse intensity, length, and frequency), and anatomical target (cf. **Figure 1.4B-E**).^{40,41} Because of the variety and the potential offered from these prosthetic approaches, the state of the art and the main features of the mentioned visual prostheses will be briefly discussed in the next paragraphs.

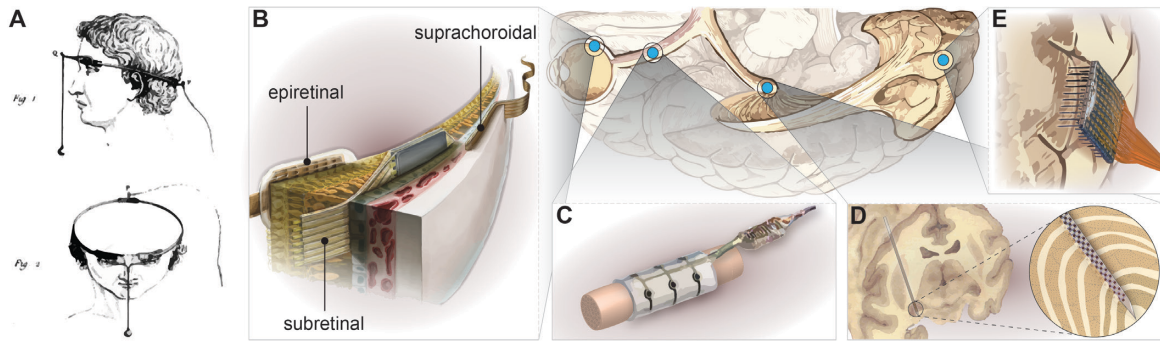


Figure 1.4 Visual prostheses. **A)** First demonstration by Charles LeRoy of visual perceptions induced by electricity to a blind volunteer (year 1755).²⁰ **B)** Modern retinal prostheses can be placed epiretinal, subretinal, or suprachoroidal. Adapted from Zrenner 2013.²⁶ Reprinted with permission from AAAS. **C)** Example of a nerve prosthesis with cuff electrodes that can be used for optic nerve stimulation.⁴² **D)** The LGN can be targeted with adapted deep brain implants. **E)** Cortical stimulation can be obtained with penetrating Utah arrays, for instance.⁴³

1.3.1 LGN and cortical visual prostheses

The LGN is a stratified compact relay structure that is found within the thalamus, deep into the brain (**Figure 1.4D**). Consequently, visual prostheses targeting the LGN have been investigated and developed only recently thanks to the progresses acquired for deep brain stimulation (used to treat Parkinson's disease among other neurological disorders).⁴⁴ The interest in stimulating the LGN to create artificial vision comprises the possibility to target many patients with damages at the level of the eye or optic nerve (such as glaucoma), the coverage of a wide visual field with overcompensation of the fovea region (i.e. possible high-acuity prosthetic vision), and the physical division of pathways for color vision.⁴⁵ However, a full coverage of the visual field would require one implant for each brain hemisphere.²⁵ The potential of the LGN electrical stimulation to elicit phosphenes has been extensively proven during the past 20 years.⁴⁶ Yet, current deep brain implants for vision restoration are found only in the preclinical phase; furthermore, adapted prostheses for the human visual thalamus are still missing from literature (hopefully, they are under development).

Cortical implants, instead, were considered as visual prostheses already more than 50 years ago and have now entered the clinical phase.^{22,25,47} Various reasons could motivate the use of such implants: from a surgical point of view, cortical visual prostheses can profit from the vast surface area and straightforward accessibility of V1; while from a functional perspective, this approach offers a solution to all blindness typologies, but cortical injuries and stroke.²⁵ A remarkable brain feature and challenging aspect to be carefully consider in V1 prosthetics is the reorganization of receptive fields due to brain plasticity.⁴⁸ Nevertheless, it has been demonstrated that patients visual perception and tasks such as reading can easily adapt to prosthetic vision and improve with learning and time.⁴⁹ Two major types of V1 implants were developed: surface electrodes, placed on the occipital visual cortex, and intracortical electrodes, penetrating the cortex as represented in **Figure 1.4E**. Although surface electrodes could potentially cause a reduced foreign body response to the brain tissue, the complex, corrugate, and large surface of the cortex makes it challenging to properly and explicitly stimulate neurons with small currents amplitudes and low electrical cross-talk.⁴⁷ Therefore, penetrating intracortical electrode arrays, such as the Utah array^{50,51}, are preferred for their higher speci-

ficity and lower threshold currents. Stimulation of V1 has indeed a great potential in visual neuroprosthetics and will offer valid solution to many causes of blindness. More advancements are for sure expected in the future.

1.3.2 Optic nerve prostheses

The optic nerve is composed by the ~1.2 million RGCs axons collected at the optic disc like a ponytail and departing the eye directed towards the optic chiasm (see **Figure 1.1C**). Thus, all visual information is transferred by this 3.5 to 6 mm wide fiber⁵², whose compactness makes it interesting as target position for a potential full-field visual prosthesis. One of the requirements to employ an optic nerve prosthesis is that RGCs and the entire following path are intact (as in the case of AMD and RP). Electrode arrays for interfacing with the optic nerve are essentially the same as for peripheral nerve stimulation.⁵³ Various techniques have been conceived to access axons' electrical receptive fields, and they essentially differ in invasiveness and, therefore, selectivity.^{54,55} The least invasive way to communicate with the neuronal cells is to wrap electrodes tight around the nerve, but without penetrating the sheath, in a form of cuff (**Figure 1.4C**). However, this type of array does not selectively target the axons distributed towards the center, where RGCs from the macula are situated.⁵⁶ To increase selectivity, intraneural multielectrode arrays (MEAs) are placed within the nerve sheath and epineurium, more precisely within and between fascicles. Longitudinal intrafascicular electrodes (LIFE) and transverse intrafascicular multichannel electrode (TIME) are the two main examples of such interfaces and they differ in the direction along which the array is implanted, as the names suggest.^{54,57} Recently, a novel three-dimensional (3D) self-opening intraneural array (SELINE) was developed for peripheral nerves, showing improved mechanical and stimulation stabilities compared to TIME and LIFE electrodes.⁵⁸ This electrodes configuration allows for a more 3D coverage within the axons bundle and, therefore, an improved specificity. An even more recent publication from our group exploited the OpticSELINE interface (adapted version of SELINE) to stimulate the optic nerve of anaesthetized rabbits, demonstrating that the intraneural MEA elicits spatially selective activation of the visual cortex.⁵⁹

Although with a low number of electrodes, pattern recognition using an optic nerve prosthesis has been reported in humans already few years ago.^{53,60} These encouraging results and the relatively easy access to the optic nerve through the extra-cranial zone make optic nerve visual prostheses a technology to behold.

1.3.3 Retinal prostheses

The visual system and in particular the retina are impressively complex in their connections, circuitry, and processing.⁶¹ We need to make it clear that there will never be an artificial device able to completely restore natural vision in patients affected by retinal degenerations. Nevertheless, visual prostheses placed at the earliest level of processing (i.e. retinal prostheses) can profit from the retinotopic organization, together with the natural reorganization and post-processing happening already at the optic nerve and chiasm and convoluting in the LGN. In cases such as AMD and RP, only the photoreceptors and RPE are directly affected by the degeneration, leaving the other cell layers (horizontal, bipolar, amacrine, and RGCs) relatively intact, even if the retina undergoes extensive remodeling and rewiring (but delimited after all).⁶² This means that many excitable cells like RGCs remain alive and accessible for electrical artificial stimulation.

The easy ocular access favors positioning of implants in three different locations (**Figure 1.4B**): epiretinal (on the retinal surface, held with retinal tacks), subretinal (between the RPE and neural retina, replacing photoreceptors), and suprachoroidal (between the sclera and the choroid).²⁶ Suprachoroidal implants have the main fundamental disadvantage of being relatively far from target cells, but they have demonstrated phosphenes appearance in clinical studies and have a lower risk in terms of retinal damaging and detachment.⁴¹ Nevertheless, the two most common retinal implant placements are epi- and subretinal. In **Table 1.1**, the advantages and disadvantages of the two placements are listed, with a slight tendency in favor of epiretinal prostheses, which allow the restoration of vision in both central and peripheral fields.

Table 1.1 Pros and cons of epiretinal and subretinal prostheses. The writings in green and red show the predominant advantages and disadvantages, respectively. Overall, they are slightly in favor of epiretinal placements.

Placement	Advantages	Disadvantages
Epiretinal	<ul style="list-style-type: none"> • Coverage of large visual field possible • Easy placement • Better heat dissipation 	<ul style="list-style-type: none"> • Need for retinal tacks • Axons of passage activation • Need for transparent substrate (for photovoltaic prostheses – see paragraph 1.4)
Subretinal	<ul style="list-style-type: none"> • Simpler use of the remaining natural circuitry • Higher mechanical stability of the implant • Higher proximity to target cells 	<ul style="list-style-type: none"> • High risk of retinal detachment • Need for thin substrates • Block of nutrients transport

In the last decade, various retinal prostheses have been developed to fight blindness in case of retinal dystrophies, such as RP and more recently AMD (Clinical Trial NCT02227498).⁶³ Reliable phosphenes activation in humans were achieved using electrical stimulation in both epi- and subretinal approaches, and several multi-center clinical trials showed the feasibility of restoring a coarse form of vision, such as single letters discrimination, simple objects recognition, and obstacles avoidance.^{64,65} Among them, the most famous one is Second Sight (USA) and their implant Argus II, an epiretinal 60-electrodes array that obtained the Certification Europe (CE) and the Food and Drug Administration (FDA) approval, and it is currently implanted in over 350 patients worldwide.^{64,66} The main components of Argus II are presented in **Figure 1.5A**: a camera installed on glasses captures the visual information that are processed by a visual processing unit (VPU) and sent wireless by an external radio frequency (RF) transmitter towards an implanted receiver and an application specific integrated circuit (ASIC) component placed around the eyeball and held by a scleral band. The stimulating Pt electrodes fabricated onto a polyimide (PI) sheet are fixed on the retina by two retinal tacks (**Figure 1.5A**, bottom-right) and are connected to the ASIC through a permanent scleral cut. Patients implanted with this system gained functional improvements and up to 20/1260 of visual acuity with 11 ° x 19 ° of field.⁶⁴

An example of subretinal implant is the Alpha-AMS from Retinal Implant AG, Germany, which received the CE approval in 2016.^{66,67} The major innovation with respect to standard MEAs is the integration of a micro-photodiode and an amplifier, together with the stimulating iridium oxide (IrOx) electrode, in the same pixel of 70 µm by 70 µm. The intrinsic light detection enables a goggle-free system and a direct retinotopic activation exploiting the natural eye optics and movements. Nevertheless, ambient light intensity levels are not sufficient to supply enough power for electrical stimulation, making it necessary to connect the chip by trans-scleral cables to an extra-ocular electronic component, which is itself wirelessly linked to an external power supply (**Figure 1.5B**). The

chip size is relatively small and covers only 11° of visual field; however, it includes 1600 pixels, achieving one of the highest measured visual acuity in human patients, i.e. 20/549.⁶⁷

A final example of retinal implant that I would like to mention is the PRIMA subretinal prosthesis developed by Stanford University and now in the hands of Pixium Vision, France, for clinical trials and commercialization.^{68,69} This implant uses another stimulation principle, which exploits near-infrared (NIR) light projected by specialized goggles to activate and power Si-based series photodiodes able to directly stimulate bipolar cells (**Figure 1.5C**). With this regard, a more extended explanation about photovoltaic-based stimulation of cells is presented in paragraph 1.4. The most innovative and undeniably beneficial feature of PRIMA implant is the wireless transmission of power *and* visual information by light from outside the body to the stimulation location. The pixels array lays free-standing under the retina, while the eye is fully sealed and does not need permanent trans-scleral passage. This strategy still needs an external camera placed on goggles, a VPU, a projection system, and eye tracking system, but it is definitively preferred compared to implanted connecting cables that could lead to functional failure and chronic inflammatory reactions.⁷⁰ Clinical studies were performed with pixels diameter of $100\ \mu\text{m}$ and pitch of $110\ \mu\text{m}$, resulting in a visual acuity of 20/460 over a field of view of 7° . Pixels of smaller diameters (70 and $50\ \mu\text{m}$) are easily produced and will be soon integrated into the studies, envisioning a theoretical visual acuity of 20/250.⁶⁸ Two aspects, however, are limiting a wide visual field restoration: the intrinsically rigid substrate material does not allow for a high curvature bending needed to cover the spherical shape of the retina; and, even if multiple rigid units could cover a large curved area, the vast subretinal placement aggressively increases the risk of retinal detachment.

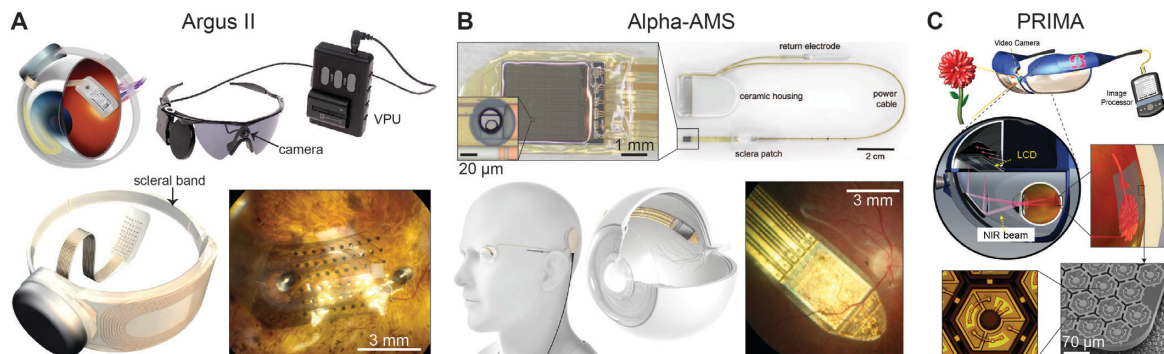


Figure 1.5 Three examples of retinal prostheses. **A**) The epiretinal Argus II (Second Sight Medical Products Inc., USA), with the external components (goggles, camera, VPU, and RF transmitter) and the internal part (extra-ocular RF receiver, ASIC and scleral band, trans-scleral cable, and intra-ocular stimulation array). At the bottom-right, the electrode array is clearly visible laying on a human retina and fixed with two titanium retinal tacks. Adapted from Luo *et al.* 2016.⁶⁴ © Second Sight Medical Products. **B**) The subretinal Alpha-AMS (Retinal Implant AG, Germany), with the implantable components at the top (RF receiver in a ceramic housing, trans-scleral cable, and intra-ocular array of micro-photodiodes and stimulating electrodes), a schematics of placement, and the array visible laying beneath a human retina (bottom-right). Adapted from Stingl *et al.* 2017 and Daschner *et al.* 2018.^{67,71} © Retinal Implant AG. **C**) The subretinal and photovoltaic PRIMA (Pixium Vision, France), with the NIR light projection system (top and middle) and images of the three-diode pixels (at the bottom). Adapted from Mathieson *et al.* 2012 and Lorach *et al.* 2015.^{68,70} © Pixium Vision.

Table 1.2 lists the three above-mentioned prostheses and some other principal retinal implants developed around the world and that have entered at least the clinical trials, but not necessarily successful for continuation and commercial approvals (some of the projects discontinued).⁷² From this table, it is possible to reveal a prevailing association of characteristics with implantation location.

Suprachoroidal prostheses have large electrodes and pitch size due to the need of higher currents, sadly renouncing to higher visual acuities. The use of photodiodes to detect the stimulation location seems to classify subretinal prostheses, which can have smaller and denser pixels for a high acuity, but they suffer from a narrow maximum visual field that they could rehabilitate. Epiretinal prostheses, instead, can reach a wider visual field, and they stimulate by means of standard MEA that therefore need an external camera.

Table 1.2 List of the principal retinal prostheses with their major characteristics.

Name (company/group)	Detection, processing, powering	Location, stimulation	Electrode array			Vis. field, Acuity (best)	Achieved stage and marks
			# electr., A (mm ²)	d (μm), p (μm)	materials		
Argus II ⁶⁴ (Second Sight)	External camera, VPU, e/o RF receiver	Epiretinal, electrical	60, 25	200, 575	PI, Pt	11x19 °, 20/1260	CE, FDA, clinical, commercial
IRIS II ⁶⁶ (Pixium Vision)	External camera, VPU, e/o IR receiver	Epiretinal, electrical	150, 2.4	250, 370	PI, Pt	n/a, n/a	CE, clinical
Epi-RET3 ^{73,74} (RWTH Aachen)	External camera, VPU, i/o RF receiver	Epiretinal, electrical	25, 6	100, 500	PI, IrOx	n/a, n/a	Clinical
Alpha-AMS ^{67,71} (Retinal Implant AG)	Photodiodes, VPU, e/o RF receiver	Subretinal, electrical	1600, 7.8	30, 70	PI, IrOx	11 °, 20/549	CE, clinical
PRIMA ^{68,69} (Pixium Vision)	External camera, VPU, NIR light	Subretinal, opto-electrical	378, 4	100, 110	Si, IrOx	7 °, 20/460	Clinical
Artificial silicon retina ⁷⁵ (Optobionics)	Photodiodes, VPU, Light	Subretinal, opto-electrical	5000, 3.2	9, 30	Si, IrOx	n/a, 20/200	Clinical
Gen 2 ⁷⁶ (Bionic Vision Technologies)	External camera, VPU, Percut. cables	Suprachoroidal, electrical	44, 144	1000, 1400	Silicone, Pt	n/a, 20/4451	Clinical
STS ⁷⁷ (Osaka University)	External camera, VPU, e/o RF receiver	Suprachoroidal, electrical	49, 26	500, 700	PI, Pt	15 °, n/a	Clinical

Abbreviations within the table. e/o: extra-ocular, i/o: intra-ocular, percut.: percutaneous, electr.: electrodes, A: total area, d: electrodes diameter, p: electrodes pitch, vis.: visual, n/a: not applicable.

Because of the above-mentioned features and opportunities, epiretinal implants represent the best option for visual prostheses, especially for profound blind patients suffering from RP. The way RGCs are naturally stimulated depends on the retinal wiring and extended interconnections with the other cell layers. **Figure 1.6A** illustrates, in a simplified manner, the intracellular responses of mudpuppy retinal cells, which can be used to describe many functions of the vertebrate retinas.^{78,79} When a photoreceptor is reached by photons, it hyperpolarizes and decreases the emission of neurotransmitters, and the connected bipolar cells depolarize (ON-center bipolar cell) or hyperpolarize (OFF-center bipolar cell) according to the type. The depolarization of bipolar cells triggers spiking activity in RGCs (ON-center RGC), while hyperpolarization triggers silencing (OFF-center RGC). Laterally, horizontal and amacrine cells also influence the activity of photoreceptors and RGCs, respectively. These complexly organized centers and receptive fields help us creating high contrast and color vision.^{79,80}

The electrical stimulation, however, influences the extracellular potential that can be perceived by the cells according to the electrode location and stimulation parameters (**Figure 1.6B**). RGCs react to electrical stimuli with either a direct, a network-mediated, or a combination of direct and network-mediated responses.⁸¹ The first type of response results from the electrical stimulation directly induced in RGCs (short latency, SL, within few ms from stimulus onset), while network-mediated responses in RGCs can rise from the activation of the INL (medium latency, ML, and long latency, LL), which in turn excites RGCs more naturally via synaptic connections (**Figure 1.6C**). Stimuli amplitude, polarity, duration, and frequency not only influence the type of RGC responses (SL, ML, LL),⁸² but they also affect the size and brightness of the phosphene appearance (**Figure 1.6D**).⁸³ For instance, percepts brightness is more influenced by stimulation frequency (10 – 120 Hz) than amplitude, while percepts size only by amplitude.

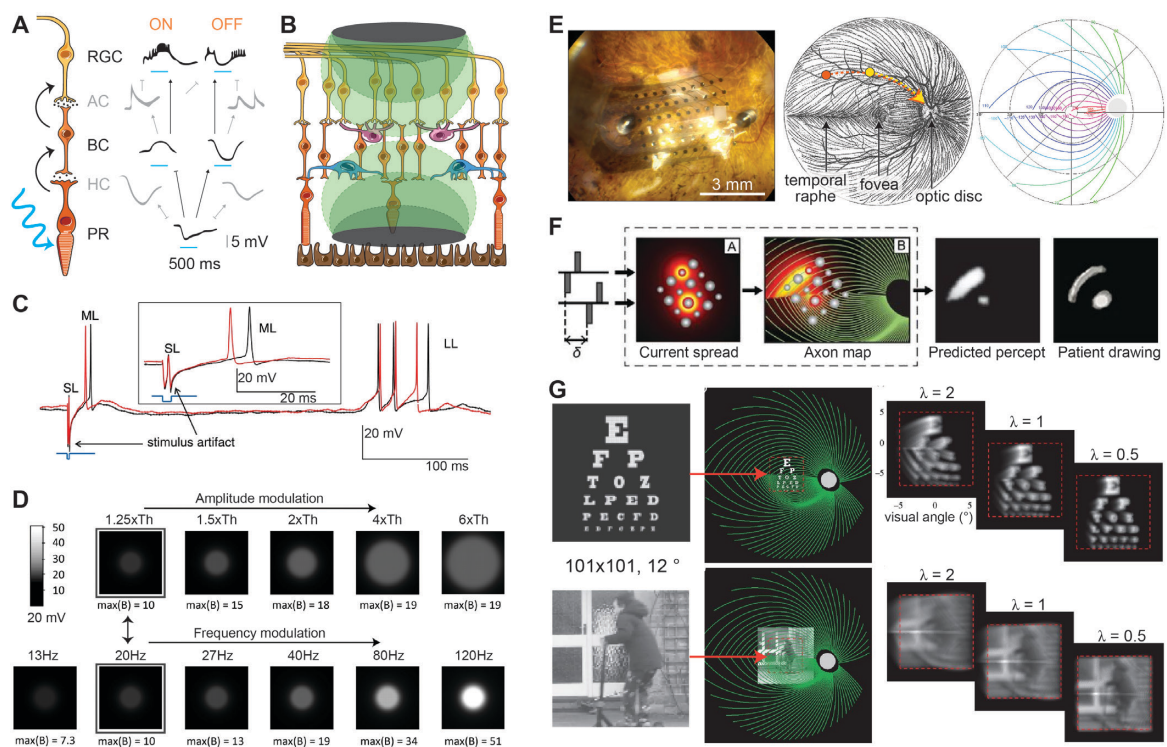


Figure 1.6 Electrical stimulation of RGCs. **A**) Natural signaling from photoreceptors (PR) hyperpolarization to RGC spiking (ON cells, left path) and RGC silencing (OFF cells, right path) in mudpuppy retinas. The curves depict intracellular voltage fluctuations/spiking. "T" ends: inhibition; arrows ends: stimulation.^{78,79} **B**) Placements of epiretinal electrodes (top), showing that voltage perturbations (stylized in green) could spread and reach bipolar cells for a network-mediated RGCs activation, such as in the subretinal case (bottom electrode). **C**) Demonstration of direct (SL) and network-mediated (ML and LL) responses of a RGC stimulated by an electrode inserted in the outer plexiform layer. Adapted from Boinagrov *et al.* 2014.⁸¹ **D**) Simulated effect on visual perceptions of epiretinal current amplitude and frequency, showing that higher currents mainly lead to larger phosphenes and slightly brighter, while faster pulses to even brighter phosphenes. Th: threshold current, max(B): maximal brightness. Adapted from Nanduri *et al.* 2012.⁸³ **E**) The Argus II prosthesis fixed on the retina (left). The distribution of axons, resulting in a specific axonal map that influences phosphene shape in epiretinal implants (middle). The axonal map can be mathematically described to build models for the prediction of phosphene shapes (right). Adapted respectively from Luo *et al.* 2016⁶⁴, Alward *et al.* 2000⁸⁴, and Jansonius *et al.* 2009⁸⁵. **F**) Models relying on axonal map and retinal tissue sensitivity to electrical stimulation can predict phosphene location and appearance, which correspond to patients drawings quite accurately. Adapted from Beyeler *et al.* 2017.⁸⁶ **G**) Based on such models, predictions of complex visual inputs allow us to understand how they can be perceived by patients. One essential parameter is the length of the

“comet tail”, which in this case was varied between 0.5, 1, and 2 ° of visual field. Adapted from Fine *et al.* 2015.⁸⁷

The epiretinal electrical activation of RGCs has clearly a great potential for artificial vision, especially if stimulation protocols are carefully implemented and adapted to individual patients. There is however a delicate challenge burdening on epiretinal electrode arrays: an efficient and selective stimulation of RGCs somas is not easily accessed because of the often large cell-electrode distance and the presence of the retinal nerve fiber layer, which is composed by the RGCs axons travelling to the optic disc.^{84,88} **Figure 1.6E** shows the Argus II epiretinal implant fixed on the retina (left), where axons are not visible, but their distribution and gathering to the optic disc is depicted in the sketch aside (middle) and can be mathematically described (as in the figure on the right).^{64,84,85} This means that, when epiretinal electrical stimulation is used, unwanted activation of axons of passage is *almost* inevitable; more explicitly, the electrical stimulation of the cell body marked in yellow on the drawing can activate the axon of the cell located on the same trajectory, for instance, the cell whose soma is located at the red point. The result of such expanded stimulation is the appearance of an elongated phosphene (banana-shaped). Thanks to axonal maps and models of the retina spatio-temporal sensitivity, it is possible to predict how the stimuli will affect the patients percepts (**Figure 1.6F**).^{86,87} The elongated phosphene origins on the pixel and spread with a tail of different length according to the electrode location (for instance, shorter tail are obtained for electrodes located at the periphery of the visual field or near the temporal raphe, as pointed in the middle drawing of **Figure 1.6E**). **Figure 1.6G** presents examples of how letters and images reproduced with a 101 x 101 pixel array distributed over 12 ° could be perceived by patients. The figure shows, for both visual inputs, three cases differentiated by the length of the phosphene tail λ (in ° of visual field).⁸⁷

Although various aspects of retinal prostheses have been thoughtfully considered and developed, several challenges remain open, such as the improvement of visual acuity and the enlargement of the visual field above the thresholds of blindness.⁸⁹ An agreed upon strategy to improve visual acuity is to increase the electrode density, while a large visual field could be attained by enlarging the retinal coverage with a larger prosthesis.

Concerning the visual field, tests on healthy subjects under pixelated vision indicated that an array of 25 × 25 pixels and 30 ° of visual angle (about 8.5 mm in diameter) could provide adequate mobility skills.^{90,91} However, the size of the prosthesis is typically limited by the maximal allowed sclerotomy, which is about 6 – 7 mm long; available prostheses are therefore in the range of 1 to 5 mm. Argus II is the largest implanted electrode array in humans and has a theoretical field of view of only 11 ° x 19 °. Increasing the size of the array is associated with two main challenges: it requires a large scleral incision and it may not conform to the eye curvature. In a flat prosthesis placed over the retina, central and peripheral electrodes may not be at the same distance from the retina. A large distance will inevitably increase the stimulation threshold and the cross-talk between adjacent electrodes.^{92,93} Preliminary attempts in designing wide-field retinal prosthesis have been proposed.⁹⁴ However, these approaches are based on materials (i.e., PI) with high elastic modulus (~ GPa), very thin substrates (e.g., 10 μm), and complex shapes (e.g., star) that could create challenges in surgical manipulation, implantation, and fixation.

Concerning the visual acuity, previous researches estimated that, to be useful in daily life, a retinal prosthesis should have 500 pixels distributed in the central area of approximately 5 mm in diameter.^{95,96} More recently, a trial on healthy subjects showed that the number of pixels required to recognize common objects is in the order of 3000 – 5000.⁹⁷ Despite microfabrication techniques allow

such electrode density, a limitation remains due to the routing of the connection tracks in the active area and the size of the cable linking the implantable components to the external electronics. To overcome these issues, in photovoltaic stimulation, the light projected into the pupil is wirelessly converted into electrical stimuli delivered to the retina, revolutionizing the way power and information are artificially transmitted by taking advantage of the eye structure and accessibility.⁷⁰

1.4 Photovoltaic stimulation of the retina

As previously briefly mentioned, photovoltaic stimulation (such as in the PRIMA prosthesis) allows the wireless transmission of power and visual information through the optics of the eye, taking advantage of the retinotopic placement of the pixels.⁷⁰ The freestanding photovoltaic implant can have high-density pixels that do not need wiring (**Figure 1.7A**), in either subretinal or epiretinal position, acknowledging that epiretinal photovoltaic implants need to have a transparent substrate to let the light reach the necessary layers.⁹⁸ To achieve photovoltaic stimulation, various opto-electronic materials and structures can be exploited in bioelectronic interfaces.⁹⁹ The most common photovoltaic structure is a planar multilayer junction of semiconductors able to absorb photons, depending on the wavelength, and create excitons that get separated in electrons and holes, and collected by anode and cathode electrodes.^{100,101} This conversion is obtainable thanks to the energy levels alignment of the semiconductors valence and conduction bands and the work function of the conductors.¹⁰² In **Figure 1.7B** a negative n-type and a positive p-type semiconductor are used as example in the energy diagram, with the p-type semiconductor absorbing light (represented in green) and generating the charges that are collected at their respective contacts, without the need for externally applied bias. The electronic equivalent circuit of a photovoltaic device is also shown in **Figure 1.7B**. The source of current by light absorption and charge generation/collection is represented by I_{pv} , with an ideal diode (I_D) modelled in parallel. The parallel shunt resistance (R_{sh}) is mostly due to manufacturing defects that cause power losses through the active layer as alternative current path; the junction capacitance (C_j) builds upon the depletion region; and the series resistance (R_s) represents the contact resistance prior the load cell.^{103,104}

The most advanced photovoltaic retinal prosthesis is PRIMA, as previously described. This implant is a prosthesis in clinical trials that has demonstrated to function with pulsed NIR light (880 – 915 nm, 4900 $\mu\text{W}/\text{mm}^2$, 4 ms).^{68,70} Each of the stimulating pixels can be composed by one, two, or three silicon (Si)-based photodiodes in series. **Figure 1.7D** shows the micrograph of the pixel structure with three photodiodes (left), the simplified circuit (middle) with the stimulating electrode (1) and the return electrode (2), and the deduced construction of the photovoltaic structure within the white square of the micrograph (right). When light reaches the intrinsic Si, charges will be accumulated at the respective doped regions (p- and n-doping) and contacts (anode and cathode). As both electrodes are exposed to the electrolytic solution of the extracellular medium, the electric field lines will be confined between the positive and negative ends during charging and discharging phases.¹⁰⁵ Cells (especially bipolar cells in PRIMA subjects) found near the electric perturbation will be excited to propagate the signal to the RGCs.

Inorganic materials, however, tend to be toxic (a part form silicon-based), might need thick structures due to low absorption coefficients, and are intrinsically rigid.^{70,106} The rise of organic technology favors the development of more biocompatible electronic medical devices, including for opto-electronic applications.^{99,107} The same energy diagram and photovoltaic effect shown in **Figure 1.7B**

can therefore be achieved by junction of donor and acceptor type organic semiconductors (conjugated polymers and small molecules) in a thin, light-weight, and flexible construction. Recently, an organic planar p-n junction has been developed by Rand *et al*¹⁰⁸ and demonstrated able to photo-stimulate neurons with high stability. Apart from being organic based, the main difference of this structure with respect to PRIMA pixels is the vertical stack orientation of the layers and the presence of only one metallic contact at the anodic end, while the cathodic end can be represented by the electrolyte (**Figure 1.7E**). The stimulation happens thanks to capacitive coupling between the top surface of the photovoltaic pixel and the cell membrane, and it depends on the magnitude of the open-circuit voltage generated by the junction. The negative surface potential obtainable with the p-n junction leads to a depolarization of the cell. Although very promising, these structures have been fabricated with big geometries (cm scale) on flat and rigid substrates, and only tested *in vitro* with cultured neurons and embryonic chick retinas (light wavelength of 660 nm, 4300 $\mu\text{W}/\text{mm}^2$, and pulses of 2 ms).

The solution-processability of organic molecules allows to create volumetric heterojunctions instead of planar ones, establishing a new class of photovoltaic structures: the bulk heterojunction (BHJ) photovoltaic cells, which consist of donor and acceptor materials blended at the nanoscale (**Figure 1.7C**, bottom) for an increased quantum efficiency.¹⁰⁹ These solution-based fabrication techniques also favor the deposition of thin films on temperature- and plasma-sensitive substrates, such as silicones or other polymeric soft materials, suitable for biomedical applications. An example of BHJ obtained with a blend of thiophene-based donor and naphthalene-based acceptor is depicted in **Figure 1.7F**.¹¹⁰ This BHJ was used to stimulate *in vitro* embryonic chick retinas with light pulses (200 ms) of various wavelengths and intensities (400 – 600 nm; 55 – 400 $\mu\text{W}/\text{mm}^2$) in an epiretinal configuration. The stimulation was achieved thanks to the electronic coupling between the cell membrane and the excited states of the BHJ.

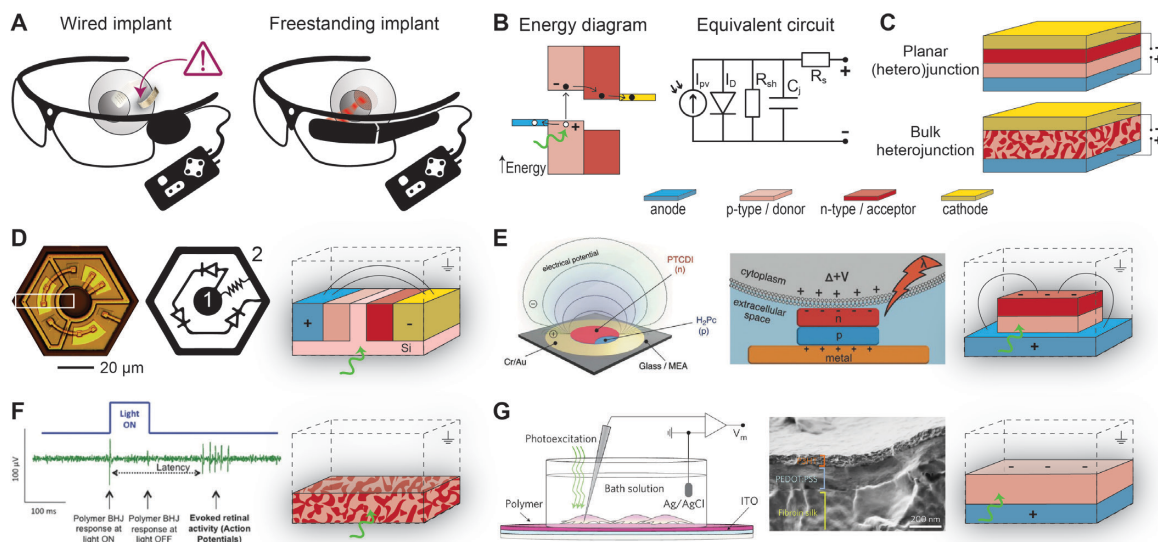


Figure 1.7 Materials and structures for photovoltaic stimulation of retinas. **A)** The evident advantage of using freestanding photovoltaic implants with respect to standard wired MEAs. **B)** Representation of an energy band diagram model (left) and corresponding equivalent circuit (right). **C)** Representation of planar (hetero)junction (top) and bulk heterojunction (bottom) photovoltaic cells. **D)** Si-based photovoltaic pixels: micrograph of three-diode pixel (left), corresponding simplified circuit (middle) with stimulating (1) and return (2) electrodes.⁶⁸ **E)** Example of an organic p-n junction used to stimulate neurons and blind embryonic chick retinas.¹⁰⁸ **F)** Example of single BHJ layer stimulating blind embryonic chick retinas.¹¹⁰ **G)** Example of a semiconducting

conjugated polymer (P3HT) stimulating blind rat retinas *in vitro* (with ITO) and *in vivo* (with PEDOT:PSS).^{111,112} In panels **D-G**, the model of the pixels working principle is deduced and schematically represented on the far right of each panel.

Due to the morphology of the BHJ active layer, the energy levels of the organic semiconductors, namely the energy levels of the highest occupied molecular orbital (HOMO) and the lowest unoccupied molecular orbital (LUMO), do not necessarily orient photogenerated currents toward a specific macroscopic direction. This means that, to engineer the device and define the direction of the created photocurrent, the contacts work functions are essential (resulting in conventional or inverted BHJs).¹¹³ Thus, by adding at least one properly chosen electrode, it is possible to guarantee cathodic photo-stimulation with BHJ systems, which is more efficient for neuronal stimulation.¹¹⁴ One of the most frequently used anodic contact in organic solar cells is indium tin oxide (ITO), which is a transparent conductor with a work function of about 4.5 eV.^{107,115} Yet, for a flexible device and a low-temperature deposition, a polymeric conductor might be more appropriate. Poly(3,4-ethylenedioxythiophene):poly(styrene sulfonate) (PEDOT:PSS), which is a conjugated polymer mixture often used as interfacial layer (holes extraction/electrons blocking layer) between ITO and the BHJ,^{116,117} demonstrated to be a useful single anodic end as well (**Figure 1.7G**).^{111,112} A fully organic subretinal prosthesis was manufactured on fibroin silk with PEDOT:PSS and the donor semiconductor poly(3-hexylthiophene) (P3HT), proving to restore vision in blind rats with light flashes of 20 cd/m² (560 nm) for 100 ms at 0.5 Hz.

A common characteristic of photovoltaic implants is that pulsed light, instead of continuous illumination, is needed to let the photovoltaic pixels time to discharge between consecutive pulses, with useful stimulation rates normally extending between 1 and 20 Hz. Faster frequencies would not let to most of the photovoltaic pixels enough time to discharge and might induce desensitization in RGCs.¹¹⁸ The maximum flicker fusion rate, defined as the frequency at which our brain naturally fuses fast consecutive images to perceive a continuous “film”, lays around 30-50 Hz for humans.¹¹⁹ However, it is also known that our brain has the amazing capability of adapting, which might allow annoying flashing phosphenes to be similarly perceived as stable.

1.5 Thesis strategy

1.5.1 Motivation and open challenges

A few million people worldwide could potentially benefit from more efficient retinal prostheses. Nowadays, reasonable expectations in vision restoration include a range of visual modalities limited to large-sized objects, such as large objects recognition, localizations, and movement detection, large letters reading, and large obstacles avoidance. Furthermore, extremely long times are necessary for the patients to detect, analyze, and react to the scene in front of them, mostly because of the poor prosthetic resolution and field coverage. Although these results are still very promising and mark an important milestone in artificial vision, an increase in pixel resolution and, particularly, a widening of the visual field will indeed reduce patients' difficulties when performing simple daily tasks. As presented in the previous paragraphs, there is currently no retinal prosthesis able to stimulate retinal cells with high pixel resolution *and* large visual field (> 30 °), therefore providing an improved and useful form of vision to people affected by AMD or RP. Perhaps, this goal might be achieved by investigating new materials, concepts, and technologies.

Hereof, the proposed thesis intends to combine organic photovoltaic technology with soft elastomers and other strategic biocompatible materials to exploit their individual or collective properties and build a wireless epiretinal prosthesis with photovoltaic pixels distributed over a wide visual angle ($> 40^\circ$) and curved substrate. The principal benefit of such prostheses is the appropriate restoration of visual functions to favor unassisted ambulation and more successful recognition of scene details without excessive scanning and analysis time. Or at least, this would represent the ultimate goal of a clinically approved prosthesis. Within the timeframe of the thesis, efforts were focused on the development of a useful technological platform for the manufacturing of the mentioned retinal prosthesis (obtained in this thesis) and, why not, other types of organic photovoltaic neural interfaces.

Among the technological challenges, questions in relation to mechanical, electrical, optical and thermal aspects of the prosthesis should be addressed. The safety of the overall implant and its optoelectronic operation, together with the safety of surgical procedures (for both the implant and the subjects), are a requirement. Implantation of a neuroprosthesis is only justified when the advantages gained from the restored prosthetic functions largely and ultimately exceed the current sensory-motor performances summed with the risk of the operation and post-implantation complications. With this regard, wide-field prostheses imply large-area implants, which can induce surgical difficulties and put biocompatibility to test. Moreover, although photovoltaic retinal implants surely appear very attractive as solution to wiring high-density stimulating electrodes, yet, they come with the challenge of possible photo-thermal and chemical damage to the retina due to the high intensity light necessary to generate enough photocurrent/voltage to efficiently excite the cells. Therefore, depending on wavelength and intensities, cautions and limitations need to be considered for both direct (light-biology) and indirect (light-implant) effects when the photovoltaic approach is applied.¹²⁰

The accomplishment of this work is motivating not only for the scientific and technological interest to build advanced neural interfaces, but also for the good it could potentially bring to humanity; even if the development of next-generation prostheses based on novel design and materials implies time-consuming and tedious characterizations and optimization procedures to only get to *in vivo* preclinical studies. Indeed, the translation to clinical studies would require further efforts and investments beyond this thesis.

1.5.2 Objectives and thesis structure

POLYRETINA (/ˈpɒlɪrɛtɪnə/) is a word composed by “poly” (standing for polymeric) and “retina”. Our lab coined this term for a polymer-based, curved, and injectable epiretinal prosthesis capable of photovoltaic stimulation with high pixels density distributed over a wide visual field. As represented in **Figure 1.8**, the photovoltaic pixels should stand wireless, covering a large surface area of the retina, and acting as artificial photoreceptors. The incoming pulsed light, whose pattern is determined according to visual information captured by a camera, carries the energy absorbed by the organic layers of the pixels and transformed into photogenerated current. The charging of the electrode surface will then influence the extracellular potential across the retinal layers, which will induce activity of RGCs and eventually the appearance of phosphenes.

The general objective of this thesis is to develop POLYRETINA. This development comprises several aspects, including:

- Selection of materials and design of structures and patterns.
- Establishment of microfabrication processes.

- Production of devices and prototypes.
- Characterization of photovoltaic, electrical, structural, mechanical, thermal, and optical properties of the materials and the prostheses.
- Optimization of the performances and stability.
- *Ex vivo* evaluation of photovoltaic stimulation with blind retinal explants.
- Assessment of injectability and development of a surgical implantation method.
- Delivery of prototypes for *in vivo* testing.
- *In vivo* evaluation of photovoltaic prosthetic stimulation of the visual cortex.

Continuing the reading of this thesis, you will find a series of three chapters (Chapter 2, Chapter 3, and Chapter 4) that chronicles the evolution of the photovoltaic and wide-field epiretinal prosthesis, POLYRETINA, towards *in vivo* applications. We first present the development and validation with proof-of-principle *in vitro* and *ex vivo* characterizations (Chapter 2); after that, we dedicate attention to the optimization of the photovoltaic pixel for a high-density prosthesis (Chapter 3); to continue with mechanical and stability improvements for *in vivo* testing in miniature pigs (Chapter 4), with details about surgical procedures and preliminary results. One last technological chapter (Chapter 5) describes the development and *in vitro* / *ex vivo* validation of a POLYRETINA with photovoltaic pixels responsive to a different wavelength. This part of the work was performed in parallel with Chapter 3 and Chapter 4, but was placed at the end of the thesis because of the clinical relevance of the reported technology. Finally, a conclusive chapter (Chapter 6) summarizes the achievements and reports the limitations and future perspectives of the developed prosthesis and technology.

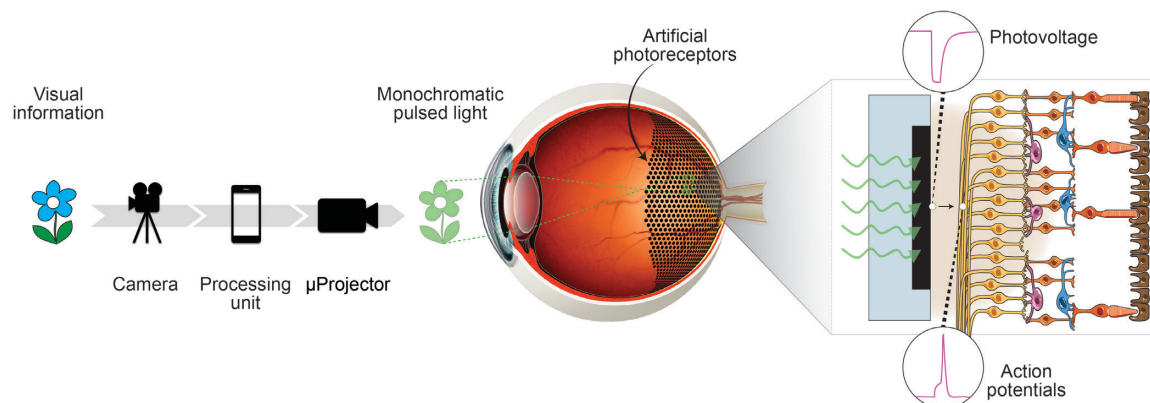


Figure 1.8 The concept of POLYRETINA. As for the photovoltaic PRIMA prosthesis, visual information is captured by a camera (situated on goggles), processed, and projected through the eye to activate and power the targeted photovoltaic pixels. Upon illumination, these artificial photoreceptors modify their surface potential and influence the activity of the retina inducing RGCs action potentials, which in turn will generate phosphene appearance.

Chapter 2 Development and validation of a wide-field and photovoltaic epiretinal prosthesis



Eyes of a brown Siberian husky (Source: Melanie Haynes)

This chapter has been adapted from: L Ferlauto*, MJI Airaghi Leccardi*, NAL Chenais* *et al*, Nature Communications, 2018, 9: 992.⁹⁸ *equal contribution.

Contributions: I designed, fabricated, and characterized the devices and the retinal prostheses; performed/analyzed photovoltage and photocurrent measures, electrochemical impedance spectroscopy, and electrical simulations. L. Ferlauto performed/analyzed KPFM, photovoltage and photocurrent measures, temperature, and accelerated ageing tests. N.A.L. Chenais performed/analyzed pH, voltage spreading, and electrophysiological experiments. M. Bevilacqua performed/analyzed PV and PC measures. S.C.A. Gilliéron performed thermal simulations. T.J. Wolfensberger and P. Vagni performed the simulated surgeries.

2.1 Introduction

We present in this first chapter the developed epiretinal prosthesis, POLYRETINA, based on organic photovoltaic materials. After the first demonstration of vision restoration in blind rats with a silicon photovoltaic subretinal prosthesis⁶⁸, a second major step was achieved with the exploitation of conjugated polymers and organic semiconductors (i.e., PEDOT:PSS; regioregular P3HT; [6,6]-phenyl-C61-butyric acid methyl ester, PCBM) to build an organic photovoltaic subretinal interface.^{112,121,122} In the latter, despite the capability of improving visual acuity in dystrophic rats after one month of implantation, several issues remain unsolved.¹¹¹ Conjugated polymers are well tolerated when exposed to the subretinal space, but they start to delaminate a few months after placement leading to an unavoidable degradation of the organic materials.¹²² Moreover, in the cases of both silicon and organic photovoltaic subretinal prostheses, the limited size of the devices (1 – 2 mm) will not allow the recovery of a large visual field, unless implanting multiple devices.¹²³ Some concerns remain about the risks associated with the implantation of multiple devices in the subretinal space (e.g., retinal detachment, movements of the devices, and device overlaps). Thus again, increasing both visual acuity and visual field size with a single retinal prosthesis remains one of the main unsolved challenges in the field.⁹⁵ This leaves to novel technologies the arduous goal of closing the gap between modern implants and future possibilities in retinal prosthetics.

2.2 Results

2.2.1 Design and fabrication

POLYRETINA is a novel foldable and photovoltaic wide-field epiretinal prosthesis based on poly(dimethylsiloxane) (PDMS) as substrate material, because of its transparency, elasticity, low Young's modulus, and high strain to failure.^{124,125} Moreover, PDMS is available as medical grade elastomer already in use in medical device applications. The device consists in a PDMS–photovoltaic interface (**Figure 2.1A** and **C**), embedding 2215 stimulating pixels (80 and 130 μm in diameter) distributed on an active area of 12.7 mm (**Figure 2.1D**). As represented in **Figure 2.1F** and **G**, each pixel is composed by a PEDOT:PSS bottom anode, a P3HT:PCBM semiconductor layer (also referred as blend), and a top cathode in titanium (Ti). Another PDMS layer encapsulates the prosthesis, avoiding the immediate delamination and degradation of the organic materials and extending its lifetime. Openings of 67 and 120 μm in diameter have been made in the encapsulation layer to expose the cathodes (**Figure 2.1E**).

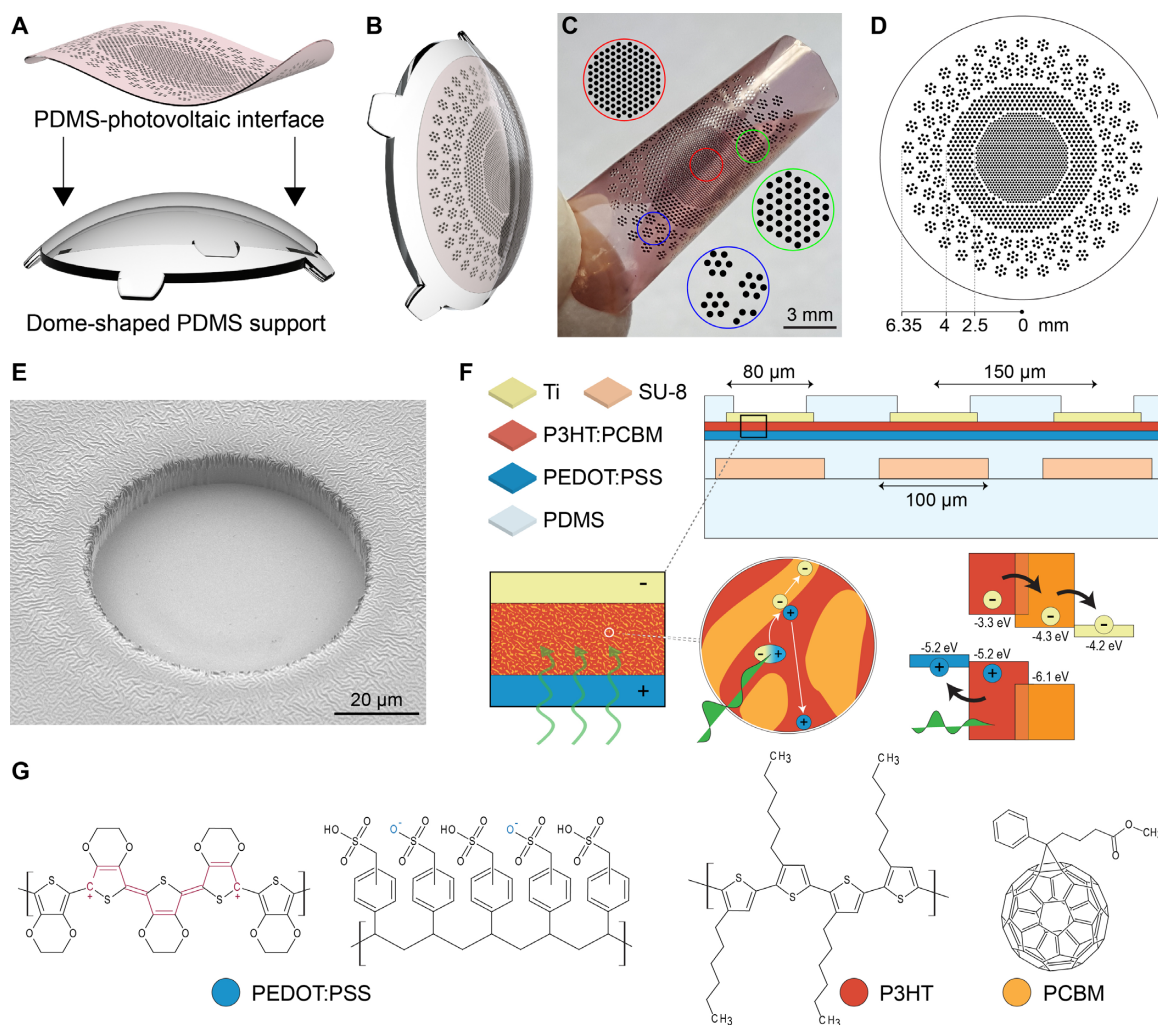


Figure 2.1 Design and materials of POLYRETINA. **A)** 3D model of the fabricated PDMS-interface and of the dome-shaped PDMS support. **B)** 3D model of the retinal prosthesis after bonding the PDMS-interface to the PDMS support. **C)** Fabricated PDMS–photovoltaic interface with pixels arranged in three areas of different sizes and densities: central area (red), diameter of 5 mm, 967 electrodes in hexagonal arrangement, electrode diameter 80 μm and pitch 150 μm , density 49.25 pixels/ mm^2 ; first ring (green), diameter of 8 mm, 559 electrodes in hexagonal arrangement, electrode diameter 130 μm and pitch 250 μm , density 17.43 pixels/ mm^2 ; second ring (blue), diameter 12.7 mm, 719 electrodes, electrode diameter 130 μm , density 9.34 pixels/ mm^2 . Circles show an enlarged view of the pixel distribution. **D)** Top view of the distribution of the photovoltaic pixels. **E)** Scanning electron microscopy image (40 $^\circ$ tilted view) of a photovoltaic pixel. **F)** Cross section of the PDMS-photovoltaic interface, including: PDMS (50 μm), a second layer of PDMS (15 μm) embedding SU-8 rigid platforms (6 μm), a layer of PEDOT:PSS (50 nm), a layer of P3HT:PCBM (100 nm), titanium cathodes (150 nm), and a final layer of PDMS (4 μm). Dimensions are not in scale. Expanded regions show the principle for photovoltaic generation of current in BHJs: excitons travel towards the donor-acceptor interface, where negative charges follow the acceptor (PCBM, orange) path towards titanium and positive charges the donor (P3HT, red) path towards PEDOT:PSS. An energy band diagram of the concerned materials with HOMO, LUMO, and work functions levels is also depicted. **G)** Chemical structures of the concerned organic materials.

Titanium is a mechanically and electrochemically stable metal, it is widely used in implantable devices, it has an appropriate work function for the photovoltaic mechanism (**Figure 2.1F**), and it is a capacitive charge-injection material (also due to the thin layer of titanium oxide (TiO_x) formed at the surface). The latter is desirable with monophasic pulses, as in this photovoltaic approach, be-

cause no chemical species are created or consumed during a stimulation pulse, thus avoiding undesired tissue reactions.¹²⁶ Under this condition, the electrode/electrolyte interface can be modeled as electrical capacitor without redox reactions.¹²⁷ To verify this statement, we measured electrochemical impedance spectroscopy (EIS) of titanium electrodes in phosphate-buffered saline (PBS, 1x) solution (**Figure 2.2A** and **B**) and concluded that the charge injection mechanism at the Ti (TiO_x) – electrolyte interface is mostly capacitive for frequencies above 0.5 Hz. The charge transfer resistance (R_{CT}), the double layer constant phase element (CPE) identified by $[C_{DL}, n]$, and the spreading resistance (R_{spread}) from the simplified equivalent circuit in **Figure 2.2B** (cf. **Appendix Equation 1**)¹²⁸ were calculated to be respectively ~ 12 GOhm, $[9.2 \text{ nF}, n = 0.965]$, and 1.45 kOhm for an electrode surface area of 0.052 mm^2 . The large R_{CT} , relatively high C_{DL} , and n close to 1 let conclude, once again, the high capacitive component of the electrode-electrolyte interface. We also measured the pH with a microelectrode positioned above the titanium electrode of the PDMS–photovoltaic interface (**Figure 2.2C-E**) during 1 h of pulsed illumination (20 Hz , 10 ms , 3.4 mW/mm^2 ; $N = 3$ devices). The irradiance has been set to a value above the maximum allowed for prosthetic application (see Thermal and optical safety in 2.2.6). During illumination, a negligible pH shift of about 0.002 pH units has been detected, which could be explained by a recording artifact due to the local temperature increase induced by the prosthesis. Local heating could reduce the resistivity of the solution and decrease the voltage difference between the pH microelectrode and the local reference.

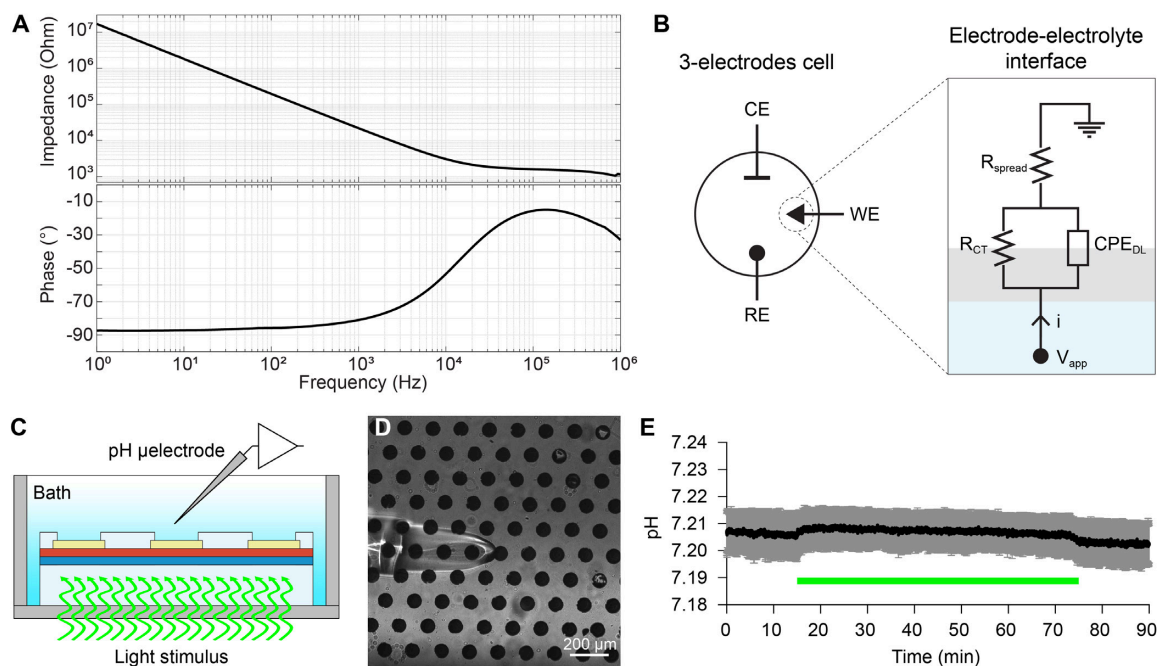


Figure 2.2 Evaluation of Ti-electrolyte charge injection mechanism. **A**) Bode plot of the EIS results of titanium electrodes (mean of $n = 5$ electrodes) in PBS against a Pt counter electrode (Ag/AgCl reference, driving voltage 50 mV). The surface area of the electrode was 0.052 mm^2 . **B**) Sketch of the three-electrode cell used for the EIS measures with the simplified equivalent circuit of the electrode-electrolyte interface. WE: working electrode; CE: counter electrode; RE: reference electrode; R_{spread} : spreading resistance of the electrode towards the counter electrode (solution resistance included); R_{CT} : charge transfer resistance (faradaic/redox mechanism); CPE_{DL} : double layer CPE with impedance $((j\omega)^n C_{DL})^{-1}$ (cf. **Appendix Equation 1**).¹²⁸ The Warburg element is not included. **C**) Sketch of the measurement set-up for pH measurements upon photovoltaic stimulation in PBS. **D**) Picture of the pH microelectrode located on top of the PDMS-photovoltaic interface. **E**) Mean (\pm s.d., $N = 3$ devices) pH measurements upon 1 h of full field pulsed illumination (10 ms , 20 Hz , 3.4 mW/mm^2 , 560 nm , illumination spot 2.2 mm).

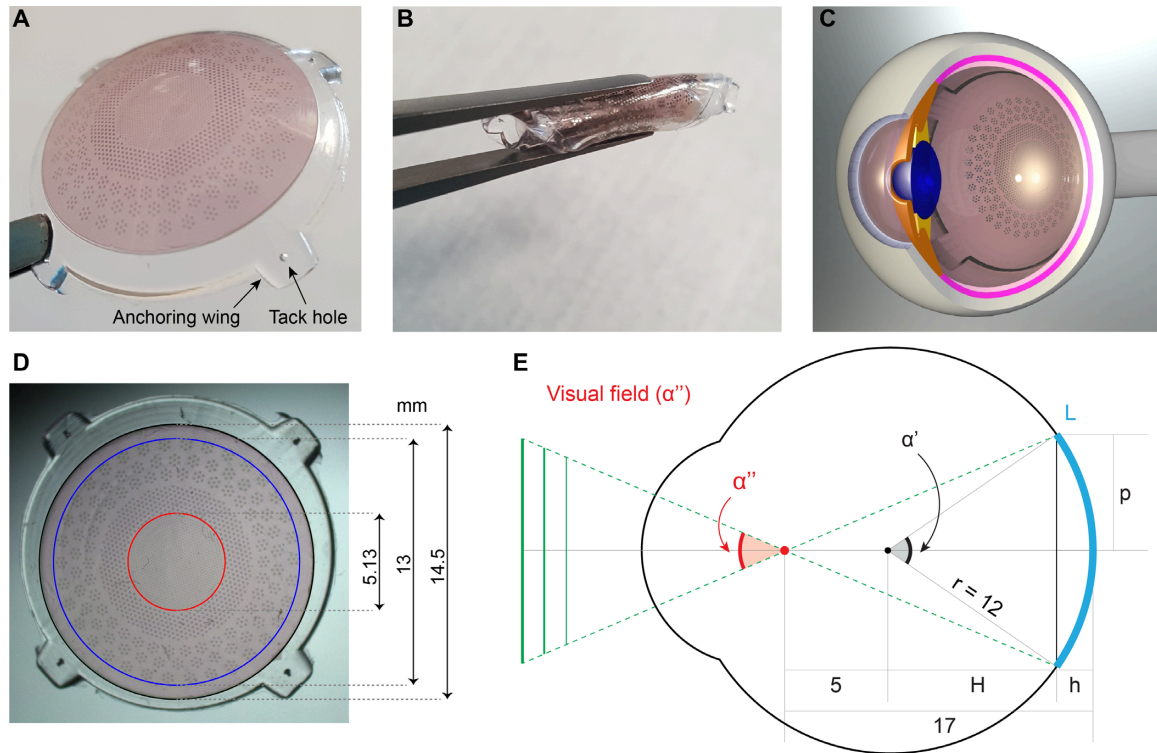


Figure 2.3 Foldable and wide-field retinal prosthesis. **A)** Picture of POLYRETINA. Four anchoring wings with holes are present for attaching the prosthesis with retinal tacks. **B)** POLYRETINA folded before injection. **C)** 3D model after epiretinal placement. **D)** Top view picture of the prosthesis. Due to the radial elongation, the central area (red) is slightly stretched from 5 to 5.13 mm, while the active area (blue) is increased from 12.7 to 13 mm. **E)** The calculated visual angle. The human eye is modelled as a sphere of 12 mm radius (r). The blue arc corresponds to the active area, where the chord length $2p$ is 13 mm and the arc length L is 13.7 mm. The nodal point is represented in red, with a distance of 17 mm from the retina. Under these conditions, the area covered by the active region of the prosthesis can be calculated as $S = 2\pi rh = 144.2 \text{ mm}^2$, and it corresponds to a visual angle α'' of 46.3° (or 808 mrad). All the distances in the sketch are in mm.

The hemispherical shape of POLYRETINA (**Figure 2.1B** and **Figure 2.3A**) is obtained by bonding the PDMS–photovoltaic interface on a dome-shaped PDMS support (**Figure 2.1A**) with a thickness of $700 \mu\text{m}$ in the center and $500 \mu\text{m}$ at the edges, and a radius of curvature of 12 mm, corresponding to the standard human eye (see **Appendix Figure 6** for details). The bonding induces a radial elongation in the PDMS–photovoltaic interface of about 3% (in diameter), which has been considered to determine the covered retinal surface and visual field (**Figure 2.3D** and **E**). The visual field has been calculated according to basic trigonometric equations as following:

$$\alpha'' = 2 \tan^{-1} \left(\frac{p}{17 - (12 - \sqrt{12^2 - p^2})} \right)$$

Equation 2.1 Calculation of visual field coverage for a human eye. p is the radius of the active area view from the top (cf. **Figure 2.3E**). The values 17 and 12 are in mm and correspond to the distance between the nodal point and the retina and the radius of curvature, respectively, for an average adult human eye.

Four anchoring wings, with holes for retinal tacks, have been included for the fixation of the prosthesis (**Figure 2.3A**). The folding of POLYRETINA, its insertion, and covering of the retinal surface have been evaluated in simulated surgeries with plastic models of the human eye (**Figure 2.4A**). The prosthesis can be folded prior implantation (**Figure 2.3B**), inserted through an aperture of

6.5 mm, released within the posterior chamber (**Figure 2.3C** and **Figure 2.4B**), and attached in epiretinal configuration. The same surgical approach has been also validated in enucleated pig eyes (**Figure 2.4C**).

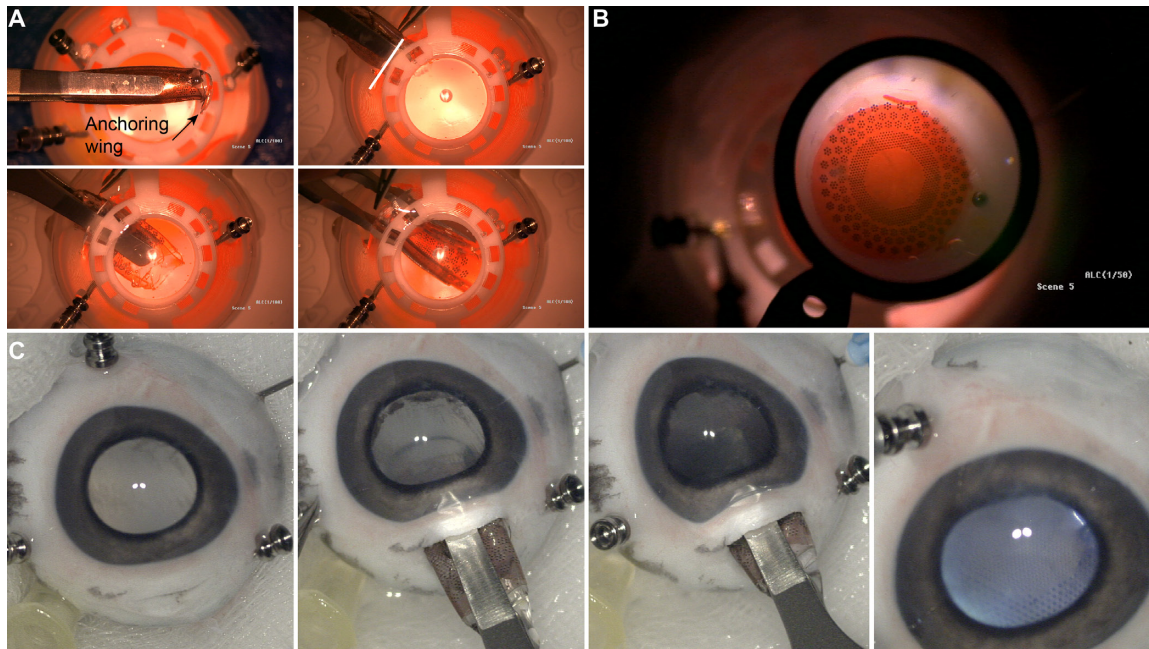


Figure 2.4 Simulated surgical implantation. **A)** Picture sequence of the implantation in a human eye plastic model. The white line in top-right panel shows the incision of 6.5 mm. **B)** Picture of POLYRETINA placed in epiretinal configuration. **C)** Picture sequence of the implantation in an enucleated pig eye.

2.2.2 Optimization of the photovoltaic pixel

First, using Kelvin probe force microscopy (KPFM), we evaluated the changes in the surface potential generated at the cathode upon illumination for different conditions of fabrication (**Figure 2.5A** and **B**). To assess the role of the bottom anode, we fabricated photovoltaic interfaces onto glass substrates including a bottom anode made of ITO, PEDOT:PSS, the semiconductor layer of P3HT:PCBM, and aluminum (Al) top cathodes. We initially used aluminum since it is one of the most common cathode material in organic photovoltaics. KPFM measures (**Figure 2.5C**) across several devices showed that the variation of the surface potential upon illumination (white LED, light from the top, 0.4 mW/mm^2) is about 15 folds higher with aluminum cathodes with respect to P3HT:PCBM only (**Figure 2.5D**). When aluminum is present (**Figure 2.5D**, left), the absence of any anode (ITO or ITO/PEDOT:PSS) significantly reduces the surface potential variation upon illumination (ITO/PEDOT:PSS/blend/Al vs blend/Al, $p < 0.0001$; PEDOT:PSS/blend/Al vs blend/Al, $p < 0.0001$; one-way ANOVA, Tukey's multiple comparison test). No significant difference has been found with or without the ITO anode if the PEDOT:PSS layer is present (ITO/PEDOT:PSS/blend/Al vs PEDOT:PSS/blend/Al, $p = 0.6219$; one-way ANOVA, Tukey's multiple comparison test). In the absence of aluminum cathodes (**Figure 2.5D**, right), the architectures with different bottom anodes do not induce any significant difference (ITO/PEDOT:PSS/blend vs PEDOT:PSS/blend, $p = 0.9997$; ITO/PEDOT:PSS/blend vs blend, $p = 0.9890$; PEDOT:PSS/blend vs blend, $p = 0.9995$; one-way ANOVA, Tukey's multiple comparison test). The maximization of the surface potential variation has been obtained with aluminum cathodes and both ITO/PEDOT:PSS

or only PEDOT:PSS anodes. Therefore, to simplify the fabrication process, we implemented PEDOT:PSS alone as bottom layer. We also verified that the surface potential variation was not altered (**Figure 2.5E**) when the interface was built over a PDMS substrate instead of bare glass with aluminum cathode diameters of both 100 and 150 μm (\bullet PEDOT:PSS/blend/Al and \circ PDMS/PEDOT:PSS/blend/Al); no statistical differences have been found among the groups (two-way ANOVA, Tukey's multiple comparison test, interaction $p = 0.9633$; factor 1, diameter, $p = 0.0887$; factor 2, substrate, $p = 0.6385$). When titanium replaces aluminum (Δ PDMS/PEDOT:PSS/blend/Ti), the surface potential is slightly reduced (for 100 μm : one-way ANOVA, $F = 25.43$, $p < 0.001$; PDMS/PEDOT:PSS/blend/Ti vs both PEDOT:PSS/blend/Al and PDMS/PEDOT:PSS/blend/Al, $p < 0.001$, Tukey's multiple comparison test; for 150 μm : one-way ANOVA, $F = 9.266$, $p < 0.01$; PDMS/PEDOT:PSS/blend/Ti vs both PEDOT:PSS/blend/Al and PDMS/PEDOT:PSS/blend/Al, $p < 0.05$, Tukey's multiple comparison test).

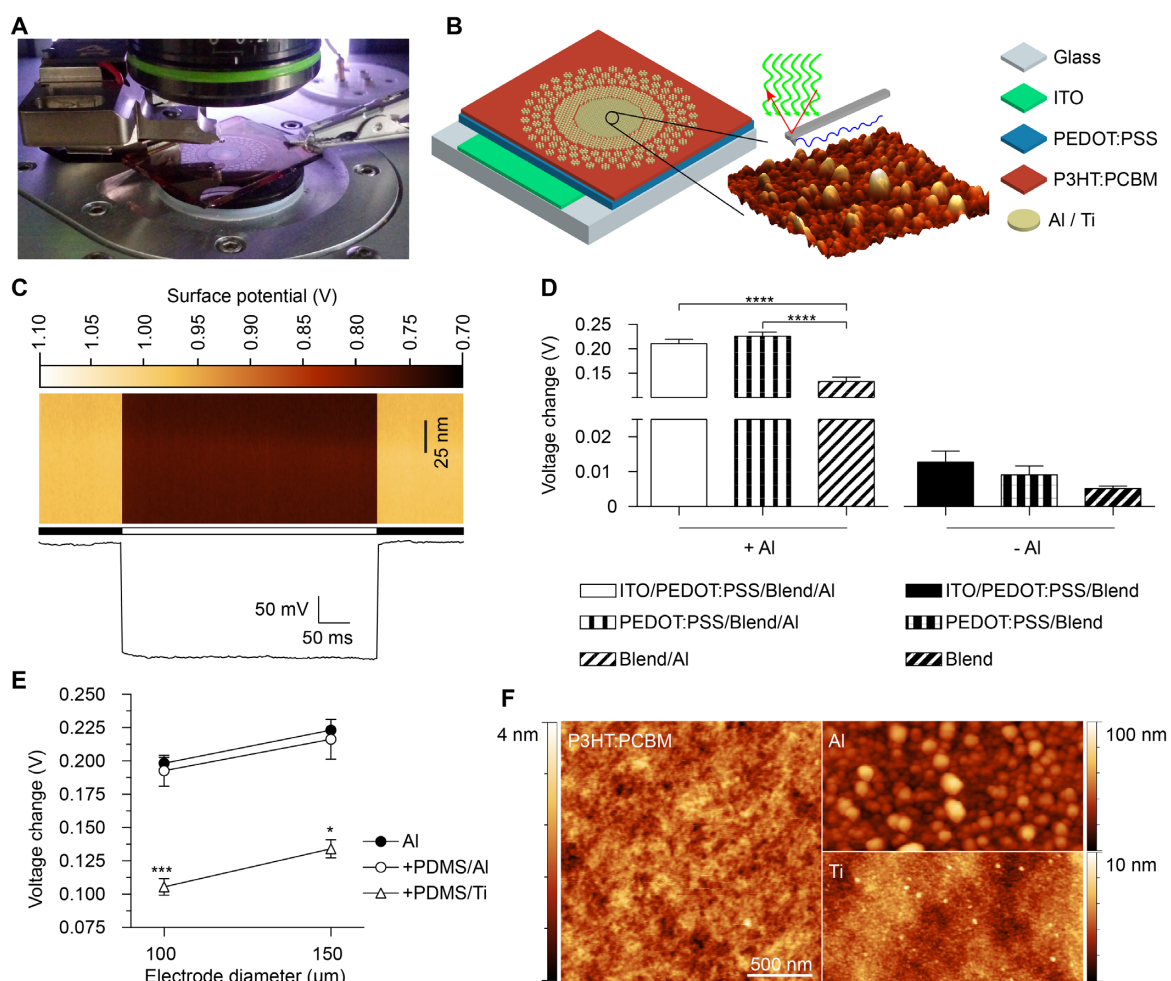


Figure 2.5 Optimization of the photovoltaic pixel. **A**) Picture of the KPFM measures. **B**) Sketch of the fabricated device. Glass substrates have been coated with a thin film of ITO (200 nm), a thin film of PEDOT:PSS (50 nm), a thin film of P3HT:PCBM (100 nm), and last aluminum (100 nm) or titanium (150 nm). **C**) Representative KPFM map on a glass/PEDOT:PSS/blend/Al device obtained by repeating a line scan of 100 nm (vertical direction). The horizontal bar indicates period of dark (black) and light (white). The bottom panel shows the average potential fluctuation during time; each point is the average potential in a single line scan. **D**) Surface potential variations (differences in voltage during light and voltage during dark) for six different architectures. Each bar is the mean (\pm s.e.m.) of at least $N = 3$ devices, in which at least $n = 3$ electrodes/points

have been measured and averaged. ITO/PEDOT:PSS/blend/Al: 0.2106 ± 0.0092 V, $N = 5$, $n = 3$; PEDOT:PSS/blend/Al: 0.2259 ± 0.0085 V, $N = 5$, $n = 3$; blend/Al: 0.1334 ± 0.0090 V, $N = 3$, $n = 3$; ITO/PEDOT:PSS/blend: 0.0128 ± 0.0032 V, $N = 3$, $n = 3$; PEDOT:PSS/blend: 0.0091 ± 0.0025 V, $N = 3$, $n = 4$; blend: 0.0052 ± 0.0007 V, $N = 3$, $n = 4$. One-way ANOVA, $p < 0.0001$, $F = 177.9$. **E)** Surface potential variations with/without a bottom PDMS layer and with Al or Ti top contacts of 100 and 150 μm in diameter. Each point is the mean (\pm s.e.m.) of at least $N = 3$ devices, in which at least $n = 3$ electrodes have been measured and averaged. PEDOT:PSS/blend/Al-100 μm : 0.1984 ± 0.0043 V, $N = 3$, $n = 3$; PEDOT:PSS/blend/Al-150 μm : 0.2232 ± 0.0082 V, $N = 3$, $n = 3$; PDMS/PEDOT:PSS/blend/Al-100 μm : 0.1927 ± 0.0115 V, $N = 5$, $n = 3$; PDMS/PEDOT:PSS/blend/Al-150 μm : 0.2163 ± 0.0150 V, $N = 5$, $n = 3$; PDMS/PEDOT:PSS/blend/Ti-100 μm : 0.1055 ± 0.0063 V, $N = 3$, $n = 6$; PDMS/PEDOT:PSS/blend/Ti-150 μm : 0.1342 ± 0.0068 V, $N = 3$, $n = 3$. **F)** Representative AFM images of PEDOT:PSS/blend, PEDOT:PSS/blend/Al, and PEDOT:PSS/blend/Ti surfaces.

KPFM measurements have been performed in air in non-contact mode; therefore, the measured variations in the surface potential may be slightly different with respect to the electric potential generated by the double layer capacitive charging occurring at an electrode–electrolyte interface, as in the case of an implanted retinal prosthesis. Therefore, we measured the photo-current (PC) and the photo-voltage (PV) generated in the presence of electrolyte solution upon illumination. We fabricated chips embedding six electrodes, each of them connected to a contact pad for measuring the signal with respect to a silver/silver chloride (Ag/AgCl) reference electrode immersed in solution (**Figure 2.6A**). Both PC and PV have been measured with illumination (565 nm) at increasing light intensities (12.75, 111.11, 225.00, 430.56, 616.67, 785.65, and 943.98 $\mu\text{W}/\text{mm}^2$) and pulse duration (10, 50, 100, and 200 ms). The PC (**Figure 2.6B**) generated by pulsed illumination (943.98 $\mu\text{W}/\text{mm}^2$) has a typical capacitive profile, peaking in about 10 ms and then decreasing with an exponential decay, while the PV (**Figure 2.6C**) reaches a steady-state value and remains constant. This is in agreement with the capacitive nature of the electrode/electrolyte interface. Moreover, the PV generated (about 180 mV) is largely below the redox potential of titanium (or titanium oxide), thus ensuring that no irreversible reactions occur at the interface. The PC density increases with irradiance, with a mean (\pm s.e.m.) peak value of 135.51 ± 26.74 $\mu\text{A}/\text{cm}^2$ (10 ms) for 943.98 $\mu\text{W}/\text{mm}^2$ (**Figure 2.6D** and **F**). According to the literature in the field, these current values should be able to induce epiretinal stimulation of RGCs.¹²⁵ The slope of the PC density profile is decreasing while increasing irradiance, and a saturation of the response could be expected for irradiance higher than 1–2 mW/mm^2 . We also measured the PC density (10 ms, 943.98 $\mu\text{W}/\text{mm}^2$) after 48 h of immersion in physiological solution (stored in dark at room temperature). The mean (\pm s.e.m.) ratio before/after has been measured in 94.44 \pm 12.28, 95.11 \pm 13.07, 93.36 \pm 13.26, 94.99 \pm 12.48%, respectively, for 10, 50, 100, and 200-ms pulses; no significant differences have been found (10 ms: $p = 0.4423$; 50 ms: $p = 0.5798$; 100 ms: $p = 0.5798$; 200 ms: $p = 0.5526$; $N = 3$ devices, $n = 6$ electrodes per device; Wilcoxon matched-pairs signed rank test).

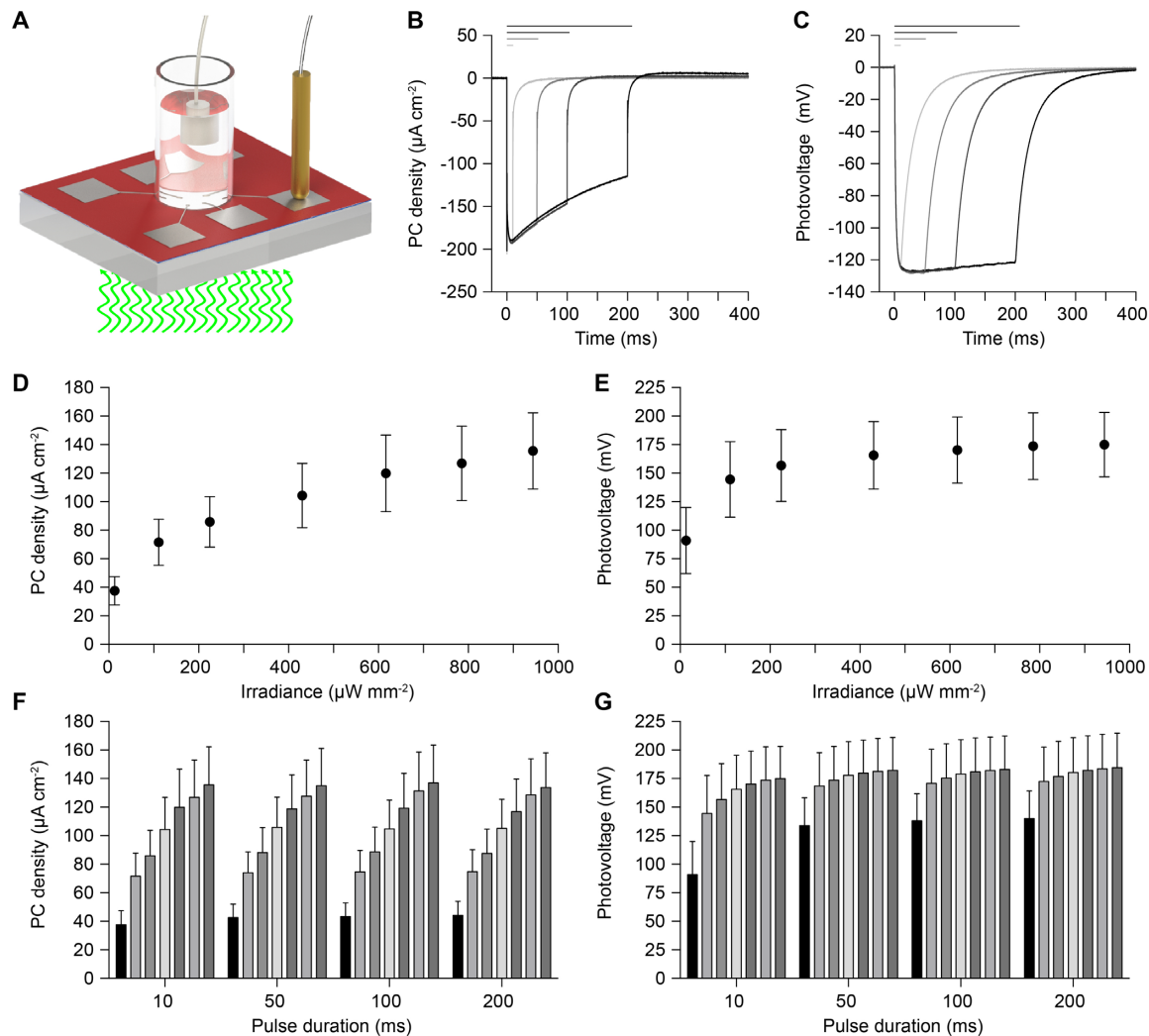


Figure 2.6 Characterization of the photo-current and photo-voltage. **A)** Drawing of the experimental setup for the measures of PC and PV; the light pulse comes from the bottom and the reference electrode in the saline solution is Ag/AgCl. **B), C)** Examples of PC density (**B**) and PV (**C**) measures obtained from 1 electrode (diameter 100 μm) at maximal light intensity (565 nm, 943.98 $\mu\text{W}/\text{mm}^2$) and for increasing pulse durations (10, 50, 100, and 200 ms). Horizontal bars represent the light pulses. **D), E)** Mean (\pm s.e.m.) PC density (**D**) and PV(**E**) measured upon illumination with 10 ms pulses at increasing light intensities. **F), G)** Mean (\pm s.e.m.) PC density (**F**) and PV (**G**) measured for increasing light intensities (12.75, 111.11, 225.00, 430.56, 616.67, 785.65, and 943.98 $\mu\text{W}/\text{mm}^2$) and pulse durations (10, 50, 100, and 200 ms). In panels D to G, the PC density and PV on every device ($N=3$) has been measured for all electrodes ($n=6$) and data have been averaged.

Ti-based photovoltaic electrodes show a full discharge (97.7%) after 100 ms (**Figure 2.7A**) when illuminated with 10 ms pulses (943.98 $\mu\text{W}/\text{mm}^2$); while they are discharged of 65.4 and of 89.9% after 25 ms and 50 ms, respectively. This suggests that POLYRETINA could operate in the 1–20 Hz range without the need of an external shunting resistor.¹²⁹ To characterize the stimulation efficiency over repetitive stimuli, we measured the PC over 1000 stimuli (**Figure 2.7B**) delivered at 1 Hz (10 ms, 943.98 $\mu\text{W}/\text{mm}^2$). The mean (\pm s.e.m.) steady state response (average of the last 20 pulses/first response) is almost unchanged ($96.99 \pm 1.51\%$). At a higher stimulation frequency, such as 10 Hz, the electrodes are entirely discharged between pulses (**Figure 2.7C** and **D**), therefore the PC density is not largely affected by repetitive stimulations; in a train of 10 pulses at 10 Hz, the mean (\pm s.e.m.) ratio last/first response is $92.20 \pm 1.52\%$ (**Figure 2.7E**). Also, in a train of 20 pulses at 20 Hz, the mean (\pm s.e.m.) ratio last/first response is $90.21 \pm 4.96\%$ (**Figure 2.7F**). Given the

possibility to stimulate at 20 Hz, we tested Ti-based photovoltaic electrodes over a long operation period (**Figure 2.7G**). Upon 320'000 stimuli (20 Hz, 10 ms, $943.98 \mu\text{W}/\text{mm}^2$), the stable steady state response (average of the last 1000 pulses/first response) is only slightly affected (88.6%).

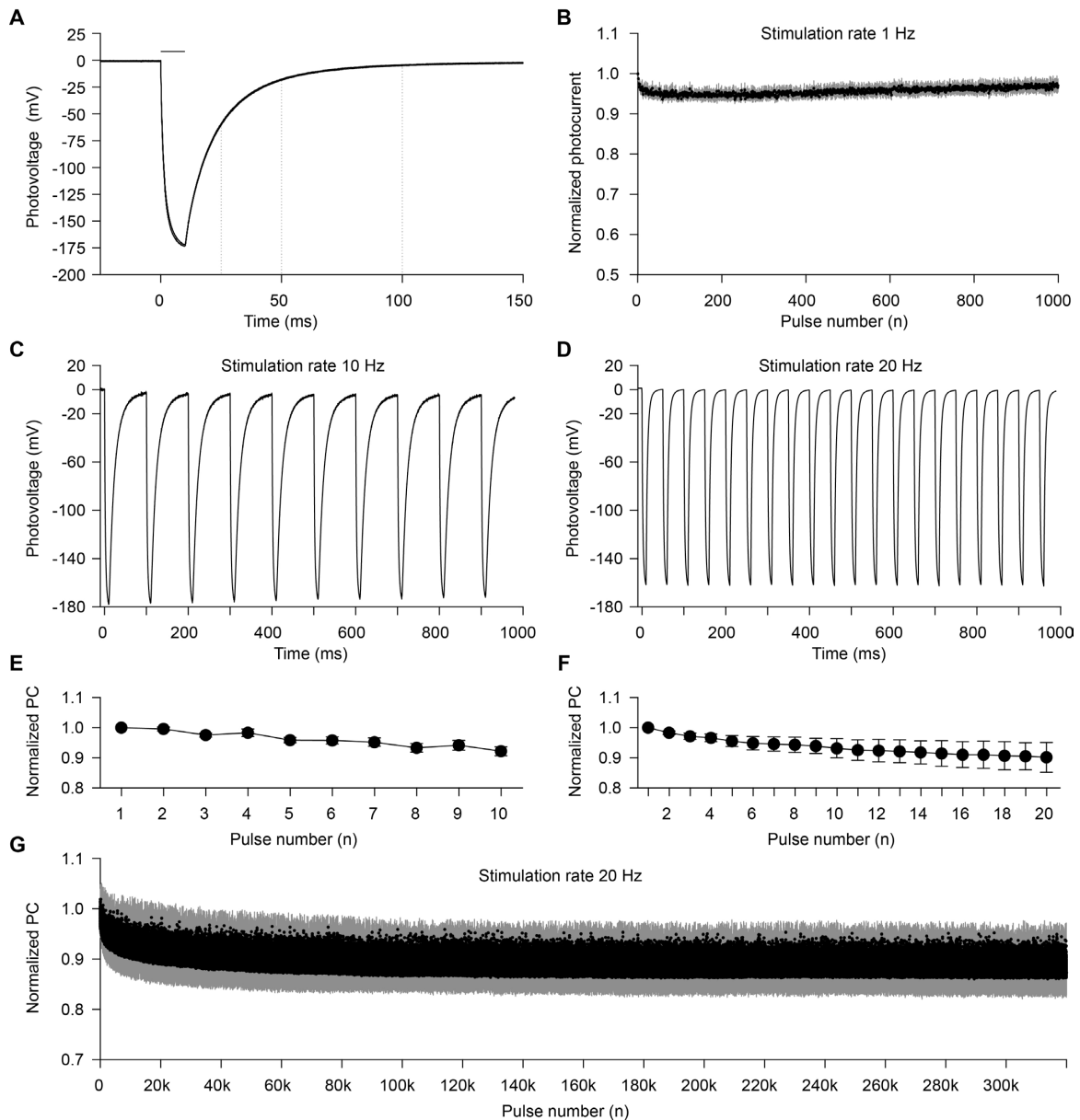


Figure 2.7 High-frequency train stimulation. **A**) Mean PV trace obtained at maximal light intensity (565 nm, 10 ms, $943.98 \mu\text{W}/\text{mm}^2$). The trace is the mean of $N = 6$ devices; in which $n = 6$ electrodes have been measured and averaged. The horizontal bars represent the light pulse. The dotted lines highlight the discharging rate of the electrode. **B**) Evolution of the PC density peaks during 1000 stimuli delivered at 1 Hz (10 ms, $943.98 \mu\text{W}/\text{mm}^2$). Each point is the mean (\pm s.e.m.) of $N = 3$ devices, in which $n = 6$ electrodes have been measured and averaged. **C**) Representative PV recording upon 10 pulses at 10 Hz (565 nm, 10 ms, $943.98 \mu\text{W}/\text{mm}^2$). **D**) Representative PV recording upon 20 pulses at 20 Hz (565 nm, 10 ms, $943.98 \mu\text{W}/\text{mm}^2$). **E**) Evolution of the PC density peaks normalized to the first pulse at 10 Hz. Each point is the mean \pm s.e.m. of $N = 10$ devices, in which $n = 6$ electrodes have been measured and averaged. **F**) Evolution of the PC density peaks normalized to the first pulse at 20 Hz. Each point is the mean \pm s.e.m. of $N = 8$ devices, in which $n = 6$ electrodes have been measured and averaged. **G**) PC generated with 320'000 stimuli delivered at 20 Hz (565 nm, 10 ms, $943.98 \mu\text{W}/\text{mm}^2$). Each point is the mean \pm s.d. of $n = 2$ electrodes from $N = 1$ device.

2.2.3 Validation *ex vivo* with explanted retinas from blind mice

Next, we tested the *ex vivo* efficacy of the PDMS–photovoltaic interface in stimulating RGCs. For this purpose, we used the retinal degeneration 10 (Rd10) mouse model, that is recognized as an excellent model for retinitis pigmentosa.^{130,131} Extracellular recordings of prosthetic-evoked spiking activity of RGCs have been collected from retinas explanted from old mice to avoid as much as possible the natural responses from surviving photoreceptors ($n = 39$ cells, $N = 15$ mice; mean \pm s.d. age 140.87 ± 20.35 days). Retinas have been layered on the central 5-mm area of the PDMS–photovoltaic interface mimicking the epiretinal configuration (**Figure 2.8A**). According to the PC density measures, we tested only 10 ms pulses (peak of the PC response) with a broad range of irradiance (from $47.35 \mu\text{W}/\text{mm}^2$ to $29.07 \text{mW}/\text{mm}^2$). Light pulses induced a prosthetic-evoked spiking activity in the recorded RGC (**Figure 2.8B**, **Figure 2.9A**, and **Figure 2.10A**). Spikes have been detected with a threshold algorithm (red lines in **Figure 2.8B** and **Figure 2.9A** and **B**), converted into a raster plot, and presented as peri-stimulus time histogram (PSTH).

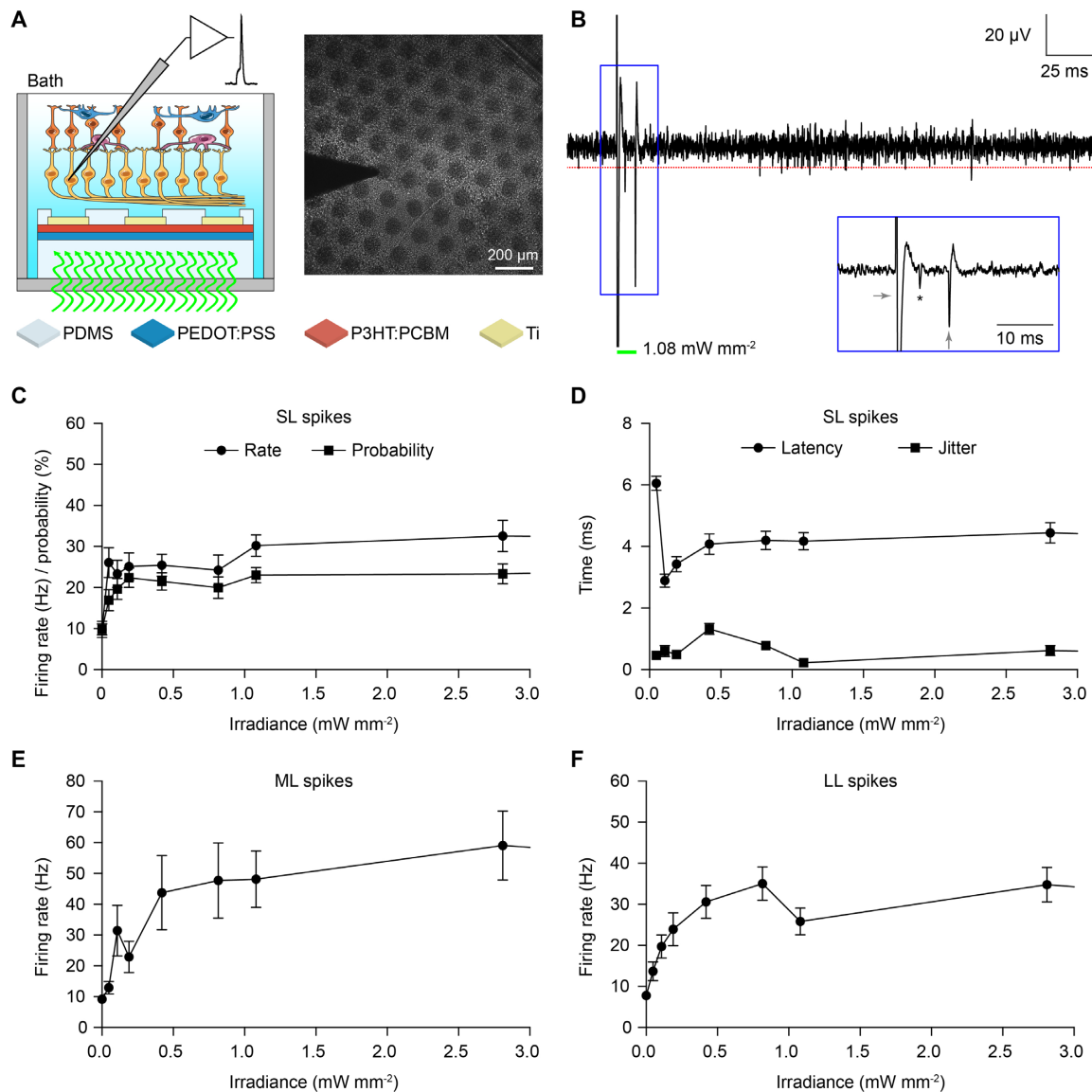


Figure 2.8 Evaluation *ex vivo* with retinal explants. **A**) Sketch of the recording set-up together with a picture of a retinal explant over the PDMS–photovoltaic interface with the metal electrode used for recordings. **B**)

Representative single-sweep recording from a retinal ganglion cell over PDMS–photovoltaic interface upon 10 ms illumination at $1081.7 \mu\text{W}/\text{mm}^2$. The red dotted line is the threshold set for spike detection. The green bar represents the light pulse. The blue insert shows a magnification of the period around the light pulse. The asterisk indicates the over-threshold spike detected, while the gray arrows are the light on-set and off-set stimulation artifacts. **C)** Mean (\pm s.e.m.) firing rate (circles) and firing probability (squares) of SL spikes, computed across all the recorded cells ($n = 39$, ten sweeps each) on the PDMS–photovoltaic interface. For each cell, the probability has been defined as the percentage of sweeps with at least a SL spike over the ten consecutive trials. **D)** Mean (\pm s.e.m.) latency (circles) and jitter (squares) of the first spike occurring in the 10 ms window after the light onset, computed across all the recorded cells ($n = 39$, ten sweeps each) on the PDMS–photovoltaic interface. For each cell, the mean latency and jitter has been computed over the ten consecutive trials. **E), F)** Mean (\pm s.e.m.) firing rate of medium (E) and long (F) latency spikes, computed across all the recorded cells ($n = 39$, ten sweeps each) on the PDMS–photovoltaic interface. In panels C-F values have been plotted up to $3 \text{ mW}/\text{mm}^2$, while the full profiles are shown in **Figure 2.9C-F**.

We observed three types of responses, classified as short, medium, and long latency (SL, ML, and LL). As mentioned in the introductory chapter of the thesis, the presence of SL spikes (elicited in the 10-ms window after the light onset, 1 bin) indicates a direct electrical stimulation of RGCs; while the presence of ML and LL spikes indicates a network-mediated activation. We have found that SL spikes can be evoked starting from the first irradiance tested ($47.35 \mu\text{W}/\text{mm}^2$), then the firing rate slowly increases and it remains stable above $1.08 \text{ mW}/\text{mm}^2$ till the highest irradiance tested (**Figure 2.8C** and **Figure 2.9C**). However, the mean (\pm s.e.m.) latency (**Figure 2.8D**) at this first irradiance is relatively long ($6.05 \pm 0.23 \text{ ms}$); it decreases with the increase of the irradiance, and it stabilizes at $4.12 \pm 0.07 \text{ ms}$ for irradiance higher than $1.08 \text{ mW}/\text{mm}^2$ (**Figure 2.8D** and **Figure 2.9D**). In this range (higher than 1.08), the mean (\pm s.e.m.) jitter of the first SL spike is $0.39 \pm 0.05 \text{ ms}$. This suggests that the SL response is saturated for irradiance higher than $1.08 \text{ mW}/\text{mm}^2$, as predicted by the measure of the PC densities. For irradiance lower than $1.08 \text{ mW}/\text{mm}^2$ the mean latency appears shorter, but the jitter is more variable, indicating a more instable response (**Figure 2.8D**). The firing rate of ML (**Figure 2.8E** and **Figure 2.9E**) and LL (**Figure 2.8F** and **Figure 2.9F**) spikes growth more progressively, but they also become stable after $1.08 \text{ mW}/\text{mm}^2$. As a control, when retinas have been layered on bare PDMS substrates ($n = 34$, $N = 13$; $143.08 \pm 32.09 \text{ days}$), no light-evoked responses have been detected for all the irradiance tested (**Figure 2.9B** and **Figure 2.10**). As already demonstrated by others,¹³² we also verified in a second subset of cells ($n = 6$, $N = 5$; $209.4 \pm 37.14 \text{ days}$) that the prosthetic activation of both ML and LL spikes is abolished by using synaptic blockers (**Figure 2.11**). This confirms the hypothesis that ML and LL are induced by the activation of the internal retinal circuit.

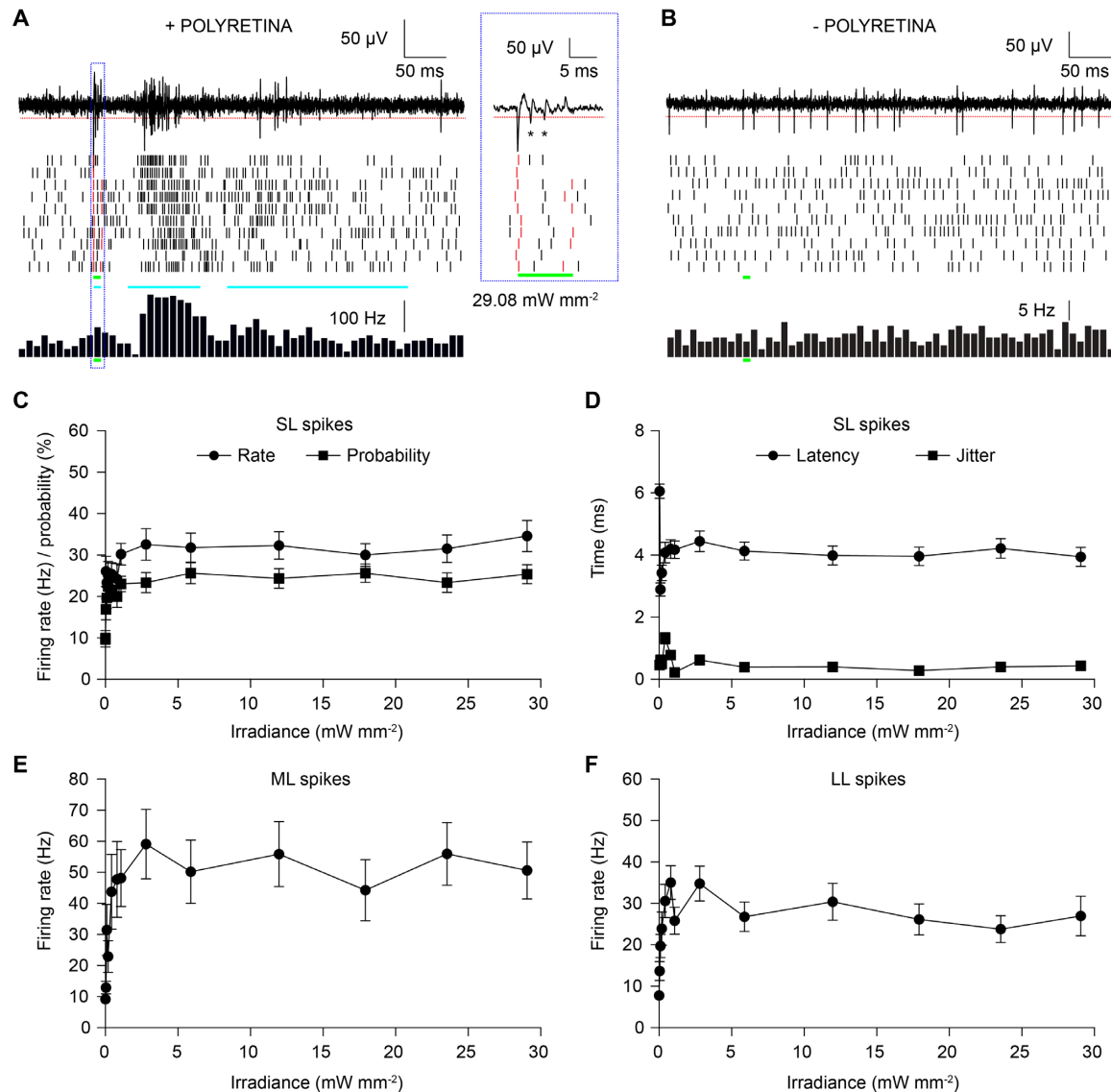


Figure 2.9 Further evaluation *ex vivo* with retinal explants. **A**) The top panel shows a representative single-sweep recording from a retinal ganglion cell over the PDMS-photovoltaic interface upon maximal illumination (10 ms, 29.08 mW/mm^2). The red dotted line is the threshold set for spike detection. The middle panel shows the raster plot based on the over-threshold events detected and classified as spikes upon ten consecutive sweeps in the same cell. The green bars represent the light illumination. The cyan bars represent the regions where SL, ML, and LL spikes have been identified. The red bars correspond to the detection of the stimulation artefacts at the onset and offset of illumination. Artefacts have been excluded in subsequent analysis. The bottom panel shows the PSTH of the cell computed over ten consecutive sweeps. The blue box shows an enlarged view of the light onset. The asterisks (*) indicate the over-threshold events detected and classified as spikes. **B**) Example from a retinal ganglion cell over bare PDMS. **C**) Mean (\pm s.e.m.) firing rate (●) and firing probability (■) of SL spikes, computed across all the recorded cells ($n = 39$) on the PDMS-photovoltaic interface. For each cell, the probability has been defined as the percentage of sweeps with at least a SL spike over the ten consecutive trials. **D**) Mean (\pm s.e.m.) latency (●) and jitter (■) of the first spike occurring in the 10 ms window after the light onset, computed across all the recorded cells ($n = 39$, ten sweeps each) on the PDMS-photovoltaic interface. **E**), **F**) Mean (\pm s.e.m.) firing rate of medium (E) and long (F) latency spikes, computed across all the recorded cells ($n = 39$, ten sweeps each) on the PDMS-photovoltaic interface.

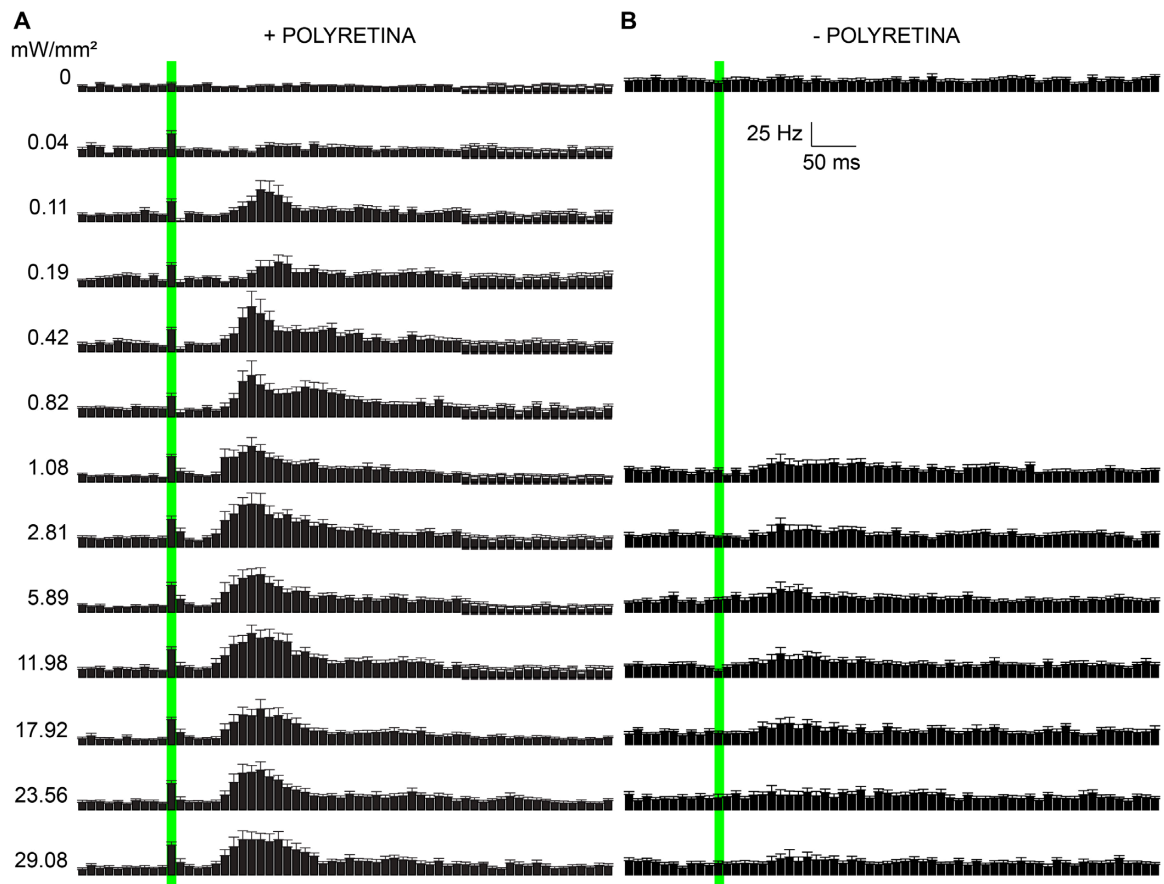


Figure 2.10 Recordings of Rd10 retinas *ex vivo*. PSTHs (bin 10 ms, mean \pm s.e.m.) obtained from $n = 39$ and $n = 34$ retinal ganglion cells, respectively for the PDMS-photovoltaic interface (A) and the bare PDMS substrate (B). Each row corresponds to a different light intensity expressed on the left in mW/mm^2 . Green bars represent the light pulses. On bare PDMS substrate, cells have been tested only for the high range of irradiance.

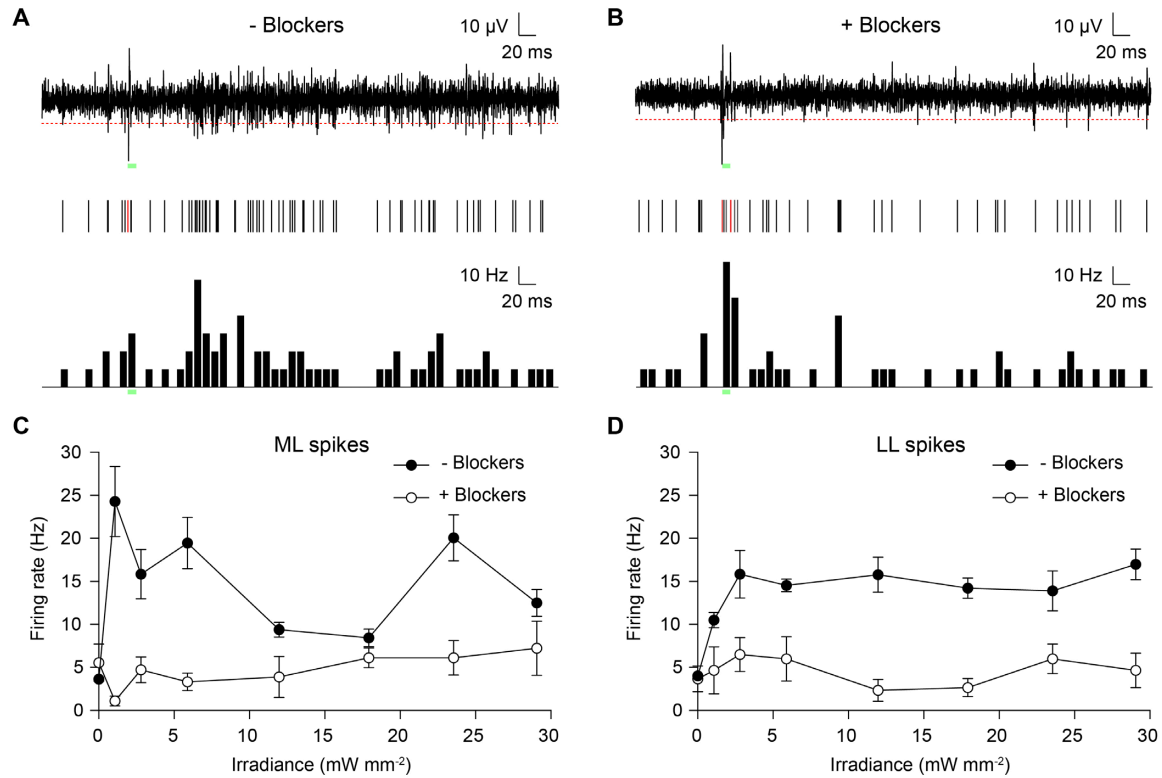


Figure 2.11 Pharmacological blockage of network activity. **A)** The top panel shows a representative single-sweep recording from a RGC over the PDMS-photovoltaic interface upon illumination (10 ms, 23.56 mW/mm²). The red dotted line is the threshold set for spike detection. The green bars represent the light pulse. The middle panel shows the raster plot based on the over-threshold events detected and classified as spikes upon ten consecutive sweeps (overlay) in the same cell. The red bars correspond to the detection of the stimulation artefacts at the onset and offset of illumination. Artefacts have been excluded. The bottom panel is the PSTH (bin 10 ms) of the cell computed over ten consecutive sweeps. **B)** Response upon illumination (10 ms, 23.56 mW/mm²) of the same RGC in **A)**, after inclusion of synaptic blockers. **C), D)** Mean (\pm s.e.m.) firing rate of ML (**C**) and LL (**D**) spikes computed across all the recorded cells ($n = 6$, ten sweeps each) on the PDMS-photovoltaic interface before (\bullet) and after (\circ) the inclusion of synaptic blockers.

2.2.4 Spatial selectivity

We then addressed the spatial selectivity by using an experimental/computation hybrid approach. First, using a glass microelectrode (**Figure 2.12A** and **B**) we measured the radial voltage spreading in three directions (D1, D2, and D3) upon illumination of a single pixel. For each illuminated pixel ($n = 4$ pixels), the normalized voltage spreading in the three principal directions have been averaged and plotted normalized to the central point (**Figure 2.12C**). The mean (\pm s.e.m.) voltage distribution across all the pixel tested has been plotted and interpolated with a Gaussian function (**Figure 2.12D**). Experimental data match with the normalized voltage profile obtained by a finite element analysis (FEA) model (**Figure 2.12D**, dotted blue line). The full width at half maximum (FWHM) of the simulated curve (**Figure 2.12D**, dotted gray line) has been taken as the effective activation area, which is about 100 μm for pixels of 80 μm . FEA simulations have been used to characterize the normalized voltage profile induced by illumination of increasing diameters (**Figure 2.12E**). Increasing the spot size from one pixel to seven and 19 pixels increases the overall potential. Last, we simulate the effect of different patterns of activation (**Figure 2.12F**). In all cases, a spatially selective potential profile corresponding to light pattern is shown.

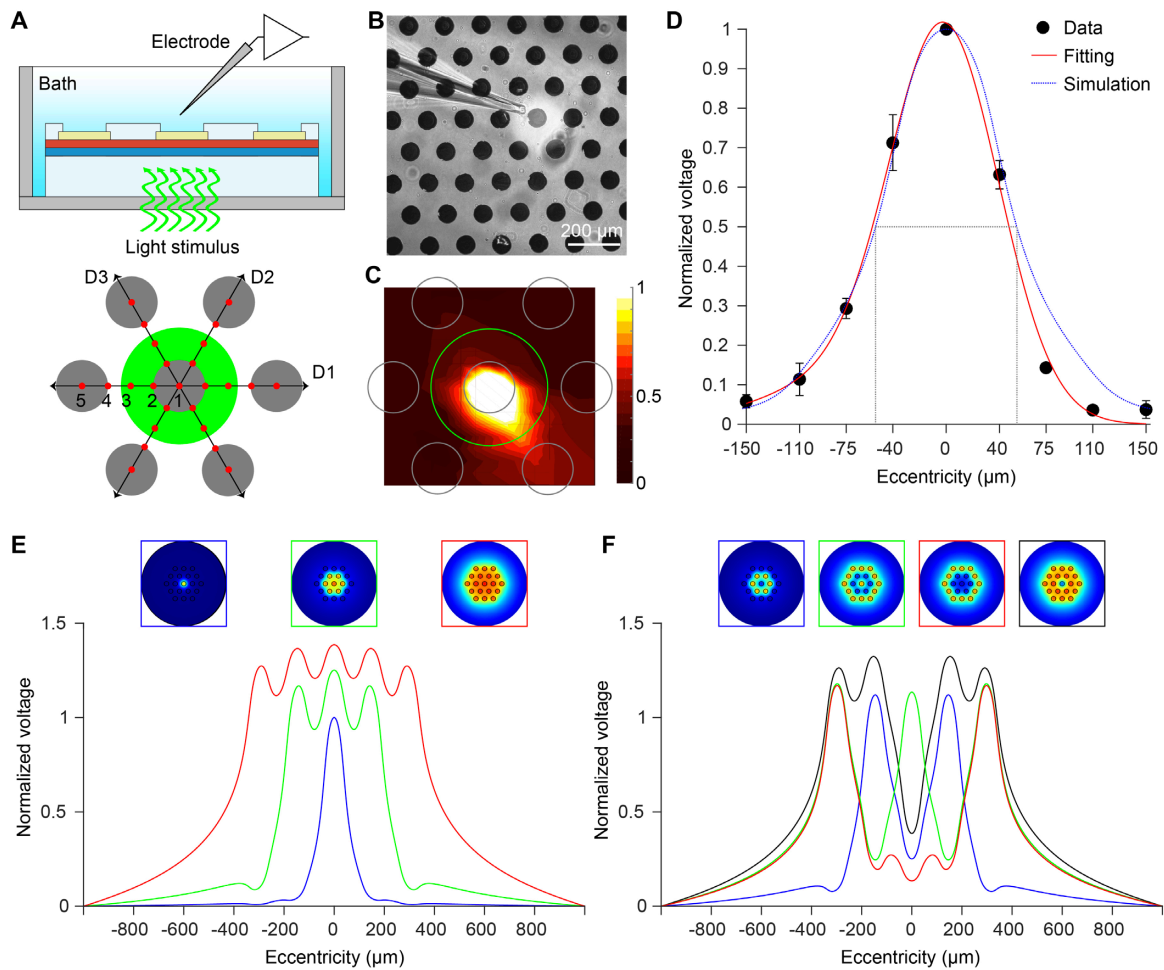


Figure 2.12 Spatial confinement of the prosthetic stimulation. **A)** Sketch of the experimental setting. The green circle corresponds to the area illuminated around the central pixel. Gray circles represent the illuminated pixel and the six surrounding ones. The voltage has been measured in nine positions (red dots) for each direction (D1, D2, and D3), all centered in the center of the illuminated pixel. **B)** Picture during recordings, where the light spot is visible (brighter area). **C)** Voltage spreading color map generated by interpolating the experimental measures with a triangulation-based linear interpolation. At each point, ten consecutive recordings have been averaged and the voltage peaks have been normalized with respect to the value obtained in the central pixel (position 1 in A). The green circle is the illuminated area, while the gray circles represent the pixels. **D)** Mean (\pm s.e.m.) normalized PV peaks from $n=4$ pixels. For each pixel, the data from the three directions have been averaged. The red line shows a Gaussian fitting, while the blue dotted line represents the normalized voltage profile obtained by FEA simulations. The gray dotted lines show the FWHM value for the simulated profile. **E)** FEA simulations for three beam sizes, normalized to the potential corresponding to the illumination of the single central pixel. **F)** FEA simulations for various patterns of activation normalized to the potential corresponding to the illumination of the single central pixel.

2.2.5 Cytotoxicity and long-term functioning

To validate the long-term functioning of POLYRETINA, we first tested the mechanical impact of the hemispherical shape. For this purpose, the PDMS–photovoltaic interface has been bonded on the dome-shaped PDMS support. The bonding procedure induces tensile stresses in the PDMS–photovoltaic interface leading to the formation of cracks in the polymers and the titanium cathodes (**Figure 2.13A**, top row). To avoid cracks in the titanium cathodes, SU-8 rigid platforms¹³³ have been integrated below each cathode in the substrate of the interface (**Figure 2.1F**). With this precaution,

the pixel above the SU-8 rigid platforms is protected from cracks (**Figure 2.13A**, bottom row); images correspond to the green area in **Figure 2.1C**. Cracks are still formed within the blend film in the area between SU-8 rigid platforms, however this is less critical since that area is encapsulated in PDMS to prevent delamination, and the carriers photo-generated outside of the area defined by the cathode do not significantly contribute to the photo-potential/current generated at the electrode-electrolyte interface. Then, we measured the changes in the surface potential by using KPFM (**Figure 2.13B**). Due to the hemispherical shape, only the electrodes at the top of the prosthesis (80 μm in diameter / 67 μm openings) can be reached by the AFM tip. The surface potential change induced by illumination (white LED, light from the top, 0.4 mW/mm^2) is not statistically different (Mann-Whitney test, $p = 0.8182$) with respect to the planar PDMS-interface (**Figure 2.13C**).

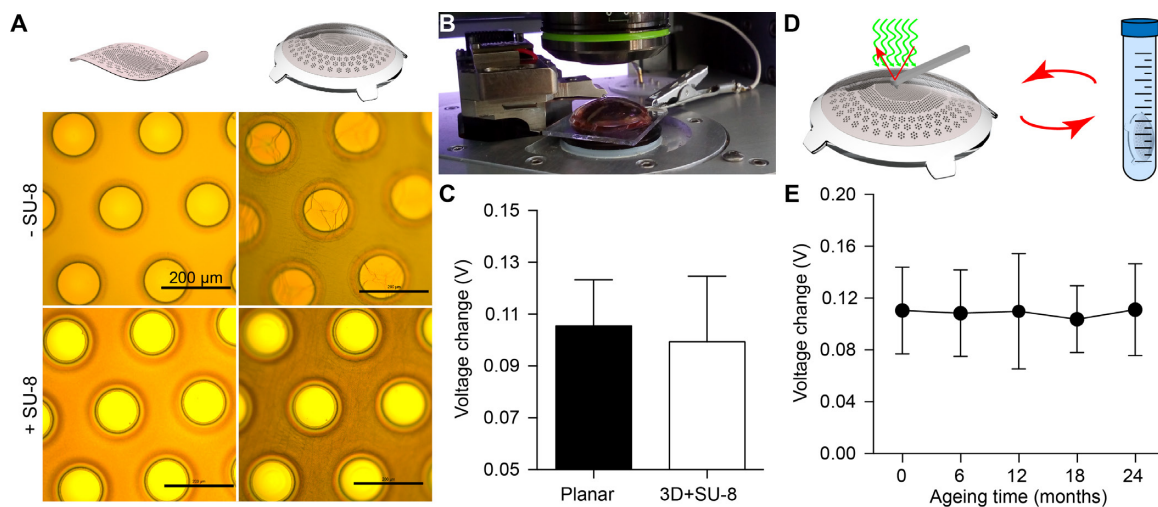


Figure 2.13 Lifetime of the retinal prosthesis. **A**) Pictures of the titanium cathodes before (left column) and after (right column) bonding on the dome-shaped PDMS support. The top row is without SU-8 rigid platforms, while the bottom row is with SU-8 rigid platforms. **B**) Picture of a KPFM measure on bonded prostheses integrating SU-8 rigid platforms. **C**) Comparison of KPFM measures on bonded prostheses integrating SU-8 rigid platforms (99.35 ± 25.26 mV, mean \pm s.d., $n = 15$; electrode diameter 80 μm) with respect to measures on PDMS-interface prior bonding (planar) (105.50 ± 17.79 mV, mean \pm s.d., $n = 36$; electrode diameter 100 μm). **D**) Sketch of the accelerated ageing tests. KPFM measures have been performed at the beginning of the experiment, then prostheses have been immersed in saline solution at 87 $^{\circ}\text{C}$ for 135 h, after that KPFM has been repeated, and on for four cycles. **E**) Quantification (mean \pm s.d., $N = 4$ prostheses, $n = 4$ electrodes per prosthesis) of the surface potential changes (difference of voltage in light with respect to voltage in dark) during accelerated ageing tests over a simulated period of 24 months (months: 0, 110.5 ± 33.53 mV; 6, 108.5 ± 33.37 mV; 12, 109.8 ± 44.59 mV; 18, 103.8 ± 25.73 mV; 24, 111.1 ± 35.48 mV).

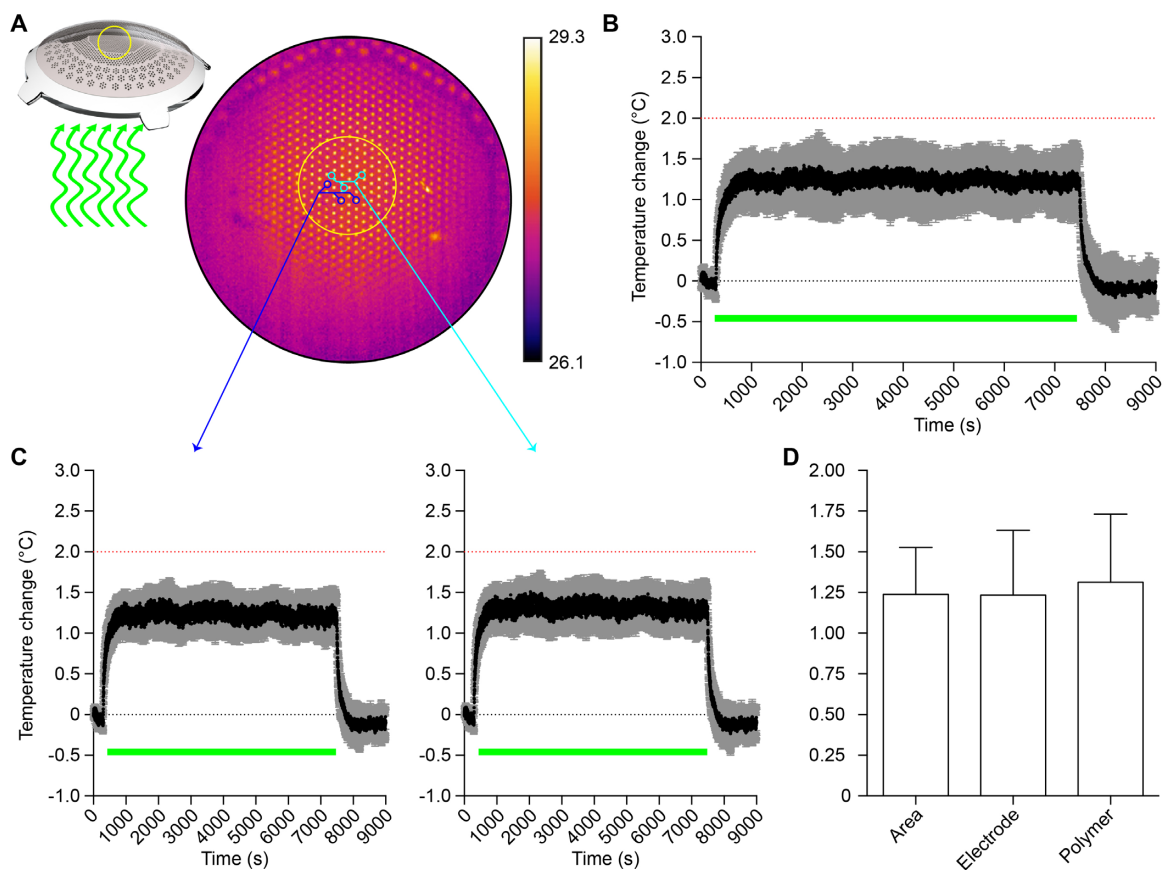
To simulate the lifetime of POLYRETINA once implanted, we performed a functional accelerating ageing test by immersion in physiological saline solution hold at 87 $^{\circ}\text{C}$ (**Figure 2.13D**). The changes of the surface potential upon illumination have been measured with KPFM before starting the ageing and at several time points during the protocol (**Figure 2.13E**). No statistically significant changes in the mean (\pm s.d.) surface potential have been detected till 24 months of accelerated ageing (one-way ANOVA, $F = 0.1252$, $p = 0.9731$).

Last, according to ISO 10993-5: Biological Evaluation of Medical Devices, *in vitro* cytotoxicity has been evaluated via an extraction test on the murine fibroblastic L929 cells. Cell viability has been estimated via an XTT cell viability assay. Results on the prosthesis showed a 100% viability, while

positive control has 0.3% viability and negative control has 100% viability (averages of three repetitions; see certificate in **Appendix Figure 3**).

2.2.6 Thermal and optical safety

According to the thermal safety standards for active implantable medical devices (ISO 14708-1 / EN 45502-1), the maximum temperature on the surface of the implant should not exceed 2 °C above the normal surrounding body temperature of 37 °C.¹³⁴ We measured in air the increase in temperature on the POLYRETINA surface (**Figure 2.14A** and **B**) due to continuous operation for 2 h under full-field pulsed illumination (20 Hz, 10 ms, 1.22 mW/mm²). The irradiance has been set to the maximal allowed by the LED. The mean (\pm s.d., N=4 prostheses) thermal increase at steady state is 1.24 ± 0.29 °C, which is below the standard limit of 2 °C. We verified also that the temperature increases on the electrodes and on the polymer surface are not different (**Figure 2.14C** and **D**). Anyhow, this experiment corresponds to the extreme case of projecting a constant full white frame, which is not realistic in daily operation when images will be presented as black and white. Under this condition, the average light dose is lower and therefore the related increase in temperature will be lower. In addition, the eye vitreous has a thermal conductivity about 30 times higher than air; therefore, heat sinking is more efficient.



baseline temperature measured for 5 min before pulsed illumination. The green bar represents the period of 2 h when light pulses have been applied (10 ms pulses, 20 Hz repetition rate, 1.22 mW/mm²). The dotted red line represents the maximal allowed temperature increase. **C)** Mean (\pm s.e.m.) changes in surface temperature measured on the electrodes (left, N = 4 prostheses) or on the polymer area (right, N = 4 prostheses). For each prosthesis, n = 3 regions have been sampled and averaged. **D)** Mean (\pm s.d.) changes in surface temperature in the overall surface, the electrode area, or the polymer area are not significantly different (1.24 ± 0.29 , 1.23 ± 0.20 , 1.31 ± 0.21 , respectively; one-way ANOVA, $F = 0.0569$, $p = 0.9451$).

Regarding optical safety, photovoltaic prostheses are limited by retinal damage upon light exposure (ANSI Z136.1 / ISO 60825 / ISO 15004).¹²⁰ According to the standards, the maximum permissible exposure (MPE) during chronic illumination of the full POLYRETINA (equivalent to a full white frame) is controlled by the photothermal damage and equals to 328.75 μ W/mm² (see paragraph 2.4.10 in the methods). However, photovoltaic prostheses operate with pulsed illumination. With pulses of 10 ms and duty cycle of 5, 10, or 20% (respectively for 5, 10, or 20 Hz), the MPE is increased to 6.58, 3.29, or 1.64 mW/mm², respectively. These values are higher than the saturation value measured with retinal explants (1.08 mW/mm²).

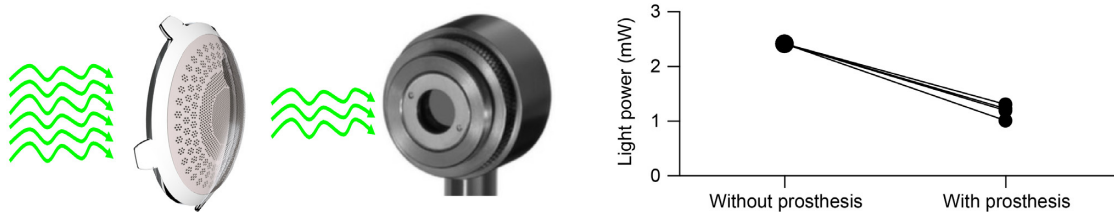


Figure 2.15 Optical absorption of POLYRETINA. Light transmittance of POLYRETINA has been evaluated by using a green LED (565 nm, 2.42 mW). Light has been measured with a power meter (PD300-R Juno, Ophir Optonics Solutions Ltd.). The retinal prostheses (N = 4) have been inserted in the light path and the light power has been compared with respect to the condition without the prostheses.

In case of POLYRETINA, the incident light is mainly absorbed by the P3HT:PCBM layer. The mean (\pm s.d., N = 4 prostheses) transmittance of POLYRETINA has been experimentally measured as $49.07 \pm 5.25\%$ (**Figure 2.15**). Therefore, only part of the incident light reaches the retina and the RPE, thus reducing the effect of retinal heating due to light absorption in the RPE. However, the light absorbed by P3HT:PCBM generates heat, that should be taken into account when evaluating the MPE. We performed FEA simulations to estimate the temperature increase in the retina upon illumination of POLYRETINA. First, we verified the temperature increase without POLYRETINA at the RPE–retina interface using the obtained MPE (328 and 1.64 mW/mm²), respectively, for continuous and pulsed (10 ms pulses at 20 Hz) illumination. After 150 s of continuous illumination (560 nm, 328 μ W/mm²), the temperature increase is stable at 0.42 °C (**Figure 2.16A and B**). Pulsed illumination (10 ms pulses at 20 Hz, 1.64 mW/mm²) generates temperature spikes of about 0.04 °C, oscillating around the profile corresponding to the continuous illumination (**Figure 2.16C and D**). This demonstrates that the scaling factor of 5 to estimate the MPE during pulsed stimulation (20% duty cycle) is correct. Continuous illumination has been used in the following simulations to reduce the computational cost. With POLYRETINA, the temperature increase after 150 s of continuous illumination (560 nm, 328 μ W/mm²) is slightly reduced to 0.37 °C (**Figure 2.17A and B**). In this case, the critical interface is the one between the retina and the prosthesis giving a slightly higher temperature increase with respect to the RPE–retina interface (0.37 vs 0.35 °C). POLYRETINA has been simulated in direct contact with the retina because this represents the worst-case scenario. A thin space of vitreous (100 μ m) between the retina and POLYRETINA reduces the temperature increase by

0.009 °C, which is negligible. The thermal damage of the retina requires a local rise in temperature higher than 10 °C;¹³⁵ the 50% probability of retinal damage (ED50) has been previously defined for a temperature rise of 12.5 °C.¹³⁴ In our model, we estimated the ED50 with (red) and without (black) POLYRETINA (**Figure 2.17C**). As expected, the ED50 for continuous illumination is slightly higher when POLYRETINA is present (10.6 vs 9.4 mW/mm²), which correspond to 53 mW/mm² for pulsed illumination. A comparison with and without POLYRETINA showed that over the broad range of irradiances the temperature increase in the retina is reduced by 11% with POLYRETINA. Therefore, the MPE could be slightly increased to 1.84 mW/mm² and POLYRETINA can safely operate at 1 mW/mm².

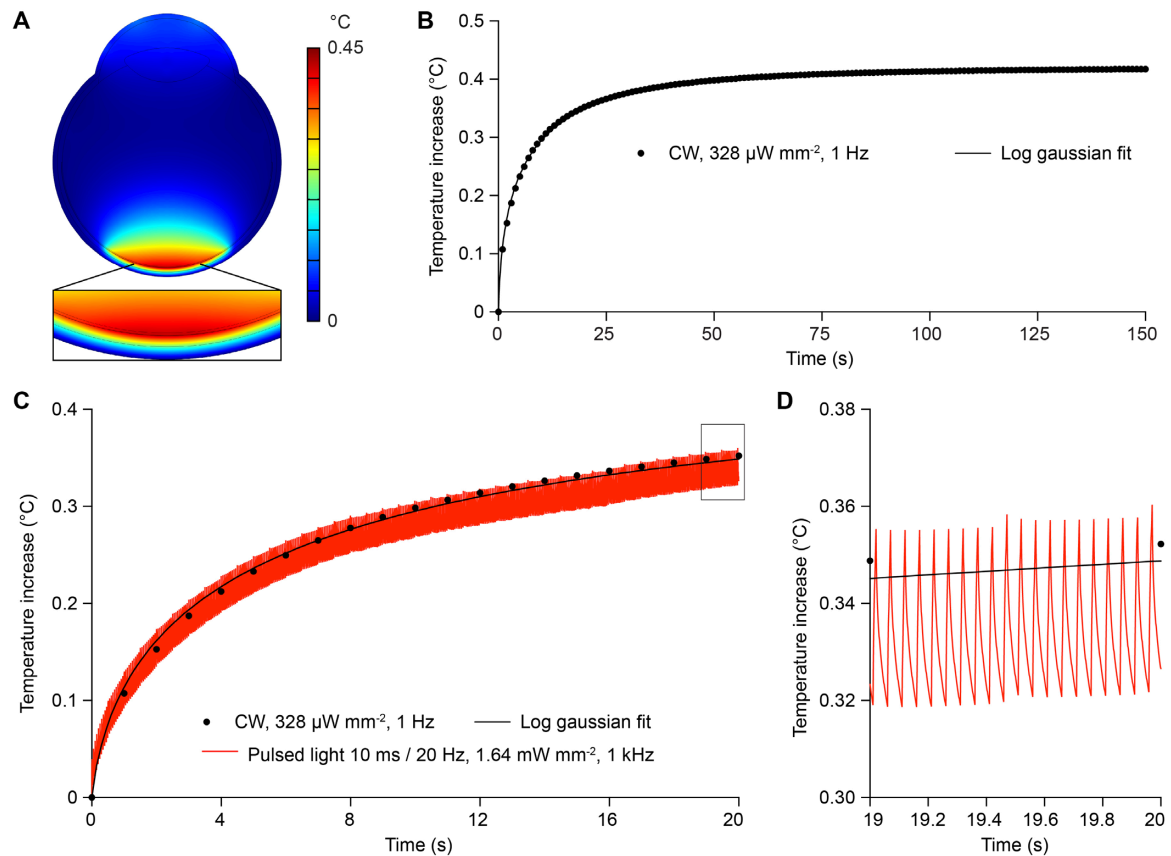


Figure 2.16 FEA simulation of thermal effects. **A**) Temperature increase in the modelled eye after 150 s of continuous illumination (continuous wave CW, 560 nm, 328 $\mu\text{W}/\text{mm}^2$). The insert shows a larger view of the modelled retina. **B**) Time course of the temperature increase in the modelled retina during 150 s of continuous illumination (CW, 560 nm, 328 $\mu\text{W}/\text{mm}^2$). The simulation frequency has been set to 1 Hz. The line is the log Gaussian fit ($R^2 = 0.9958$). **C**) Comparison of the temperature time course during continuous illumination at 328 $\mu\text{W}/\text{mm}^2$ (black dots) and pulsed illumination with 10 ms pulses at 20 Hz and 1.64 mW/mm² (red line) for 20 s of simulation. The simulation frequency for the pulsed illumination has been set to 1 kHz. **D**) Magnification of the last 1 s of the simulation in C.

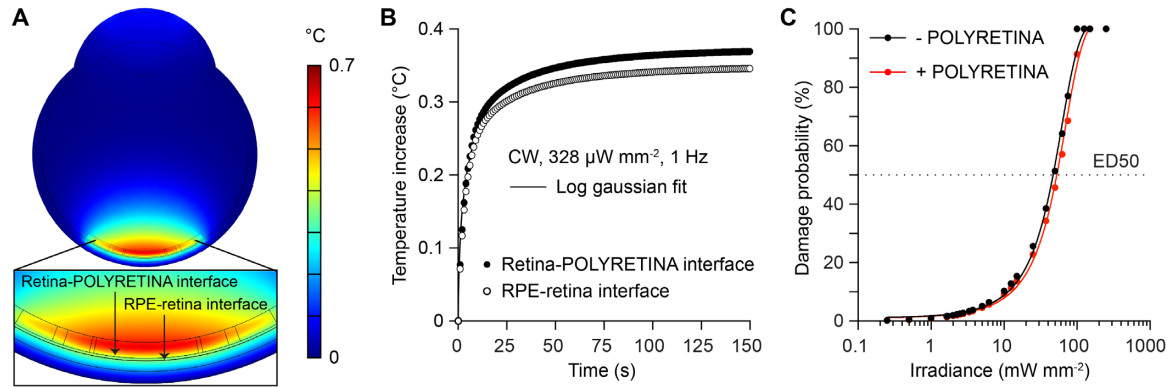


Figure 2.17 FEA simulation of thermal effects with POLYRETINA. **A)** Temperature increase in the modeled eye with POLYRETINA after 150 s of continuous illumination (CW, 560 nm, $328 \mu\text{W}/\text{mm}^2$). The insert shows a larger view of the modeled retina and POLYRETINA. **B)** Time course of the temperature increase at the RPE-retina (\circ) and retina-POLYRETINA (\bullet) interface during 150 s of continuous illumination (CW, 560 nm, $328 \mu\text{W}/\text{mm}^2$). The simulation frequency has been set to 1 Hz. The solid line is the log Gaussian fit ($R^2 = 0.9934$). **C)** Probability of retinal damage as a function of irradiance with (red) and without (black) POLYRETINA. ED50 corresponds to a temperature increase of $12.5 \text{ }^\circ\text{C}$. The irradiance has been expressed for pulsed illumination (20% of duty cycle). The solid lines are the Sigmoidal fits ($R^2 = 0.9971$ for black and 0.9977 for red).

2.3 Discussion

One of the most important open questions in the field of retinal prostheses concerns how to increase both visual acuity and visual field size together. From the engineering point of view, this implies to increase the density of the stimulating electrodes and enlarge the size of the prosthesis. POLYRETINA is a novel foldable and photovoltaic wide-field epiretinal prosthesis with a remarkable increase in its size and in the number of stimulating pixels compared to other epiretinal prostheses.^{64,136}

Concerning visual field, POLYRETINA has the potential to cover a retinal surface corresponding to a visual angle of 46° , which is larger than the threshold for both legal blindness (20°) and adequate mobility skills (30°). Concerning spatial resolution, the presence of a continuous semiconductor layer does not represent a limitation. In organic photovoltaics, the low carrier mobility and lifetime of charges limit the carrier-transport length to tens of nm for holes and few hundreds of nm for electrons.¹³⁷ It has been shown by another group that the PC detected at the cathode is reduced to about 10% of the maximum if the illumination spot (size $1 \mu\text{m}$) is moved laterally by about $12 \mu\text{m}$ from the electrode edge.¹³⁸ This large decay length, beyond the simple diffusion processes, has been explained by a steady state nonlocal electric field inducing a lateral flow of the separated carriers. For this reason, an internal cross-talk between electrodes due to charge carriers generated under one electrode traveling laterally towards an adjacent electrode can be excluded (at least down to an edge-to-edge distance of about $20 \mu\text{m}$). By measuring the voltage spread in solution together with FEA simulations we showed that the area of activation (about $100 \mu\text{m}$) of 1 pixel is comparable to the pixel size. Concerning visual acuity, with a pitch of $150 \mu\text{m}$ the theoretical visual acuity restored by POLYRETINA is in the order of $20/600$;⁸⁹ which is better than the current epiretinal prostheses (e.g., Argus II) but still below the threshold of legal blindness. However, the technology of POLYRETINA is highly scalable and pixels size and pitch can be reduced to obtain better visual acuity values. Indeed, these values come from theoretical computation, and therefore must be validated with proper *in vivo* experiments in animals and later in humans. Moreover, the reduction of the pixel size will

reduce the PC generated by the interface, therefore the efficiency in stimulating RGCs should be validated again.

To be used as retinal prosthesis, POLYRETINA must operate with a stimulation rate higher than 1 Hz. The subretinal prosthesis Alpha IMS operates in a frequency range of 1 to 20 Hz (variable from patient to patient) with a pulse duration of 1–4 ms.¹³⁹ Available pulse rates in the Argus II are in the range of 3–60 Hz;¹⁴⁰ however, also in this case, the effect of pulse rate have been reported to be very variable among subjects.¹⁴¹ This suggests that, even if overall the variation in the pulse rate does not have a significant effect, an optimal pulse rate can be defined for each subject. Moreover, the recent identification of an optimal pulse duration of 25 ms per phase may limit the operating range of Argus II to a theoretical limit of 20 Hz.¹⁴² For the silicon photovoltaic subretinal prosthesis, the stimulation frequency is mainly limited by the discharge rate of the electrode, therefore a shunt resistor has been included to allow faster stimulations (20–40 Hz) up to flicker fusion.^{68,129} POLYRETINA shows a fast discharge of the Ti-based photovoltaic electrodes (probably due to the high shunting capacity of the P3HT:PCBM layer), and we demonstrated its functioning up to 20 Hz of stimulation rate without an additional shunting resistor. This is within the operation range of other epiretinal (e.g., Argus II) and subretinal (e.g., Alpha IMS) prostheses.

The activation of RGCs has been obtained already at $47.35 \mu\text{W}/\text{mm}^2$ with a response saturation above $1.08 \text{ mW}/\text{mm}^2$. However, recordings *ex vivo* with retinal explants may not be representative of the complexity of retinal stimulation *in vivo* in humans, where the electrode-to-cell distance could be larger and could increase during years of implantation, thus increasing the perceptual threshold.¹⁴³ The hemispherical design is a solution to reduce the electrode-cell distance over the large area of the prosthesis. Moreover, the capability of activating RGCs at low irradiance is promising in perspective of an *in vivo* application. In a future development, titanium/titanium nitride electrodes can be fabricated in order to improve the stimulation efficiency (because of their higher charge injection capacity).¹²⁶

The presence of SL spikes is an evidence in support of a direct activation of RGCs. On the contrary, ML and LL spikes are due to the activation of the internal retinal circuit. In literature, SL spikes are reported to be very close (i.e., 0.5–4 ms) to the stimulus, which is typically a sharp squared pulse.⁸¹ The photo-voltage generated by POLYRETINA has a less shaper transition from 0 to the peak (in about 10 ms). This may explain why the average latency is 4.12 ± 0.07 ms and we considered as SL spikes those with a latency in the 0–10 ms window. It is known that brief (hundreds of μs) cathodic epiretinal stimulation preferentially excite RGCs, while pulses longer than 1 ms excite both RGCs and bipolar cells.^{144,145} It has been recently demonstrated that the use of pulses shorter than 8 ms results in the activation of axons of passage that causes streak responses, while longer pulses results in a more focal activation.¹⁴² Using calcium imaging techniques, authors explained this result via a shift from direct to indirect activation of RGCs. We showed by electrophysiological recordings and pharmacological experiments that the cathodic stimulation provided by POLYRETINA is also indirectly activating RGCs. This represents a promising result for the *in vivo* translation of POLYRETINA in order to obtain a focal activation. Further experiments aiming at dissecting the circuit activated by POLYRETINA will help in defining the appropriate stimulation parameters to obtain a more focal stimulation.

Taking advantage of accelerated ageing experiments, we demonstrated that POLYRETINA preserves its optoelectronic functions unaltered for at least two years. However, more experiments (such as

ageing tests with pulsed light) with additional time points should be added to investigate the entire functional lifetime of the prosthesis. Last, POLYRETINA fulfils the requirements for *in vitro* cytotoxicity according to ISO 10993-5 and for thermal safety (ISO 14708-1/EN 45502-1). Indeed, cytotoxicity of the implant under illumination would be an interesting data to evaluate.

POLYRETINA is foldable to allow implantation through a small scleral incision and it self-opens once released into the eye, recovering the ocular curvature. Although it could operate in both epiretinal and subretinal conditions, it has been designed as an epiretinal prosthesis, since the implantation of a large retinal prosthesis in the subretinal space may result in an excessive damage to the remaining retinal tissue. Moreover, an epiretinal placement may allow an easier replacement in case of malfunction (e.g., due to ageing or detachment). The hemispherical shape has been obtained by bonding the PDMS-photovoltaic interface on a dome-shaped PDMS support with a radius of curvature of 12 mm. However, the flexibility in the fabrication process of the dome-shaped PDMS support (PDMS molding) allows the fabrication of prostheses designed to fit the real eye curvature and shape of a patient.¹⁴⁶ This opens up the possibility to an optimized retinal prosthesis according to personal needs. Last, the shape of the prosthesis and the insertion strategy have been inspired by the widely used intra-ocular lenses. With further investigations, a similar ‘injection’ approach could also be envisaged for POLYRETINA, simplifying even more the surgical approach. On the functional point of view, the next step is the design and material optimization followed by the electrophysiological validation *in vivo* with large animal models, such as swine models.

2.4 Methods

2.4.1 Prosthesis microfabrication

PDMS-photovoltaic interfaces were fabricated on silicon wafers as represented in **Figure 2.18**. A thin sacrificial layer of poly(4-styrene sulfonate) solution (PSS, 561223, Sigma-Aldrich) was spin-coated on the wafers (1000 rpm, 40 s) and baked (120 °C, 15 min). Degassed PDMS pre-polymer (10:1 ratio base-to-curing agent, Sylgard 184, Dow-Corning) was then spin-coated (1000 rpm, 60 s) and cured in oven (80 °C, 2 h) (**Figure 2.18-1**). After surface treatment with oxygen plasma (30 W, 30 s), a 6- μm thick SU-8 (GM1060, Gersteltec) layer was spin-coated (3800 rpm, 45 s), soft-baked (130 °C, 300 s), exposed (140 mJ/cm^2 , 365 nm), post-baked (90 °C, 1800 s; 60 °C, 2700 s), developed in propylene glycol monomethyl ether acetate (48443, Sigma-Aldrich) for 2 min, rinsed in isopropyl alcohol, and dried with nitrogen (**Figure 2.18-2**). After surface treatment with oxygen plasma (30 W, 30 s), a second layer of degassed PDMS pre-polymer (10:1) was spin-coated (3700 rpm, 60 s) and cured in oven (80 °C, 2 h) (**Figure 2.18-3**). PEDOT:PSS (HTL Solar, Ossila) was filtered (1 μm PTFE filters) and then spin-coated (3000 rpm, 60 s) onto the O₂-plasma treated (30 W, 30 s) PDMS surface. Subsequent annealing (120 °C, 30 min) was performed. The preparation of the organic semiconductor blend was performed in a glovebox under argon atmosphere. Twenty milligrams of P3HT (698997, Sigma Aldrich) and 20 mg of PCBM (M111, Ossila) were dissolved in 1 ml of anhydrous chlorobenzene each and let stirring overnight at 70 °C. The solutions were then filtered (0.45 μm PTFE filters) and blended [1:1 v:v]. The P3HT:PCBM blend was then spin-coated at 1000 rpm for 60 s (**Figure 2.18-4**). Titanium cathodes were deposited by DC sputtering through a shadow mask aligned with the SU-8 pattern (**Figure 2.18-5**, **Appendix Figure 1**, and **Appendix Figure 2**). After surface treatment with oxygen plasma (30 W, 15 s), the encapsulation layer of degassed PDMS pre-polymer (5:1 ratio) was spin-coated (4000 rpm, 60 s) and cured in oven (80 °C,

2 h) (**Figure 2.18-6**). To expose the cathodes, aluminum hard mask was deposited (**Figure 2.18-7**), then photolithography (**Figure 2.18-8**) and PDMS dry etching in a gas mixture of O_2 and SF_6 (**Figure 2.18-9**) were performed. Aluminum was then removed by photolithography developers (**Figure 2.18-10**). The wafers were then placed in deionized water to allow dissolution of the PSS sacrificial layer and the release of the PDMS-photovoltaic interfaces (**Figure 2.18-11**). The floating membranes were finally collected and dried in air. The dome-shaped PDMS supports were fabricated using a milled PMMA mold (see **Appendix Figure 6**), filled with PDMS pre-polymer (10:1), which was then degassed and cured in oven ($80\text{ }^\circ\text{C}$, 2 h). The supports were released from the molding parts and perforated with a hole-puncher ($330\text{ }\mu\text{m}$ in diameter) at the locations dedicated to the insertion of retinal tacks. The released PDMS-photovoltaic interfaces were clamped between two O-rings and, together with the PDMS supports, were exposed to oxygen plasma (30 W, 30 s). The activated PDMS surfaces were put in contact and allowed to uniformly bond thanks to radial stretching of the fixed membrane (**Appendix Figure 6**). The excessive PDMS used to clamp the array was removed by laser cutting.

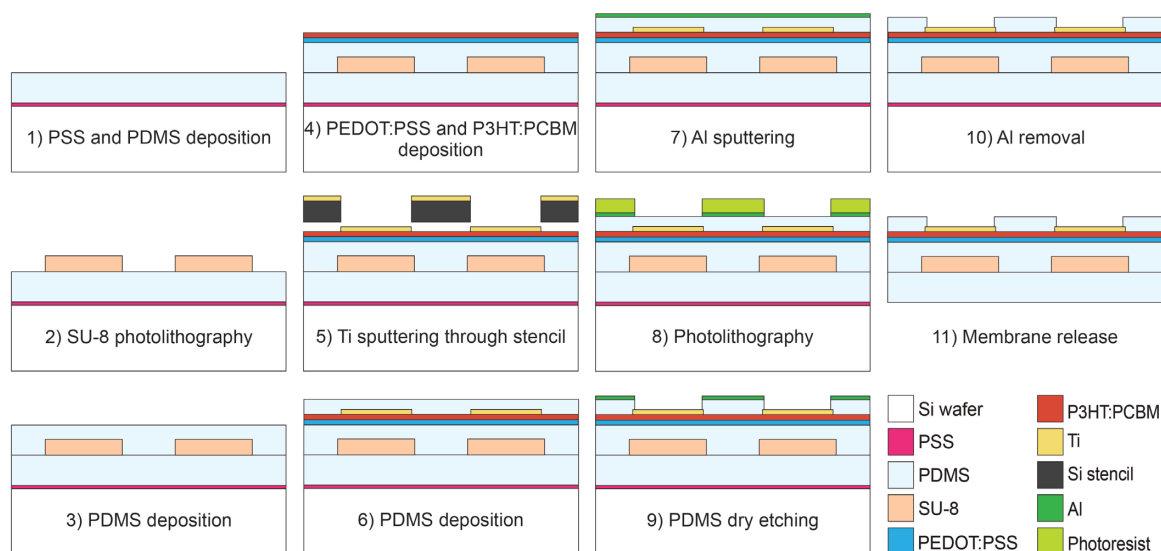


Figure 2.18 Microfabrication process flow of POLYRETINA photovoltaic interface. The material stack is represented for two pixels in cross-sectional view and not in scale.

2.4.2 Chips microfabrication

Chips for KPFM and PC/PV measurements were fabricated on $20 \times 24\text{ mm}^2$ glass substrates ($2947\text{--}75 \times 50$, Corning Incorporated). Before microfabrication, glass chips were cleaned by ultra-sonication in deionized water, acetone, and isopropyl alcohol for 15 min each and then dried with nitrogen. When present, ITO (200 nm) was deposited on glass chips by RF sputtering. PEDOT:PSS (HTL Solar, Ossila) was filtered ($1\text{ }\mu\text{m}$ PTFE filters) then spin-coated at 3000 rpm for 60 s on each chip. Subsequent annealing at $120\text{ }^\circ\text{C}$ for 30 min was performed. The preparation of the organic semiconductor blend was performed as described before. The P3HT:PCBM blend was then spin-coated at 1000 rpm for 60 s on each chip. Aluminum cathodes were deposited by thermal evaporation using a shadow mask; titanium cathodes were deposited by DC sputtering using a shadow mask. When present, degassed PDMS pre-polymer (10:1) was deposited on the glass substrate by spin-coating (1000 rpm, 60 s) and then cured in oven ($80\text{ }^\circ\text{C}$, 2 h).

2.4.3 Ti electrochemical characterization

Electrochemical impedance spectroscopy was performed in PBS (1x) at RT with an Ivium potentiostat (Compactstat, Ivium Technologies) and Ivium software. The three-electrode cell (**Figure 2.2B**) was composed by Ti working electrode (WE) of about 0.051 mm², Ag/AgCl reference electrode (RE), and Pt counter electrode (CE). The driving voltage was set to 50 mV between 0.05 and 10⁷ Hz. The data was averaged and plot in Bode diagram with Matlab (Mathworks) and the component of the circuit were extracted from the EIS plot by fitting **Appendix Equation 1** (R_{spread} was determined at the plateau with the highest phase above 10⁵ Hz, and R_{CT} , C_{DL} , and n were determined using Matlab Zfit script)¹⁴⁷.

2.4.4 pH measurements

Experiments have been performed in phosphate-buffered saline at room temperature. Illumination was carried out on a Nikon Ti-E inverted microscope (Nikon Instruments) by the Spectra X system (Emission filter 560/32, Lumencor). The microscope was equipped with a dichroic filter (FF875-Di01–25 × 36, Semrock) and a 10× (diameter of the illumination spot 2.2 mm; CFI Plan Apochromat Lambda) objective. Light pulses of 10 ms where delivered at 20 Hz for 1 h with an irradiance of 3.4 mW/mm². pH was measured with a microelectrode (tip diameter of 200 μm) with internal reference (pH-200C, Unisense). Data were sampled at 1 Hz.

2.4.5 Kelvin probe force microscopy

KPFM characterization was performed in ambient air conditions with an Asylum Research Cypher S microscope using PtIr coated tips (AC240TM, Asylum Research, Oxford Instrument) in surface potential imaging mode. To measure the surface potential variation, KPFM images were collected by repetitively scanning a single line of 100 nm under dark and illumination conditions. The white LED of the microscope positioned above the tip and sample was acting as light source and it was manually turned 100% off and 100% on to reach the desired conditions. KPFM images were analyzed using Gwyddion 2.36 software. For each image, the average surface potential variation value was obtained by subtracting the surface potential in dark to the one under illumination (voltage in light – voltage in dark).

2.4.6 Accelerated ageing tests

Accelerated ageing was performed in a dry oven set to $T = 87$ °C. Samples were immersed in physiological saline solution (0.9% NaCl, pH 7.4) within a sealed 50-ml falcon tube. Under this condition, the acceleration factor A was 32, according to **Equation 2.2**.^{148,149}

$$A = 2^{\frac{T-37^{\circ}\text{C}}{10}}$$

Equation 2.2 Acceleration factor for accelerated ageing tests

KPFM measures were obtained before starting the ageing protocol and at several time points during ageing. Each accelerated ageing session between KPFM measures lasted for 135 h, corresponding to six months. Before KPFM, samples were removed from the sealed falcon tube, rinsed with de-ionized water, and dried under nitrogen flow.

2.4.7 Measure of PV and PC

In this experiment, the photovoltaic interface has been fabricated directly on glass (without PDMS) to avoid breaking the connecting lines from the electrode to the pad when contacted. The titanium electrodes have been fabricated with a diameter of 100 μm ; however, when evaluating the PC density generated by the interface, also the area of the connecting line exposed to light has been considered (on average: 0.077 mm^2). A plastic reservoir was attached to the chip using PDMS as adhesive, leaving about 0.051 mm^2 of Ti exposed to the solution. Chips were placed on a holder, and each pad was sequentially contacted. Silver paste was used to improve the electrical contact. An Ag/AgCl pellet immersed in physiological saline solution (NaCl 0.9%) was used as reference electrode. Light pulses were delivered by a 565-nm Green LED (Thorlabs, M565L3-C5) focused at the sample level. PV was measured using a voltage amplifier (DL-Instruments, 1201; gain 20, band DC-3000 Hz) and PC using a current amplifier (DL-Instruments, 1212; gain 10^{-6} A/V). Data sampling (16 kHz) and instrument synchronization were obtained via a DAQ board (PCIe-6321, National Instruments) and a custom-made software. Data analysis was performed in Matlab (Mathworks). Due to a limitation in the acquisition system, long pulse trains (**Figure 2.7E-G**) have been delivered in packages of 20 pulses at 20 Hz (total of 1 s), while each package was separated by 1 s needed by the system to save data before starting the next package.

2.4.8 Electrophysiology

Experiments were conducted under the animal authorizations VD3055 and GE3717. Retinas were explanted in normal light conditions from mice sacrificed by injection of Sodium Pentobarbital (150 mg kg^{-1}). After eye enucleation, retinas were dissected in carboxygenated (95% O_2 and 5% CO_2) Ames' medium (A1420, Sigma-Aldrich) and transferred to the microscope stage for recordings. In the experiment with synaptic blockers, Ames' medium was supplemented with DL-AP4 (250 $\mu\text{M l}^{-1}$, No. 0101, Tocris Bioscience), DL-AP5 (50 $\mu\text{M l}^{-1}$, No. 0105, Tocris Bioscience), DNQX (10 $\mu\text{M l}^{-1}$, No. 0189, Tocris Bioscience), Carbenoxolone (100 $\mu\text{M l}^{-1}$, No. 3096, Tocris Bioscience). Retinas were placed mimicking an epiretinal configuration, therefore with RGCs facing the substrate (bare PDMS or prosthesis). On the prosthesis, retinas were layered in the central part of the array with electrodes of 80 μm in diameter and 150 μm pitch. Recordings were performed in dim light at 32 $^\circ\text{C}$ with a sharp metal electrode (PTM23BO5KT, World Precision Instruments), amplified (Model 3000, A-M System), filtered (300–3000 Hz), and digitalized at 30 kHz (Micro1401–3, CED Ltd.). Illumination was carried out on a Nikon Ti-E inverted microscope (Nikon Instruments) by the Spectra X system (Emission filter 560/32, Lumencor). The microscope was equipped with a dichroic filter (FF875-Di01–25 \times 36, Semrock) and a 10 \times (diameter of the illumination spot 2.2 mm; CFI Plan Apochromat Lambda) objective. The stimulation protocol consisted in a repetition of ten pulses at 1 Hz for each irradiance; irradiance was increased sequentially: LED at 0% (0 $\mu\text{W}/\text{mm}^2$), 2% + ND4 (47.38 $\mu\text{W}/\text{mm}^2$), 3% + ND4 (107.91 $\mu\text{W}/\text{mm}^2$), 2% (189.50 $\mu\text{W}/\text{mm}^2$), 3% (421.12 $\mu\text{W}/\text{mm}^2$), 3% (815.92 $\mu\text{W}/\text{mm}^2$), 5% (1081.75 $\mu\text{W}/\text{mm}^2$), 10% (2.81 mW/mm^2), 20% (5.89 mW/mm^2), 40% (11.98 mW/mm^2), 60% (17.92 mW/mm^2), 80% (23.56 mW/mm^2), and 100% (29.08 mW/mm^2). Spike detection and sorting were performed by threshold detection using the Matlab-based algorithm Wave_clus¹⁵⁰ and further data processed in Matlab (Mathworks). The threshold for spike detection has been defined as 3.7 times the standard deviation of the background noise. The minimum refractory period between spikes of the same class was set to 1.4 ms. To ensure the rejection of artifacts, an exclusion period of \pm 1 ms around light onset and offset was applied.

However, the spikes in the first 10 ms after the light onset (SL) have been manually verified. PSTHs for each condition of illumination were computed discretizing and averaging spike raster obtained over ten stimulations repetitions into bins of 10 ms. Spikes were sorted from individual PSTHs and classified according to their timing after light onset (cyan bars in **Figure 2.9A**) in SL (<10 ms), ML (from 40 to 120 ms), and LL (from 150 to 350 ms).⁸¹ Firing rates in the three groups were measured as follow. For SL spikes the first bin (10 ms) after the pulse was used. For ML spikes 3 bins (30 ms) in the defined time range, centered in the highest bin, were used. For LL spikes 5 bins (50 ms) in the defined time range, centered in the highest bin, were used.

2.4.9 Spatial selectivity measures and modeling

Measures of the voltage spread have been performed in Ames' medium (A1420, Sigma-Aldrich) at 32 °C with a glass micropipette (tip diameter about 15 μm). Data were amplified (Model 3000, A-M System), filtered (DC-1000 Hz), and digitalized at 30 kHz (Micro1401-3, CED Ltd.). Illumination was carried out on a Nikon Ti-E inverted microscope (Nikon Instruments) by the Spectra X system (Emission filter 560/32, Lumencor). The microscope was equipped with a dichroic filter (FF875-Di01-25 × 36, Semrock) and a 10 × objective. A pin-hole was used to limit the spot diameter to about 150–170 μm. After alignment of the illumination spot on a target pixel of the central area of POLYRETINA, ten pulses of 10 ms were delivered at 1 Hz with an irradiance of 29.07 mW/mm². The resulting voltage has been measured at nine positions in three directions around the illuminated pixel. Data analysis was conducted in Matlab (Mathworks). Voltage peaks above noise level (mean noise threshold 6.2 μV) have been detected and their amplitude normalized respect to the central pixel value. Simulations were performed in COMSOL Multiphysics 5.2, with a stationary electric currents study. The titanium cathodes were set at 0.1 V, while PEDOT:PSS was put at 0 V. The ground was situated at the bath top and lateral walls that were placed 2 mm and 1 mm away from the central pixel, respectively (cylindrical geometry). Line plots shown in the results were taken at a distance of 20 μm from the titanium surface. For each material, the conductivity (S/m) and relative permittivity are listed: titanium (2.6 × 10⁶/1), P3HT:PCBM (0.1/3.4), PEDOT:PSS (30/3), Saline (1/80), PDMS (2 × 10⁻¹⁴/2.75).

2.4.10 Optical safety

Retinal damage upon light exposure can occur because of three main factors: photo-thermal damage, photo-chemical damage, and thermo-acoustic damage.¹³⁴ The first one is related to retinal heating upon light absorption by the melanin in the RPE. The second one occurs at short wavelengths (less than 600 nm) and for exposures longer than 1 s. The latter occurs for short pulses (less than 1 ns) and is associated with nonlinear photo-mechanical effects. POLYRETINA functions with 10 ms green light pulses; therefore, this limit could be controlled by the photo-thermal or photo-chemical damage. According to the ANSI Z136.1 Standard,¹²⁰ the MPE allowed for ophthalmic applications can be calculated (in W) according to **Equation 2.3** for photo-thermal damage (MPE_T) and **Equation 2.4** for photo-chemical damage (MPE_C). Those equations are valid for λ = 560 nm and α = 808 mrad (**Figure 2.3E**).

$$MPE_T = 6.93 \cdot 10^{-5} C_E C_T \frac{1}{P}; C_E = 6.67 \cdot 10^{-3} \alpha^2; C_T = 1; P = 5.44$$

Equation 2.3 MPE_T calculation for optical safety

$$MPE_C = 5.56 \cdot 10^{-10} C_B \alpha^2; C_B = 10^{0.02(\lambda-450)}$$

Equation 2.4 MPE_C calculation for optical safety

MPE_T results in 47.41 mW, which corresponds to 328.75 $\mu\text{W}/\text{mm}^2$ for an exposed area of 144.22 mm^2 . MPE_C results in 57.55 mW, which corresponds to 399.02 $\mu\text{W}/\text{mm}^2$.

2.4.11 Thermal measurements

Measures have been performed with a thermal camera (FLIR A325sc Infrared Camera, FLIR Systems, Inc.) focused on the top surface of the POLYRETINA prosthesis. Images have been acquired at 1 frame per second. Light pulses (10 ms, 20 Hz, 1.22 mW/mm^2) were delivered by a 565-nm Green LED (Thorlabs, M565L3-C5) focused at the sample level.

2.4.12 Thermal modeling

Simulations were performed in COMSOL Multiphysics 5.2 with the Bioheat module for the heat transfer equation and the General PDE module for the Beer–Lambert light propagation. Illumination has been modeled as a uniform beam with a diameter of 13 mm. The eye is a 2D axi-symmetric model composed of several spheres representing each domain. A total of eight domains (Cornea, Aqueous Humor, Lens, Vitreous Humor, Retina, RPE, Choroid and Sclera) are defined in the model, with the parameters listed in **Table 2.1**. POLYRETINA was modeled as a single composite material, with volume averaged properties of PDMS, PEDOT:PSS, P3HT:PCBM and titanium (**Table 2.2**). It was simplified into five domains with homogeneous properties: the center, the first ring, the second ring, the domains where no titanium is present, and PDMS only (**Figure 2.19**). A volume average has been performed on each of this domain, to obtain the parameters for the aggregated material. To account for the non-uniform distribution of titanium, the fraction area of titanium was considered. To validate the parameters of the aggregated model, a simulation has been performed with POLYRETINA in air exposed to continuous illumination (560 nm, 244 $\mu\text{W}/\text{mm}^2$) corresponding to pulsed illumination of 1.22 mW/mm^2 . The heat losses at the prosthesis interface-air were radiative (emissivity = 0.9) and convective (heat transfer coefficient = 38.5 $\text{W m}^{-2} \text{K}^{-1}$). In agreement with our experimental results, the average transmittance was measured to be 51.67% (49.07% in **Figure 2.15**) and the steady-state temperature increase was 1.25 $^\circ\text{C}$ (1.24 $^\circ\text{C}$ in **Figure 2.14**).

Table 2.1 FEA simulation of thermal effects. Parameters used in the thermal model obtained from references [151–164].

Material	Thickness	Heat Capacity	Thermal Conductivity	Density	Absorption (at λ in nm)	Perfusion rate	Self Heat
	μm	$\text{J kg}^{-1} \text{K}^{-1}$	$\text{W m}^{-1} \text{K}^{-1}$	kg m^{-3}	cm^{-1}	s^{-1}	W m^{-3}
Eye	\varnothing 24000						
Aqueous Humor	3100	3997	0.58	1000	0.00025 (500)	0	0
Blood	/	3840	0.53	1050	0	0	0
Choroid	430	3840	0.53	1050	150 (500)	0.0091	10000
Cornea	500	4178	0.58	1050	0.51 (514.5)	0	0
Lens	3600	3000	0.4	1000	0.025 (514.5)	0	0
Retina	100	3680	0.565	1000	4 (500)	0	0

RPE	10	4178	0.603	1050	1100 (500)	0	0
Sclera	500	4178	0.58	1000	5.9 (550)	0	0
Vitreous Humor	/	3997	0.595	1050	0.00025 (500)	0	0
PDMS	669	1460	0.15	970	3.58 (514.5)	0	0
PEDOT:PSS	0.15	1978	0.29	1011	1700 (500)	0	0
P3HT:PCBM	0.1	1400	0.2	1100	40000 (530)	0	0
Titanium	0.05	5263	6.7	4430	120000 (500)	0	0

Table 2.2 FEA model of POLYRETINA. Parameters used to generate the aggregated model of POLYRETINA used in the thermal simulations.

Domain	Heat Capacity	Thermal Conductivity	Density	Absorption (at λ in nm)	Fraction of Ti
	$\text{J kg}^{-1} \text{K}^{-1}$	$\text{W m}^{-1} \text{K}^{-1}$	kg m^{-3}	cm^{-1}	%
Center	1460.89	0.15	970.07	16.91	27
First ring	1460.89	0.15	969.90	12.30	10
No titanium	1459.70	0.15	969.80	9.73	0
Second ring	1460.89	0.15	969.85	11.09	0.5
PDMS	1460.00	0.15	970.00	3.58	0

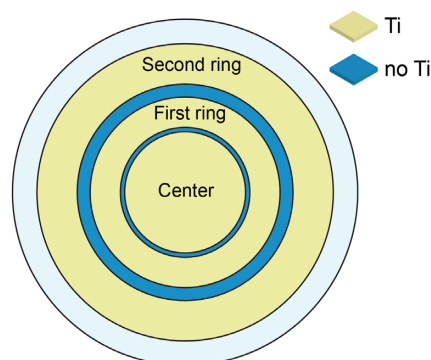


Figure 2.19 Aggregated model of POLYRETINA. Drawing of the simplified model of POLYRETINA.

2.4.13 *In vitro* cytotoxicity test

The study validation was performed by an accredited company (Medistri SA). The test was conducted according to the requirement of ISO 10993-5: Biological Evaluation of Medical Devices, *in vitro* cytotoxicity test; ISO 10993-12: Test article preparation and reference materials; USP 35-NF30 (87): Biological Reactivity test, *in vitro*; Medistri internal procedure WI 47 and WI 56. Prostheses were sterilized with EtO prior the test. The test on extraction was performed with two retinal prostheses for a total surface area of 3.54 cm^2 , with a ratio of the product to extraction vehicle of $3 \text{ cm}^2 \text{ ml}^{-1}$. Extraction vehicle was Eagle's Minimum Essential Medium supplemented with fetal bovine serum, penicillin–streptomycin, amphotericin B, and l-glutamine. The extraction was performed for 24 h at 37°C . The extract was added on triplicate cultures wells containing a sub-confluent L929 cell monolayer (1:1 dilution). The test samples and the control wells were incubated at 37°C in 5% CO_2 for 24 h. Following incubation, the cell cultures were examined for quantitative

cytotoxic evaluation. 50 μ l per well of XTT reagent was added to the cells then incubated at 37 °C in 5% CO₂ for further 3–5 h. An aliquot of 100 μ l was then transferred from each well into the corresponding wells of a new plate and the optical density was measured at 450 nm.

2.4.14 Surgical implantation

Plastic eye models (Eyelabinnovations, Austria) and enucleated pig eyes were used. First three 23-gauge transconjunctival valved canulas (DORC, Zuidland, The Netherlands) were inserted into the eye at 4 mm from the limbus at the following positions: nasal superior, temporal superior and temporal inferior. A balanced salt solution infusion was hooked up to the eye to maintain a constant intraocular pressure through one of the cannulas. A 6.5-mm long incision was then performed using a 15 ° scalpel. The implant was folded using special forceps and then inserted through the incision into the posterior cavity. Once inside the eye the forceps grip was released and the implant could unfold. Using a light pipe and an intraocular 23-gauge forceps inserted through the other two cannulas the implant was then manipulated and fixed in epi-retinal configuration.

2.4.15 Statistical analysis and graphical representation

Statistical analysis and graphical representation were performed with Prism (GraphPad Software Inc.). The normality test (D'Agostino & Pearson omnibus normality test) was performed in each dataset to justify the use of a parametric or non-parametric test. In each figure p-values were represented as: * $p < 0.05$, ** $p < 0.01$, *** $p < 0.001$, and **** $p < 0.0001$. Data are reported as mean \pm s.e.m. or mean \pm s.d., n is used to identify the number of electrodes or cells used; N is used to identify the number of devices or animals.

2.5 Acknowledgements

We would like to acknowledge the EPFL center of micro nanotechnology (CMi) for the support. Prof. Matthias Lütolf for having reviewed our manuscript and Prof. Stéphanie Lacour for her advices. This work has been supported by École polytechnique fédérale de Lausanne, Medtronic, European Commission (EU project 701632), Fondation Pierre Mercier pour la science, and Velux Stiftung (Project 1102).

Chapter 3 Optimization of the POLYRETINA pixel



Eyes of a robber fly (Source: Thomas Shahan)

The publication related to this chapter is in review.

Contributions: I designed, fabricated, and characterized the devices and the retinal prostheses; performed/analyzed photovoltage and photocurrent measures, imaging, KPFM, and mechanical simulations. N.A.L. Chenais performed and analyzed voltage spreading and electrophysiological experiments.

3.1 Introduction

POLYRETINA and its design have proven *in vitro* to be a potential valuable visual prosthesis for an enhanced restoration of visual acuity and visual field with respect to other state-of-the-art implants. However, the finish line of the journey towards preclinical trials is not behind the corner. Adaptation of “delicate” implantable prostheses such as POLYRETINA to *in vivo* testing can be intense due to the novel materials and design involved. A large area, curved, stretchable, transparent, organic-based, opto-electronic device conceives for us mechanical, electrical, and optical challenges, whose potential solutions will be presented in the following chapters.

In this chapter, we will present few appreciated improvements of POLYRETINA pixels on the materials and design aspects to obtain beneficial characteristics in vision of preclinical trials. First, the performances of the retinal prosthesis could be improved by densifying the pixels resulting in a theoretical visual acuity towards the limit of legal blindness (20/400).³² However, considering merely technical aspects, electrical cross-talks (photovoltage summation) and stimulation efficiency (injected charges per pulse) could be negatively affected when the pitch size and diameters of the photovoltaic pixels are reduced. One interesting aspect yet in favor of increasing the pixel density of POLYRETINA was identified *ex vivo* with retinal explants. We measured and compared the activity of RGCs when stimulated with capacitive-like pulses, such as the ones obtained from POLYRETINA pixels, or with rectangular monopolar (monophasic) pulses (**Figure 3.1**).¹⁶⁵

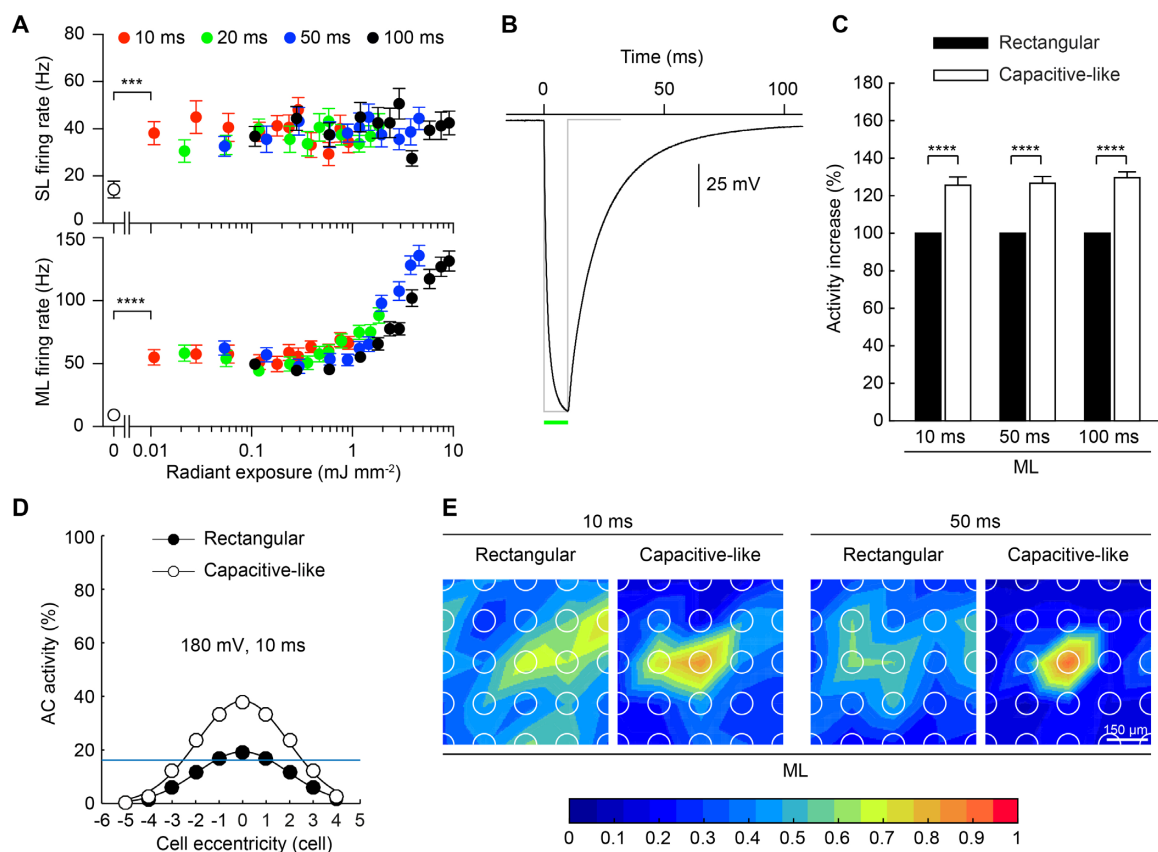


Figure 3.1 Capacitive-like (photovoltaic) vs rectangular monopolar stimulation of RGCs. **A)** Evidence of the direct and the indirect activities evoked by photovoltaic stimulation. Mean (\pm s.e.m; $n = 16$ cells, $N = 9$ retinas) firing rates of SL (top) and ML (bottom) responses as function of the radiant exposure (mJ/mm^2), obtained by multiplying the irradiance (mW/mm^2) with the pulse duration (s). For each RGC, ten consecutive sweeps were averaged. **B)** Photovoltage profile (black line) generated by POLYRETINA pixels upon a 10 ms light pulse (green

bar) at 0.94 mW/mm^2 . The grey line shows a 10 ms rectangular voltage pulse of identical peak amplitude. **C)** Percentual increase in the RGC ML activity induced by non-rectangular capacitive-like voltage pulses compared to rectangular voltage pulses. **D)** Mean normalized activation profile and Gaussian fit of the activity of ACs upon 10 ms rectangular or non-rectangular capacitive-like voltage pulses with amplitudes of 180 mV. 10 x 10 cells have been averaged over four directions. The blue line indicates the AC membrane potential threshold for ML indirect activity. **E)** Mean heatmaps of normalized ML activities recorded with 10 ms and 50 ms rectangular or non-rectangular capacitive-like voltage pulses, with a peak voltage of 179 mV ($n = 8$ cells, $N = 8$ retinas). For each RGC, ten consecutive sweeps have been averaged. Heatmaps have been generated from linear interpolation of experimental values recorded from individual electrode stimulations. Figures adapted from Chenais *et al.* 2019.¹⁶⁵

As mentioned in the previous chapter, ML spikes in RGCs are characteristic from network-mediated activation and can be evoked by the photovoltaic pixels, especially when increasing the radiant exposure (obtained by light intensity times pulse duration, **Figure 3.1A**). The capacitive-like voltage profile from the photovoltaic pixels has slower rising and decay phases (**Figure 3.1B**) that increase the network-mediated activation of RGCs compared to rectangular pulses of similar duration and peak amplitude (**Figure 3.1C**), also leading to similar injected charges. In fact, amacrine cells (ACs) activity is increased with capacitive-like pulses (**Figure 3.1D**), which results in a more focused RGCs stimulation due to the ACs inhibitory activity (**Figure 3.1E**). Therefore, the non-rectangular capacitive-like stimulation favors a focused network-mediated RGCs activation and, thus, a densification of the POLYRETINA pixels can be envisioned.

Consequently, to move forward with a high-density POLYRETINA, the photovoltaic pixels should prove to stimulate even with reduced size and with single-pixel illumination (as previously only full-field illumination was used). Electrode coatings, for instance, could help improving both efficiency and stability in aqueous solution of the photovoltaic pixels.

3.2 Results

3.2.1 Impact of the pixels density

The first prototype of POLYRETINA, presented in Chapter 2, was developed to prove that photovoltaic pixels based on conjugated polymers can stimulate RGCs and can be fabricated on a stretchable PDMS membrane bonded onto a spherical support, which is then folded, injected into the eye, and self-opens to match the retinal curvature over a 46° of visual field.⁹⁸ However, the design of the pixel array was not optimal for a high-density stimulation, which could be beneficial for improving visual acuity. Therefore, the POLYRETINA design has been upgraded to a homogeneous distribution of pixels over the 13 mm in diameter and with four designs (design A, B, C, and D in **Figure 3.2**), in which the electrode diameter and pitch size are progressively decreased. Design A (Ti diameter $80 \mu\text{m}$, SU-8 diameter $100 \mu\text{m}$, and pitch $150 \mu\text{m}$, as the central region of the previous version of POLYRETINA) results in $6'720$ pixels with a pixels density of 51 pixels/mm^2 (2215 pixels were present in the previous POLYRETINA); design B (Ti diameter $80 \mu\text{m}$, SU-8 diameter $100 \mu\text{m}$, and pitch $120 \mu\text{m}$) has $10'498$ pixels and 79 pixels/mm^2 ; design C (Ti diameter $60 \mu\text{m}$, SU-8 diameter $75 \mu\text{m}$, and pitch $90 \mu\text{m}$) $18'692$ pixels and 141 pixels/mm^2 ; and design D (Ti diameter $40 \mu\text{m}$, SU-8 diameter $50 \mu\text{m}$, and pitch $60 \mu\text{m}$) $42'196$ pixels and 318 pixels/mm^2 . For all the designs, SU-8 diameters were 25% larger than Ti electrodes and the encapsulation covered $4 \mu\text{m}$ at the electrode edges, resulting in an exposed electrode diameter $8 \mu\text{m}$ shorter with respect to the total Ti size.

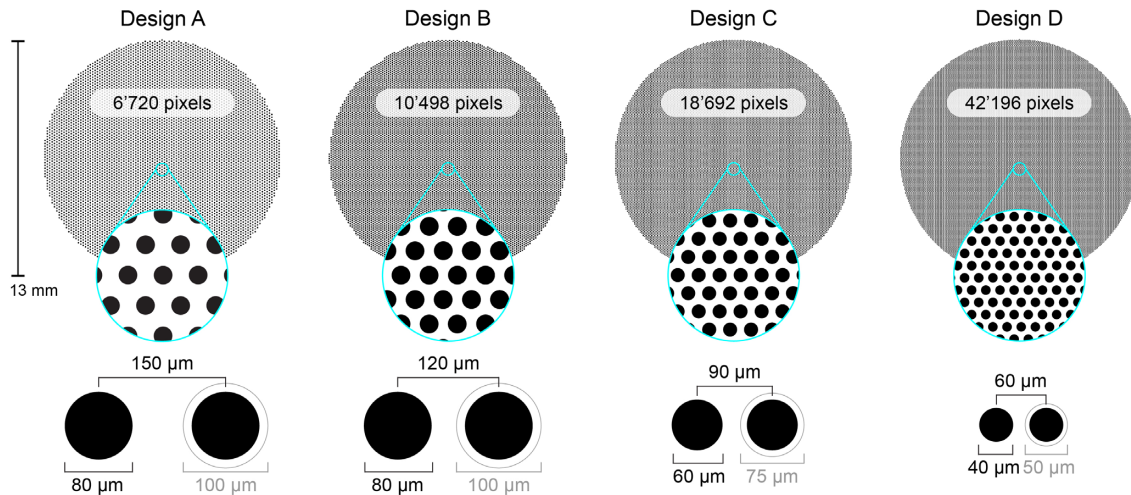


Figure 3.2 Improved designs for a high-density POLYRETINA. The layouts of the proposed designs are represented in the same scale with one another. Full black circles depict Ti electrodes and empty grey circles SU-8 (only shown on one pixels). Design A: 51 pixels/mm²; design B: 79 pixels/mm²; design C: 141 pixels/mm²; design D: 318 pixels/mm².

Table 3.1 Calculated visual field and theoretical acuity for the four POLYRETINA designs (framed with thick lines) and other commercialized (or on the route to be) products. The calculation for both visual field and acuity were performed as stated in the previous chapter (**Figure 2.3E** and **Equation 2.1**). The asterisk (*) indicates that more than 7° of visual field (up to 30°) can be obtained by inserting multiple implants. D: array diameter/diagonal, d: electrode diameter, p: electrodes pitch, α'' : visual angle, logMAR: log of MAR (see **Figure 1.2A**), Th.: theoretical.

	D (mm)	Th. field (°)	d (μm)	p (μm)	α'' (°)	logMAR	Th. acuity (Snellen)	Best measured acuity
Design A	13	46.6	80	150	0.51	1.48	20/607	
Design B			80	120	0.40	1.38	20/485	
Design C			60	90	0.30	1.26	20/364	
Design D			40	60	0.20	1.08	20/243	
Argus II	5	18	200	575	1.94	2.07	20/2327	20/1260
Alpha-AMS	3.2	11	30	70	0.24	1.15	20/283	20/549
PRIMA	2	7 - 30*	100	110	0.37	1.35	20/445	20/460

The calculated visual field (46.6°) and the theoretical visual acuity limit (determined from the corresponding natural/subretinal stimulation) for the new layouts are listed in **Table 3.1** with Argus II, Alpha-AMS, and PRIMA retinal implants for comparison. From 20/607 (design A), the theoretical visual acuity can be improved to 20/485 for design B and to 20/364 and 20/243 for design C and D, respectively, which are both above the limit considered blindness. The best theoretical visual acuity among the commercial products is 20/283, obtained with Alpha-AMS; yet, the best ever measured acuity in a patient lays around 20/549 and the covered field is only 11°. The large discrepancy between theoretical and measured visual acuity values makes it extremely important to do not rely merely on theory, since several features of retinal prostheses can influence acuity results (such as the extent of visual impairment, the implant fixation location and direction, irregular cell-electrode distances, and a distinct psychophysical component between subjects and timepoints). However, since measuring visual acuities and visual fields with prostheses like POLYRETINA requires human

studies, tools such as virtual reality could be exploited to obtain estimations about the POLYRETINA-evoked artificial vision under ideal conditions (**Appendix Figure 4**).

The fabrication process of POLYRETINA, presented in Chapter 2.4.1, allows a certain degree of scalability. The minimum electrode size is however limited by the home-made stencil architecture used during Ti sputtering (see **Appendix Figure 1** and **Appendix Figure 2**), which was not conceived for nano-patterning¹⁶⁶ but for manual alignment handling and patterning on soft and adhesive surfaces. Nevertheless, it was possible to pattern the Ti electrodes following the four layouts and with high precision manual alignment with the SU-8 islands patterned accordingly. **Figure 3.3A** shows the Ti electrodes sputtered on the organic layers (PEDOT:PSS/P3HT:PCBM). The pixels size of 40 μm was at the limit of the minimum achievable size, as electrodes borders were not properly defined in some regions of the array. An additional improvement compared to the first POLYRETINA prototype is that the polymers between the Ti electrodes are etched away by oxygen plasma and Ti as mask. The result can be visualized in **Figure 3.3B**, where the SU-8 discs appear more evident underneath each pixel after the removal of the organic layers around Ti.

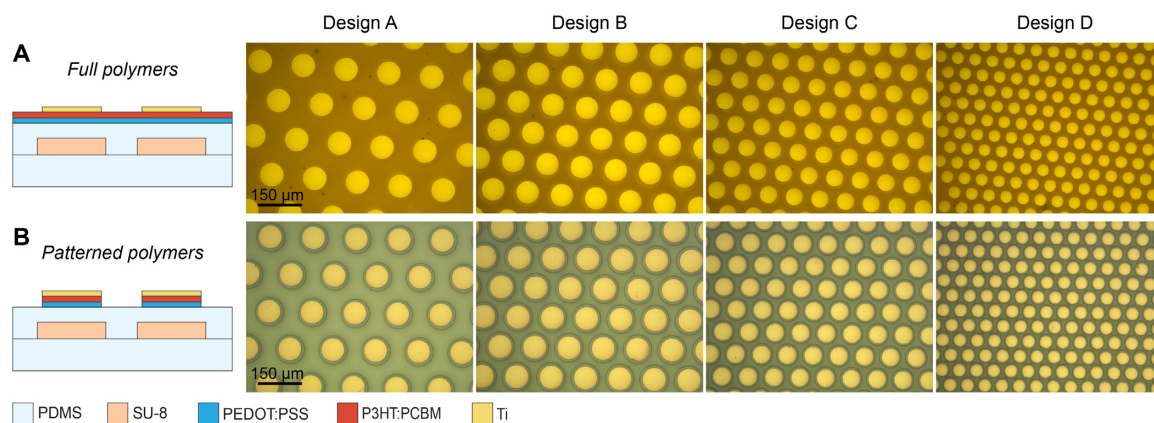


Figure 3.3 Fabrication of patterned pixels with the four layouts. **A)** As for the previous version of POLYRETINA, the Ti electrodes are sputtered through a stencil mask onto P3HT:PCBM and aligned with the SU-8 discs embedded in PDMS. The four designs were possible to obtain with the same deposition system. **B)** P3HT:PCBM and PEDOT:PSS patterning by oxygen plasma and Ti as mask. The resulting images are shown for the four designs and SU-8 appears more visible underneath each pixel.

To enquire about the new layouts mechanical consequences and ensure that the densification of pixels does not cause cracking of the Ti electrodes when bonded onto the PDMS dome, we performed FEA mechanical simulations of the photovoltaic array bonding. From a flat and stretchable surface to the spherical shape, the PDMS in between the pixels stretches and the stress on Ti surface rises (**Figure 3.4A**). For the densest array, the von Mises Ti stress is augmented until reaching a maximum slightly less than 630 MPa (in the central region), while it is less substantial for the other geometries, especially for the lowest pixels density. The maximum tensile stress that Ti thin films can stand prior cracking depends on the film properties, which in turn depends on various criteria such as substrate and deposition technique and parameters. In the literature, values ranging from 600 to 1000 MPa are found for tensile strength of sputtered Ti.^{167,168} To verify the Ti integrity, we fabricated the POLYRETINA prostheses with the four designs and imaged the pixels on the top of the dome (**Figure 3.4B** and **C**). No damage to the Ti surfaces were found for all the layouts when bonding to the PDMS domes; however, the tight rolling needed for injection into the eyes (see **Figure 2.4**)

caused major cracking of the 40 μm Ti electrodes (qualitatively assessed). For this reason and because of the less reproductive Ti sputtering with these stencil dimensions, design D was not considered any further for characterizations.

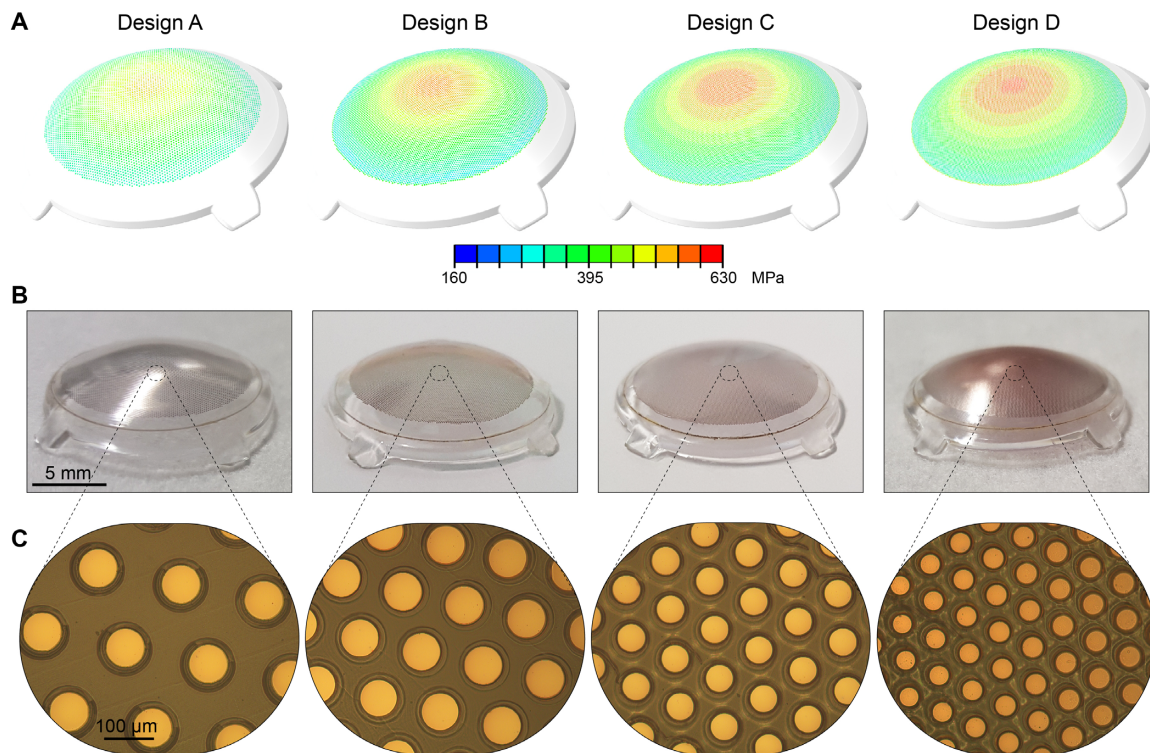


Figure 3.4 Mechanical validation of the new POLYRETINA layouts. **A)** FEM of the von Mises stresses on Ti surface during bonding process. **B)** Fabricated POLYRETINA prostheses with the corresponding designs. **C)** Micrographs of the photovoltaic pixels after bonding.

3.2.2 Spatial selectivity of stimulation

As previously mentioned, one of the concerns when reducing the pixels pitch size is the increased electrical crosstalk, or voltage summation, between the electrodes. We therefore measured the radial voltage spreading upon illumination of a single pixel at $\sim 3\text{-}5\ \mu\text{m}$ from the Ti top surface (**Figure 3.5A**). The voltage change measurements along three principal radial directions (D1, D2, and D3 in **Figure 3.5B**) have been averaged and plotted normalized to the center of the central pixel (as illustrated in **Figure 3.5C**). To evaluate crosstalk when illuminating neighboring pixels, the light has been patterned to activate the two coronas around the central pixel (**Figure 3.5D**). The mean (\pm s.e.m.) voltage distribution across the three directions and all the pixel tested has been plotted and interpolated with a two-term gaussian fitting for pixel arrays distributed according to design B (80 μm diameter and 120 μm pitch) and C (60 μm diameter and 90 μm pitch), which are denser than design A (80 μm diameter and 150 μm pitch) (**Figure 3.5E**).

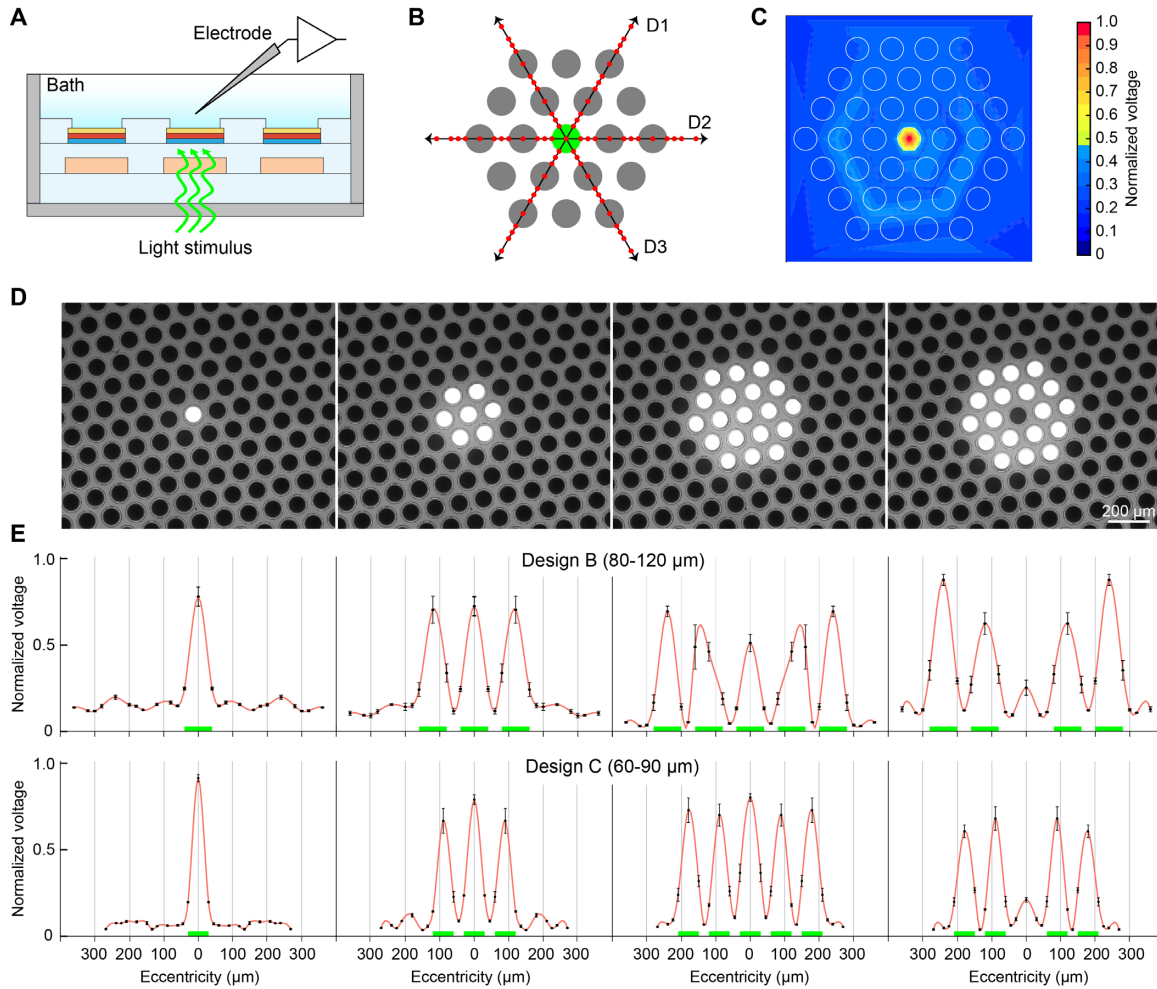


Figure 3.5 Evaluation of the electrical crosstalk of the photovoltaic pixels. **A)** Measurements setup with recording electrode at $\sim 3\text{-}5\ \mu\text{m}$ from the Ti top surface. **B)** Measurements locations with respect to the central pixel. **C)** Exemplary voltage spreading color map generated by interpolating the experimental measures (as shown in A and B) with a triangulation-based linear interpolation. For each point, ten consecutive sweeps have been averaged and the voltage peaks have been normalized with respect to the value obtained in the central pixel. The white circles represent the pixels. **D)** Top view of the tested light pattern with $80\ \mu\text{m}$ pixels and $120\ \mu\text{m}$ pitch (design B). **E)** Mean (\pm s.e.m.) normalized photovoltage peaks from $n = 4$ pixels for both design B and C (diameter-pitch). For each pixel, the data from the three directions have been averaged. The red line shows a two-term gaussian fitting of the voltage profile, while the green bars represent the illuminated pixels.

3.2.3 Single pixel electrophysiology

The other concern when scaling down the layouts is if the reduced pixel area can generate enough charges to safely stimulate the retinal cells. From a material point of view, coating of the Ti electrodes with titanium nitride (TiN) is known to improve charge injection and storage capacity, as well as mechanical and chemical stability.^{126,169} This coating could be simply obtained by subsequent sputtering of TiN after Ti, in the same tool and with the same mask (stencil). Therefore, we added TiN coatings and characterized photovoltage and photocurrent generated by the improved pixels (**Figure 3.6**). We first measured the surface potential change upon illumination of single pixels with KPFM of TiN-coated pixels with respect to Ti only (**Figure 3.6A** and B). The results indicate a significantly larger potential change for the pixels coated with TiN. Unfortunately, exact absolute

voltage values should not be considered as the pixels were free-standing (polymers were patterned between pixels) and could not easily be grounded.

Photovoltage (PV) and photocurrent density (PCD) measurements of the photovoltaic pixels (PEDOT:PSS/P3HT:PCBM) with Ti and Ti-TiN electrodes were performed as described in paragraph 2.2.2, with illumination (565 nm) at increasing light intensities (**Figure 3.6C, G-H**). The PC profile (**Figure 3.6D**) generated by the pulsed illumination (10 ms, 1 mW/mm²) has a strong capacitive component for both Ti and TiN-coated electrodes. TiN-coated electrodes show higher PCD and PV (**Figure 3.6D-F**) than Ti only. This is probably due to the lower electrode-electrolyte impedance (lower charge transfer resistance and higher double layer capacitance) of sputtered TiN and an increased open-circuit potential rising from an improved cathodic interface due to the additional TiN.¹⁶⁹ Ti and TiN-coated electrodes follow the same trend of PCD and PV with increasing light irradiance, with Ti-TiN electrodes being more efficient for all the intensities tested (**Figure 3.6G and H**).

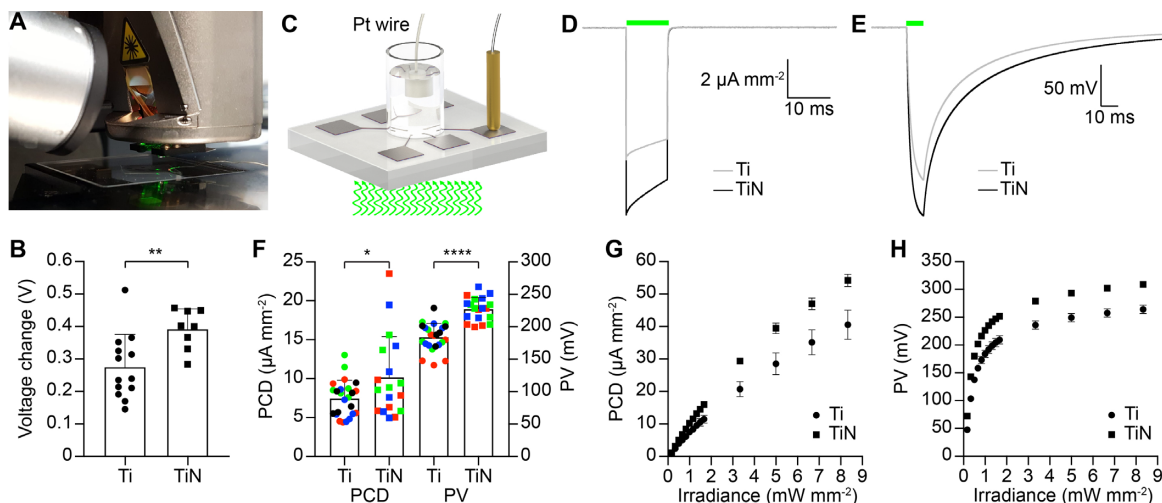


Figure 3.6 Characterization of the photovoltaic pixels with Ti-TiN electrodes. **A**) Picture of a sample during KPFM. **B**) Mean (\pm s.d.) surface potential change measured with KPFM upon illumination (565 nm, 870 μ W/mm², 60 s) of the bare Ti ($n = 13$) and the TiN-coated ($n = 8$) 80 μ m pixels. Ti (0.275 ± 0.100 V) vs TiN (0.392 ± 0.062 V): two-tailed unpaired t-test, $p = 0.0083$. The single pixels could not be grounded; therefore, the reference voltage is floating. **C**) Sketch of the experimental setup for the measures of PC and PV of samples with patterned polymers and electrode diameter of 100 μ m; the light pulse comes from the bottom. **D**), **E**) Grand-average of PC density (**D**) and PV (**E**) measures at light intensity of 1 mW/mm² (565 nm) and pulse durations of 10 ms. Horizontal green bars represent the light pulses. **F**) Mean (\pm s.d.) peak PC density (PCD) and PV of Ti and TiN-coated electrodes measured upon illumination with 10 ms pulses at 1 mW/mm² (565 nm). PCD Ti (7.5 ± 2.3 μ A/mm²) vs TiN (10.2 ± 5.2 μ A/mm²): two-tailed unpaired t-test, $p = 0.0288$; PV Ti (184 ± 21 mV) vs TiN (227 ± 18 mV): two-tailed unpaired t-test, $p < 0.0001$. **G**), **H**) Mean (\pm s.e.m.) peak PC density (**G**) and PV (**H**) of Ti and TiN-coated electrodes measured for 10 ms pulses at increasing light intensities. In panels **D** to **H**, the PC density and PV on every device ($N = 4$ for Ti and $N = 3$ for TiN-coated electrodes) have been measured for all electrodes ($n = 6$) and data have been averaged.

The effect of TiN coating of the photovoltaic pixels has been evaluated with *ex vivo* electrophysiology experiments as described in section 2.2.3 (**Figure 3.7A**). Prosthetic-evoked extracellular RGC ML activities have been measured upon illumination with 10 ms pulses of 565 nm light of a large-field area (**Figure 3.7B**) or of a 80 μ m (respectively 60 μ m) single-pixel (**Figure 3.7C**) and compared between Ti only and TiN-coated electrodes. As one could expect, large-field illumination induces more activity and TiN-coated electrodes perform generally better than Ti (**Figure 3.7D-G**) for

both sizes of the electrodes. However, the design with 60 μm electrodes (**Figure 3.7F and G**) stimulates less efficiently than 80 μm pixels (**Figure 3.7D and E**); the evoked responses were difficult to detect for light irradiances below 3 mW/mm^2 and was therefore discharged from further characterizations and use. With TiN, the threshold light irradiance to induce ML activity is overall lower for both large-field and single-pixel illumination (**Figure 3.7H and I**). For instance, the threshold irradiance for TiN and large-field illumination was equal or below 0.9 mW/mm^2 for all the measured cells (21/21), while only for 16 cells over 20 for Ti. Likewise, for single-pixel illumination, threshold irradiance for TiN was equal or below 0.9 mW/mm^2 for 12 cells over 21, while similar results could be obtained for only seven cells over 20 for Ti electrodes. Measurements with Ti-TiN electrodes (single-pixel) showed that ML responses could be induced in RGCs with irradiance levels as low as 78 $\mu\text{W}/\text{mm}^2$.

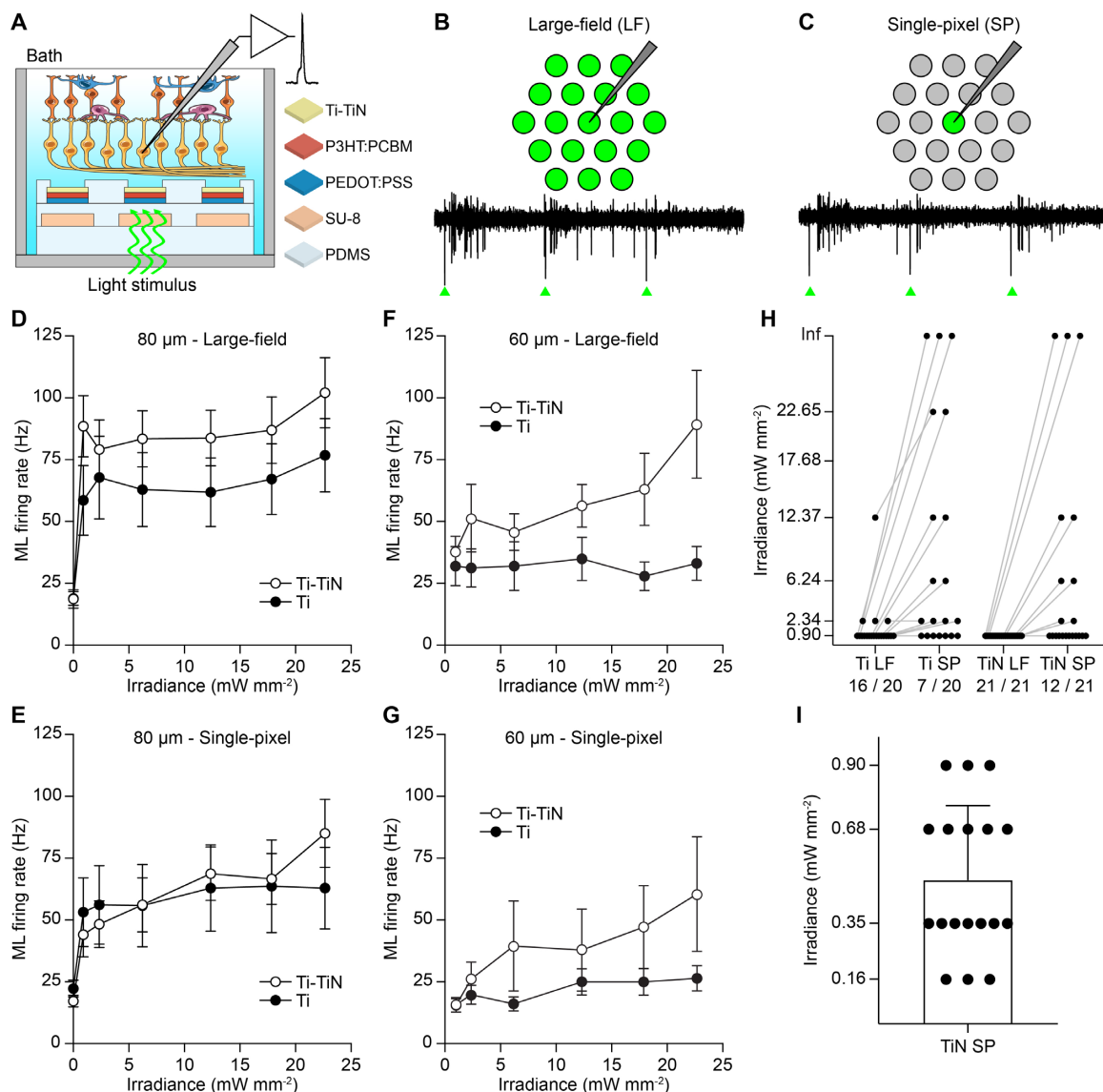


Figure 3.7 Responses of RGCs stimulated upon illumination of photovoltaic pixels with Ti and Ti-TiN electrodes. **A**) Experimental setup with mice Rd10 retinas placed RGCs down in contact with the photovoltaic interface with either Ti or Ti-TiN electrodes. Pixels design **B** (80 μm diameter and 120 μm pitch) and **C** (60 μm diameter and 90 μm pitch) were tested. **B**), **C**) Examples of RGC raw responses upon large-field (**B**) or single-pixel (**C**) illumination with 80 μm Ti electrodes. Green triangles represent the light pulses (565 nm, 10 ms, 0.9 mW/mm^2). **D**), **E**) Mean (\pm s.e.m, respectively $n = 20$ cells, $N = 8$ retinas and $n = 21$ cells, $N = 6$

retinas) ML activity of RGCs with 80 μm Ti and Ti-TiN electrodes at increasing light irradiance for large-field (D) and single-pixel (E) illumination. Already at 0.9 mW/mm^2 (565 nm) the firing rate is higher than the base activity for all the cases. **F), G)** Mean (\pm s.e.m, respectively $n = 9$ cells, $N = 3$ retinas and $n = 10$ cells, $N = 3$ retinas) ML activity of RGCs with 60 μm Ti and Ti-TiN electrodes at increasing light irradiance for large-field (F) and single-pixel (G) illumination. **H)** Increase of ML threshold irradiance for each RGC from large-field to single-pixel stimulation and for Ti and Ti-TiN electrodes (80 μm electrodes). The numbers on the horizontal axis depict the fraction of cells responding to irradiance levels equal or lower than 0.9 mW/mm^2 . “Inf” on the y-axis means that those cells were not responding. **I)** Mean (\pm s.e.m, $n = 18$ cells, $N = 4$ retinas) ML threshold irradiance for 80 μm single-pixel stimulation with TiN-coated electrodes. For panels D-I, ten consecutive sweeps were averaged for each RGC.

3.3 Discussion

POLYRETINA with higher pixels density could be easily fabricated by adapting the SU-8 photolithography mask and the stencil holes layout down to an electrode diameter of 40 – 50 μm . Moreover, an additional patterning step in the fabrication procedure was introduced (and depicted in **Figure 3.3**) to remove the organic electronic layers between the cathodes, leading to various improvements of the photovoltaic array. First, the lateral traveling of photo-generated charge carriers (which was previously excluded because irrelevant for edge-to-edge distances of more than 20 μm) and PEDOT:PSS potential fluctuations can induce cross-talks between neighboring electrodes. Second, the organic materials are not stretchable enough to stand bonding of the photovoltaic interface to the curved PDMS dome. Their inevitable cracking between electrodes, although insignificant for charge photo-generation, might lead to device failure due to delamination. Therefore, removal of PEDOT:PSS and P3HT:PCBM between electrodes solved the cracking issue. Third, the semiconducting blend absorbs light and generates – together with electron-hole pairs – heat, which might be reduced by the removal of unnecessary absorbing layers (particularly for NIR sensitive blends). And finally, more in vision of PDMS encapsulation replacement, fullerene-derivative substrates, such as P3HT:PCBM, could induce compatibility problems with the material chosen for encapsulation. PDMS did not cause any issue; nevertheless, for a more stable and long-term functioning prosthesis, other less permeable materials should be considered for pixels encapsulation and might be incompatible with the exposed organic semiconductor chemistry (cf. Chapter 4).

The fabrication of POLYRETINA prostheses includes bonding the photovoltaic array to a spherical PDMS support, which can be obtained without damaging the pixels for all the four tested designs (**Figure 3.4**). Yet, the strain needed at the array surface during the tight rolling/folding prior trans-scleral eye injection induced too high stresses on the Ti electrodes for the densest designs (design D). Nevertheless, simulations were carried out with Ti thicknesses of 80 nm (which is the average thickness that is deposited through the stencil holes when a nominal thickness of 150 nm is set), and it was noticed that by increasing the thickness (such as with the TiN coatings), the von Mises stress on electrode surfaces decreases (see **Appendix Figure 5**), which might be one way to guarantee mechanical stability of the pixels.

Particularly for denser arrays, the voltage spreading of stimulating pixels can cause reduction in visual acuity (eclipsing of OFF-pixels in the middle of ON-pixels) and inconsistent stimulation parameters across the prosthesis (voltage summation results in stronger activation of cells with respect to others). The measured photovoltage change with patterned light revealed that a clear peaks distinction can still be obtained for pixel arrays as dense as design B and C (**Figure 3.5**). For both designs, the OFF-pixel in the middle of ON-pixels is not completely eclipsed by the illuminated

surrounding coronas (**Figure 3.5E**, last column). Moreover, voltage summation was not detectable, as the voltage generated by the central pixels did not increase when the coronas were illuminated and the voltage between activated pixels remained low.

Full-field *ex vivo* electrophysiology of RGCs from explanted Rd10 mice retinas was thoroughly characterized in the paragraph 2.2.3. However, full-field (or large-field) illumination activates many pixels which can contribute to stimulate the retinal cells. Electrophysiology with single-pixel illumination showed a decreased activity and a higher irradiance threshold levels for ML spikes activation (**Figure 3.7**). An option for improving single-pixel RGC excitation was to add a TiN coating on the Ti electrodes, which improved photo-generated current and voltage (**Figure 3.6**). In fact, Ti-TiN electrodes could increase the ML activity of RGCs and decrease the activation threshold. ML spiking activity reflects efficient photovoltaic network-mediated stimulation, desired to increase resolution and decrease axonal activation.

In visual prosthetics, it is generally accepted – within certain limits – that smaller and denser pixel arrays can lead to better visual acuity. The new POLYRETINA designs (**Figure 3.2**) offer the possibility to induce phosphenes theoretically above the threshold considered blindness. This is an important feature for better recognition of details. However, *ex vivo* electrophysiological experiments with a smaller pixel diameter (60 μm) and pitch size (90 μm) showed a reduced ML activity compared to 80 μm electrodes (with or without TiN coatings, **Figure 3.7F** and G). ML activation with 60 μm pixels could be obtained only with higher light irradiances (starting 3 mW/mm^2), not suitable for *in vivo* applications.

The main advantage of POLYRETINA design, and I think we can all agree, lies in the distribution of relatively high-resolution pixels over a wide visual angle. The definition of a design, together with an *ex vivo* validation of single-pixels activation, lead to an optimization of the photovoltaic pixels, which is relevant (however not exhaustive) towards *in vivo* applications. Further characteristics and improvements will be discussed in the next Chapter 4.

3.4 Methods

3.4.1 Prostheses and chip microfabrication

The fabrication of prostheses and chips was performed as described in paragraphs 2.4.1 and 2.4.2; however, PEDOT:PSS was purchased from Heraeus (Clevios PH1000) because of its higher electrical conductivity and 0.1 vol% of GOPS ((3-glycidylxypropyl)trimethoxysilane) was added to increase adhesion. As specified, the other differences with previous microfabrication are the design and the additional polymers patterning step, which was obtained by exposing the wafers/chips to an O_2 plasma (Corial 210 IL etcher, RF power 100 W, ICP power 500 W, 50 sccm O_2 and 15 sccm He, 10 mTorr) after deposition of Ti (150 nm) or Ti-TiN (150 nm – 150 nm) by magnetron sputtering (400 W DC for Ti and 200 W RF for TiN).

3.4.2 Mechanical FEA simulations

The simulations of the photovoltaic interface bonding were performed in Abaqus/CAE 6.14, using a 3D deformable shell (representing the photovoltaic interface) moving against a static spherical solid (representing the PDMS dome) and creating a full hard contact. The 15 mm in diameter de-

formable shell was constructed as shown in **Figure 3.8**, with the exact array design used for prostheses fabrication, and with parameters listed in **Table 3.2**. The edges of the shell were fixed (clamped) to move only in the vertical direction toward the solid dome. Surface roughness and intrinsic thin-film stresses rising from deposition techniques were not considered.

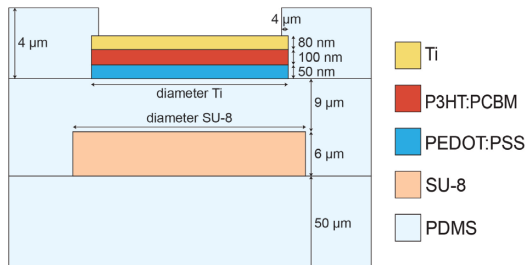


Figure 3.8 Thicknesses and sizes used for construction of the deformable membrane in Abaqus. The diameters for Ti and SU-8 and the pitch size were set for the different designs as shown in **Figure 3.2**.

Table 3.2 Materials parameters used for the mechanical simulations in Abaqus. Apart from PDMS, the behaviors of the other materials were considered isotropic elastic. The values for the Young's modulus and poisson's ratio of the used materials and the hyperelastic coefficients for PDMS were taken from references [168,170–174].

Material	Young's modulus (MPa)	Poisson's ratio	Density (kg/m ³)
PDMS (Neo-Hookean)	Coefficients: $C_{10}=0.662$, $D_1=0.255$	0.5	970
SU-8	2920	0.22	-
PEDOT:PSS	1900	0.34	-
P3HT:PCBM	1970	0.35	-
Ti	90000	0.34	-

3.4.3 Voltage spreading

In Ames' medium (A1420, Sigma-Aldrich) at 32 °C with a glass micropipette (tip diameter about 15 μm). Data were amplified (Model 3000, A-M System), filtered (DC-1000 Hz), and digitalized at 30 kHz (Micro1401–3, CED Ltd.). Illumination was carried out on a Nikon Ti-E inverted microscope (Nikon Instruments) by the Spectra X system (Emission filter 560/32, Lumencor). The microscope was equipped with a dichroic filter (FF875-Di01–25 × 36, Semrock) and digital mirror device allowing the simultaneous illumination of pixel sized spots. Light patterns were projected through a 10× (CFI Plan Apochromat Lambda) objective. For each light pattern, ten pulses of 10 ms were delivered at 1 Hz with an irradiance of 22.65 mW/mm². The resulting voltage has been measured at nine positions in three directions around the illuminated pixel. Data analysis was conducted in Matlab (Mathworks). Voltage peaks above noise level (mean noise threshold 6.2 μV) have been detected and their amplitude normalized respect to the central pixel value.

3.4.4 KPFM

KPFM characterization was performed in ambient air conditions with a Bruker Dimension icon microscope using doped (n) Si tips (SCM-PIT-V2, Bruker) in surface potential, amplitude-modulated imaging mode. To measure the surface potential variation, KPFM images were collected by repetitively scanning a single line of 100 nm under dark and illumination conditions. The green LED (565 nm) was positioned below the sample, focused on the pixels, and manually turned off and 3% on (870 μW/mm²) for about 60 s, for three times each pixel. Overall, the samples were grounded with

help of a silver paste; however, individual pixels could not be all connected to the paste and were therefore floating. The voltage bias was sent to the AFM tip. KPFM images were then analyzed using Gwyddion 2.36 software. For each image, the average surface potential variation value was obtained by subtracting the surface potential in dark to the one under illumination (voltage in light – voltage in dark).

3.4.5 PC and PV measurements

Experiments for PC and PV measurements were carried out as described in 2.4.7.

3.4.6 Electrophysiology

Experiments were conducted as described in 2.4.8.

3.4.7 Statistical analysis and graphical representation

Statistical analysis and graphical representation were performed with Prism (GraphPad Software Inc.). The normality test (D'Agostino & Pearson omnibus normality test) was performed in each dataset to justify the use of a parametric or non-parametric test. In each figure p-values were represented as: * $p < 0.05$, ** $p < 0.01$, *** $p < 0.001$, and **** $p < 0.0001$. Data are reported as mean \pm s.e.m. or mean \pm s.d., n is used to identify the number of electrodes or cells used; N is used to identify the number of devices or animals.

3.5 Acknowledgements

We would like to acknowledge the EPFL center of micro nanotechnology (CMi) and the Neural Microsystems Platform of the Wyss center at Campus Biotech, Geneva, for the support. This work has been supported by École polytechnique fédérale de Lausanne, Medtronic, European Commission (EU project 701632), Fondation Pierre Mercier pour la science, and Velux Stiftung (Project 1102).

Chapter 4 POLYRETINA for *in vivo* experiments in miniature pigs



Eyes of a cat (Source: Tina Engstrøm Grytdal)

The manuscript related to this chapter is in preparation.

Contributions: I designed, fabricated, and characterized the retinal prostheses and the OSTEmer-based samples; performed/analyzed electrochemical impedance spectroscopy, cyclic voltammetry, imaging (light microscopy, SEM, AFM), mechanical stability, and transmission measures; evaluated rolling and injection procedures; entirely prepared the prostheses for *in vivo* experiments. E. Borda performed/analyzed the OSTE tensile tests. C.H. Vila developed the injectors and performed/analyzed the OCT scans. P. Vagni performed/analyzed the electrophysiological experiments with minipigs. E.G. Zollinger performed the histological analyses. T.J. Wolfensberger performed the surgeries on minipigs.

4.1 Introduction

Translating a neuroprosthetic implant to preclinical applications frequently requires features that are not necessary or do not emerge during *in silico*, *in vitro*, and *ex vivo* experiments. A critical aspect comes from the manipulation and fixation of implants during surgeries, which essentially differ from how samples are handled during microfabrication, assembly, and characterization. Preserving the mechanical stability when the device is bent, twist, and pulled is for instance a requirement.¹⁷⁵ POLYRETINA pixels have been conceived to mechanically stand a good amount of load, necessary for delivering the prosthesis into the eye, thanks to the presence of rigid SU-8 discs underneath the photovoltaic pixels and embedded in the elastic PDMS matrix. However, this construction might still be insufficient to avoid further mechanical stresses. Preliminary *in situ* experiments showed that, after explantation, the pixels were cracked and the PDMS encapsulation layer was occasionally delaminated. A question that raised at that moment was: were the pixels damaged already after in-eye manipulation and fixation? Possible. Further mechanical improvements were still necessary and could be obtained thanks to the use of parylene-C as rigid islands, bringing the POLYRETINA process flow and some of its mechanical and functional characteristics to an optimized level.

Another important aspect to consider with POLYRETINA is the materials (electro)chemical and functional stability in body,^{176,177} which is crucial for implantable prostheses and even more crucial for organic-based implantable prostheses. Water and oxygen are dangerous molecules leading to delamination and active layer degradation.^{178–180} The encapsulation layer that protects the organic materials from the aqueous solution in POLYRETINA is PDMS, which is known to be a relatively permeable elastomer, thus not optimal for such applications, even though we could previously demonstrate up to two years of pixels functioning (**Figure 2.13**). The permeability of PDMS do not only lead to a faster degeneration of organic materials, but it also induces layers delamination, which was observed during *in situ* preliminary experiments after implant removal. We therefore introduce a new material for a potentially more efficient encapsulation: an off-stoichiometry thiol-ene-epoxy soft polymer, which – among other beneficial properties – can be directly photo-patterned with UV light.

In the next pages, we will present the technological and materials advances in POLYRETINA leading to a functionally and mechanically more stable prosthesis, with features adapted for preclinical trials. On the other side, we will also present the characteristics and preliminary results in the chosen animal model for POLYRETINA testing: blind Göttingen miniature pigs (minipigs).

Miniature pigs are routinely used in translational ocular research, for instance in preclinical studies to validate the surgical procedures for the implantation of retinal prostheses and the device functionality.¹⁸¹ Notably, the challenge behind the functional validation of light-based and photovoltaic prostheses lies in the need of a blindness model, such as photoreceptor degeneration, to decouple the effect of the prosthesis activation from the response of remaining retinal photoreceptors. However, such animal model is not easy to obtain using genetic manipulation in large mammals. An alternative approach consists in rapidly inducing photoreceptor degeneration using a chemical substance that interferes with the metabolism of photoreceptor cells. The best documented strategy of induced photoreceptor degeneration relies on the intravenous injection of iodoacetic acid (IAA), whose effect was studied in various animal models, particularly in rabbits and pigs.^{182–188} IAA suppresses glycolysis by inhibiting the function of the glyceraldehyde-3 phosphate dehydrogenase in a concentration-

dependent way.¹⁸⁹ Long-term studies in rabbits showed a degeneration restricted to the photoreceptor layer and that IAA administration did not lead to any remodeling of the surviving retinal cells, contrarily to what is observed in genetic models of inherited retinal degeneration.¹⁸⁵ In pigs, IAA leads to a strong rod degeneration and partial cone inactivation.¹⁸⁸ From the functional point of view, IAA induces a dose-dependent stable decline of full-field flash electroretinogram in both dark- and light-adapted animals; however, the dark-adapted functions are more affected, while the light-adapted responses can be partially spared.¹⁸⁷

Here, we provide a short characterization of an IAA-induced model of photoreceptor degeneration caused by the systemic injection of IAA at the concentration of 12.5 mg/kg in adult Göttingen minipigs up to three months after the injection. After that, preliminary data on *in vivo* experiments with POLYRETINA will also be presented.

4.2 Results

4.2.1 Improving mechanical stability

To prevent excessive mechanical stresses on the photovoltaic pixels, SU-8 was introduced in the original version of POLYRETINA as protective rigid platforms. The direct patterning by photolithography makes it interesting and compatible; however, an extra PDMS layer covering the discs and homogenizing the surface structure was necessary for the spin-coating of PEDOT:PSS and P3HT:PCBM (see **Figure 2.18**, step 3 and 4). This reduces the maximum strain and handling resistance. Hence, to adjust the implant for *in vivo* experiments, a second generation of POLYRETINA has been developed by replacing SU-8 with parylene-C, a materials with similar mechanical and optical properties and that can be deposited by chemical vapor deposition at room temperature with homogeneous thickness.^{190,191} The patterning of parylene can be obtained by dry etching using a standard photoresist as mask. Therefore, the updated microfabrication process flow consists of deposition of 5 μm of parylene-C, spin-coating PEDOT:PSS and P3HT:PCBM, sputtering Ti-TiN at full-wafer (without the need for a stencil mask), photolithography (possible on PDMS thanks to the additional parylene layer), and a series of dry etchings to pattern Ti-TiN, the polymers, parylene-C, and the residual photoresist. In **Figure 4.1A** the main steps of the process flow are presented. The result is that the photovoltaic pixels composed by PEDOT:PSS/P3HT:PCBM/Ti-TiN seat on top of the parylene-C islands, eliminating the strains from the PDMS directly underneath the pixels that were rising from bonding, rolling, and handling of the prosthesis.

A micrograph showing the new pixels on top of parylene is depicted in **Figure 4.1B**. It is to notice, that the size of the pixel is now the same size of the rigid parylene island and not 20% smaller as it was with SU-8. The design B presented in the previous chapter can now be composed by pixels of 100 μm with pitch size of 120 μm . The SEM image of the same pixels released from the wafer (**Figure 4.1C**) shows how these photovoltaic stimulating sites are protruding from the PDMS surface, envisioning possible 3D structures for a closer cell-electrode distance. The resulting extreme mechanical stability of the new array is largely improved compared to the previous version based on SU-8 and it allows bending, crinkling, and stretching without damaging the pixels (**Figure 4.1D** and **E**). This new array can be stretched until the PDMS between the pixels breaks (overall of $\sim 100\%$ unidirectional) without any crack on the Ti-TiN surface nor any delamination (**Figure 4.1E**).

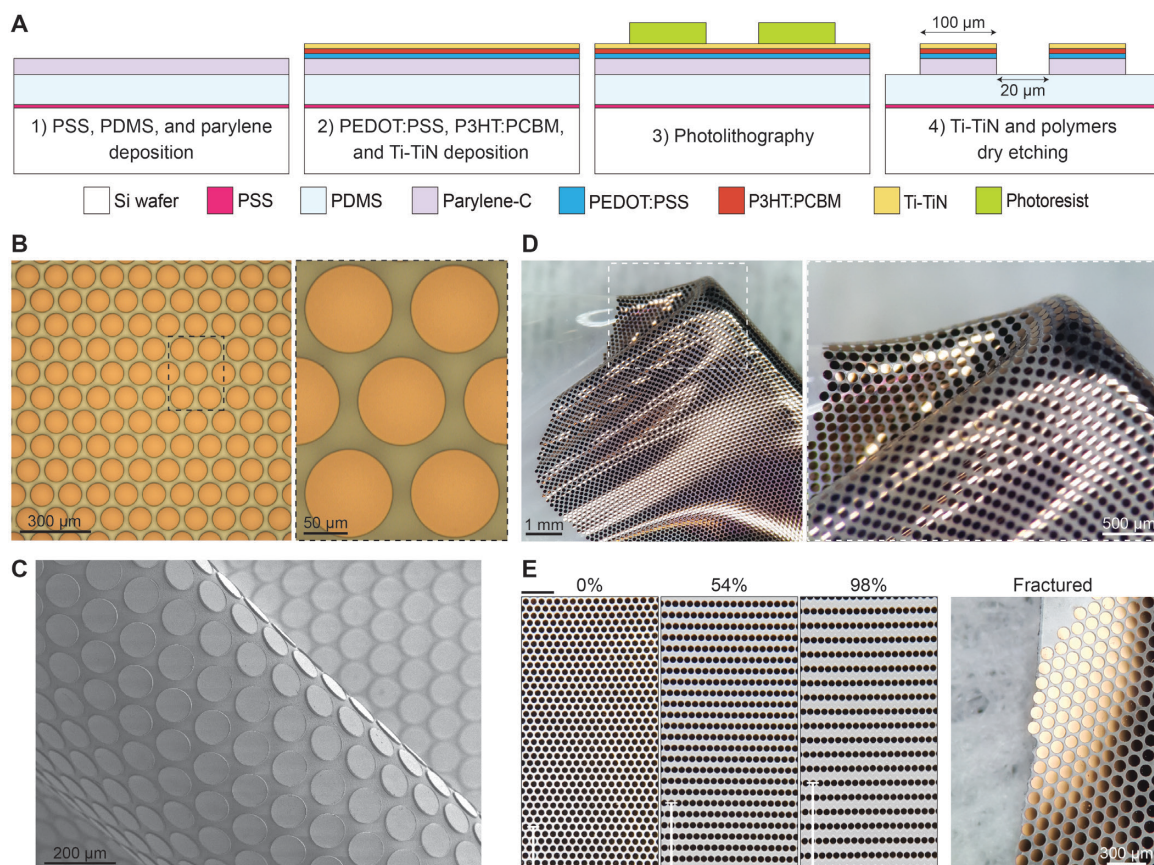


Figure 4.1 Parylene-C for improved mechanical stability. **A)** Main microfabrication steps for the production of the photovoltaic pixels deposited directly onto 5 μm of parylene-C and patterned via photolithography. PSS, PDMS, PEDOT:PSS, and P3HT:PCBM are deposited by spin-coating; parylene-C is deposited by CVD; Ti (100 nm) and TiN (100 nm) are deposited by magnetron sputtering. Details about the fabrication steps can be found in the methods (section 4.4.1 and **Figure 4.11**). **B)** Micrographs of the fabricated pixels with 100 μm diameter and 120 μm pitch. **C)** SEM picture of the pixels on parylene-C on PDMS released from the wafer and folded to obtain tilted views on the pixels. **D)** Membrane of PDMS with the array of photovoltaic pixels stretched and wrinkled with tweezers. **E)** Micrographs taken at 0%, 54%, 98% of strain, and after fracture during stretching test of the parylene-based photovoltaic array. Black scalebar: 500 μm ; white T-bar: six rows of pixels in the stretching direction. The last picture shows the PDMS fracture and the pixels intact.

Further beneficial consequences of parylene-based pixels patterning, apart from the augmented pixels size and the elimination of a critical manual step of alignment with stencil, are a total design freedom (the stencils have limited design choice due to the needed connected structure), a better control on deposited thickness (the quantity of a material deposited through the holes of a stencil is highly dependent on the holes size and geometry), and an increased surface roughness of Ti and Ti-TiN pixels. This last surprising point has been attributed to the absence of the stencil, which allows sputtered materials to be deposited with more degree of isotropy and homogeneous temperature distributions (which might in turn help to obtain larger grains). The surface roughness has been evaluated with AFM and the results are depicted in **Figure 4.2A-C**. A clear increase in roughness for materials sputtered without stencil can be observed with SEM and AFM images, together with roughness measurements, for both Ti and Ti-TiN electrodes. According to the measurements, the TiN coatings do not increase surface roughness; however, the resulting grains, visible from the SEM and AFM images, look denser and sharper. This might increase the total electrochemical surface area of the electrodes.

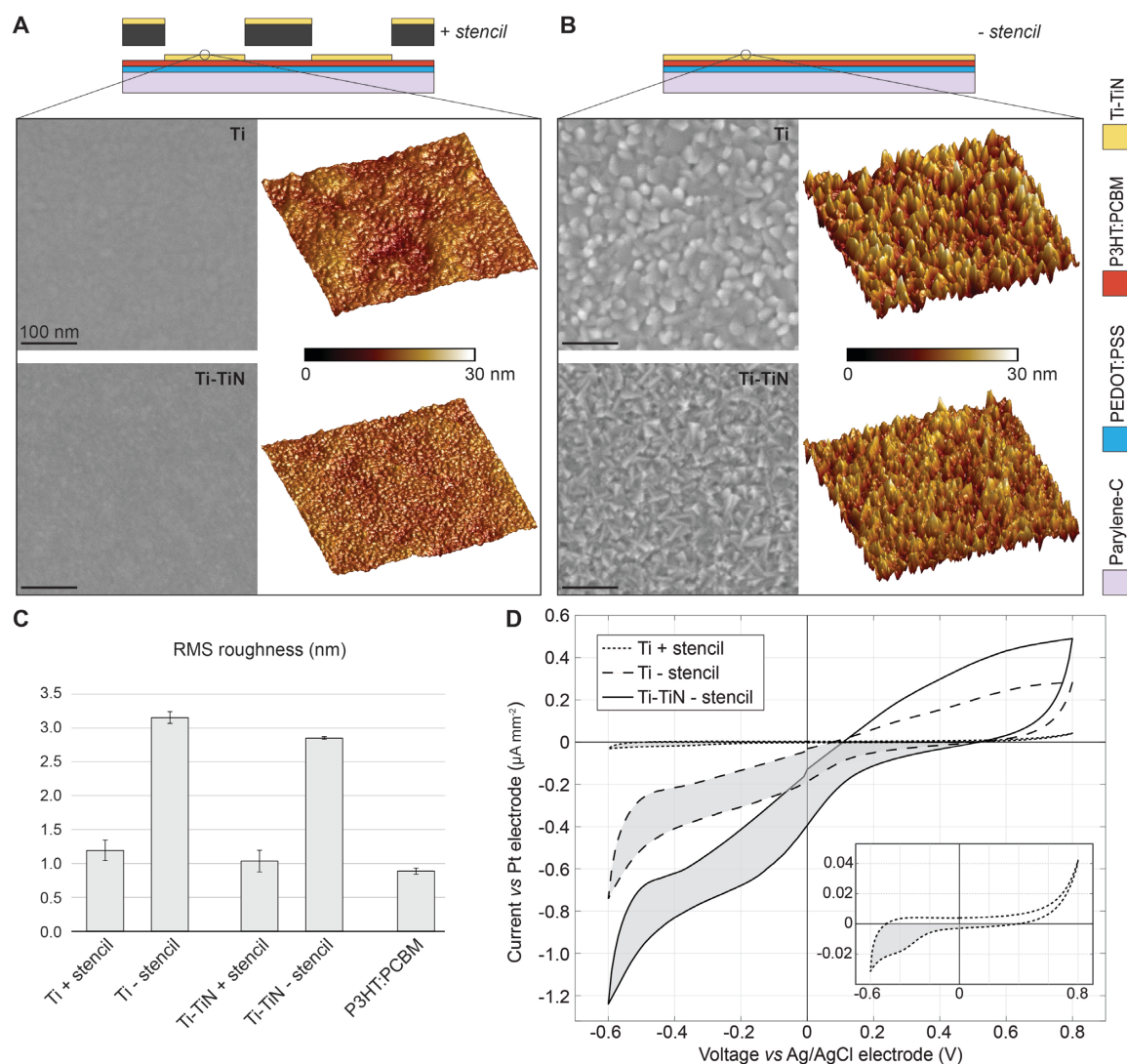


Figure 4.2 Increased roughness of Ti and Ti-TiN electrodes. **A), B)** SEM and AFM images of the Ti and Ti-TiN surfaces sputtered through the stencil (A) or directly onto the wafer (B). 100 nm of Ti (+ 100 nm of TiN) were deposited on the wafer, but only 55% of the thickness was deposited through the stencil, which had holes of 100 μm in diameter with a pitch size of 150 μm . The AFM images were 500 nm x 500 nm large. **C)** Mean (\pm s.d., $n = 3$ measures) of the root mean square (RMS) surface roughness measured on a 500 nm x 500 nm area of the samples represented in A)-B) and P3HT:PCBM. Ti + stencil: 1.19 ± 0.15 nm; Ti - stencil: 3.15 ± 0.09 nm; Ti-TiN + stencil: 1.03 ± 0.16 nm; Ti-TiN - stencil: 2.85 ± 0.02 nm; P3HT:PCBM surface: 0.89 ± 0.04 nm. **D)** Mean ($n = 5$ electrodes) cyclic voltammetry curves of electrodes fabricated on glass directly through stencil (+ stencil) or full-wafer and patterned by photolithography and etching (- stencil). The measurements were performed in PBS (1x) at 50 mV/s. The cathodic areas highlighted in grey were used to calculate the charge storage capacity.

We also performed cyclic voltammetry (CV) (**Figure 4.2D**) and EIS (not shown) to characterize the effect of increased surface roughness and TiN coating. From the CV curves, it is evident that the surface roughness largely increases the current levels generated by the applied voltage. Even higher currents can be obtained with TiN coating. The charge storage capacity (CSC) values for cathodic currents were calculated from the highlighted area in **Figure 4.2D** and are listed in **Table 4.1**. The surface area-weighted charge transfer resistance (R_{CT}) and the double layer CPE (C_{DL} , n) (also listed in **Table 4.1**) could be extrapolated from EIS data. The electrode surface area (also depending on

the roughness) seems to reduce the R_{CT} and increase the C_{DL} , with a slightly more resistive behavior of the impedance in the low frequency range (<1 Hz).

Table 4.1 Characterization of electrode-electrolyte interface with different materials and surface roughness. R_{CT} , C_{DL} , and the factor n were extrapolated from EIS fitting as described in 2.4.3 (and in relation to **Appendix Equation 1**). The cathodic CSC was calculated from the area between the CV curves with cathodic current (in grey in **Figure 4.2D**). The values represent the mean \pm s.d. of $n = 5$ electrodes.

Electrode	R_{CT} (M Ω ·mm ²)	C_{DL} (nF/mm ²), n	CSC (μ C/mm ²)
Ti + stencil	611.5	181, 0.965	0.15 \pm 0.04
Ti - stencil	14.2	344, 0.835	2.74 \pm 0.55
Ti-TiN - stencil	6.8	476, 0.845	4.06 \pm 2.34

4.2.2 OSTEmer encapsulation

As mentioned, the second version of POLYRETINA needed to improve encapsulation efficiencies with respect to PDMS. The chosen material in replacement of PDMS is an off-stoichiometry thiol-ene-epoxy polymer, aka OSTEmer or OSTE (**Figure 4.3A**). OSTE is known as a novel polymer thermoset for molding and low-temperature, adhesive- and plasma-free bonding, resulting in transparent, soft, and biocompatible microfluidic devices with superior sealing properties.^{192–194} The process for obtaining the OSTE-based structures is represented in **Figure 4.3B** and consists of submitting a mixture of three types of monomers with either thiol, allyl, or epoxy groups to UV radical thiol-ene polymerization, resulting in a soft solid with chemically reactive surface (thiol and epoxy groups exposed). Then, a thermal anionic thiol-epoxy polymerization leads to a more rigid solid with no reactive groups on the surface, because they either reacted with one another or they were used for bonding to another surface. Thanks to the UV sensitivity of the OSTE pre-polymer, the UV light can be used to locally cure the mixture and ethyl lactate to develop the pattern. We could obtain structures down to 2 μ m by 2 μ m with a thickness of about 4 μ m (**Figure 4.3C**) using a maskless aligner (375 nm, 600 mJ/cm², MLA 150, Heidelberg), i.e. a direct laser writer. Patterned films could be obtained with direct laser writing also with thicknesses up to 20 μ m. This practical and compatible processability of OSTE allowed us to develop OSTE-based implants, where OSTE is used as substrate and encapsulation material for, as example, functional Pt electrodes (**Figure 4.3D**). The surface chemistry and sealing properties of fully cured OSTE could be beneficial for implantable MEAs or other devices that need chronic in-body stability. Another property of OSTE, beneficial for implants, lies in its temperature-dependent stiffness.¹⁹³ The implants could be designed to be stiff for tissue penetration at room/low temperature and turn softer once inside the body to reduce immune system reaction.

Because of the mentioned characteristics, we decided to use OSTE as encapsulation material of POLYRETINA pixels (**Figure 4.3D**), which simplifies the process flow and theoretically improve, together with the parylene-C platforms underneath the organic materials, the long-term functionality of the photovoltaic pixels.

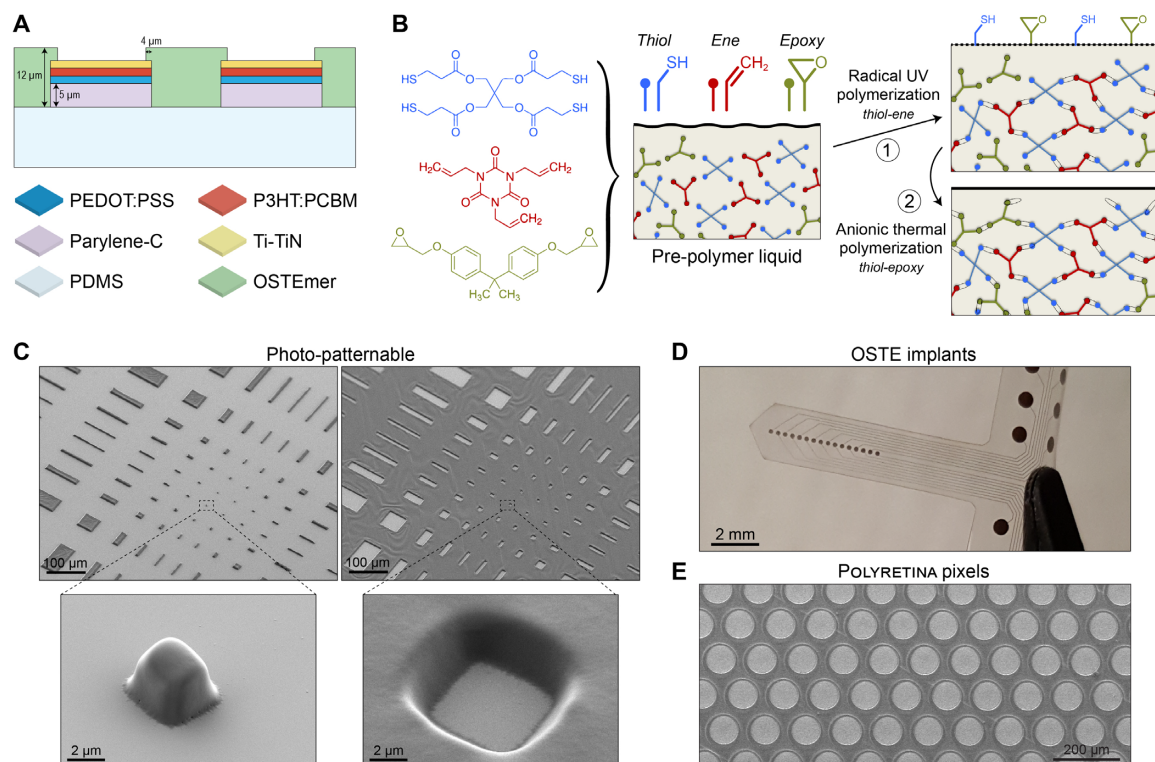


Figure 4.3 OSTEmer material. **A)** OSTEmer as encapsulation material for POLYRETINA with Ti-TiN electrodes. The thickness of OSTEmer is 12 μm from the PDMS surface. **B)** Examples of thiol (blue; pentaerythritol tetrakis(3-mercaptopropionate)), allyl (ene) (red; 1,3,5-triallyl-1,3,5-triazine-2,4,6(1H,3H,5H)-trione), and epoxy (green; bisphenol A diglycidyl ether) components used to produce OSTEmer. The monomers are mixed together in a liquid pre-polymer; then a first radical UV polymerization creates a soft solid with reactive thiol and epoxy groups at the surface that bind together in a second thermal curing leading to a solid bulk with tunable stiffness and a non-reactive surface. Adapted from Haraldsson *et al.*¹⁹⁵ **C)** Features with relatively high resolution can be obtained with direct laser writing (UV light) of the OSTEmer pre-polymer. Here, a thickness of about 4 μm was spin-coated. **D)** The process-ability of OSTEmer allows to manufacture functional OSTEmer-based implants (here with Pt electrodes). **E)** SEM image of the POLYRETINA pixels encapsulated with OSTEmer.

POLYRETINA prostheses have been fabricated with parylene-C islands, OSTEmer encapsulation, and an updated PDMS curved support for an optimized implant addressed to minipig eyes. The new PDMS dome is 500 μm thick in the center and 400 μm thick at the edges (smooth decrease), 14 mm large, and with an ellipsoidal curvature of 18 mm x 22 mm. Further specifications of the new dome design and its mold can be found in the **Appendix Figure 6**. In **Figure 4.4A**, pictures of the prosthesis show its overall look and the superior mechanical stability of the photovoltaic pixels even when the entire prosthesis is folded multiple times. We performed a “pinching” experiments (**Figure 4.4B**) demonstrating that pixels do not damage even after strong squashing of the prosthesis with tweezers.

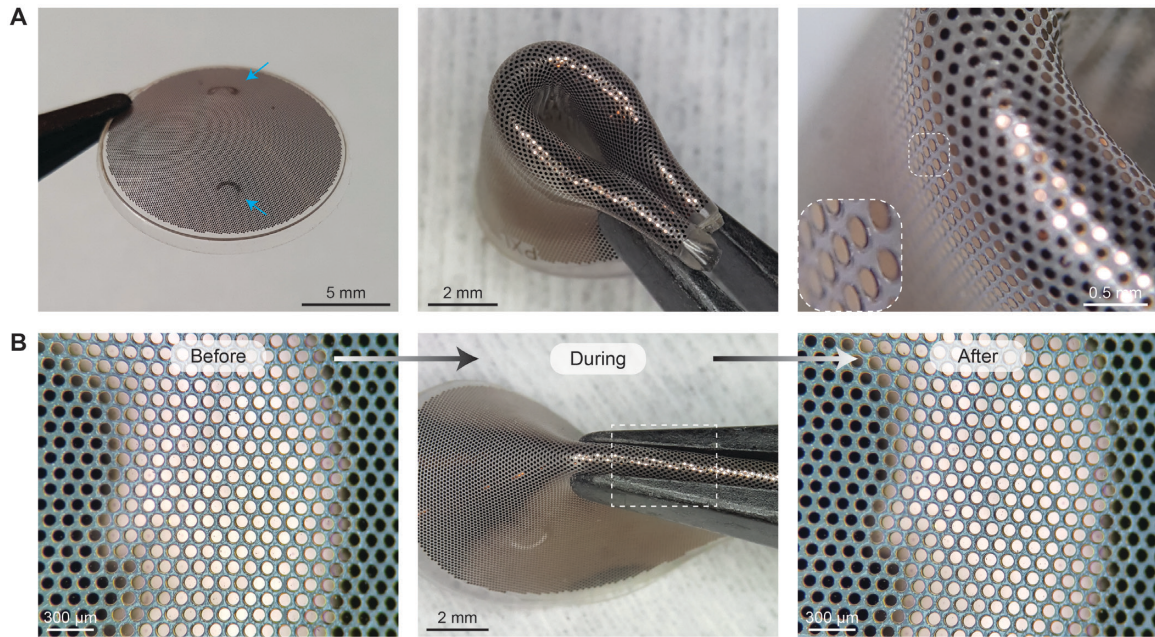


Figure 4.4 The POLYRETINA version with improved stability for preclinical trials with minipigs. **A)** Photograph of the high-density (100 μm pixels with 120 μm pitch) POLYRETINA for minipigs experiments (left) and after being folded in four (middle), with a magnification of a region (right) showing no pixels cracking. The blue arrows on the left image indicate the indentation in the PDMS support for the tack holes. **B)** Pinching experiments: micrograph of the pixels before (left), during (middle), and after (right) strong squashing of the prosthesis with tweezers. The pictures before and after pinching correspond to the same region pointed out in the middle image.

4.2.3 Black POLYRETINA

Before *in vivo* experiments with minipigs, another aspect of the prosthesis was required to be adapted for green-light based stimulation: the needless transparency of POLYRETINA around the opaque Ti-TiN pixels, which lets the projected light pass through the thickness of the implant and reach the retina. The reason why it is important to avoid light penetration lies in the blindness model for minipigs, i.e. the IAA-induced photoreceptor degeneration adapted by our group (see section 4.2.5). It is possible that residual photoreceptors can still respond to light after IAA injections. In order to minimize the natural response from residual photoreceptors when evaluating the performances of the retinal implant, we developed a black POLYRETINA, in which the OSTE encapsulation layer is darkened by the addition of black nanoparticles into the pre-polymer liquid (**Figure 4.5**). Carbon black (CB) nanoparticles (Nanografi Nanotechnology, 148 nm) were mixed at 2 wt% with OSTE pre-polymer and the resulting black OSTE was spin-coated and photopatterned around the photovoltaic pixels (**Figure 4.5A**). The UV light intensity emitted by the direct laser writer needed to be increased of about 75% to compensate the presence of the black nanoparticles. Finally, the resulting black coating should block the light travelling from the PDMS dome to the retina (**Figure 4.5A**, last sketch). Micrographs of the fabricated photovoltaic interface with black OSTE coatings show the relatively clean and accurate patterning of the encapsulation (**Figure 4.5B**), and the good mechanical stability of the membrane (**Figure 4.5C**) as obtained without encapsulation or with normal OSTE. The overall look of the final black POLYRETINA and enlarged pictures on the curved pixels can be seen in **Figure 4.5D** and **E**, showing that black OSTE is a valid material for photo-patterned encapsulation.

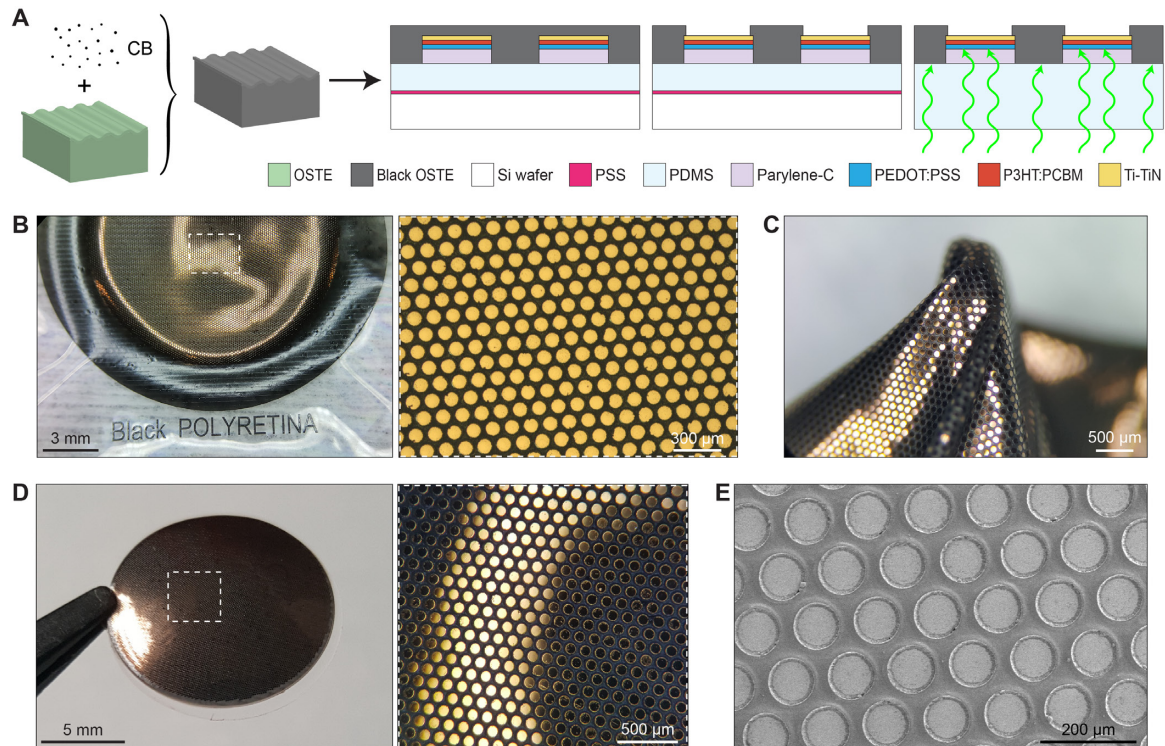


Figure 4.5 Development of black POLYRETINA. **A)** Fabrication of black OSTE encapsulation: the mixture of CB nanoparticles with OSTE is spin-coated, exposed to UV light, and developed for encapsulation patterning (12 μm thickness from PDMS). **B)** Pictures of the photovoltaic pixels array fabricated on the thin PDMS membrane and encapsulated with black OSTE. **C)** Folding, crinkling, and stretching of the black membrane. **D)** Photograph of the black POLYRETINA prosthesis with an enlarged micrograph of the photovoltaic pixels. **E)** SEM image of the prosthesis pixels encapsulated with black OSTE.

We then characterized the black OSTE encapsulation with optical and mechanical measurements (**Figure 4.6**). Compared to the normal POLYRETINA, the black POLYRETINA is visibly darker (**Figure 4.6A** and **B**). We measured how much light (565 nm) can be transmitted through both POLYRETINAS with a similar setup as shown in **Figure 2.15**. 93% of the light can be transmitted through the PDMS curved support of $\sim 500 \mu\text{m}$, about 30% through the normal POLYRETINA, and less than 6% through the black POLYRETINA (**Figure 4.6C**). The difference between the support and the POLYRETINA transmittance (93% – 30% = 63%) is mostly due to the presence of the photovoltaic pixels, which, not by chance, cover 63% of the total interface area. Instead, the difference between POLYRETINA and black POLYRETINA lies around 24% and is entirely caused by the thin black OSTE coating ($\sim 12 \mu\text{m}$).

Tensile characterizations of black OSTE revealed that its mechanical properties are very similar to normal OSTE (**Figure 4.6D** and **E**). It is important to mechanically evaluate the effect of additional nanoparticles, since they might reduce the overall stability and increase the risk of tearing. The small difference in stiffness and maximal elongation (**Figure 4.6E**) of black OSTE could be attributed respectively to the lower degree of cross-link and elongation capabilities, both due to the presence of stiff nanoparticles. Consequently, black OSTE has a slightly reduced tensile strength ($13.9 \pm 1.9 \text{ MPa}$ ($n = 5$) vs $22.6 \pm 3.9 \text{ MPa}$ ($n = 4$) of OSTE, mean \pm s.d.).

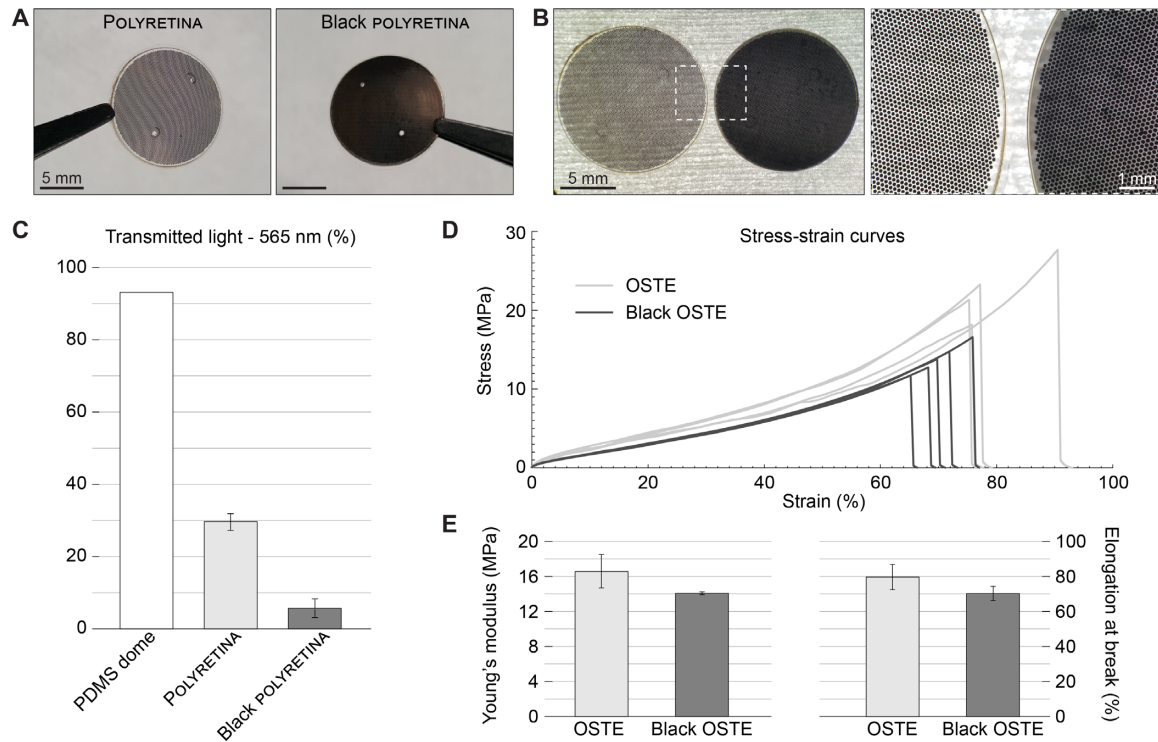


Figure 4.6 Characterization of the black OSTE coating. **A)** Photographs of the final POLYRETINA and black POLYRETINA prostheses for *in vivo* experiments with minipigs. The pair of holes (0.5 mm in diameter) in both implants are dedicated to tacks insertion for the epiretinal fixation. **B)** Micrograph of POLYRETINA and black POLYRETINA observed with transmission light settings, together with an enlarged view at high light intensity (background saturated). **C)** Mean (\pm s.d.) of the transmitted light (565 nm, 0.54 mW/mm²) through the PDMS dome (93%, n = 1), normal POLYRETINA (29.7 \pm 2.3%, n = 5), and black POLYRETINA (5.8 \pm 2.6%, n = 8). **D), E)** Mechanical characterization of OSTE and black OSTE by tensile tests, with the resulting stress-strain curves performed at 1% of initial length in mm s⁻¹ (D), and the extracted values (mean \pm s.d.) of Young's modulus (OSTE: 16.5 \pm 1.9 MPa, black OSTE: 14.0 \pm 0.2 MPa) and maximal elongation (OSTE: 79.6 \pm 7.2%, black OSTE: 70.2 \pm 4.0%) of n = 4 OSTE and n = 5 black OSTE samples (E).

4.2.4 POLYRETINA injector

We previously showed that POLYRETINA can be tightly rolled without any mechanical damage on the photovoltaic pixels (**Figure 4.4**). This is a necessary feature for the insertion of the 14 mm wide implant through a small scleral or corneal cut of maximum 6.5 mm in length. Yet, a tool for POLYRETINA injection is needed in order to achieve a proper, easier, and safer surgical implantation. We therefore developed an injector and a procedure inspired by the ones used for intraocular lenses. The 3D model of the developed injector is presented in **Figure 4.7A**. The two components, a beveled tube of 4 mm in external diameter and a narrow cylinder with thin and flexible extensions, can be assembled and can slide smoothly back and forth. The cylinder is equipped with the parallel extensions (0.35 mm x 1.7 mm x 16 mm) that can accommodate the rolled prosthesis. The implant rolling and loading procedure into the injector is shown in **Figure 4.7B-D**. POLYRETINA can be tightly folded with help of tweezers at a rolled external diameter of maximum 2.8 mm (**Figure 4.7B**) to fit within the flexible extension of the cylinder (already assembled into the beveled tube, **Figure 4.7C**). The loading is complete when the cylinder is retracted into the tube by sliding, taking the rolled POLYRETINA with it (**Figure 4.7D**). Finally, we simulated injection procedures in saline solution by pushing the cylinder and the prosthesis towards the edge of the tube (**Figure 4.7E**). The elasticity of

the PDMS dome allows for the prosthesis to unfold, free itself from the flexible wings, and return to its original shape.

To evaluate if the injection procedure causes mechanical damage on the black POLYRETINA, such as electrodes cracking, support tearing or distortion, and encapsulation shearing deformations, we imaged the prosthesis before and after the simulated injection (**Figure 4.7F** and **G**). The overview look (**Figure 4.7F**) and the enlarged view on the pixels (**Figure 4.7G**) both showed no such damages.

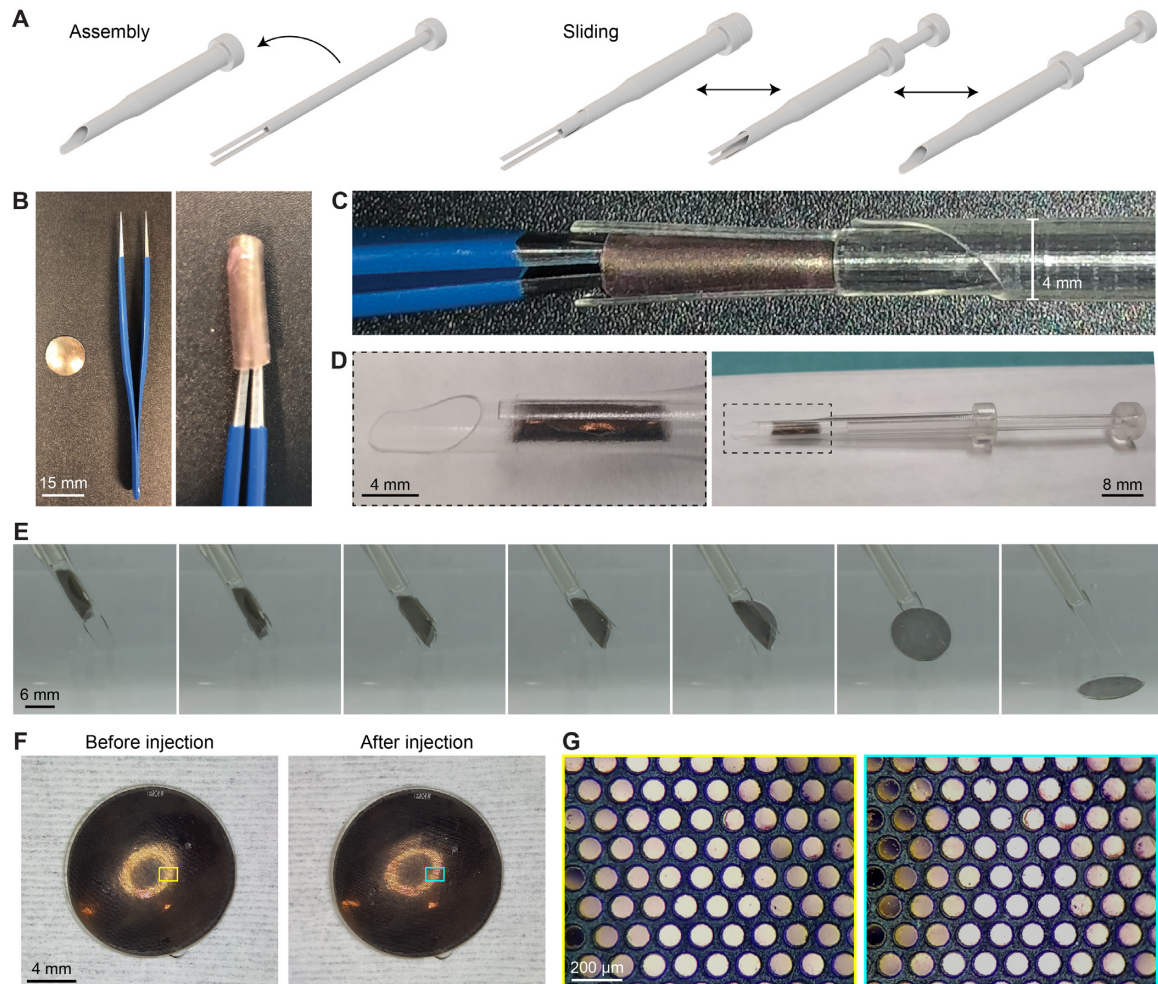


Figure 4.7 POLYRETINA injection. **A)** Model of the injector composed by two parts: a hollowed, beveled tube of 4 mm external diameter and a smaller cylinder equipped with flexible, thin, parallel extensions that fits and slides inside the tube. **B)** The rolling of POLYRETINA can be obtained with help of tweezers. **C)** Loading of the rolled implant within the extensions of the cylinder. **D)** Photographs of the POLYRETINA loaded into the beveled tube. **E)** Simulations of injection procedure in saline solution. When the implant is pushed by the narrow cylinder towards the edge of the beveled tube, the unfolding of the PDMS-based dome displaces the thin extensions that relieve the prosthesis. **F), G)** Evaluation of injection procedure damage. The black POLYRETINA is imaged before (left) and after (right) the injection procedure at overview (**F**) and magnified view (**G**).

To be used for *in vivo* experiments, POLYRETINA and the injector parts are separately sterilized (see 4.4.6 for sterilization procedures) and the loading process is carried out under sterile conditions. It is also possible to load the injector with the prosthesis for *in vivo* testing one day before the implantation and leave it (under dark) in a sterile bag until needed.

4.2.5 Preliminary *in vivo* results

4.2.5.1 Animal model of photoreceptor degeneration

We started with the evaluation of the IAA-induced blindness due to photoreceptors degeneration in minipigs. For all the *in vivo* experiments, an intravenous injection of IAA in the animal was delivered at the concentration of 12.5 mg/kg, chosen based on previous studies in pigs^{186,187}. We first performed spectral domain optical coherence tomography (SD-OCT), which is a fast, non-invasive, and relatively high-resolution technique enabling the acquisition of cross-sectional images of the retina, showing clearly distinguishable layers such as the choroidal vessels, retinal pigment epithelium (RPE), outer plexiform layer (OPL), inner plexiform layer (IPL), and retinal nerve fiber layer.¹⁹⁶ We used OCT scans to monitor the retinal thickness in minipigs before and after the administration of IAA (**Figure 4.8A** and **B**, left panels). The scans suggest that minipigs might be light-insensitive already after one month post-IAA, because of the reduced thickness of the outer retina (which includes photoreceptors) marked with red rectangles, clearly visible in **Figure 4.8A** and **B** (left-center panels). To obtain a better idea of the morphological changes induced by the administration of IAA and to investigate which cells are most affected, we performed histological examinations of the retina before and after the injection of the toxin. We conducted fluorescent immunohistochemistry (IHC) on samples from IAA treated minipigs before and one month after the IAA administration (**Figure 4.8A** and **B**, right panels). We used antibodies against L/M opsin and rhodopsin to identify cone and rod photoreceptors respectively, while DAPI is used to locate the other cells. The immunostaining shows that there are no rod photoreceptors visible in the image after one month from the treatment. On the other hand, some cones survive, although they lack the outer segment and express L/M opsin in the cell body. The Hematoxylin and Eosin (H&E) staining of retinas before and up to three months after IAA injection (**Figure 4.8C**) confirms that the photoreceptor layer, clearly visible in the control image on the left, is completely absent starting from two months after the injection. On the other hand, the INL of the retina looks less affected by the toxin and almost intact even after three months (image on the right). Furthermore, the toxin does not seem to have any impact on the RGCs, at least at the tested timepoints. These observations present anatomical evidence of complete retinal degeneration in Göttingen minipigs following IAA injection; however, to confirm that the degeneration observed in the retina translates to a complete loss of visual functions, we performed some electrophysiological tests.

We recorded electroretinographic (ERG) responses using a lens electrode placed on the cornea of the stimulated eye and, as a reference, the same type of electrode on the other eye, which was also kept covered. ERG refers to the measurement of the variation of the retinal resting potential in response to light stimulation. It is a non-invasive way to directly and quickly assess the functionality and integrity of the retina. The electrodes are generally placed on the cornea in order to pick up the signal generated by the activation of retinal cells.¹⁹⁷ To obtain recordings in photopic condition, which isolates the functionality of cone photoreceptors, we exposed the eye to a bright light (20 cd s m⁻²) for 10 minutes and then recorded the response to bright light flashes (30 cd s m⁻²). 30 flashes of 4 ms each were delivered at a frequency of 0.1 Hz and the responses were averaged. **Figure 4.8D** shows an example of ERG response from a treated animal (top panel) before (black) and one month after (red) IAA delivery, and from an untreated control animal (bottom panel). The a- and b-waves are two characteristics of ERG traces, whose amplitudes are proportional to the activation degree of photoreceptors and post-synaptic cells respectively. The mean (\pm s.d.) of the a- and b-waves from

the ERG response before and one month post-IAA is depicted in **Figure 4.8D** on the right. A statistically significant decrease in amplitude after IAA treatment is obtained for both waves.

In addition to the experiment described above, which is related to the functionality of retinal circuits, we also measured the visually evoked potentials (VEPs) from the primary visual cortex in response to flashes of light (30 flashes of 4 ms each, at 0.1 Hz and at 30 cd s m⁻²). Two k-wires used as electrodes were placed above the two visual cortices and the responses were recorded from each electrode while stimulating the contralateral eye and normalized by a reference electrode implanted outside the visual cortex (**Figure 4.8E**, left). The averaged VEPs (as shown in **Figure 4.8E** on the right) are evaluated by their main negative peak amplitude (which is often found within 40 and 80 ms from the light onset). The mean (\pm s.d.) of the peak amplitude from the VEPs response before and one month post-IAA is depicted in **Figure 4.8F**, showing a statistically significant decrease in amplitude after IAA treatment.

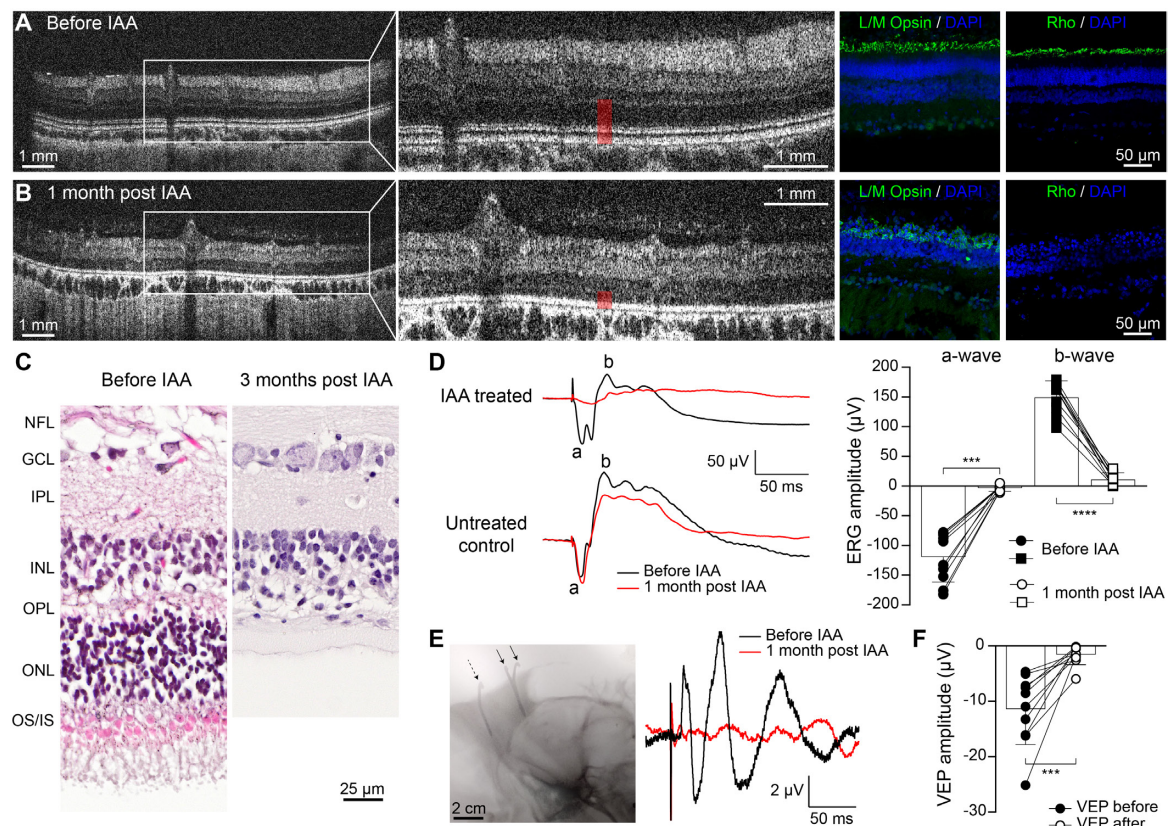


Figure 4.8 Göttingen minipig model of IAA-induced photoreceptor degeneration. **A), B)** Spectral domain-OCT images (left) and IHC sections (right) of minipig retinas before (A) and one month post-injection of IAA (B). The red rectangles in the OCT scans indicate the thickness of the outer retina, including the photoreceptors layer. In the IHC images, antibodies against rhodopsin and L/M opsin were used to label rod photoreceptors and cone photoreceptors, respectively. **C)** H&E staining on retinal sections before and three months after IAA administration. On the side, the different cells layers are reported (cf. **Figure 1.1B**). **D)** Light-adapted ERG responses of an IAA-treated minipig before and 1 month after IAA injections (top left and right graphs) and the same responses for an untreated control minipig (bottom left). The light stimulus was 4 ms flashes of 30 cd s m⁻², repeated 30 times at a frequency of 0.1 Hz. The a- and b-waves are noted on the recording traces. Both a- and b-waves have a significantly reduced amplitude already after one month from IAA treatment (mean \pm s.d., N = 10 eyes, a-wave before treatment: 120.31 \pm 39.12 μ V vs a-wave after treatment: 4.93 \pm 3.31 μ V, $p < 0.001$, paired t-test; b-wave before treatment: 150.07 \pm 25.75 μ V vs b-wave after treatment: 11.86 \pm 9.77 μ V, $p < 0.0001$, paired t-test). **E)** On the left, a radiography showing the position of the VEP recording

electrodes (two solid arrows) and the reference electrode (dashed arrow). On the right, example of average VEP recordings in treated animals before (black) and one month after IAA injection (red). Light flashes of 4 ms and 30 cd s m⁻² were repeated 30 times at a frequency of 0.1 Hz. **F**) Mean (\pm s.d.) amplitude of the negative wave of the VEPs before (filled markers; 11.45 ± 6.04 μ V; N = 10 eyes) and one month after IAA injection (empty markers; 1.78 ± 1.69 μ V; N = 10 eyes, paired t-test: $p < 0.001$).

4.2.5.2 Surgical implantation of POLYRETINA in minipig eyes

Surgical implantation in Göttingen minipigs can be obtained after a vitrectomy, removing the lens and its suspensory ligaments as well (**Figure 4.9A**), and a corneal tunnel incision at the limbus of up to 6.5 mm (**Figure 4.9B**). The insertion of POLYRETINA is obtained by sliding the smooth beveled opening of the injector into the incision, pushing the cylinder with the prosthesis gently inside the eye chamber (while this is pressurized with perfusion) until the implant is released, and then retracting the cylinder and the tube from the eye (**Figure 4.9C**). Once released, the prosthesis regains its original spherical shape and can be adapted on the retina (**Figure 4.9D**). The fasten of POLYRETINA in epiretinal position is obtained with two custom-made stainless steel retinal tacks (**Figure 4.9E**), adapted for securing a 500 – 600 μ m thick implant against the retina by clamping the bottom side of the implant with the outside of the sclera, where the sharp pyramidal tip is supposed to exit. The circular discs at the base of the tacks are 1 mm wide, which is two times larger than the holes pre-punched in the implant (0.5 mm in diameter), ensuring an adequate holding. Once the prosthesis is fixed, the corneal incision is carefully sealed by suturing (**Figure 4.9F**) and the minipig can then recover in a short period of time. The implantation procedure was developed in order to minimize traumatic manipulation and takes about 60 minutes from the vitrectomy to the final suturing.

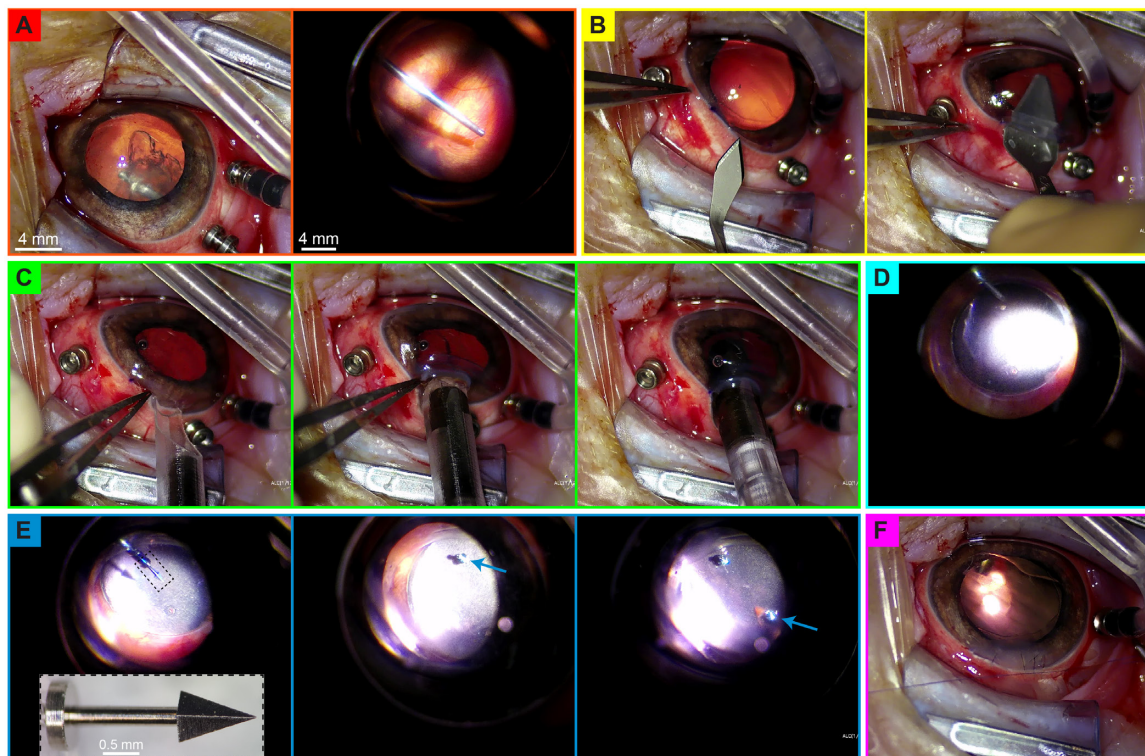


Figure 4.9 Surgical implantation of POLYRETINA in Göttingen minipig eyes. **A)** Vitrectomy. **B)** Corneal incision: narrower knives are applied first, then the incision is enlarged progressively to maximum 6.5 mm. **C)** Insertion of POLYRETINA with the injector. The implant is pushed by the cylinder with the extension as soon as the opening of the beveled tube is completely inserted. At this point, only the cylinder with the implant moves. **D)** Release and epiretinal placement of POLYRETINA. **E)** Epiretinal fixation of the implant with custom-

made stainless steel retinal tacks (the segment between the disc and the base of the pyramidal tip is 1.5 mm long and 0.3 mm wide; the height of the pyramidal tip is 1.2 mm; the axes of the trapezoidal base of the tip are 0.8 and 0.5 mm; and the diameter of the disc is 1 mm, while its thickness 0.25 mm). Two tacks *per* implant are necessary. The blue arrows indicate the tack just inserted prior the image frame. **F)** Suturing of the corneal incision.

In the frame of surgical procedures, the removal of the retinal implants is of importance for the replacement after a period of time of damaged or degenerated prostheses with fresh and upgraded ones. The absence of connecting wires makes the removal surgery relatively simple: after the extraction of the retinal tacks from both the retina and the implant, POLYRETINA can be either folded or cut and retrieved through a small corneal or scleral incision.

4.2.5.3 Prosthetic-evoked potential recordings

VEPs in minipigs were stimulated and recorded in the same eye before, immediately after, and two weeks after POLYRETINA implantation as performed in the previous paragraph (4.2.5.1) with, however, a green LED (565 nm, 10 ms *per* flash) instead of white light to better induce photovoltaic activation of the PEDOT:PSS/P3HT:PCBM/Ti-TiN pixels. We achieved successful implantations and recordings of the black POLYRETINA with 100 μm pixels and 120 μm pitch and with 6% of green light transmittance. **Figure 4.10A** shows exemplary recording traces (average of ten sweeps) of VEPs upon green light (10 ms flashes) before IAA treatment (black), after two months from IAA injection (grey), and after two weeks from POLYRETINA implantation (red). The principal negative peak (marked with an arrow) is clearly visible for the untreated vision, whereas is almost absent two months after the injection of IAA, but it reappears when the minipig was implanted with POLYRETINA. These prosthetic-evoked waves happened to peak between 10 and 40 ms after light onset, which is earlier with respect to the natural VEPs measured prior IAA treatment. The reason probably lies in the faster triggering of RGCs action potential due to direct (SL) electrical stimulation of RGCs, while natural phototransduction is a slower process, resulting in later RGCs spiking. **Figure 4.10B** depicts the absolute value of the VEP negative peaks from two eyes. The effect of the toxin after one and two months from injection is represented in grey and the important recovery after the prosthesis implantation is marked in red. When the prosthesis is implanted, the VEP peaks seem to proportionally depend on the green light intensity, while little effect is deducible from the recordings in blind minipigs prior implantation of black POLYRETINA (**Figure 4.10C**).

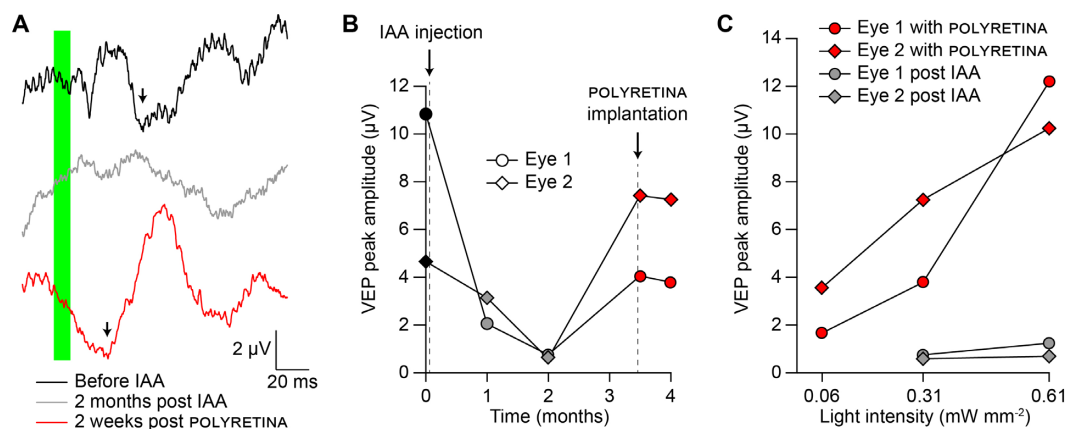


Figure 4.10 Prosthetic-evoked recordings in minipigs primary visual cortex. **A)** Average (of ten repetitions at a frequency of 0.1 Hz) traces from one eye before IAA treatment (black), two months after IAA treatment (grey), and two weeks after black POLYRETINA implantation (red). The green vertical bar represents the green light flash of 10 ms (565 nm, 0.31 mW/mm^2). The black arrows indicate the clear occurrence of the main

negative VEP peak. **B)** Evolution of the absolute main peak amplitude value in A: before IAA treatment (black), one- and two-months post IAA injection (grey), and immediately after and two weeks after black POLYRETINA implantation (red) for two eyes. **C)** Absolute main peak amplitude values according to light intensity from responses with (red) and without (grey, post IAA) black POLYRETINA.

Unfortunately, retinal detachment below the implanted devices was often noticed after two weeks of implantation, which is indeed an aspect to improve. There are three main reasons that could have contributed to this situation: the incomplete insertion of the tacks through the sclera (they will come off after a certain period of time), the possible mismatch between the curvature of the prosthesis and the one of the minipig eye, and the unclear effect of IAA toxin on the expanded blood vessels of the choroid (visible in **Figure 4.8A** and **B**). All these problems will be addressed in future experiments.

4.3 Discussion

The technological development of POLYRETINA, such as the use of parylene-C, lead to beneficial characteristics of the prosthesis and its manufacturing. Among them, a simplified and faster process flow, an improved electrode-electrolyte interface thanks to larger and rougher TiN-coated electrodes (**Figure 4.2**), and an extreme mechanical stability of the photovoltaic pixels (**Figure 4.1** and **Figure 4.4**). The latter is a requirement imposed by the envisioned insertion and manipulation procedure of POLYRETINA for *in vivo* applications. This technological evolution of POLYRETINA not only involved standard and well-established materials (parylene-C), but it also took advantage of novel and less usual materials such as OSTE polymers (**Figure 4.3**). The main advantages of OSTE polymer compared to PDMS are its superior sealing properties (tested in literature¹⁹⁴) and its capability to be locally polymerized by UV light, improving POLYRETINA stability and manufacturing process, respectively.

It is more and more frequent for materials sciences to contribute with resources of more valuable properties for implantable bioelectronic interfaces. Indeed, new materials means many performance, biocompatibility, and long-term stability tests, which take time and were partially neglected in this thesis but intended for future experiments. Furthermore, one improvement can lead to another: OSTEmer allowed the development of black POLYRETINA, which can block up to 95% of the projected light (**Figure 4.5** and **Figure 4.6**). This feature, although likely temporary (for instance, less necessary for NIR illumination; see Chapter 5), is an important upgrade for the *in vivo* evaluation of green light activated retinal prostheses, which necessitates an animal model with light-insensitive retinas to separate the prosthetic-evoked responses from the natural phototransduction.

The IAA toxin interferes with the metabolism of cells and, given the photoreceptors' high metabolic rate, they are especially sensitive to it. This allowed us to induce a fast retinal degeneration without relying on complicated genetic manipulations, which can be difficult to perform in large animals. From the characterizations performed on Göttingen minipigs, this toxin induced a strong reduction of electrophysiological responses to light pulses, visible with ERG and VEPs recordings, together with a clear absence of the photoreceptors layer in OCT scans and histological samples (**Figure 4.8**). We can therefore conclude that the IAA-induced photoreceptor degeneration can stand as appropriate model for the preliminary validation of light-dependent retinal prostheses, especially if black POLYRETINA can further reduce the possibility of residual natural responses conflicting with the photovoltaic stimulation.

Implantation procedures are an essential component generally related to the prosthesis characteristics. Although one of the major benefits of POLYRETINA (i.e. its wireless power transmission) represents a valuable surgical advantage (i.e. absence of wires), the other major benefit (i.e. its wide visual field coverage) represents a main surgical challenge (i.e. insertion of large implants through a small incision). POLYRETINA's ability of tight rolling/folding without damage to its structures, together with the developed custom-made injector, overcome this challenge, offering to the surgeon and the animal a facile, quick, and safe implantation (**Figure 4.7** and **Figure 4.9**). In addition, the size of the minipig eye (comparable to the human) enables the implantation of clinical size devices, allowing the surgeon to train on the required surgical techniques.

Preliminary *in vivo* results (**Figure 4.10**) showed a clear primary negative peak in various VEP measurements after POLYRETINA implantation, while almost no evident peaks were found in the responses of blinded minipigs (post IAA). The earlier occurrence of the peaks compared to natural VEPs and the proportionality of the amplitudes with light intensity, although the reduced light passing through the black implant, let us further conclude that these responses are due to the prosthesis. The reproducibility of the prosthetic-evoked responses remains however questionable (likely due to other surgical issues and the common retinal detachment). Indeed, more animals are necessary to reliably conclude that POLYRETINA induces visual responses and to quantify and discuss in detail the effects of the prosthetic stimulation. Nevertheless, an important, positive, preliminary result could be obtained, which represents a relevant step justifying further animal experiments.

In conclusion, preclinical trials need to overcome various complicated challenges. As researchers and microfabrication engineers, we are obliged (or at least we should *feel* obliged) to develop implants that are as flawless as possible (particularly after the proof-of-concept phase), which is not always trivial especially for implants based on novel materials and complex design. Moreover, many challenges are sometimes unforeseen in the laboratory environment until preliminary preclinical (and clinical) trials are carried out. This makes it necessary to involve animal experiments in parallel with the implant development phase, which, unfortunately, leads to a scientific, ethical, and sentimental conflict that will always burden on *some* researchers' shoulders.

4.4 Methods

4.4.1 Prostheses microfabrication

PDMS-photovoltaic interfaces were fabricated on silicon wafers as represented in **Figure 4.11**. A thin sacrificial layer of poly(4-styrene sulfonate) solution (PSS, Sigma-Aldrich, 561223) was spin-coated on the wafers (1500 rpm, 60 s) and baked (130 °C, 10 min). Degassed PDMS pre-polymer (10:1 ratio base-to-curing agent, Sylgard 184, Dow-Corning) was then spin-coated (900 rpm, 60 s) and cured in oven (75 °C, 2 h). After surface treatment with oxygen plasma (30 W, 30 s) and with silane Silquest A-174NT, a 5- μm thick parylene-C layer was deposited (CVD, Comelec C25S) by pyrolyzing 10 g of Galxyl C precursor (**Figure 4.11-1**). PEDOT:PSS (Clevios PH1000, Heraeus) was mixed with 0.1 vol% GOPS ((3-glycidylpropyl) trimethoxysilane, Sigma-Aldrich, 440167), filtered (0.2 μm PES filters, Corning), and then spin-coated (3000 rpm, 40 s, 90 nm) onto the O₂-plasma treated (30 W, 30 s) parylene-C surface. Subsequent annealing (115 °C, 30 min) was performed. The preparation of the organic semiconductor blend was performed in a glovebox under N₂ atmosphere: 20 mg of P3HT (M1011, Ossila) and 20 mg of PCBM (M111, Ossila) were dissolved in 1 mL of anhydrous chlorobenzene each and let stirring overnight at 70 °C. The solutions were

then filtered (0.45 μm PTFE filters) and blended (1:1 v:v). The P3HT:PCBM blend was then spin-coated at 1000 rpm for 45 s (80 nm) and annealed at 115 $^{\circ}\text{C}$ for 30 min still under N_2 atmosphere (**Figure 4.11-2**). Ti (100 nm) and TiN (100 nm) were deposited by DC (400 W) and RF (200 W) magnetron sputtering respectively (**Figure 4.11-3**). Photolithography with 8 μm photoresist was performed to pattern the pixels (**Figure 4.11-4**). Then, Ti and TiN dry etching were obtained with a gas mixture of 20 sccm Cl_2 , 30 sccm Ar, and 15 sccm He (Corial 210 IL etcher, RF power 50 W, ICP power 800 W, pressure 10 mTorr) (**Figure 4.11-5**); subsequently, in the same etcher, O_2 plasma was applied to etch P3HT:PCBM, PEDOT:PSS, parylene-C, and the residual photoresist (Corial 210 IL etcher, RF power 150 W, ICP power 500 W, 50 sccm O_2 and 17 sccm He, 5 mTorr) (**Figure 4.11-6**). An endpoint detection system was used to determine the duration of the etch and stop it as soon as the layers were removed. For the encapsulation, OSTEmer (324 flex, Mercene labs) was prepared by mixing the two components as instructed (1.24:1), spin-coated at 1500 rpm for 60 s (12 μm from PDMS surface) onto the O_2 -plasma treated (30 W, 30 s) array, and exposed to UV laser (375 nm, 800 mJ/cm^2) with a maskless aligner (MLA 150, Heidelberg). After 3 minutes baking at 75 $^{\circ}\text{C}$, the OSTE layer was developed in ethyl L-lactate (77367, Sigma-Aldrich) for 3.5 minutes, rinsed in IPA and DI water, and finally dried with a N_2 gun (**Figure 4.11-7**). For encapsulation with black OSTE, OSTEmer (324 flex, Mercene labs) pre-polymer was mixed with 2 wt% of carbon black nanoparticles (Nanografi Nanotechnology, 148 nm) with help of vortex and 3-roll mixer prior spin-coating at 2500 rpm for 60 s. The other difference compared to normal OSTE encapsulation was the dose of UV exposure, i.e. 1400 mJ/cm^2 .

The wafers were then placed in deionized water to allow dissolution of the PSS sacrificial layer and the release of the PDMS-photovoltaic interfaces (**Figure 4.11-8**). The floating membranes were finally collected and dried in air. The dome-shaped PDMS supports were fabricated using a milled PMMA mold, filled with PDMS pre-polymer (5:1), which was then degassed and cured in oven (80 $^{\circ}\text{C}$, 2 h). The supports, released from the molding parts, and the PDMS-photovoltaic interface, clamped between two O-rings, were exposed to oxygen plasma (Diener ZEPTO, 15 W, 30 s) and put in contact with a drop of uncured PDMS to allow uniform bond thanks to radial stretching of the fixed membrane (**Appendix Figure 6**). The parts in contact were placed under load (1 kg) in an oven at 80 $^{\circ}\text{C}$ for at least 2 h (where OSTEmer underwent thermal curing as well), released after cooling, and the excessive PDMS used to clamp the array was removed by laser cutting. The last step consists of perforating the prosthesis with a hole-puncher (500 μm in diameter) at the locations dedicated to the insertion of retinal tacks. **Appendix Table 1** contains the details about the materials, machines, and parameters used for the fabrication.

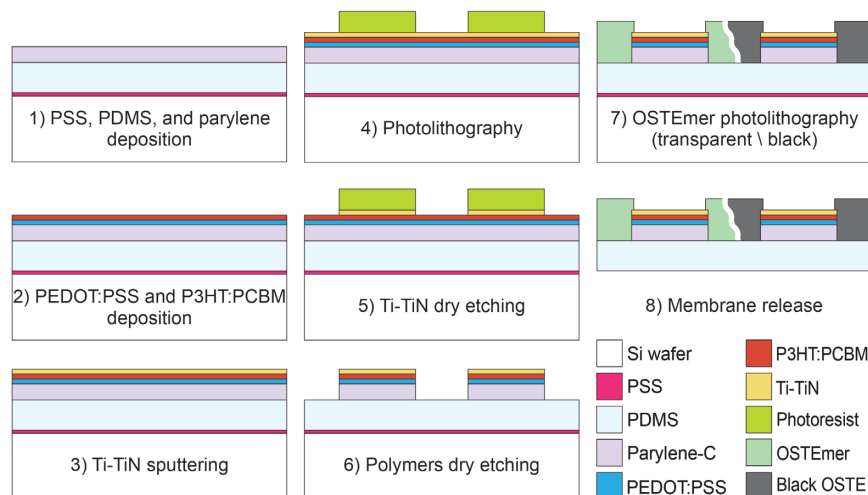


Figure 4.11 Microfabrication process flow of the second-generation POLYRETINA photovoltaic interface. The material stack is represented for two pixels in cross-sectional view and not in scale.

4.4.2 AFM and roughness measurements

AFM images and roughness measurements were obtained with a Bruker Dimension icon microscope and scanasyst-air Si tips. Images (500 nm x 500 nm) were plotted and the root mean square roughness was calculated with NanoScope analysis 1.9 software.

4.4.3 Ti and TiN electrochemical characterization

Electrochemical impedance spectroscopy (EIS) was performed as described in 2.4.3, as well as the extraction of circuit components. Cyclic voltammetry was performed with the same setup and three-electrodes configuration as for EIS. The applied voltage was scanned between -0.6 and 0.8 V at a rate of 50 mV/s, and the current was measured and averaged for each electrode (six cycles, the first cycle was discarded). The cathodic phase area (shaded area in **Figure 4.2D**) was measured to determine the charges generated per cycle (area/scan rate) and the normalized cathodic charge storage capacity (CSC, charges/electrode surface area).

4.4.4 Transmittance measurements

Light transmittance of normal and black POLYRETINA has been evaluated by using a green LED (565 nm, 0.54 mW/mm²). Transmitted light has been measured with a power meter (PD300-R Juno, Ophir Optronics Solutions Ltd.). The retinal prostheses have been inserted in the light path (of 5 mm diameter) and the power has been compared with respect of the condition without the prostheses using the Ophir Starlab software.

4.4.5 Mechanical characterizations

The mechanical properties of the OSTEm and black OSTEm were determined with an MTS[®] tensile testing machine (MTS Systems Corporation). The dog-bone shaped specimens (ASTMD-415-D, OSTEm 69 μm thick and black OSTEm 58 μm thick) were mounted in the grips of the MTS system and the crosshead speed was set at 1% of the length between the grips (in mm/s). The displacement and the corresponding force during the test were recorded automatically using MTS TestSuite™ TW Software. The Young's modulus was then calculated as the slope of the curve between 0.2 and 0.35

strain using Matlab Software, while the elongation at break was defined as the strain with the highest stress value before fracture.

4.4.6 Sterilization procedures

The retinal prostheses were sterilized as following: a quick ethanol (70%) dip followed by drying in oven at 80 °C for 1 h, O₂ plasma (Diener ZEPTO) for 60 s at 15 W and 0.5 mbar, and again in oven at 80 °C for 4 h. Retinal tacks, tack holders, and tweezers were dipped in ethanol (70%) and placed in oven at 80 °C for 4 h. POLYRETINA injectors were sterilized in ozone, as they are sensitive to increase in temperature and solvents.

4.4.7 Animals and anesthesia

Animal experiments were approved by the Département de l'emploi, des affaires sociales et de la santé (DEAS) and the Direction générale de la santé of the République et Canton de Genève (Switzerland, authorization GE14118). Female Göttingen minipigs (Ellegaard), weighting between 18 and 25 kg, were used for the experiments. On the day of the scheduled surgical procedures, animals received a prophylactic antibiotic by intramuscular administration of enrofloxacin (Batriol 10%, 2.5 mg/kg). The antibiotic administration was repeated the two following days, once per day. The minipigs were then premedicated with a mixture of azaperone (0.4 mg/kg), midazolam (0.75 mg/kg), and atropine (40 µg/kg), administered via deep intramuscular injection. Approximately 30 minutes after premedication, anesthesia was induced by inhalation of sevoflurane up to 6% and an intravenous line was inserted in the ear vein. To facilitate tracheal intubation, atracurium (0.5 mg/kg) was administered intravenously. After intubation, the sevoflurane was stopped and the anesthesia was maintained with continuous intravenous administration of propofol (8-10 mg/(kg h)) and ketamine (2 mg/(kg h)), while analgesia was assured via intravenous injection of Fentanyl (2 µg/kg, 5-6 m/h). The minipigs were constantly ventilated using 30% oxygen fraction, with a tidal volume of 7 ml/kg, and a respiratory rate of 15 per minute. The animals were placed on a heating pad to prevent them from hypothermia and continuous monitoring of heart rate, ECG, temperature, blood pressure, end-tidal saturation, and oxygen saturation was performed using a real-time anesthesia monitoring system (Datex, Engstrom).

After the procedure, the anesthesia perfusion was interrupted, and the oxygen fraction increased to 100%. The ventilator was set on pressure support to monitor the initiation of spontaneous ventilation. Upon giving signs of spontaneous ventilation, the minipigs were extubated and the respiration was assisted with a mask until signs of awakening were detected. The animals were then returned to their habitat and monitored until complete recovery. Analgesia was provided every 48 hours by patches of buprenorphine (Transtec®, 35 µg/h), applied on the interscapular area.

4.4.8 IAA injection

Iodoacetic Acid (IAA, Sigma-Aldrich) was dissolved in saline solution and injected at the concentration of 12.5 mg/kg intravenously. The injection was performed with a perfusion pump, maintaining a constant flux for 15 minutes. The IAA solution was prepared the same day of the procedure and kept on ice until the moment of injection. A perfusion of 5 minutes with 3 ml of saline solution followed to wash the tubing. All the injections were performed at the end of the first day of recordings.

4.4.9 Spectral domain-OCT

Cross-sectional images of the retina were obtained using spectral domain optical coherence tomography (OCT). The images were acquired with an ophthalmic imaging system (Leica Bioptigen Envisu™ R2210 VHR SDOIS) with a central wavelength of 840 nm, an optical power $\leq 750 \mu\text{W}$, and an axial length of 1.6492 mm in tissues. The covered area measured 12 x 12 mm. Each scan image consisted of 100 to 1'000 scans at a scanning rate of 32'000 scans/s. Raw OCT images were exported as TIFF files and imported in ImageJ for processing. The whole retinal thickness was measured from the edge of the RPE layer (defined as the end of the first hyperreflective band) to the edge of the ganglion cell's fiber layer (defined as the edge of the most inner hyperreflective layer).

4.4.10 Immunohistochemistry

At the end of the last recording session and while still under anesthesia, the animals were euthanized by intravenous injection of pentobarbital (Eskonarkon® 300 mg, 90 mg/kg) and the eyes were enucleated from the orbital cavity and placed in PFA for 1-4 h. They were cryoprotected in sucrose 15% for 6 h and then in sucrose 30% overnight. The eyecups were embedded in optimal cutting temperature compound (Tissue-Tek®), frozen, and stored at $-80 \text{ }^\circ\text{C}$. 30 μm thick sections of the retina were obtained using a Leica cryostat (CM3050S) and placed on microscope slides. The sections were washed in PBS, permeabilized with PBS + Triton 0.1% (Sigma-Aldrich), blocked with blocking buffer (PBS-T + 5% Normal Goat Serum), and incubated with primary antibodies (AB5417 Mouse Anti-rhodopsin 1:500 and AB5405 Rabbit Anti-L/Mopsin 1:300, Abcam) overnight at $4 \text{ }^\circ\text{C}$. The following day, they were incubated with secondary antibodies for 2 h (Goat Anti Mouse AlexaFluor 488 and Goat Anti Rabbit AlexaFluor 488, 1:500, Thermofisher) and counterstained with DAPI 1:300 (Sigma-Aldrich). Finally, they were mounted with Fluoromount (Sigma-Aldrich) and imaged using a confocal microscope (LSM880, Zeiss).

4.4.11 Hematoxylin and Eosin staining

The animals were euthanized as described above. The eye was enucleated and placed in formalin 10% overnight. The eyes were dehydrated in increasing concentrations of ethanol, followed by xylene, and finally embedded in paraffin. They were cut with a microtome (HM355S, ThermoScientific). Hematoxylin and Eosin staining was performed on the sections (ST5020, Leica). Images were acquired using a slide scanner microscope (Olympus VS120).

4.4.12 Electrode implantation and electrophysiological recordings

The pupils of the minipig were dilated with atropine 0.5% (Théa Pharma), applied directly on the eye 30 minutes prior starting the experiments. Light adaptation was performed exposing the eye to a continuous light at the intensity of 20 cd s m^{-2} for 10 minutes. Electroretinography (ERGs) responses were recorded with lens electrodes (ERG-Jet™, Fabrinal), using conductive gel to make them adhere better to the eye. The ERG responses were normalized by the activity of the not-stimulated eye, which was kept covered during the entire procedure. To record the visually evoked potentials (VEPs), the skin was opened to expose the skull, and k-wires (1.6 mm x 150 mm, Medeco-CH) were implanted on top of the visual cortex (identified in reference to lambda), while one k-wire was implanted in the caudal part of the skull to serve as reference. The electrodes were connected to the headstage using alligator clips. The recordings were acquired simultaneously in two channels

connected respectively to the lens electrode on the stimulated eye (ERG) and to the k-wire on the contralateral visual cortex (VEP). White light flashes (4 ms) were delivered using a mini Ganzfeld stimulator (BM6007IL, Biomedica Mangoni) positioned at 1-2 cm from the eye and the recorded signals were amplified, filtered (0.1 – 500 Hz), and digitalized (BM623, Biomedica Mangoni). Green light flashes (10 ms, 0.1 Hz) were delivered using a LED light (565 nm, Thor Labs) positioned at 20 cm from the eye and controlled with the Pulse Pal pulse train generator (Sanworks). The responses to white and green light were recorded for 500 ms (50 ms pre-stimulus and 450 ms post-stimulus) at 8 kHz using the WinAver program (Biomedica Mangoni). Photopic responses to 30 cd s m⁻² (0.1 Hz) were recorded after light adaptation. The data was extracted as text files and analyzed using custom script in MATLAB (MathWorks).

4.4.13 Surgical procedure and POLYRETINA implantation

At the beginning of the surgery, the minipigs were set in lateral decubitus with the head slightly tilted in order to expose the eye to be implanted on a flat plane. The skin surrounding the orbit was disinfected by applying a solution of Povidone Iodine 5% (Betadine) and let to act for 5 minutes before being wiped off using sterile gauzes. Sterile fields were then laid leaving only the orbit visible. Eyelid retractors and drops for pupil enlargement (atropine 0.5%) were applied and a small incision of 1 - 2 mm was performed on the lateral/dorsal canthus so as to enlarge the access to the sclera. The surgery was performed under a Leica microscope with OCULUS BIOM® 5 lens allowing visibility of both the anterior/posterior chamber and as well the retina. An incision was performed on the limbus and a hydrostatic pressure regulated irrigation tube (Associate® 2500 Compact System from Dutch Ophthalmic, USA) was set in place to maintain ocular pressure throughout the surgery. Two other incisions were performed allowing the insertion of two cannulas (Calburn 23G Cannulas 1-step, self-sealing) enabling easy access to 23G instruments in the orbit. To allow intra-ocular manipulations and insertion of the prosthesis, a phacoemulsification of the lens was performed and was followed by a vitrectomy (Associate® 2500 Compact System from Dutch Ophthalmic, USA). To ensure that the prosthesis would be in close contact with the retina, Triamcinolone was used to stain and visualize membranes and remaining vitreous ensuring its complete removal. A crescent knife was used to perform a corneal tunnel incision at the limbus, which was further enlarged by slit knives up to 6.4 mm. The custom POLYRETINA injector containing the pre-rolled prosthesis (as described in 4.2.4) was inserted into the incision and its piston pushed completely. Once passed the cannula, the flexible wings naturally opened allowing the prosthesis to unroll and to be released in the posterior chamber. Immediately after the insertion, the injector was removed and the incision sutured, ensuring a tight seal and a well-controlled ocular pressure. Two custom made stainless steel retinal tacks (LOVIS décolletage, Perrefitte CH) were then inserted through the prosthesis and sclera to keep the device in place. Following the successful delivery and implantation of the prosthesis, all incisions were sutured. Antibiotic drops of Tobradex were applied and the eyelid retractors removed.

4.4.14 Statistical analysis and graphical representation

For the electrophysiological data, data analysis and graphical representation were performed with Matlab and Python. The data of the recordings were extracted as text files and analyzed using a custom script in Matlab to calculate the amplitude of the a- and b-wave for the ERG responses and of the negative wave for the VEP responses. The histological and OCT data were analyzed using

ImageJ. Statistical analysis and graphical representation were performed with Prism (GraphPad Software Inc.). The normality test (D'Agostino & Pearson omnibus normality test) was performed in each dataset to justify the use of a parametric or non-parametric test. In each figure p-values were represented as: * $p < 0.05$, ** $p < 0.01$, *** $p < 0.001$, and **** $p < 0.0001$.

4.5 Acknowledgments

We would like to acknowledge the EPFL Center of Micronanotechnology and The Neural Microsystems Platform at Wyss Center for their support. Walid Habre, Sylvie Roulet, and Jean-Pierre Giliberto from the University of Geneva for their help with mining experiments. We also thank Prof. Thomas J. Wolfensberger, from Hospital Ophthalmic Jules-Gonin - Fondation Asile Des Aveugles in Lausanne, for the surgeries and fruitful discussions. This work was supported by École polytechnique fédérale de Lausanne, Medtronic, European Commission (Project 701632), Fondation Mercier pour la science, Velux Stiftung (Project 1102), Gebert Rűf Stiftung (Project GRS-035/17), and Fondation Pro Visu.

Chapter 5 Toward a NIR-responsive POLYRETINA



Eyes of a Tokay gecko (Source: Warren photography)

This chapter has been adapted from: MJI Airaghi Leccardi *et al*, *Communications Materials*, 2020, 1:21.¹⁹⁸

Contributions: I designed, fabricated, and characterized the devices and the retinal prostheses; performed/analyzed photovoltage and photocurrent measures, thickness and resistance measures, soaking tests, thermal simulations, and analysis of ToF-SIMS data and morphological assumptions. N.A.L. Chenais performed ex-vivo electrophysiology. L. Ferlauto performed the absorbance measurements. M. Kawecki performed ToF-SIMS measurements. E.G. Zollinger performed in-vitro cytotoxicity.

5.1 Introduction

Organic technology has proven to be an efficient tool in bioelectronic interfaces and neuroprostheses for neuronal activity modulation by converting light pulses into electrical or thermal stimulation.^{121,161,199–208} In the previous chapters, we demonstrated the potential of POLYRETINA photovoltaic pixels based on the P3HT:PCBM bulk heterojunction (BHJ) to activate retinal ganglion cells *in vitro*, *ex vivo*, and *in vivo* with short pulses of light. Flexibility, lightweight, and biocompatibility are among the main advantages of using organic technology in bioelectronic interfaces. Nevertheless, compared to their inorganic counterparts (e.g. silicon), some challenges about functional organic materials remain open. First, water-induced swelling, degradation, and delamination are among the most critical aspects of organic interfaces implanted into the body. Second, in the case of photovoltaic interfaces, the electrical properties of the photovoltaic cell must be tailored to meet the desired conditions of electrical stimulation. Last, organic semiconductors used in photovoltaic bioelectronic interfaces typically have low photoconversion efficiency, and high sensitivity only in the visible spectrum. However, in a general manner, the use of near-infrared (NIR) light would be preferable in bioelectronic interfaces: for example, because of its higher penetration into the tissue.

The proposed retinal prosthesis POLYRETINA activates retinal cells with pulses of green light; thus, this BHJ system might not be the optimal choice for photovoltaic retinal stimulation, because of its absorption spectrum limited to the visible range. In humans and primates, color vision is based on three types of opsins associated to three different cones: the short (S-), the medium (M-), and the long (L-) wavelength sensitive cones having distinct but overlapping absorption spectra (**Figure 5.1A**).²⁰⁹ The L-cone has the most red-shifted spectral absorbance with a maximum around 564 nm (**Figure 5.1A**, circles). The absorbance spectra of the P3HT:PCBM BHJ and the retinal photoreceptors largely overlap; thus, the green light used to excite this BHJ may not be optimal due to the possible activation of remaining cones and rods in patients with residual natural vision, such as in age-related macular degeneration. Moreover, the irradiance levels typically required to stimulate retinal neurons with photovoltaic prostheses (hundreds of $\mu\text{W}/\text{mm}$) may still be perceived (when visible light is used) even in blind patients without residual vision. NIR illumination activates photovoltaic retinal prostheses without necessarily interfering with the residual natural vision. Also, according to the standard for optical safety, the maximum permissible exposure (MPE) for ophthalmic applications increases in the NIR spectrum.¹²⁰

Therefore, in parallel with the development and validation of a “green-sensitive” POLYRETINA (as model for a photovoltaic, foldable, and wide-field epiretinal prosthesis with a well-established BHJ system), we investigated the possibility to obtain photovoltaic stimulation with NIR-sensitive materials. In this chapter, we demonstrate that implantable stimulating devices based on conjugated polymers can operate in the NIR spectrum (i.e. wavelength longer than 700 nm). We also document the relevance of the electrical and adhesive properties of the conjugated polymers in the fabrication of a photovoltaic implant with optimized photovoltaic characteristics to achieve an efficient neural stimulation. As proof-of-principle, we designed an organic photovoltaic interface based on the poly[2,6-(4,4-bis-(2-ethylhexyl)-4H-cyclopenta [2,1-b;3,4-b']dithiophene)-alt-4,7(2,1,3-benzothiadiazole)] blended with PCBM (PCPDTBT:PCBM) BHJ (see **Appendix Figure 7** for details about the materials).^{201,210} We also show that this BHJ can generate electrical responses at safe irradiance levels suitable for retinal stimulation. Furthermore, we investigate the impact of a cross-linking molecule on adhesive properties and morphology of the organic interface. Last, we also verify that this

BHJ is not cytotoxic. These results enable the development of a NIR-sensitive foldable and photovoltaic wide-field epiretinal prosthesis, here called nir-POLYRETINA.

5.2 Results

5.2.1 Optimization of the bulk heterojunction

To evaluate the performance of the BHJs in the NIR spectrum, we fabricated chips embedding six photovoltaic pixels, each composed of three layers: an anode made of PEDOT:PSS (HTL Solar, here “HTL”), the BHJ (P3HT:PCBM or PCPDTBT:PCBM), and a cathode made of titanium (Ti). The cathode of each photovoltaic pixel was contacted to measure its output signal referenced to a platinum counter electrode immersed in saline solution (**Figure 5.1B**). We measured the responses of photovoltaic pixels based on both BHJs upon 10-ms light pulses at two NIR wavelengths (730 nm and 780 nm, where the response of cones should be minimal) and compared them to the ones obtained upon green light illumination (565 nm). In all the experiments, for each chip, the responses from the six electrodes were measured, and the peak amplitudes were quantified and averaged.

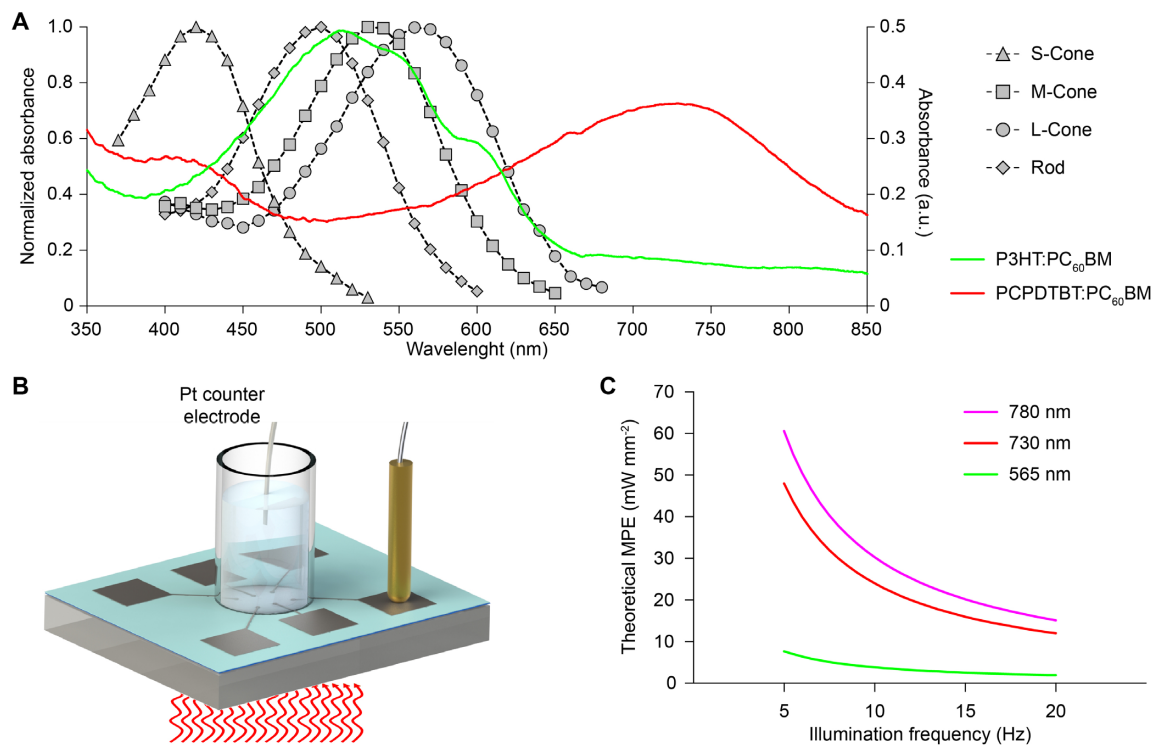


Figure 5.1 Relevance of NIR illumination for organic photovoltaic retinal prostheses. **A**) Normalized absorbance spectra of S-cones, M-cones, L-cones and rods on the left axis (redrawn from Bowmaker *et al.*²⁰⁹). Absorbance spectra of the P3HT:PCBM and the PCPDTBT:PCBM BHJs on the right axis. **B**) Sketch of the PC and PV recording setup. **C**) Theoretical MPEs for 10-ms pulses as a function of the illumination pulse rate.

As expected, the P3HT:PCBM BHJ showed the strongest photo-current density (PCD) at 565 nm (**Figure 5.2A**, white circles). However, to evaluate the responsivity at the three wavelengths, we should take into account the theoretical MPE for each wavelength, which is dependent on the pulse duration, the illumination rate, and the angle of illumination (fixed to 46.3°, according to the design of the POLYRETINA device). For chronic illumination, the MPEs are 384.75 $\mu\text{W}/\text{mm}^2$, 2.40 mW/mm^2 , and 3.03 mW/mm^2 respectively for 565, 730, and 780 nm. In case of 10-ms pulsed illumination (**Figure 5.1C**), the theoretical MPE is increased by a factor of 5 for 20 Hz repetition rate

(1.92, 12.00, and 15.15 mW/mm² respectively for 565, 730, and 780 nm), by a factor of 10 for 10 Hz repetition rate (3.85, 24.00, and 30.30 mW/mm² respectively for 565, 730, and 780 nm), and by a factor of 20 for 5 Hz repetition rate (7.70, 48.00, and 60.60 mW/mm² respectively for 565, 730, and 780 nm). Therefore, we set the irradiance levels to the following normalized values: 1, 6, and 7.5 mW/mm² respectively for 565, 730, and 780 nm. These normalized irradiance levels correspond to approximately 50% of the theoretical MPEs at 20 Hz, 25% at 10 Hz, and 12.5% at 5 Hz.

For the P3HT:PCBM BHJ, the mean PCD obtained at 565 nm with pulses of 1 mW/mm² (white circles, green line) is 1.85 times higher than the mean PCD obtained at 730 nm (black circles, red line) with pulses of 6 mW/mm² (**Figure 5.2A**). At 780 nm (black/white circles) the maximal irradiance obtained from the LED was 5.35 mW/mm², which is lower than the normalized irradiance (7.5 mW/mm²). Therefore, the theoretical PCD value was computed using the interpolating curve ($R^2 = 0.74$). In both cases (730 and 780 nm), the PCD obtained at the normalized irradiance levels is largely lower than the one obtained with a green light (565 nm). The photo-voltage (PV) had a similar behavior (**Figure 5.2B**). The theoretical PV at 780 nm and 7.5 mW/mm² (black/white circles, magenta line) was computed using the interpolating curve ($R^2 = 0.91$). Based on these results, we decided to investigate a different BHJ based on the PCPDTBT:PCBM blend, which might be more efficient for a NIR-responsive retinal prosthesis.

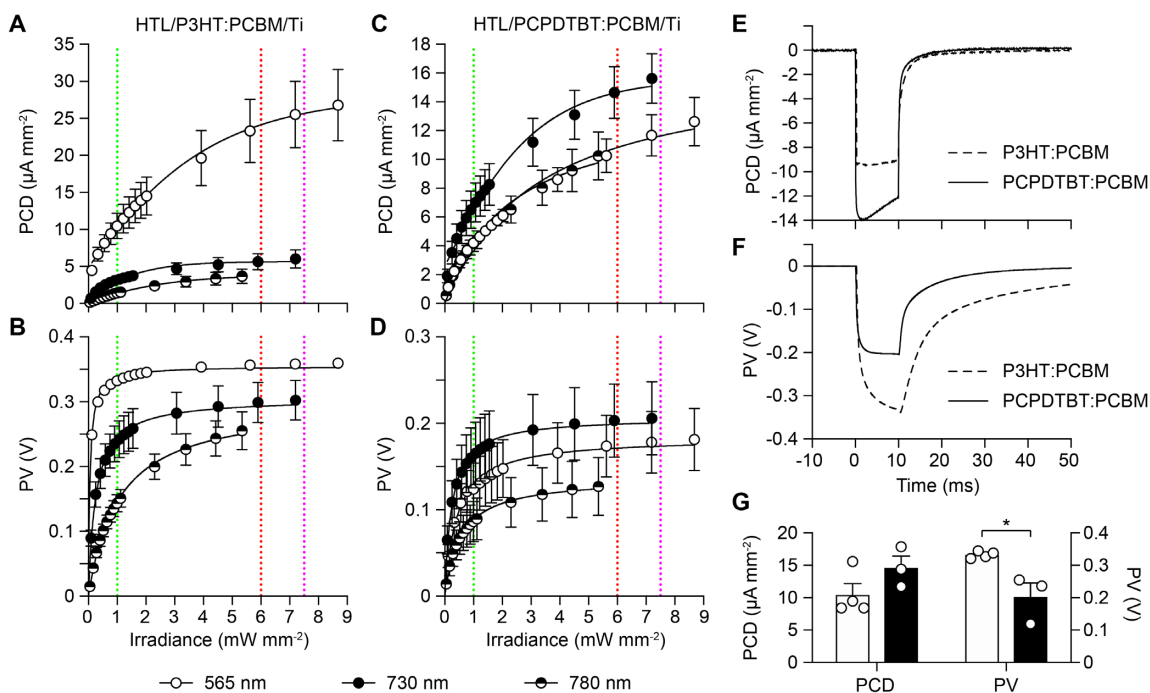


Figure 5.2 Optimization of the bulk heterojunction. **A), B)** Mean (\pm s.e.m., $n = 4$ chips) PCD (A) and PV (B) with HTL/P3HT:PCBM/Ti. **C), D)** Mean (\pm s.e.m., $n = 3$ chips) PCD (C) and PV (D) with HTL/PCPDTBT:PCBM/Ti. In panels A-D, the vertical dotted lines represent the normalized irradiance levels respectively for 565 nm (green, 1 mW/mm²), 730 nm (red, 6 mW/mm²), and 780 nm (magenta, 7.5 mW/mm²). The solid lines are the interpolations with an asymmetrical, five-parameter, logistic dose-response function for PCDs and a hyperbola function for PVs. **E), F)** Grand-average PCD (E) and PV (F) traces with HTL/P3HT:PCBM/Ti (dashed line, 565 nm, $n = 4$ chips) and HTL/PCPDTBT:PCBM/Ti (solid line, 730 nm, $n = 3$ chips) BHJs respectively at their normalized irradiance levels. **G)** Mean (\pm s.e.m.) PCD and PV obtained with HTL/P3HT:PCBM/Ti (white bars, 565 nm, $n = 4$ chips) and HTL/PCPDTBT:PCBM/Ti (black bars, 730 nm, $n = 3$ chips) respectively at their normalized irradiance levels.

In this case, the wavelength with the highest PCD (**Figure 5.2C**) and PV (**Figure 5.2D**) is 730 nm (black circles). Moreover, if compared at the normalized irradiance levels, the PCD obtained at 730 nm with HTL/PCPDTBT:PCBM/Ti is 1.4 times higher than the PCD obtained at 565 nm with HTL/P3HT:PCBM/Ti (**Figure 5.2E** and G; two-tailed t-test, $p = 0.1571$). On the other hand, the PV is slightly lower (**Figure 5.2F** and G; two-tailed t-test, $p = 0.0158$). These results suggest that the PCPDTBT:PCBM BHJ (at 730 nm) should be as efficient as the P3HT:PCBM blend (at 565 nm) previously used in the POLYRETINA device, considering irradiance levels adjusted to their respective theoretical MPEs. Also, the photovoltaic electrodes based on the PCPDTBT:PCBM BHJ are fully discharged in less than 40 ms from the pulse offset (**Figure 5.2F**), allowing a stimulation pulse rate up to 20 Hz.

5.2.2 Optoelectronic optimization of the anodic layer

Photovoltaic organic retinal prostheses typically rely on a bottom anode made of PEDOT:PSS.^{98,110–112,122} We therefore investigated the optoelectronic effect of its conductivity by using two formulations from Clevios Heraeus: HTL Solar (“HTL”, 0.47 S/mm, average of five measures from one sample; film thickness of 60 nm) and PH1000 (“PH1000”, 1.17 S/mm, average of five measures from one sample; film thickness of 90 nm). At 730 nm, the mean PCD obtained with the PH1000/PCPDTBT:PCBM/Ti pixel (grey squares) is considerably higher than the HTL/PCPDTBT:PCBM/Ti pixel (black circles), while the mean PV increases with a lower rate but it reaches the same value at the normalized irradiance for 730 nm (**Figure 5.3A-C**). To summarize our findings (**Figure 5.3D** and E), the PV and PCD values obtained with the three configurations presented were compared at their best operational wavelengths (565 nm for P3HT and 730 nm for PCPDTBT) and at the normalized irradiance levels (1 mW/mm² for 565 nm and 6 mW/mm² for 730 nm). The PH1000/PCPDTBT:PCBM/Ti pixels (grey squares) showed the highest PCD (one-way ANOVA, $p = 0.0018$, $F = 15.48$; Tuckey’s multiple comparisons test: HTL/P3HT:PCBM/Ti vs HTL/PCPDTBT:PCBM/Ti $p = 0.9235$, HTL/P3HT:PCBM/Ti vs PH1000/PCPDTBT:PCBM/Ti $p = 0.0024$, HTL/PCPDTBT:PCBM/Ti vs PH1000/PCPDTBT:PCBM/Ti $p = 0.0062$). On the other hand, the HTL/P3HT:PCBM/Ti pixels (white circles) showed the highest PV (one-way ANOVA, $p = 0.0019$, $F = 15.21$; Tuckey’s multiple comparisons test: HTL/P3HT:PCBM/Ti vs HTL/PCPDTBT:PCBM/Ti $p = 0.0070$, HTL/P3HT:PCBM/Ti vs PH1000/PCPDTBT:PCBM/Ti $p = 0.0024$, HTL/PCPDTBT:PCBM/Ti vs PH1000/PCPDTBT:PCBM/Ti $p = 0.8937$). The HTL/PCPDTBT:PCBM/Ti pixels (black circles) showed the lowest PCD and PV. Interestingly, the different configurations also have different photovoltage discharge rates at the offset of the light pulse (**Figure 5.3F**). The PH1000/PCPDTBT:PCBM/Ti pixel showed the faster discharge rate, probably because of the higher electrical conductivity of PH1000 (bi-exponential decay; HTL/P3HT:PCBM/Ti: $\tau_{\text{fast}} = 4.59$ ms and $\tau_{\text{slow}} = 33.36$ ms, $R^2 = 0.93$; HTL/PCPDTBT:PCBM/Ti: $\tau_{\text{fast}} = 1.03$ ms and $\tau_{\text{slow}} = 11.31$ ms, $R^2 = 0.95$; PH1000/PCPDTBT:PCBM/Ti: $\tau_{\text{fast}} = 0.47$ ms and $\tau_{\text{slow}} = 3.58$ ms, $R^2 = 0.82$).

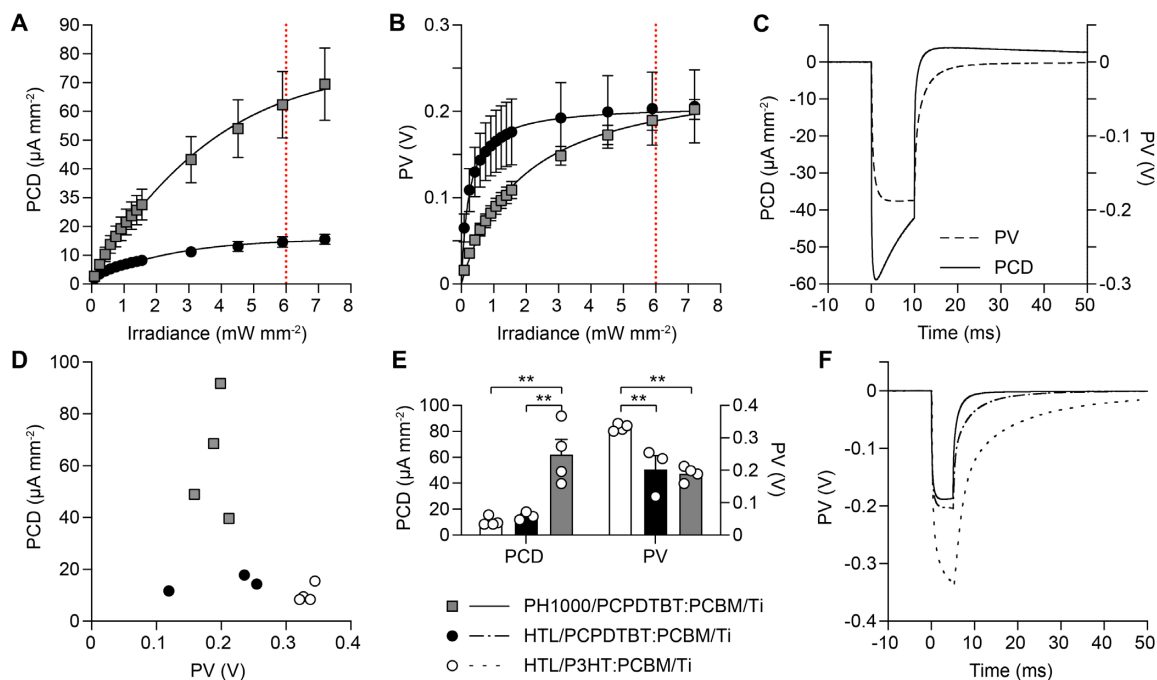


Figure 5.3 Optimization of the anodic layer. **A), B)** Mean (\pm s.e.m.) PCD (A) and PV (B) obtained at 730 nm for HTL/PCPDTBT:PCBM/Ti (black circles, $n = 3$ chips) and PH1000/PCPDTBT:PCBM/Ti (grey squares, $n = 4$ chips). The solid lines are the interpolations with an asymmetrical, five-parameter, logistic dose-response function for PCDs and a hyperbola function for PVs. The vertical red dotted lines represent the normalized irradiance for 730 nm ($6 \text{ mW}/\text{mm}^2$). **C)** Grand-average PCD (solid line) and PV (dashed line) traces obtained with PH1000/PCPDTBT:PCBM/Ti with 730 nm at the normalized irradiance ($n = 4$ chips). **D)** PV/PCD plot for HTL/P3HT:PCBM/Ti (white circles, $n = 4$ chips, 565 nm , $1 \text{ mW}/\text{mm}^2$), HTL/PCPDTBT:PCBM/Ti (black circles, $n = 3$ chips, 730 nm , $6 \text{ mW}/\text{mm}^2$), and PH1000/PCPDTBT:PCBM/Ti (grey squares, $n = 4$ chips, 730 nm , $6 \text{ mW}/\text{mm}^2$). **E)** Mean (\pm s.e.m.) PCD and PV obtained with HTL/P3HT:PCBM/Ti (white bars, $10.46 \pm 1.72 \text{ } \mu\text{A}/\text{mm}^2$, $332.5 \pm 5.35 \text{ mV}$, $n = 4$ chips, 565 nm , $1 \text{ mW}/\text{mm}^2$), HTL/PCPDTBT:PCBM/Ti (black bars, $14.65 \pm 1.79 \text{ } \mu\text{A}/\text{mm}^2$, $203.4 \pm 42.37 \text{ mV}$, $n = 3$ chips, 730 nm , $6 \text{ mW}/\text{mm}^2$), and PH1000/PCPDTBT:PCBM/Ti (grey bars, $62.28 \pm 11.54 \text{ } \mu\text{A}/\text{mm}^2$, $189.6 \pm 11.32 \text{ mV}$, $n = 4$ chips, 730 nm , $6 \text{ mW}/\text{mm}^2$) respectively at their normalized irradiance levels. **F)** Comparison of the PV grand-average traces for HTL/P3HT:PCBM/Ti (dotted line, $n = 4$ chips, 565 nm , $1 \text{ mW}/\text{mm}^2$), HTL/PCPDTBT:PCBM/Ti (dashed-dotted line, $n = 3$ chips, 730 nm , $6 \text{ mW}/\text{mm}^2$), and PH1000/PCPDTBT:PCBM/Ti (solid line, $n = 4$ chips, 730 nm , $6 \text{ mW}/\text{mm}^2$).

5.2.3 Optimization of the anodic layer adhesion

Strong adhesion between materials is a prerequisite for the long-term functioning of an implantable device. However, in organic-based prostheses, the adhesion of the PEDOT:PSS layer over a substrate in aqueous environment is limited by the delamination and solubility of PSS. A common strategy to obtain water-stable thin films of PEDOT:PSS is to add the (3-glycidyloxypropyl)trimethoxysilane (GOPS) crosslinker (typically 1 v/v%), which prevents both dissolution and delamination of PEDOT:PSS films.²¹¹ On the other hand, it was reported that the electrical conductivity of PEDOT:PSS films decreases as a function of the GOPS content.^{211,212} We found that the addition of 1 v/v% of GOPS to PH1000 reduces the PCD (**Figure 5.4A** and C) and increases the PV peak (**Figure 5.4B** and D) generated by the PH1000/PCPDTBT:PCBM/Ti pixels at 730 nm. Moreover, it causes a very slow photovoltage discharge (bi-exponential decay, $\tau_{\text{fast}} = 11.21 \text{ ms}$ and $\tau_{\text{slow}} = 72.52 \text{ ms}$, $R^2 = 0.96$). Indeed, such configuration does not allow a full discharge and recharge of the electrode voltage between each pulse during 20 Hz train stimulation (**Figure 5.4E**), in contrast to the case

when GOPS is not added (**Figure 5.4F**). This slower discharge rate is very likely caused by the reduction of the electrical conductivity due to the addition of 1 v/v% of GOPS (0.21 S/mm, average of five measures from one sample; film thickness of 170 nm).

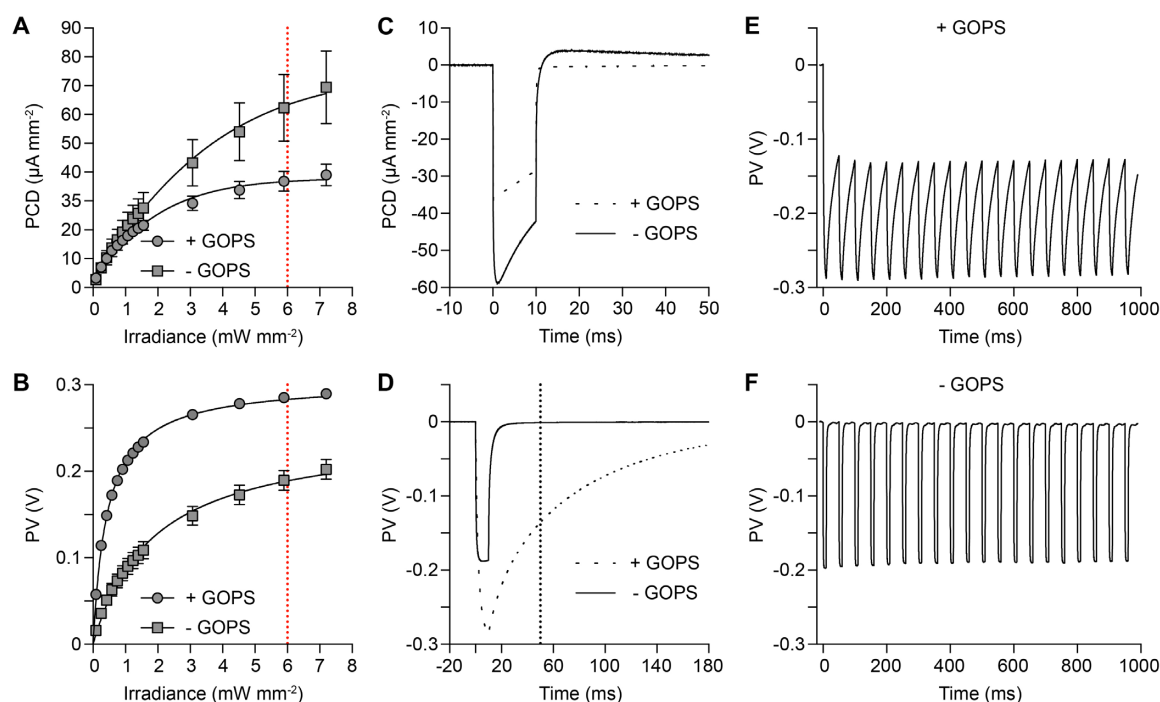


Figure 5.4 Optoelectronic responses with GOPS. **A), B)** Mean (\pm s.e.m.) PCD (**A**) and PV (**B**) obtained with pristine PH1000/PCPDTBT:PCBM/Ti (grey squares, $n = 4$) and PH1000/PCPDTBT:PCBM/Ti supplemented with 1 v/v% GOPS (grey circles, $n = 3$) at 730 nm. The solid lines are the interpolations with an asymmetrical, five-parameter, logistic dose-response function for PCDs and a hyperbola function for PVs. The vertical red dotted lines represent the normalized irradiance for 730 nm (6 mW/mm^2). **C), D)** Grand-average PCD (**C**) and PV (**D**) traces obtained upon 10-ms pulses (730 nm , 6 mW/mm^2) with pristine PH1000 (solid line, $n = 4$) and PH1000 with GOPS (dashed line, $n = 3$). The vertical dotted lines in panel D highlights the 50 ms time period for train stimulation at 20 Hz. **E), F)** Representative traces from single electrodes of PV upon the delivery of a train stimulation composed of 20 pulses (10 ms, 730 nm , 6 mW/mm^2) delivered at 20 Hz with pristine PH1000 (**F**) and PH1000 with 1 v/v% of GOPS (**E**).

Hence, we investigated which concentration of GOPS could simultaneously increase the adhesion of the PEDOT:PSS film (PH1000) while preserving the photovoltaic performance. We fabricated a set of samples with five concentration of GOPS (0, 0.1, 0.25, 0.5, and 1 v/v%) and measured the PCD and PV. The mean PV peak (730 nm , 6 mW/mm^2) increased immediately upon addition of GOPS, and it remained stable regardless of the concentration (**Figure 5.5A**). Conversely, the mean PCD peak remains high up to 0.1 v/v% of GOPS, and then it decreased. Therefore, one can designate a concentration of 0.1 v/v% as the best compromise, since higher concentration would induce a strong reduction of the PCD generated by the photovoltaic pixels. In parallel, the increase in the concentration of GOPS increases the decay time at the offset of the light pulse (**Figure 5.5B**). The fitting with a two-phase exponential decay function showed that both τ_{fast} and τ_{slow} increase with the GOPS concentration (**Figure 5.5C**). However, with 0.1 v/v% of GOPS, the electrode is fully discharged (i.e., the PV returns to equilibrium baseline) in 40 ms from the pulse offset (**Figure 5.5D**), allowing a stimulation pulse rate up to 20 Hz. In summary, the chemical modification of PEDOT:PSS with 0.1 v/v% of GOPS allowed the optimization of the photovoltaic performance for an efficient stimulation. Both the resistance (**Figure 5.5E**, white circles) and the thickness (**Figure**

5.5F) of the PEDOT:PSS thin film are affected by the GOPS concentration. Accordingly, the film conductivity (computed by normalizing the average film resistance by the average film thickness) decreases with the increase of the GOPS concentration (Figure 5.5E, black circles). This confirms that the conductivity of the PEDOT:PSS films plays a significant role in the optoelectronic properties of photovoltaic pixels.

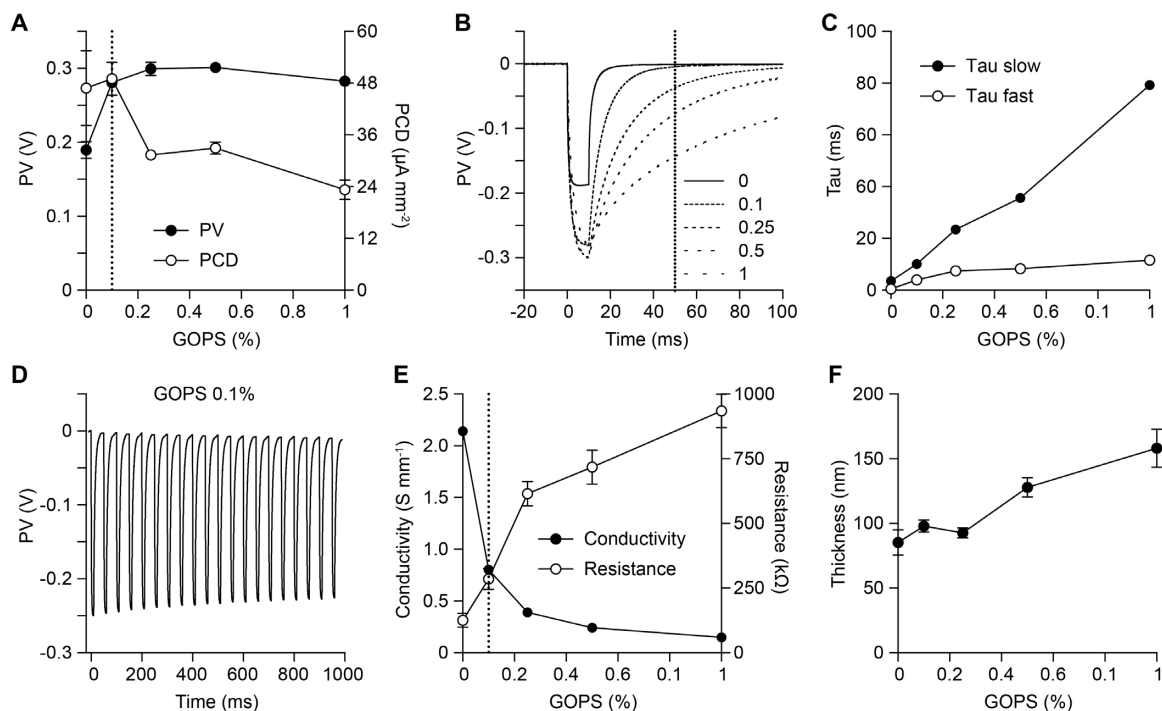


Figure 5.5 Electrical tuning with the GOPS concentration. **A)** Mean (\pm s.e.m.) PCD (right axis) and PV (left axis) obtained upon 10-ms pulses (730 nm, 6 mW/mm²) with PH1000/PCPDTBT:PCBM/Ti supplemented with various concentrations of GOPS (0, 0.1, 0.25, 0.5, 1 v/v%, $n = 4$ chips for each concentration). **B)** Grand-average ($n = 4$ chips for each concentration) PV traces obtained at the same conditions as in (A). **C)** Evolution of τ_{fast} and τ_{slow} as a function of the GOPS concentration. **D)** Representative traces from a single electrode of PV upon 20 pulses (10 ms, 730 nm, 6 mW/mm²) delivered at 20 Hz with PH1000 supplemented with 0.1 v/v% of GOPS. **E)** Mean (\pm s.d.; 12 measures from $n = 2$ samples for each condition) resistance (white circles, right axis) and average conductivity (black circles, left axis) of PH1000 films with various concentrations of GOPS. **F)** Mean (\pm s.d.; 12 measures from $n = 2$ samples for each condition) thickness of PEDOT:PSS (PH1000) films with various concentrations of GOPS. The vertical dotted lines in panels A and E highlight the 0.1 v/v% of GOPS concentration, while in panel B the 50 ms time period for train stimulation at 20 Hz.

To further investigate the role of GOPS in the adhesion of the PEDOT:PSS layer, we fabricated on PDMS photovoltaic retinal interfaces using the PCPDTBT:PCBM BHJ (nir-POLYRETINA). In this case, the photovoltaic interface was not encapsulated to expose the organic layers to direct contact with water and allow faster delamination (Figure 5.6A and B). Soaking experiments in saline solution revealed that the addition of 0.1 v/v% of GOPS (Figure 5.6C, middle) increases the adhesion of the photovoltaic pixels to the PDMS substrate compared to pristine PEDOT:PSS (Figure 5.6C, left). On the other hand, a higher concentration of GOPS (0.25 v/v%; Figure 5.6C, right) does not increase adhesion but induces delamination again. The addition of GOPS not only crosslinks the PSS molecules together, but it also anchors them to the substrate (e.g. PDMS). This explains the strengthened adhesion of PEDOT:PSS to PDMS. Nevertheless, a further increase in the GOPS concentration (e.g. from 0.1 to 0.25 v/v% and above) induced delamination again, but at the interface between PEDOT:PSS and PCPDTBT:PCBM rather than at the interface with PDMS.

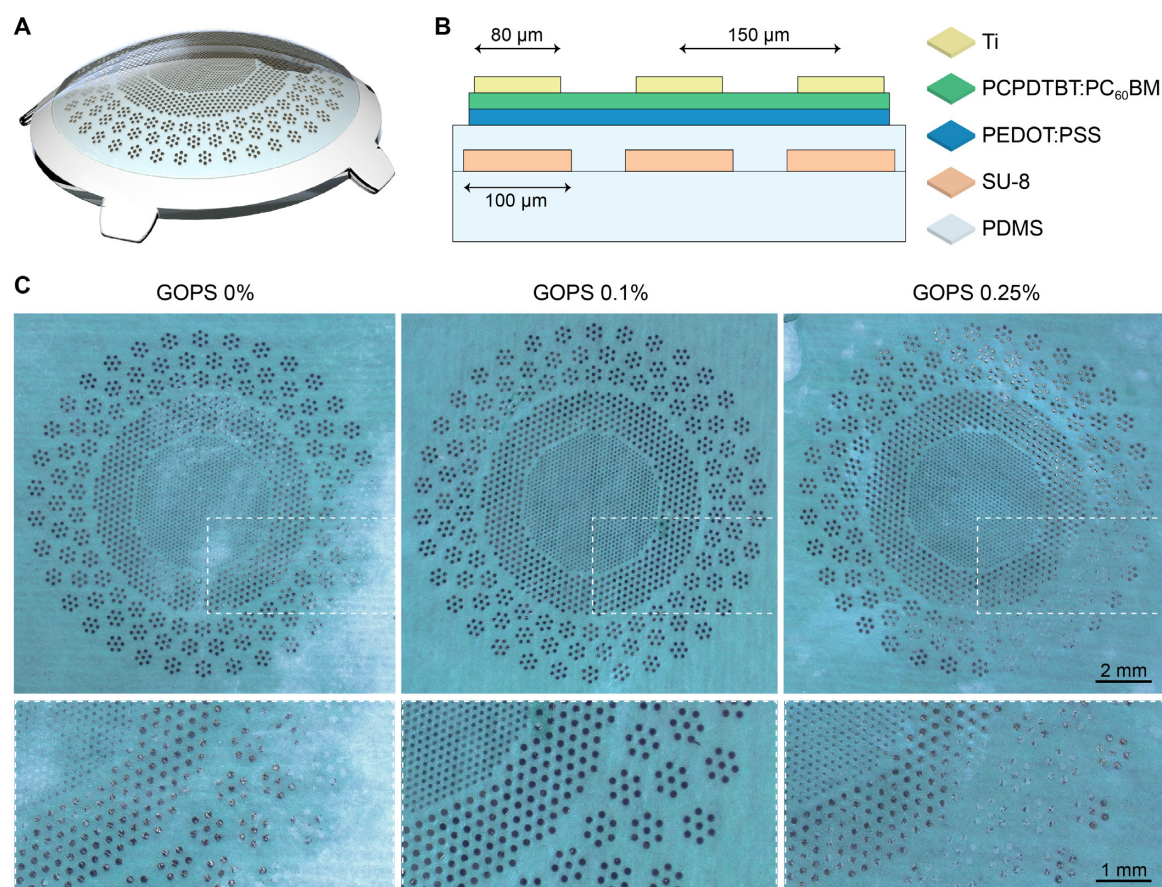


Figure 5.6 Adhesion of the interface. **A)** 3D model of the nir-POLYRETINA prosthesis. **B)** Cross-section of the nir-POLYRETINA active interface, including: PDMS (50 μm), a second layer of PDMS (14 μm) embedding SU-8 rigid platforms (6 μm), a layer of PEDOT:PSS with various percentages of GOPS, a layer of PCPDTBT:PCBM (100 nm), and titanium cathodes (150 nm). **C)** Pictures of nir-POLYRETINA devices prepared with 0, 0.1, and 0.25 v/v% of GOPS after soaking in saline solution (37 °C) and ultra-sonication for 5 min.

We hypothesize that the increase of the cross-linking degree with GOPS could impair the diffusion of the PCPDTBT molecules into PEDOT:PSS during the thermal treatment after deposition. This reduced interaction between the two polymeric layers would inevitably decrease the adhesion forces. To verify this hypothesis, we performed depth-profiling measurements with time-of-flight secondary ion mass spectrometry (ToF-SIMS) from the top surface of PCPDTBT:PCBM to the bottom side of PEDOT:PSS (i.e., to the substrate) at various concentration of GOPS (**Figure 5.7A**). The analysis of the negative polarity spectra indicates that with increasing GOPS concentration, PCBM molecules (red curve, C_{60}^- fragments) tend to accumulate at the interface towards PEDOT:PSS. Furthermore, the depth distribution of the CN^- fragments (green curve) suggests a penetration of PCPDTBT molecules into the PEDOT:PSS layer when GOPS is not added. Based on the depth profiles of the relevant fragments, we predicted the organization of the organic molecules and represented it for the two extreme GOPS concentrations: 0 and 1 v/v% (**Figure 5.7B**). In **Appendix Figure 8**, the hypothesized molecular interactions between the organic materials are represented, which are the possible reason for the observed molecules organization. In **Figure 5.7C**, the normalized intensities of the PCPDTBT signal (CN^- fragments) for the three different GOPS concentrations are plotted to efficiently compare their slopes, representing their distinct penetration depths into PEDOT:PSS. Moreover, the slope of the normalized intensities of the PEDOT signal (SC_2O^- fragments) also shows a diffuse interface (slow rise) for 0 v/v% and a sharper one (faster rise) for 1 v/v% (**Figure 5.7D**).

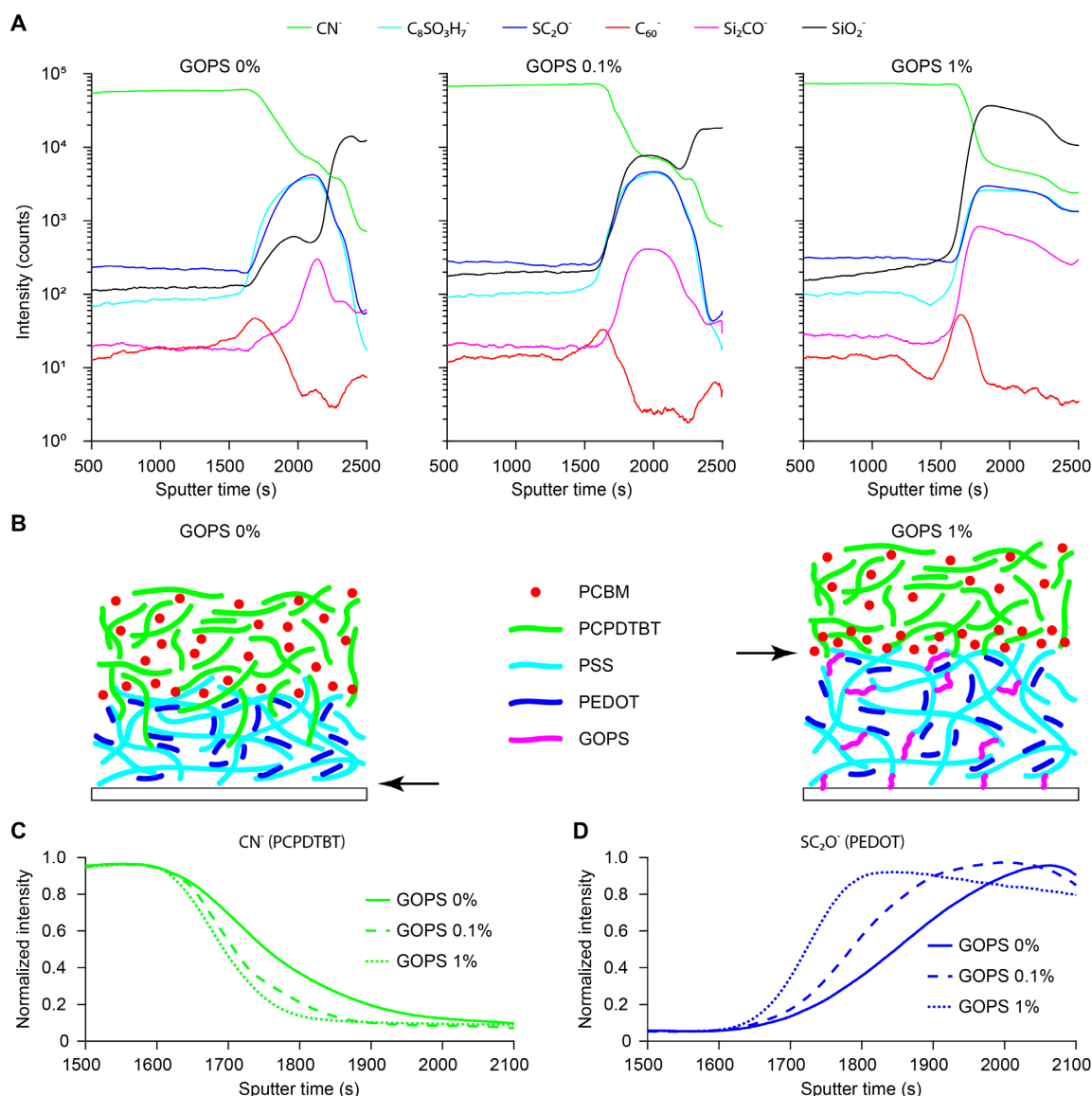


Figure 5.7 Redistribution of molecules as a function of the GOPS concentration. **A)** Smoothed ToF-SIMS depth profiles (negative polarity) conducted on the organic layers with 0, 0.1, and 1 v/v% of GOPS. CN^- , $\text{C}_8\text{SO}_3\text{H}_7^-$, SC_2O^- , C_{60}^- , Si_2CO^- , and SiO_2^- are used as proxies respectively for PCPDTBT, PSS, PEDOT, PC_{60}BM , GOPS, and both glass and GOPS. The interface between PCPDTBT:PCBM and PEDOT:PSS is roughly at 1700 s, while the one between PEDOT:PSS and the glass substrate is roughly at 2100 s, 2250 s, and 2400 s for pristine PEDOT:PSS, with 0.1 v/v% GOPS, and with 1 v/v% GOPS, respectively. **B)** Schematic representation of the deduced organization of the organic molecules for 0 v/v% (left) and 1 v/v% (right) of GOPS. The arrows indicate the observed delamination interface within the organic layers. **C), D)** Normalized intensities of the depth profiles for PCPDTBT (CN^-) (C) and PEDOT (SC_2O^-) (D) for the three GOPS concentrations.

Therefore, we assume that PCPDTBT molecules are more easily able to penetrate the PEDOT:PSS network if the latter is less cross-linked, allowing an adhesive interface against delamination. Conversely, if PEDOT:PSS is supplemented with GOPS, PCBM is placed at the interface with PEDOT:PSS, creating a brittle and more fragile interface where delamination can occur.²¹³ The presence of GOPS probably affects the parasitic resistances of the photovoltaic pixel as well, due to both PEDOT:PSS conductivity changes and the molecular reorganizations within the PCPDTBT:PCBM

layer. Hence, a concentration of 0.1 v/v% of GOPS is found optimal to enhance both the photovoltaic performance and the adhesion of the two interfaces.

5.2.4 Thermal management

The theoretical MPEs were computed based on safety standards¹²⁰ without considering the presence of a photovoltaic implant in contact with the retina. When a photovoltaic retinal prosthesis (e.g. nir-POLYRETINA) is implanted, the incident light absorbed by the prosthesis generates additional heat that needs to be considered into the MPE. At 730 nm, the theoretical MPE for continuous illumination is 2.4 mW/mm². We used a finite element method (FEM) to estimate the temperature increase in the retina upon photovoltaic illumination (**Figure 5.8**). Without the photovoltaic retinal prosthesis, the temperature increase upon chronic illumination (730 nm, 2.4 mW/mm², 46.3 °, 150 s) at the interface between the retina and the retinal pigmented epithelium is stable at 0.78 °C (**Figure 5.8A** and **D**). This value might not exactly correspond to the real eye temperature increase due to the model approximations, such as the absorption and thermal coefficients of the eye structures, and will therefore only be used as a reference value. In this simulation, the POLYRETINA structure is present in the model, but all its domains were set exactly as the vitreous humor. This solution allows a better comparison with the case when the nir-POLYRETINA is modelled in epiretinal configuration (**Figure 5.8B** and **E**). In the latter, the total temperature increase (at the retina-prosthesis interface) reaches a value of 1.36 °C (730 nm, 2.4 mW/mm², 46.3 °, 150 s), which is 1.7 times higher than without the prosthesis. FEM simulations showed that the temperature increase with the photovoltaic retinal prosthesis is lowered back to 0.78 °C (as without the implant) for a continuous irradiance of 1.4 mW/mm², which is the adjusted MPE with nir-POLYRETINA for chronic photovoltaic stimulations at 730 nm (**Figure 5.8C** and **E**). In the case of 10-ms pulsed illumination, the adjusted MPEs are 7, 14, and 28 mW/mm² respectively for an illumination rate of 20, 10, and 5 Hz.

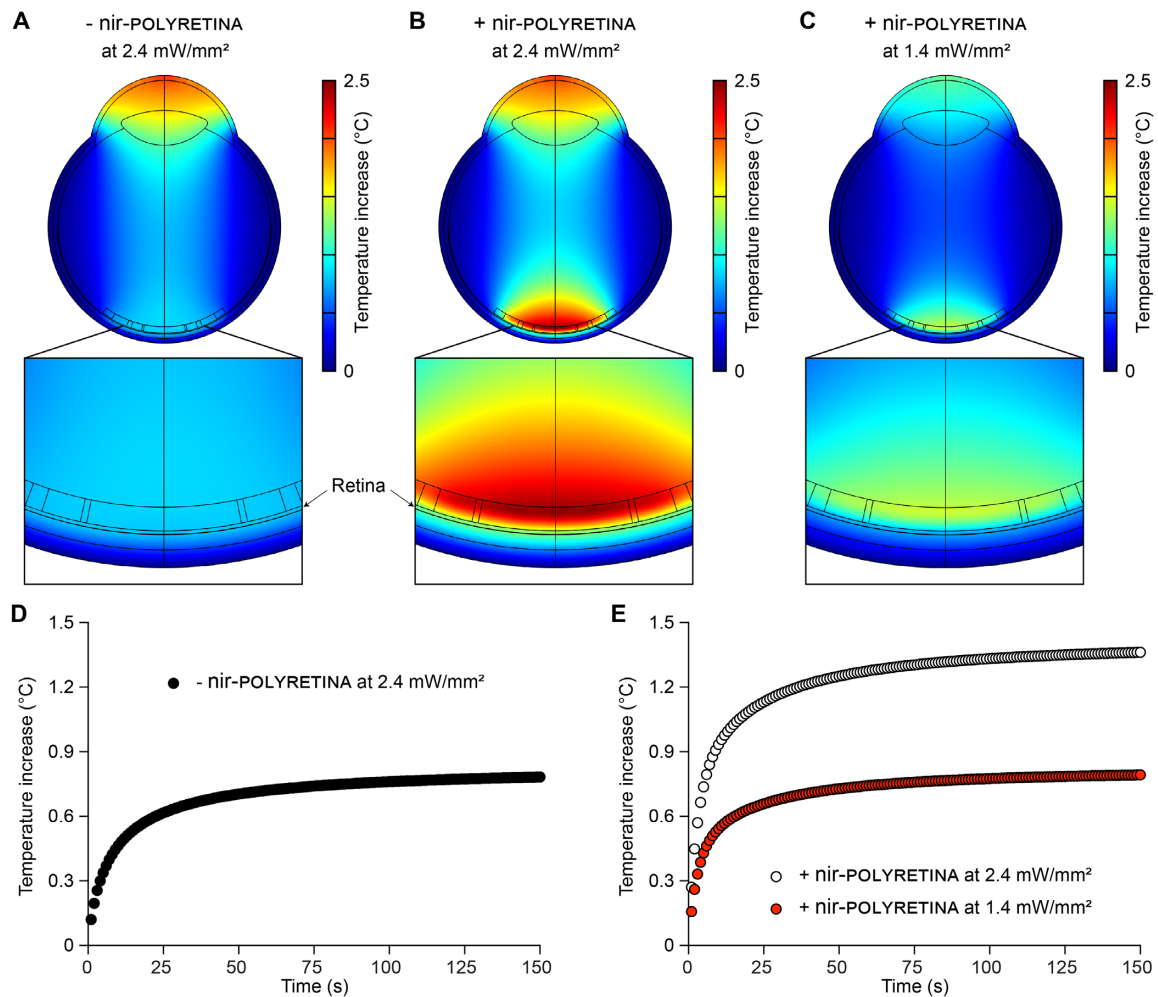


Figure 5.8 Thermal simulations. **A)** Temperature increase in the modelled eye after 150 s of continuous illumination (730 nm, 2.4 mW/mm²). The insert shows a larger view of the modelled retina with phantom nir-POLYRETINA borders. **B), C)** Temperature increase in the modelled eye with nir-POLYRETINA after 150 s of continuous illumination at 2.4 mW/mm² (730 nm, B) and at 1.4 mW/mm² (730 nm, C). The inserts show a larger view of the modelled retina and nir-POLYRETINA. **D), E)** Time courses of the temperature increase in the modelled retina during 150 s of continuous illumination without nir-POLYRETINA at 2.4 mW/mm² (730 nm; D, black circles), with nir-POLYRETINA at 2.4 mW/mm² (730 nm; E, white circles), and with nir-POLYRETINA at 1.4 mW/mm² (730 nm; E, red circles).

5.2.5 Functional validation of the NIR-responsive photovoltaic prosthesis

PCPDTBT was used for bioelectronic interfaces only in few reports.^{201,204} Therefore, we first investigated the *in vitro* cytotoxicity of the NIR-responsive photovoltaic prosthesis fabricated on a PDMS substrate (**Figure 5.9A**). A mean cell viability (\pm s.e.m.; $n = 4$ samples) of 107.72 ± 0.52 % was obtained (negative control 100%, $n = 1$ sample; positive control 0%, $n = 1$ sample), thus confirming the non-toxicity of the prosthesis in passive condition (i.e. without pulsed illumination). For each sample, the test was performed on triplicate culture wells and data were averaged (**Figure 5.9B**). A one-way ANOVA analysis ($p < 0.0001$, $F = 223.9$) revealed that all the four prostheses tested resulted in a cell viability significantly higher than the positive control ($p < 0.0001$ for all, Tukey multiple comparisons); similarly, the negative control is significantly higher than the positive control ($p < 0.0001$, Tukey multiple comparisons). There was no statistically significant difference among the four prostheses and against the negative control (1 vs 2: $p = 0.9947$; 1 vs 3: $p > 0.9999$; 1 vs 4: p

> 0.9999; 2 vs 3: $p = 9989$; 2 vs 4: $p = 0.9920$; 3 vs 4: $p > 0.9999$; 1 vs negative control: $p = 0.5401$; 2 vs negative control: $p = 0.2888$; 3 vs negative control: $p = 0.4598$; 4 vs negative control: $p = 0.5678$; Tukey multiple comparisons).

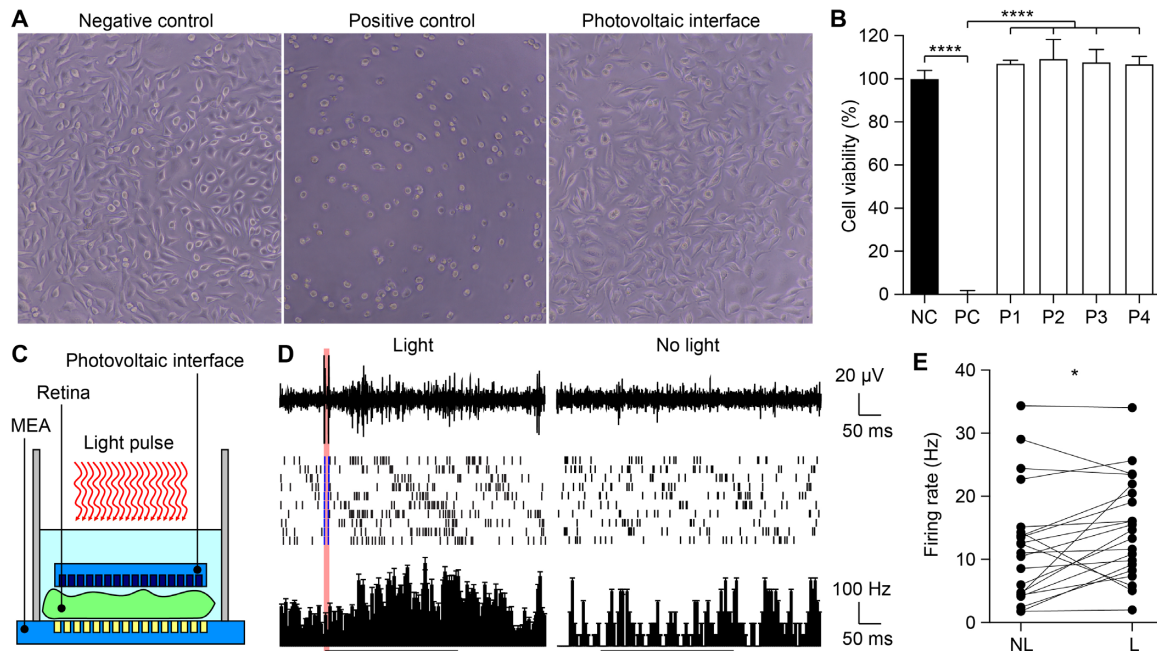


Figure 5.9 Functional validation *in vitro* and *ex vivo*. **A**) Representative images of *in vitro* cytotoxicity of the NIR-responsive photovoltaic prosthesis (right). Optical images of cell culture as negative control and positive controls are also shown (left and middle, respectively). **B**) Quantification of cell viability of the four prostheses tested (from P1 to P4) along with the negative and positive controls (respectively NC and PC). **C**) Sketch of the setup used for *ex vivo* electrophysiology. **D**) Representative response of one retinal ganglion cell upon NIR stimulation (10 ms, 4.7 mW/mm²; identified by the red bar) on the left, and without light pulse on the right. The top row shows the electrophysiological recordings upon one NIR light pulse. The middle row shows the raster plots upon ten consecutive NIR light pulses. The blue lines in the raster correspond to the events classified as stimulus artefacts. The bottom row shows the corresponding mean PSTH (\pm s.d., bins of 5 ms). The 300-ms black bar corresponds to the time window averaged to determine the post-stimulus mean firing rate. **E**) Quantification of the post-stimulus mean firing rate in retinal ganglion cells with (L) and without (NL) NIR light pulses ($n = 21$ retinal ganglion cells; two-tailed paired t-test, $p = 0.034$).

We also verified that the NIR-responsive photovoltaic prosthesis was able to stimulate retinal cells *ex vivo*. Explanted retinas from 4-months old Rd10 mice, an established model for retinitis pigmentosa²¹⁴⁻²¹⁶, were placed onto a microelectrode array and the responses evoked by photovoltaic stimulation (10-ms light pulses, 4.7 mW/mm²) were recorded from retinal ganglion cells (**Figure 5.9C**). At this age, such retinas do not anymore exhibit light responsivity.¹⁶⁵ NIR light pulses were able to induce network mediated firing activity in retinal ganglion cells (**Figure 5.9D** left) at a safe irradiance level, compared to equivalent recordings without light pulses (**Figure 5.9D** right). We measured the average post-stimulus firing rate in a 300-ms window after the light onset, or in the equivalent window when light pulses were not delivered. This large window compensates for the cell to cell variability in the onset of the spiking response and accounts for both transient and sustained responses, even if the response of transient retinal ganglion cells might result underestimated. NIR light pulses induced a significantly higher response compared to recordings without light pulses (**Figure 5.9E**; $p = 0.034$, two-tailed paired t-test). This result showed that the NIR-responsive photovoltaic prosthesis can potentially be used for retinal stimulation. The irradiance level used (4.7 mW/mm²) corresponds to 67% of the adjusted MPEs at 20 Hz illumination rate, 33.5% at 10 Hz,

and 16.75% at 5 Hz. It remains to determine what will be the optimal illumination rate for photovoltaic retinal prostheses, like POLYRETINA. Clinical results tend to suggest that an increase of the pulse rate above 10 Hz might not necessarily be the most benefiting strategy to elicit relevant perception in implanted patients. A personalized trade-off between high stimulation rates allowing flicker fusion (e.g. 40 Hz in Argus II patients) but affecting the percept strength and duration, and lower stimulation rates resulting in sustained but blinking percepts should be determined.²¹⁷ Patients implanted with either subretinal or epiretinal prostheses tend to prefer low stimulus frequencies.^{139–141,218,219} Recent *ex vivo* evidence also identifies stimulation frequencies from 5 to 10 Hz as the preferred frequency range to activate bipolar cells from the epiretinal side and trigger network-mediated responses in retinal ganglion cells.^{220,221}

5.3 Discussion

Photovoltaics is an attractive approach in bioelectronic medicine and neuroprosthetics to stimulate or modulate neuronal activity. Our results show that organic photovoltaic interfaces can be optimized to achieve higher stability, better optoelectronic performances, and adjusted sensitivity in order to match the desired target application. In a proof-of-concept, we demonstrated the advantage of a NIR-responsive neuroprosthesis for retinal stimulation that allows for higher compliance with the standards for optical safety and reduces the interfering with the residual natural vision.

The use of NIR light for artificial vision was first introduced with silicon-based photovoltaic retinal prostheses, which were considered better suited for photovoltaic stimulation because of the higher NIR photoconversion efficiency of silicon compared to conjugated polymers.^{68,70,222} In organic technology, previous researches attempted to perform retinal stimulation at longer wavelengths, even if still in the visible spectrum¹⁰⁸, and a computational study showed that a photovoltaic interface based on conjugated polymers could operate in the NIR spectrum²²³; however, in the latter study, an experimental validation was not provided. We demonstrated that also organic photovoltaic interfaces can efficiently stimulate blind retinas at NIR wavelengths (i.e. 730 nm; **Figure 5.2**). This represents an important contribution to the development of organic retinal implants. Organic photovoltaic bioelectronic interfaces are facing additional challenges, such as optimizing the electrical properties of the photovoltaic cell to meet the required working conditions and the weak stability of the organic materials due to water-induced swelling, degradation, and delamination. Our study addressed these open challenges to advance the exploitation of conjugated polymers in photovoltaic organic prostheses, with a particular interest in retinal prostheses. The adjustment of photovoltaic and stability properties of the PEDOT:PSS/PCPDTBT:PCBM/Ti pixels were obtained thanks to the morphological and electrical tuning of conjugated polymers by the addition of a simple cross-linking molecule into the anodic layer solution (**Figure 5.3**, **Figure 5.4**, **Figure 5.5**, and **Figure 5.6**). Molecules reorganization within the bulk, film, and at their interfaces is a general characteristic of polymers, whose macroscopic features (such as mechanical, optical, electrical, opto-electronic, and thermal) are directly influenced. Inorganic materials, on the other side, do not possess this accessible manipulation of properties, unless the material is chemically modified (for instance by doping or thermal oxidation and nitridation). Not only polymers properties can be adjusted by simple, fast, and cost-effective treatments like low-temperature baking or cross-linker concentration adjustment, but they can also be synthesized with various (co)monomers, chain length, and side groups. This exponentially increases the diversity of the final macro-properties and, together with their practical control

and miniaturization potential, is making organic materials, and in particular conjugated polymers, the future for (opto)electronic neural interfaces.

The next steps include the single pixel illumination evaluation and the transfer of this NIR technology to the latest version of POLYRETINA for *in vivo* testing. If, eventually, an increase in photoconversion efficiency is needed, various solutions could be considered; for instance, tandem photovoltaic cells could offer an improvement in stimulation efficiency without losing any space on the photovoltaic array, i.e. without modifying the pixels spatial resolution.

5.4 Methods

5.4.1 Chip microfabrication

Samples were fabricated on 20 x 24 mm² glass substrates (2947-75X50, Corning Incorporated) cleaned by ultra-sonication in acetone, isopropyl alcohol, and deionized water for 15 min each and then dried with a nitrogen gun. The deposition of the PEDOT:PSS and the preparation of the bulk heterojunctions were performed in a glovebox under nitrogen atmosphere. PEDOT:PSS (HTL Solar and PH1000, Clevios) was filtered (1 μm PTFE filters) then spin-coated at 3000 rpm for 40 seconds on each sample. Subsequent annealing at 115 °C for 30 min was performed. When present, GOPS was added to the solution before filtering. 20 mg of P3HT (698997, Sigma Aldrich) or PCPDTBT (754005-100MG, Sigma) and 20 mg of PC₆₀BM (M111, Ossila) were dissolved in 1 mL of anhydrous chlorobenzene each and let stirring overnight at 70 °C. The solutions were then filtered (0.45 μm PTFE filters) and blended [1:1 v:v]. The P3HT:PCBM (nominal thickness 100 nm) and PCPDTBT:PCBM (nominal thickness 100 nm) blends were then spin-coated at 1000 rpm for 45 seconds. Subsequent annealing at 115 °C for 30 min was performed. Titanium cathodes (diameter 100 μm, nominal thickness 150 nm) were deposited by DC magnetron sputtering through a shadow mask. A plastic reservoir was then attached to the sample using PDMS as adhesive, leaving about 0.051 mm² of Ti exposed to the solution.

5.4.2 Measure of photo-voltage and photo-current

Samples were placed on a holder, and each electrode was sequentially contacted. A platinum wire immersed in physiological saline solution (NaCl 0.9%) was used as counter electrode. 10-ms light pulses were delivered by a 565-nm (M565L3, Thorlabs), 730-nm (M730L4, Thorlabs), or 780-nm (M780LP1, Thorlabs) LED focused at the sample level. Photo-voltage and photo-current were measured using respectively a voltage amplifier (1201, band DC-3000 Hz, DL-Instruments) and a current amplifier (1212, DL-Instruments). Data sampling (40 kHz) and instrument synchronization were obtained via a DAQ board (PCIe-6321, National Instruments) and custom-made software. Data analysis was performed in MATLAB (MathWorks). When evaluating the photo-current density generated by the interface, also the area of the connecting line exposed to light has been considered (on average 0.077 mm²).

5.4.3 Spectral absorbance

The preparation of the bulk heterojunctions was performed as before. The thicknesses were 80 and 62 nm for P3HT:PCBM and PCPDTBT:PCBM respectively. The absorbance spectra of the thin films were measured using a UV-vis-NIR UV-3600 Shimadzu spectrophotometer.

5.4.4 Resistance measurements

The preparation of the PEDOT:PSS was performed as before. The film resistance was measured with a custom 4-point prober (2.5 mm pitch distance) using a Keithley 2400 source-meter. Each sample was measured on five different locations randomly distributed on the surface.

5.4.5 Thickness measurements

Thin-film thickness was measured in PeakForce tapping mode (ScanAsyst Air silicon tip, $f_0 = 70$ kHz, $k = 0.4$ N/m) with a Dimension Icon AFM (Bruker).

5.4.6 Time-of-flight secondary ion mass spectrometry measurements

The measurements were performed on a ToF-SIMS.5 instrument (IONTOF, Germany) operated in the spectral mode using a 25 keV Bi^{3+} primary ion beam with an ion current of 0.81 pA. A mass resolving power in the range of 5000 $m/\Delta m^{-1}$ was reached. For depth profiling, a 500 eV Cs^+ sputter beam with a current of 43.47 nA was used. The raster area of the sputter beam was $500 \mu\text{m} \times 500 \mu\text{m}$, and the mass-spectrometry was performed on an area of $200 \mu\text{m} \times 200 \mu\text{m}$ in the center of the sputter crater. A low-energy electron flood gun was used for charge compensation.

5.4.7 Fabrication of nir-POLYRETINA prostheses

Prostheses were prepared as previously described (paragraph 2.4.1). A thin sacrificial layer of poly(4-styrenesulfonic acid) solution (561223, Sigma-Aldrich) was spin-coated on 4" Si wafers (1000 rpm, 40 s) and baked (120 °C, 15 min). Degassed PDMS pre-polymer (10:1 ratio base-to-curing agent, Sylgard 184, Dow-Corning) was then spin-coated (1000 rpm, 60 s) and cured in oven (80 °C, 2 h). After surface treatment with oxygen plasma (30 W, 30 s), a 6 μm thick SU-8 (GM1060, Gersteltec) layer was spin-coated (3800 rpm, 45 s), soft-baked (110 °C, 300 s), exposed (140 mJ/cm^2 , 365 nm), post-baked (90 °C, 1800 s; 60 °C, 2700 s), developed in propylene glycol monomethyl ether acetate (48443, Sigma-Aldrich) for 2 min, rinsed in isopropyl alcohol, and dried with nitrogen gun. After surface treatment with oxygen plasma (30 W, 30 s), a second layer of degassed PDMS pre-polymer (10:1) was spin-coated (3700 rpm, 60 s) and cured in oven (80 °C, 2 h). The PEDOT:PSS (PH1000) film, the PCPDTBT:PCBM film, and the titanium cathodes were prepared as described above. The photovoltaic membrane was then released from the wafer and plasma bonded to a PDMS dome-shaped support with a 12 mm curvature radius an average thickness of 600 μm .

5.4.8 Cytotoxicity test

The test was conducted according to ISO 10993-5: Biological Evaluation of Medical Devices, in-vitro cytotoxicity test. Prostheses were sterilized in a dry oven for 2 h at 120 °C. The test on extraction was performed with samples for a total surface area of 3.54 cm^2 each, with a ratio of the product to extraction vehicle of 3 cm^2/ml . Extraction vehicle was Eagle's Minimum Essential Medium supplemented with fetal bovine serum, penicillin-streptomycin, amphotericin B, and L-glutamine. The extraction was performed for 24 h at 37 °C and in the dark. For each sample, the extract was added on triplicate cultures wells containing a sub-confluent L929 cell monolayer. The test samples and the control wells were incubated at 37 °C in 5% CO_2 for 24 h. Following incubation, the cell cultures were examined for quantitative cytotoxic evaluation. 50 μl per well of XTT reagent were added to

the cells then incubated at 37 °C in 5% CO₂ for further 3 to 5 h. An aliquot of 100 µl was then transferred from each well into the corresponding wells of a new plate and the optical density was measured at 450 nm.

5.4.9 Electrophysiology *ex vivo*

Animal experiments were performed according to the animal authorizations GE3717 approved by the Département de l'Emploi, des Affaires sociales et de la Santé (DEAS), Direction Générale de la Santé of the République et Canton de Genève (Switzerland). Male and female mice from a homozygous colony of retinal degeneration 10 mice (B6.CXB1-Pde6b^{rd10}/J, The Jackson Laboratory, Stock number: 004297) were used for the experiments. All animals were kept in a 12 h day/night cycle with access to food and water ad libitum. All the experiments were carried out during the day cycle. Eyes were enucleated from euthanized mice (sodium pentobarbital, 150 mg/kg) and dissected in carboxygenated (95% O₂ and 5% CO₂) Ames' medium (A1420, Sigma-Aldrich) under dim red light. Retinas were placed ganglion cells down and maintained in contact with a transparent micro-electrode array with 256 electrodes (256MEA200/30iR-ITO, Multi Channel Systems). The NIR-responsive, polymeric and photovoltaic neuroprosthesis was placed on top of the retina, and both the retina and the prosthesis were kept in position using a 1 mm nylon mesh. Retinas were continuously superfused with carboxygenated Ames' medium at 32 °C and maintained under dim red light during all the experiments. Light stimuli were generated using a 730-nm light emitting diode (M730L4, Thorlabs) paired to a 20x objective (CFI Plan Apochromat Lambda, Nikon Instruments). The diameter of the light spot was 4.16 mm. The signal from the 256 recording electrodes was amplified, filtered (300 – 3000 Hz), and digitalized at 10 kHz (USB-MEA256-System, Multi Channel Systems). Spike detection was performed with the MC_rack software (Multi Channel Systems), and the results were further processed with Neuroexplorer (Neuronexus) and MATLAB. For each cell, the post-stimulus mean firing rate was measured from the PSTH within a 300-ms time window after the light onset.

5.4.10 Optical safety

MPE were calculated as shown in paragraph 2.4.10 with **Equation 2.3** and **Equation 2.4**. However, for $\lambda = 730$ nm and 780 nm, only the MPE_T applies and

$$C_E = 6.67 \cdot 10^{-3} \alpha^2 ; C_T = 10^{0.002(\lambda-700)} ; P = 1 ; C_B = 1000.$$

Therefore, for $\lambda = 730$ nm, the MPE_T is 346.59 mW, which corresponds to 2.40 mW/mm² for an exposed area of 144.22 mm². For $\lambda = 780$ nm, the MPE_T is 436.33 mW, which corresponds to 3.03 mW/mm² for an exposed area of 144.22 mm².

5.4.11 Thermal model

COMSOL Multiphysics 5.3 was used with the Bioheat module and the General PDE module for the heat transfer and Beer-Lambert light propagation. A uniform beam with a diameter of 13 mm was used as illumination source. The eye model was built with several spheres representing each component (cornea, aqueous humor, lens, vitreous humor, retina, retinal pigmented epithelium, choroid, and sclera). All the parameters used in the model are listed in **Table 5.1**.

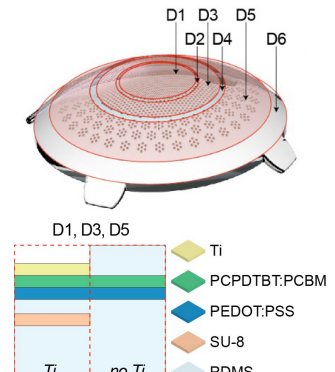
Table 5.1 Eye parameters for the FEM model. The parameters were obtained from references [151,152,156,159,160,224–237]. Parameters in *italic* were experimentally measured at 730 nm.

Material	Thick-ness	Heat Capacity	Thermal Conductivity	Density	Absorption (700-750 nm)	Perfusion rate	Self-Heat
	μm	$\text{J kg}^{-1} \text{K}^{-1}$	$\text{W m}^{-1} \text{K}^{-1}$	Kg m^{-3}	m^{-1}	s^{-1}	W m^{-3}
Aqueous Humor	3100	3997	0.58	1000	17	0	0
Choroid	430	3840	0.53	1050	600	0.0091	10000
Cornea	500	4178	0.58	1050	125	0	0
Lens	3600	3000	0.4	1050	17	0	0
Retina	100	3680	0.565	1000	125	0	0
RPE	10	4178	0.603	1050	20000	0	0
Sclera	500	4178	0.58	1000	180	0	0
Vitreous Humour	/	3997	0.6	1000	17	0	0
PDMS	670	1100	0.18	970	<i>217</i>	0	0
SU-8	6	1200	0.3	1200	<i>4367</i>	0	0
PEDOT:PSS	0.1	2370	0.29	1011	<i>539579</i>	0	0
PCPDTBT:PCBM	0.09	2800	0.15	1100	<i>2979723</i>	0	0
Titanium	0.08	522	5	4430	<i>19809072</i>	0	0

The nir-POLYRETINA was divided into six domains with homogeneous properties. For each domain, the heat capacity, the thermal conductivity (thermal resistance circuit), the density, and the absorption coefficient (Beer-Lambert law; for titanium, a reflectance of 0.63 was considered¹⁵²) were computed as described in **Appendix Equations 2, 3, 4, and 5** (and listed in **Table 5.2**). In case of domains D1, D3, and D5, the thermal conductivity and absorption coefficient were computed independently for the area with titanium/SU8 and for the area without. The two values were weighted proportionally to their respective area to obtain the final aggregated values listed in **Table 5.2**. For the density and the heat capacity, the aggregated values were directly weighted proportionally to the volume of each materials composing the domain. Domains D2 and D4 do not contain titanium nor SU8, while domain D6 is composed by PDMS only.

Table 5.2 Aggregated parameters for nir-POLYRETINA. Parameters used in the FEM thermal model of the nir-POLYRETINA.

Domain	Heat Capacity	Thermal Conductivity	Density	Absorption (at 730 nm)	Area Ti / no Ti
	$\text{J kg}^{-1} \text{K}^{-1}$	$\text{W m}^{-1} \text{K}^{-1}$	Kg m^{-3}	m^{-1}	mm^2
D1	1101	0.1805	971.0	1325	4.9 / 13.7
D2	1100.5	0.18	970.0	694	- / 2.4
D3	1101	0.1805	970.9	1329	7.4 / 20.7
D4	1100.5	0.18	970.0	694	- / 7.5
D5	1101	0.1803	970.4	1021	9.5 / 60.7
D6	1100	0.18	970.0	217	- / 50.0



5.4.12 Statistical analysis and graphical representation

Statistical analysis and graphical representation were performed with Prism (GraphPad Software Inc.). The normality test (D'Agostino & Pearson omnibus normality test) was performed in each dataset to justify the use of a parametric or non-parametric test. In each figure p-values were represented as: * $p < 0.05$, ** $p < 0.01$, *** $p < 0.001$, and **** $p < 0.0001$.

5.5 Acknowledgments

We would like to acknowledge the EPFL Center of Micronanotechnology and The Neural Microsystems Platform at Wyss Center for their support. We also acknowledge Prof. Kevin Sivula and Dr. Nestor Guijarro Carratala of EPFL for the support with the UV-Vis spectroscopy measurements. This work was supported by École polytechnique fédérale de Lausanne, Medtronic, European Commission (Project 701632), Fondation Mercier pour la science, Velux Stiftung (Project 1102), Gebert Rűf Stiftung (Project GRS-035/17), the Wyss Center for Bio and Neuroengineering, and Swiss National Science Foundation (Project CR23I2-162828).

Chapter 6 Conclusions and Outlook



Eyes of a scallop (Source: Sciencemag, vol 358, issue 6367, 2017)

6.1 Summary of performed research

Millions of people worldwide could benefit from more advanced visual prostheses. This thesis faces the technological limitations necessary to develop unconventional, novel retinal prostheses for improving the state of the art in artificial vision. Namely, although implants with high spatial pixel resolution have been produced for subretinal prostheses, the restoration of a useful form of vision over a large visual field was not achieved neither for subretinal, nor for epiretinal implants. To address this challenge, we developed a wide-field, curved, and foldable epiretinal prosthesis – named POLYRETINA – able to induce RGCs activity by photovoltaic (i.e. wireless) stimulation.

The developed photovoltaic pixels are based on organic electronic materials along with conventional biomaterials such as Ti. We demonstrated that the pixels composed of PEDOT:PSS/P3HT:PCBM/Ti generate enough photovoltage and a capacitive cathodic photocurrent able to stimulate RGCs by absorption of green (565 nm) light. The pixels induced spiking activity with short pulses of light of irradiances below the safety limit imposed by regulations about photo-thermal and chemical damage to the retina. These results demonstrated *in vitro* and *ex vivo* the photovoltaic pixels efficiency in promoting RGCs ML activity, as sign of network-mediated responses suitable for focused prosthetic-induced pattern stimulation.

To be used as retinal prostheses, the photovoltaic pixels were fabricated on a PDMS membrane, mechanically adapted to be stretched and shaped spherically thanks to a PDMS dome substrate matching the eye's radius of curvature. The resulting curved prosthesis has pixels distributed over a large surface area (140 mm²) covering a visual field of about 46 °. The major advantage of this approach lies in the close and homogeneous contact between the photovoltaic interface and the retina, despite the exceptionally wide visual field coverage. Consequently, a safe delivery method into the eye was designed to face the surgical implantation challenge of large prostheses. Inspired by intraocular lenses and made possible thanks to the POLYRETINA mechanical capability of being folded and self-open, a custom-made injector was developed to deliver the wide implant through a small corneal incision. Moreover, POLYRETINA can be easily replaced following eventual malfunctioning or damaging thanks to the absence of wires.

After proof-of-concept validations, POLYRETINA required further characterizations and optimizations towards *in vivo* experiments. First, various designs with denser pixel arrays were considered along with the related consequences in microfabrication, mechanical stability, and electrical cross-talk. A high-density prosthesis was selected with optimal spatial resolution (79 pixels/mm²) and the ability to activate RGCs with single pixel illumination (efficiency increased by TiN coating on the electrodes). Second, an extreme mechanical stability of the pixels and an improved electrode-electrolyte interface could be obtained by exploiting parylene-C properties. And third, the PDMS encapsulation layer was replaced by OSTEmer polymer, which has superior sealing properties beneficial for chronic applications. The manufacturing advantages of OSTEmer allowed to develop black POLYRETINA, through which only about 94% of green light can pass and reach the retina.

Miniature pigs were the chosen animal model for the first *in vivo* experiments. We induced photoreceptors degeneration by injection of the IAA toxin, causing death of the outer nucleus layer within one to two months and significantly reducing electrophysiological visual responses to flashes of light. After a successful delivery of POLYRETINA into the eyes, the implantation completes with

fixation of the implant using retinal tacks. Subsequently, preliminary recordings at the primary visual cortex revealed signals of prosthetic-induced potentials upon flashes of green light, indicating a first positive result in pursuing POLYRETINA as visual prosthesis.

The promising results achieved so far, together with the variety of suitable organic semiconductors, motivated investigations about a NIR-sensitive POLYRETINA, which is beneficial for further preclinical (and eventual clinical) trials due to the spectral distinction with natural vision. The BHJ PCPDTBT:PCBM was used in replacement of P3HT:PCBM to generate photocurrents upon illumination of NIR (730 nm) light. The engineering of the anodic PEDOT:PSS layer allowed to obtain adhesive and photovoltaic properties appropriate for stimulation frequency up to 20 Hz.

These results demonstrated the benefit and the potential of POLYRETINA to be used in fighting blindness caused by retinal degenerations. Further animal experiments will be needed to address encountered challenges and obtain solid preclinical studies.

6.2 Limitations

Organic photovoltaic technology was introduced as bioelectronic interfaces for the wireless stimulation of the central and peripheral nervous systems only recently. Consequently, the variety of potential organic materials and their characteristics might not be entirely acknowledged. Although this assortment represents more a possibility than a limitation, the inquiry and the doubts about their performances, adhesion, and long-term stability are inevitable. Compared to silicon technology, organic photovoltaics are still (for now) less efficient. In retinal prostheses, the use of visible light to trigger photovoltaic stimulation is not ideal, and therefore, as proposed in Chapter 5, NIR (or IR) light would be more appropriate. However, single pixel stimulation with light intensities within the limits of thermal damage need to be verified and might not be successful, particularly if the pixel size is reduced.

In the thesis, we also discussed the possibility to increase the visual acuity by increasing the photovoltaic pixels density. From the technical point of view, the final fabrication method is extremely scalable (pixels density of 318 pixels/mm² or more); however, from a functional point of view, the further increase in pixels spatial resolution might not benefit as much as hoped due to activation of axons of passage and, as mentioned, the possibly “large” and irregular electrode-cell distance. Visual performances such as object recognition and readings might not substantially improve with further reduction of pixels size and pitch beyond 60-80 μm and 90-120 μm, respectively. Therefore, visual acuity in epiretinal prostheses will generally be limited by those two aspects, unless further discoveries and technologies come into play. On the other hand, the enlargement of the visual field can greatly improve visual performances and potentially the patients’ quality of life.

At the moment, the main limitation of POLYRETINA in *in vivo* applications is by far the fixation method that uses retinal tacks to hold the prosthesis against the retina. Although the sharpness of the tip, the different mechanical properties of the minipig sclera made it difficult to properly perforate and anchor the tack on the sclera. Even when a successful fixation was obtained, after two to four weeks many implants moved away from the back of the eye and made the retinas detach. This event could be even more serious in subjects implanted for longer times. Furthermore, we cannot guarantee a close cell-electrode distance, which could render the efforts in obtaining the optimal *in vitro* photovoltaic properties ineffective.

Regarding the animal models, the IAA-induced degeneration of photoreceptors in minipigs is not the ideal model for blindness in large animals. First, the IAA-induced blindness does not correspond to a genetic degeneration as for humans, and thus, it does not follow the same clinical progress. Second, the possible residual vision might influence the electrophysiological experiments for the assessment of prosthetic-evoked responses. Therefore, the necessary long-term and reliable evaluation might be performed in a different large animal model. Moreover, the features and the purpose of POLYRETINA need a large animal model with the possibility of training (such as non-human primates) to perform quantifiable tasks with numerous iterations, and this might raise further ethical questions.

6.3 Future perspectives

The development of POLYRETINA consisted in proof-of-concept studies and, although major technological challenges could be overcome, further straightforward improvements can be indeed envisioned. First, some manufacturing steps of POLYRETINA, once the photovoltaic membrane is released from the supporting wafer, are too manual and operator-dependent (i.e. the bonding onto the PDMS dome and the rolling and placement of polyretina into the eye injector). Nevertheless, potential solutions can be proposed for an improved automatization of these steps (such as application of advanced alignment supports and automated three-roll systems) and the establishment of a reliable and reproducible manufacturing.

Second, although various *in vitro*, *in silico*, *ex vivo*, and preliminary *in vivo* characterizations have been performed, many more are required to translate from preliminary *in vivo* to consistent preclinical studies. Among them, chronic safety and stability under working conditions (i.e. under illumination) need to be guaranteed. Aging and cytotoxicity experiments should be performed again but with train pulses of light applied during incubation of the implant. Aging tests will be useful to determine not only the stability of organic electronic materials, but also the encapsulation and adhesion properties of the other polymers, such as OSTemer. However, *in vivo* chronic investigations will be more appropriate to extensively evaluate the implant biocompatibility and stability in the target anatomical location and possibly with activated foreign body reactions.

Third, an adaptation and investigation of the photovoltaic materials for a NIR (or IR) sensitive POLYRETINA will be necessary to avoid making the animals blind and minimizing interferences with electrophysiological and behavioral experiments during preclinical (and clinical) trials. Consequently, the efficiency of RGCs photovoltaic activation with single pixel NIR (or IR) illumination requires to be verified and ensured. In case of inefficiency, solutions to enhance photovoltaic efficiency will have to be considered (such as different materials and additives, tandem cell photovoltaics, integration of nanoparticles for boosting quantum efficiency, and so on).

Fourth, the placement of the electrodes in proximity of the RGCs is an important parameter that guarantees an adequate and more focused stimulation. Hence, protruding 3D electrodes might be considered in the future to decrease the cell-electrode distance.²³⁸ The protruding parts of the stimulating pixels could be damaged during rolling, loading into the injector, and delivery into the eye; therefore, protective coatings could be applied that degrade or are surgically removed after implant unfolding in the eye chamber. Another future improvement may also include the removal of stimulating pixels in correspondence of the optic disc (for avoiding stimulating *all* the RGCs) and the

creation of small holes within the substrate to allow metabolic exchange between the vitreous and the retina.

And last, as stated in the limitations, retinal tacks were not effective to keep the implant in place. Although the human sclera and its elasticity could allow successful penetration and clamping, the risk is still too high. Therefore, in the near future, a better solution to secure the implant should be implemented by either modifying the retinal tacks or investigating other out-of-the-box ideas, such as magnetic clamping or injection of a supporting gel replacing the vitreous body and pushing the implant against the retina.²³⁹

What comes next?

POLYRETINA represent one way to fight blindness by exploiting technological and materials advancements. Further improvements will allow to develop a second generation of POLYRETINA and to upgrade the animal model to non-human primates, which will represent an important milestone. From there, *in vivo* visual acuity assessment could finally be achieved and the translational potential for further clinical applications established.

According to preclinical outcomes, POLYRETINA is destined to help people with retinal degeneration that have lost their vision and suffer from an extensively reduced quality of life. Feasibility studies in humans are essentials to get cognitive, sensory, and perceptual feedbacks that cannot be obtained in any animal model: “only humans can decide whether the advantages they experience outweigh the risks and side effects of such a treatment option”.²⁴⁰ The translation from animal to human studies generally requires dealing with scaling issues (fortunately none for POLYRETINA), medical approval, and high levels of reproducibility, reliability, quality control, and performances. In particular, the manufacturing and other routine procedures are expected to be flawless; only biological and psychophysical variations have the right to bring uncertainty to the system.

What about fighting blindness?

POLYRETINA, such as other prosthetic implants, are intermediary solutions. They are a product of the modern technological era, and their commercialization followed a rather straightforward path. The artificial vision abilities of visual prostheses can be indeed very useful and could help many people; however, they are limited in restoring high quality vision for the reasons explained throughout this thesis (unless we rethink the prosthetic concepts by exploring, for instance, nanotechnologies and nanomaterials). In research nowadays, there are other more biological approaches, such as photoreceptors transplants and opto-genetics, that hold important promises and that could offer better solution for fighting blindness. This is especially truth for opto-genetics thanks to the direct access of light into the eye and the recent advances in broader spectrum sensitivity and delivery efficiency.^{241,242} However, clinical studies and commercialization of such approaches may require extended periods of research and preclinical investigations due to the involved biological and genetic manipulations, complicating the control on reproducibility and reliability. Yet, in the meantime, we can propose a temporary solution based on prosthetic vision, enhanced by advanced retinal implants such as POLYRETINA.

Opportunities of the developed technology for bioelectronic interfaces

POLYRETINA exploits organic materials and their optoelectronic properties to wireless stimulate retinal neurons. However, although the simpler optical access to the retina, these materials are not

limited to retinal prostheses. Organic photovoltaics can be used to interface other neuronal cells in the CNS and PNS.²⁴³ Among the various advantages of organic materials, such as lightness and biocompatibility, conjugated polymers and their various properties hold a special place in the future of bio-(opto)electronic interfaces, as demonstrated in this thesis. Moreover, the exceptional mechanical and large-area capabilities of the developed photovoltaic pixels might become very useful for numerous neurotechnological applications involving curved and complex surfaces, as the human body is very fond of.

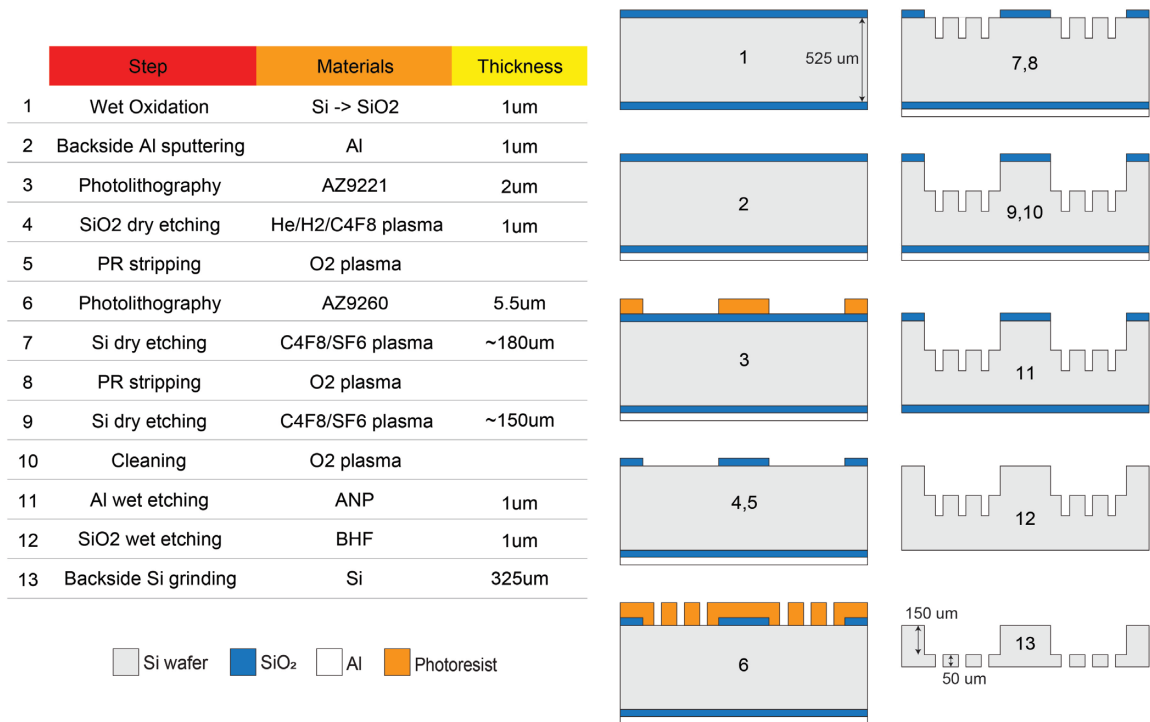
Appendices

Appendix Equation 1 Equivalent model of electrode-electrolyte impedance (Z_{eq}):

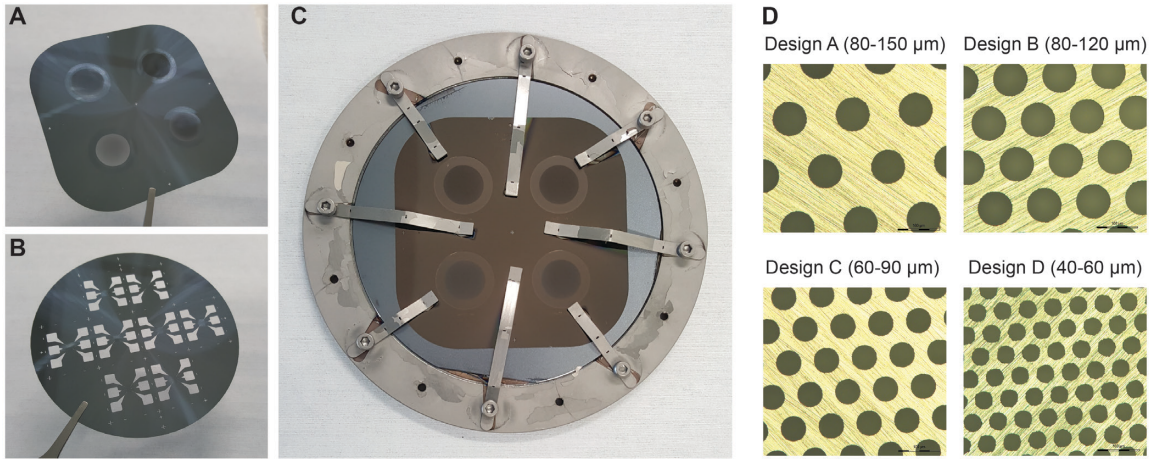
$$\text{Impedance of constant phase element: } Z_{DL}^{CPE} = \frac{1}{C_{DL}(j\omega)^n}$$

$$Z_{eq} = \frac{R_{CT} \cdot \frac{1}{C_{DL}(j\omega)^n}}{R_{CT} + \frac{1}{C_{DL}(j\omega)^n}} + R_{spread} = \frac{R_{CT}}{R_{CT} \cdot C_{DL}(j\omega)^n + 1} + R_{spread} ; \omega = 2\pi f$$

R_{CT} : charge transfer resistance, C_{DL} : double layer capacitance, n : empirical factor ($0 \leq n \leq 1$),
 j : imaginary unit, ω : angular frequency, R_{spread} : spreading resistance, f : frequency.



Appendix Figure 1 Microfabrication process flow of the Si stencils. Left: steps with materials and thicknesses. Right: cross-sectional view of the corresponding fabricated steps (not in scale).



Appendix Figure 2 Photographs of Si stencils and application. **A), B)** Two examples of used stencils for POLYRETINA fabrication (A) and photovoltaic chips characterization (B) view from the bottom (grinded) side. **C)** Application of the stencil custom-made holder during sputtering for a better adhesion with the substrate. **D)** Micrographs of the stencils grinded side of the four POLYRETINA designs discussed in Chapter 3.

Medistri . SA
a must in medical chain

Rte de l'Industrie 95
Case postale 115
1564 Dondillier
Switzerland

Tel: +41 (0) 26 676 90 80
Fax: +41 (0) 26 676 90 85
TVK: 645 904

www.medistri.com
contact@medistri.com

Medistri . SA
a must in medical chain

Rte de l'Industrie 95
Case postale 115
1564 Dondillier
Switzerland

Tel: +41 (0) 26 676 90 80
Fax: +41 (0) 26 676 90 85
TVK: 645 904

www.medistri.com
contact@medistri.com

Routine analysis / Résultat d'analyse de routine

Biological evaluation of medical devices: in vitro cytotoxicity test

Evaluation biologique des dispositifs médicaux: test de cytotoxicité in vitro

General Information				
Customer name	E.P.F.L.			
Customer address	Chemin des Mines 9 CH-1202 Genève			
Date of reception of the product	18 th April 2017			
Product identification (name and reference)	Sample ID	Name of the Product	Manufacturing Batch Reference	
	I	POLYRETINA	ALPHA01 / ALPHA02	
Customer's reference (Delivery note #; order #...)	EPFL			
Product surface area (cm ²)	Sample ID	Product surface area (cm ²) / piece		
	I	1,77 cm ²		
Packaging conditions	<input type="checkbox"/> Under vacuum packaging <input checked="" type="checkbox"/> Standard packaging			
Sterilization conditions	<input checked="" type="checkbox"/> Sterile: Medistri SA : Site batch # 17-0375-1 / 17-0377-1 <input type="checkbox"/> Other <input type="checkbox"/> Non sterile			
Quantity of samples	1 pool of 2			
Method				
The study was conducted according to the requirement of SN ISO 10993-5 : Biological Evaluation of Medical Devices, <i>in vitro</i> cytotoxicity test, SN ISO 10993-12: Test article preparation and reference materials, USP 35-NF30 (87). Biological Reactivity test, <i>in vitro</i> and Medistri internal procedure WI 47 and WI 56. All current versions				
Test method	<input type="checkbox"/> Direct contact <input type="checkbox"/> Agar diffusion <input checked="" type="checkbox"/> Test on extract			
Tested surface area (cm ²)	Sample ID	Product surface area (cm ²) / piece	Number of pieces tested	Total surface area (cm ²) tested
		1,77 cm ²	2	3,54 cm ²
Ratio of the product to extraction vehicle (cm ² /ml)	3 cm ² /ml			
Extraction vehicle	<input checked="" type="checkbox"/> EMEM medium Batch #: RNBF3691 <input type="checkbox"/> other (specify): N.A. Batch #: n.a.			
Medium supplemented with	<input checked="" type="checkbox"/> Fetal bovine serum Batch #: 1110D <input checked="" type="checkbox"/> Penicillin-streptomycin Batch #: A2213 <input checked="" type="checkbox"/> Amphotericin B Batch #: 1407D <input checked="" type="checkbox"/> L-glutamine Batch #: 0951C			
Extraction conditions	<input checked="" type="checkbox"/> (24±2) h at (37±1)°C <input type="checkbox"/> other (specify): N.A.			
Test system	L929 cell line (ECACC n°88102702). The murine fibroblastic L929 cells are recommended by ISO 10993-5.			
Incubation conditions for cells	37 ±1°C and 5 ±1% CO ₂			
Date of start	18 th April 2017			
Date of end	20 th April 2017			

Medistri Labo Batch #: 13731
This report can not be reproduced partially.
All results on this report are only related to the tested samples.

F38-e Version: B2
SOP ref. 7.5.1-5
MCR: 158/16

Medistri Labo Batch #: 13731
This report can not be reproduced partially.
All results on this report are only related to the tested samples.

Description

The product or its extract was added on triplicate culture wells containing a sub-confluent L929 cell monolayer. The test sample and the control wells were incubated at 37 ± 1°C in 5 ± 1% CO₂ for a minimum of 24 hours.

Following incubation, the cell cultures were examined for qualitative and/or quantitative cytotoxic evaluation. For qualitative evaluation, cells were stained and examined macroscopically for cell decolorization around the portion of the product. The cultures were then examined microscopically to verify any decolorized zones and to determine cell morphology in proximity to and beneath the tests and controls.

For quantitative evaluation, 50 µl/well of XTT reagent was added to the cells then incubated at 37 ± 1°C in 5 ± 1% CO₂ for further 3-5h. An aliquot of 100 µl was then transferred from each well into the corresponding wells of a new plate and the optical density (OD) was measured at 450nm.

Results 96 well microplate				
Samples ID	Sample dilution	% viability** (quantitative evaluation)	Acceptance criteria	Cytotoxic effect
I	1:1	100	If < 70% (compared to negative control), it has a cytotoxic effect	Yes <input type="checkbox"/> No <input checked="" type="checkbox"/>
Samples	Sample dilution	% viability** (quantitative evaluation)	Acceptance criteria	Pass/Fail
Positive control	1:1	0,3	n.a.	Pass <input checked="" type="checkbox"/> Fail <input type="checkbox"/>
Negative control	1:1	100	n.a.	Pass <input checked="" type="checkbox"/> Fail <input type="checkbox"/>
Blank	1:1	n.a.	n.a.	n.a.

** Viability max is 100%.

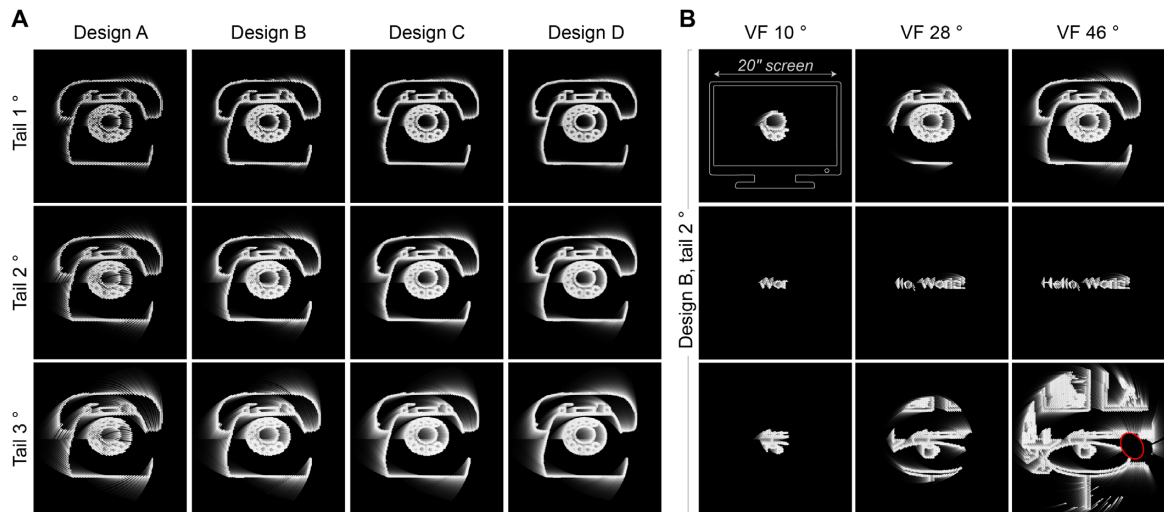
Conclusion

The device tested is not cytotoxic under the condition of the test.

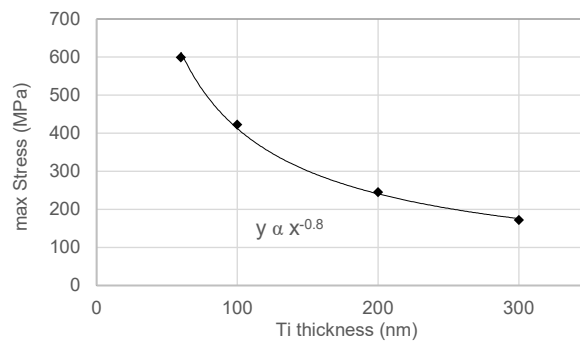
Approvals

Date : 21 st April 2017	Date : 24 th April 2017
Responsible for analysis: [Redacted]	Quality Department: [Redacted]

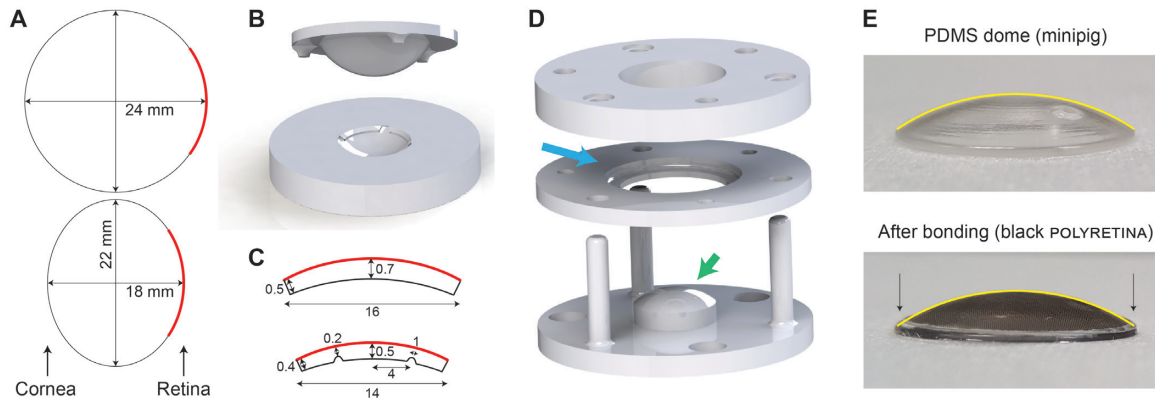
Appendix Figure 3 ISO certificate for *in vitro* cytotoxicity of POLYRETINA.



Appendix Figure 4 Simulation with virtual reality of phosphenes appearance from POLYRETINA stimulation. **A)** Simulation of a telephone according to the different designs (presented in Chapter 3) and tail length. **B)** Effect of visual field (VF) covering with design B and tail length 2 °. In the first row the telephone shown in B) is represented; in the second row the words “Hello, World!”; in the third row a room in which a coffee cup on top of a round table is in the center of the scene with paintings on the wall at the back. The size of the VF is compared to the extent of a 20” (51 cm) computer screen at a distance of 60 cm in the first panel. The red oval in the last panel shows the location of the optic disc, where no pixels should be activated. POLYRETINA covers a VF of 46.6 °, while Alpha-AMS of 11 °. Contribution: J. Thorn.



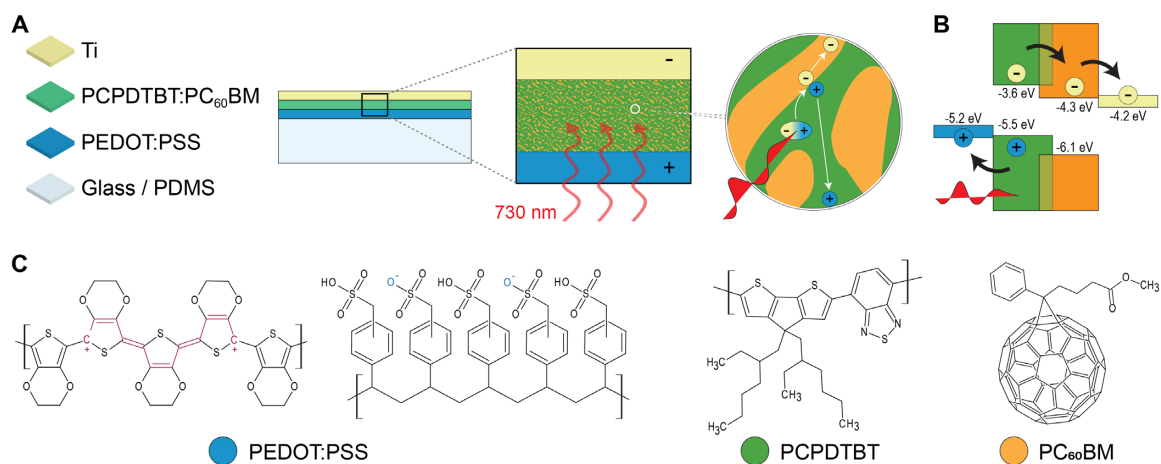
Appendix Figure 5 Dependence of von Mises tensile stress from Ti thickness determined by mechanical simulation with Abaqus. The graph represents the maximal registered stress on Ti electrodes during bonding procedure for the case of design C (60 μm electrodes with 90 μm pitch) discussed in Chapter 3.



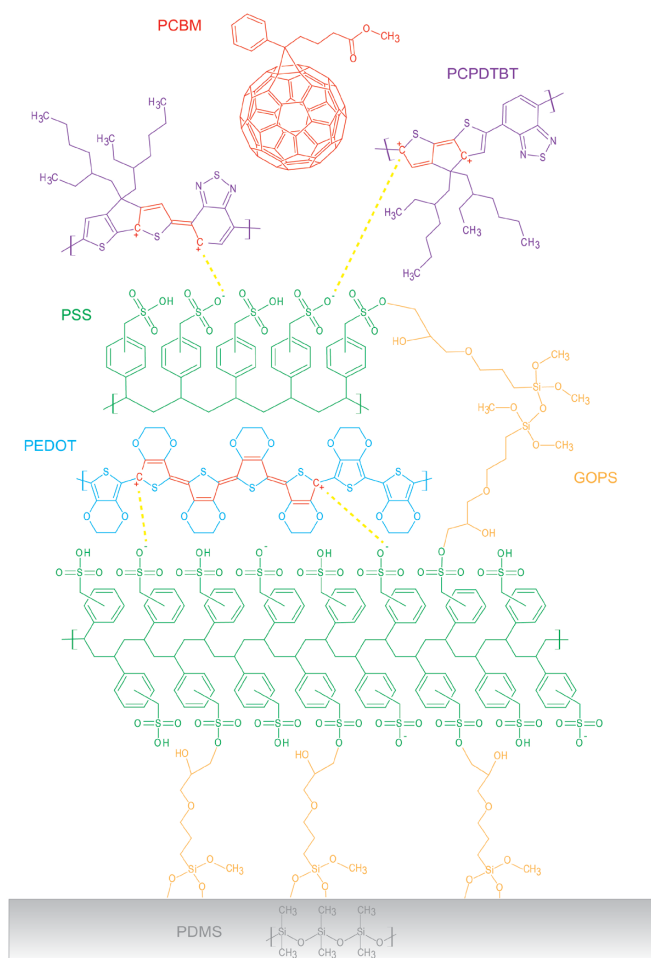
Appendix Figure 6 Details about the PDMS domes, molding, and bonding. **A)** Axial view of the used eye size for humans (top) and minipigs (bottom). The POLYRETINA is shown in red. **B)** 3D model of the parts in PMMA used to produce PDMS domes by cast molding. These parts were drilled and polished. **C)** Size used for the construction of the PDMS domes for humans (top) and minipigs (bottom). The red lines correspond to the curvatures depicted in A. Units are in mm. The minipig dome has two indentations dedicated to tack holes of 0.5 mm. **D)** 3D model of the bonding setup. The photovoltaic membrane, after being activated by oxygen plasma, is placed where the blue arrow indicates, clamped with an O-ring, and held with the top circular part. The PDMS dome, also activated, goes on the specific, curved, protruding part indicated by the green arrow. The whole is then assembled with help of a drop of PDMS pre-polymer between the dome and the membrane, then 1 kg of load is applied from the top for at least 2 h at 80 °C. **E)** Curvature of the finished POLYRETINA (bottom) compared to the original curvature (yellow line) from the PDMS dome after molding (top). The stresses built due to the membrane stretching during bonding could influence the final spherical shape. In fact, the black arrows indicate a slight upward deflection of the edges; however, the rest matches well with the original outline.

Appendix Table 1 Microfabrication details for POLYRETINA presented in Chapter 4.

Purpose	Step	Materials	Thickness / quantity	Machines, brand/type	Parameters, recipes, time	Comments on step
Base layer	PSS spin-coating and baking	Poly(4-styrenesulfonic acid) solution, Mw 75000, 18wt% H ₂ O, Aldrich	2.5 mL, 1-2 um	Spin-coater, Solar semi EL 200, PLM 707-1. Hotplate, Isotemp Fisher Sci	"MAL_PSS 1500rpm"; 1500rpm, 1000rpm/s, 60s. 145°C + tissue, 10min	Blow N2 gun whenever possible to remove any dust
	PDMS spin-coating and baking	PDMS 184 Sygard, 10:1 curing agent	4-5 g/wafer, 60um	Mixer Thinky, ARE-250, with 100mL cups. Spin-coater, Solar semi EL 200, PLM 707-1. Oven Binder	Mixer 2x. "Std 900rpm"; 900rpm, 100rpm/s, 60s. Oven @75°C for minimum 2hrs up to 1day	Blow N2 gun whenever possible to remove any dust
Parylene	Oxygen plasma + silanization	O ₂ ; silane Silquest A-174NT	200ul, silane	Plasma Diener Nano RFG 13.56/300. Parylene deposition Comelec C25S.	"LSBI std": 30W, 30s. Silane std recipe parylene	
	Parylene deposition	Parylene-C	5um	Parylene deposition Comelec C25S.	10g of Galxyl C precursor	
Pixels	PEDOT:PSS spin-coating and baking	PEDOT:PSS (+0.1vol% GOPS)	1mL, 90-100nm	Plasma Diener Nano RFG 13.56/300. Coater glovebox MBraun. Hotplate glovebox MBraun.	Plasma "surface activation"; 100W, 30s. Coat 3000rpm, 40s. Bake 115°C, 30min.	Do not cool down wafers prior coating blend
	P3HT:PCBM spin-coating and baking	P3HT:PCBM (20mg/mL)	300ul, 80-90nm	Coater glovebox MBraun. Hotplate glovebox MBraun.	Coat 1000rpm, 45s. Bake 115°C, 30min.	Coat blend warm (70°C from stirrer-HP)
	Ti/TiN deposition	Ti, TiN	100nm, 100nm	@ CMI: Magnetron sputter DP650, Alliance concept	"RTU_Ti-TiN" Ti: 333s, DC 400W, 5e-3. TiN: 666s, RF 200W, 5e-3.	Full wafer
	Photolithography	PR AZ9260	8um	Semi-automatic coater SolarSemi MLA 150 Heidelberg, Developer SolarSemi	Coat "AZ9260_8um", bake 5min @ 110°C + slow cooling from 40°C. EBR on same coater 5mm, 2x. Exposure 405nm, 410mJ/cm ² , +2 defocus. Develop "AZ9260_8um" + in case 1min	design 4POLY OEM 100-120 43000 PXL neg.
Encapsulation	Ti/TiN + polymers + parylene dry etching	Ti, TiN, polymers, parylene	200nm + 190nm + 5um	Dry etcher CORIAL 210 IL	"Al Ti Pt etch" 60 sec. "PY pure O ₂ " 6 min. Oven @75deg for 1-2 hrs.	
	OSTEmer spin-coating	OSTEmer 324 flex, Mercene labs. OR: black OSTE (see comments column for details).	12-14um	Balance GENSET Sartorius. Mixer Thinky, ARE-250, with 100mL cups. Plasma Diener Nano RFG 13.56/300. Spin-coater, Solar semi EL 200, PLM 707-1.	Mixer 2x. Plasma "LSBI std": 30W, 30s. Coat: 1500rpm, 100rpm/s, 60s; peak 2500rpm, 1000rpm/s, 1s. Black OSTE: 2500rpm, 100rpm/s, 60s; peak 3500rpm, 1000rpm/s, 1s.	Quick rinse of wafers in EtOH before starting. EBR acetone 1.5cm at 500rpm. Black OSTE preparation: OSTEflex part B + 2wt% of carbon black NPs (Nanografi 148nm), vortex for at least 1hr at 5-6, add part A OSTEflex (1 B: 1.24 A) and vortex for 30min again. Use roll mixer from wyss nanolab if possible (distance rolls 1.5um).
Bonding	OSTEmer exposure, development, and bake.	OSTEmer 324 flex. OR: black OSTE. Etchyl lactate, Sigma	4um	Mask aligner MJB4 Süss Microtec. Solvent bench. Hotplate C-MAG HP10, IKA lab.	MLA (375nm): 800mJ/cm ² , +3 defocus. Black OSTE : 1400mJ/cm ² . Bake 3min @ 75°C. Develop 3min30 in ethyl lactate, then strong IPA rinse + DI H ₂ O rinse. Bake @ 80°C overnight.	Baking of OSTE is recommended to be done after bonding on PDMS curved supports (when needed).
	Plasma			O ₂ Plasma Diener ZEPTO	15W, 30s, 0.5mbar	On PDMS support and bottom side of membrane
	Bonding	PDMS 184 Sygard, 5:1 curing agent		3D printed parts, Lab oven	Apply 1kg of pressure and keep @80°C overnight	See figure about bonding setup in annexes.
	Laser cutter			Laser cutter WS Turret 200	Galvo settings (300, 300, 75, 75, 85, 135, 200 rep)	Circle with radius 6.8mm aligned with pixels



Appendix Figure 7 Materials for nir-POLYRETINA. **A)** Stack of material and photovoltaic principle for the generation of charges. Holes will travel within PCPDTBT towards the anode PEDOT:PSS, while electrons will travel within PCBM towards the cathode Ti. **B)** Band diagram showing the conductors work functions and semiconductors HOMO-LUMO levels.²⁴⁴ **C)** Molecular structure of the concerned organic materials.



Appendix Figure 8 Possible molecular interactions between the organic layers of nir-POLYRETINA.

Appendix Equation 2 Calculation of equivalent absorption coefficients (Beer-Lambert law):

$$\alpha_{eq} = \frac{\sum \alpha_i t_i}{t_{eq}}$$

$$\alpha_{eq \text{ Domain}} = \frac{\alpha_{eq \text{ Ti}} \cdot A_{\text{Ti Domain}} + \alpha_{eq \text{ noTi}} \cdot A_{\text{noTi Domain}}}{A_{\text{tot Domain}}}$$

$$R = \frac{(\eta-1)^2 + \kappa^2}{(\eta+1)^2 + \kappa^2} = 0.63 \text{ for Ti (730 nm)}^{152}$$

$$\alpha_{\text{Ti}} = -\frac{1}{t} \log\left(\frac{T}{1-R}\right)$$

α : absorption coefficient, t : thickness, A : area, R : reflectance, η/κ : optical constants, T : transmittance

Appendix Equation 3 Calculation of equivalent specific heat capacity (rule of mixtures):

$$c_{eq} = \frac{\sum c_i m_i}{m_{eq}} \quad m_i = \delta_i V_i \quad m_{eq} = \sum m_i$$

c : specific heat capacity, m : mass, δ : density, V : volume

Appendix Equation 4 Calculation of equivalent thermal conductivity (equivalent thermal circuit):

$$R_{eq \text{ Domain}} = \frac{R_{eq \text{ Ti}} \cdot R_{eq \text{ noTi}}}{R_{eq \text{ Ti}} + R_{eq \text{ noTi}}}$$

$$R_{eq \text{ Ti (or noTi)}} = \sum R_i = \sum \frac{t_i}{k_i \cdot A_i}$$

$$k_{eq \text{ Domain}} = \frac{t_{\text{Domain}}}{R_{eq \text{ Domain}} \cdot A_{\text{Domain}}}$$

R : thermal resistance, t : thickness, k : thermal conductivity, A : area

Appendix Equation 5 Calculation of equivalent density (rule of mixtures):

$$\delta_{eq} = \frac{m_{eq}}{V_{eq}} = \frac{\sum \delta_i V_i}{V_{eq}}$$

m : mass, δ : density, V : volume

References

- [1] G. J. Andrews. “Ageing and Health.” In *International Encyclopedia of Human Geography*; **2009**; 31–35.
- [2] G. Vardi & J. Merrick. “Neurological Disorders: Public Health Challenges.” *Journal of Policy and Practice in Intellectual Disabilities* **2008**, 5 (1), 75–75.
- [3] J.-W. W. Jeong, G. Shin, S. Il Park, K. J. Yu, L. Xu, & J. A. Rogers. “Soft Materials in Neuroengineering for Hard Problems in Neuroscience.” *Neuron* **2015**, 86 (1), 175–186.
- [4] J. Rivnay, H. Wang, L. Fenno, K. Deisseroth, & G. G. Malliaras. “Next-Generation Probes, Particles, and Proteins for Neural Interfacing.” *Science Advances* **2017**, 3 (6), e1601649.
- [5] M. D. Ferro & N. A. Melosh. “Electronic and Ionic Materials for Neurointerfaces.” *Advanced Functional Materials* **2017**, 28 (12), 1704335.
- [6] S. Luan, I. Williams, K. Nikolic, & T. G. Constandinou. “Neuromodulation: Present and Emerging Methods.” *Frontiers in Neuroengineering* **2014**, 7, 27.
- [7] B. Roska & J.-A. Sahel. “Restoring Vision.” *Nature* **2018**, 557 (7705), 359–367.
- [8] L. Bruns, D. Mürbe, & A. Hahne. “Understanding Music with Cochlear Implants.” *Scientific Reports* **2016**, 6 (1), 32026.
- [9] F. M. Petrini, M. Bumbasirevic, G. Valle, V. Ilic, P. Mijović, P. Čvančara, F. Barberi, N. Katic, D. Bortolotti, D. Andreu, K. Lechler, A. Lesic, S. Mazic, B. Mijović, D. Guiraud, T. Stieglitz, A. Alexandersson, S. Micera, & S. Raspopovic. “Sensory Feedback Restoration in Leg Amputees Improves Walking Speed, Metabolic Cost and Phantom Pain.” *Nature Medicine* **2019**, 25 (9), 1356–1363.
- [10] P. Blomstedt, A. Fytagoridis, & S. Tisch. “Deep Brain Stimulation of the Posterior Subthalamic Area in the Treatment of Tremor.” *Acta Neurochirurgica* **2009**, 151 (1), 31–36.
- [11] F. B. Wagner, J.-B. Mignardot, C. G. Le Goff-Mignardot, R. Demesmaeker, S. Komi, M. Capogrosso, A. Rowald, I. Seáñez, M. Caban, E. Pirondini, M. Vat, L. A. McCracken, R. Heimgartner, I. Fodor, A. Watrin, P. Seguin, E. Paoles, K. Van Den Keybus, G. Eberle, B. Schurch, E. Pralong, F. Becce, J. Prior, N. Buse, R. Buschman, E. Neufeld, N. Kuster, S. Carda, J. von Zitzewitz, V. Delattre, T. Denison, H. Lambert, K. Minassian, J. Bloch, & G. Courtine. “Targeted Neurotechnology Restores Walking in Humans with Spinal Cord Injury.” *Nature* **2018**, 563 (7729), 65–71.
- [12] C. H. Chang, H. Y. Lane, & C. H. Lin. “Brain Stimulation in Alzheimer’s Disease.” *Frontiers in Psychiatry*. Frontiers Media SA **2018**, 201.
- [13] B. D. Greenberg, K. D. Askland, & L. L. Carpenter. “The Evolution of Deep Brain Stimulation for Neuropsychiatric Disorders.” *Frontiers in Bioscience* **2008**, Volume (13), 4638.
- [14] J. Luijckes, W. van den Brink, M. Feenstra, P. van den Munckhof, P. R. Schuurman, R. Schippers, A. Mazaheri, T. J. De Vries, & D. Denys. “Deep Brain Stimulation in Addiction: A Review of Potential Brain Targets.” *Molecular Psychiatry* **2012**, 17 (6), 572–583.
- [15] M. R. Mulvey, H. E. Radford, H. J. Fawkner, L. Hirst, V. Neumann, & M. I. Johnson. “Transcutaneous Electrical Nerve Stimulation for Phantom Pain and Stump Pain in Adult Amputees.” *Pain Practice* **2013**, 13 (4), 289–296.
- [16] H. Zhang, L. Xiao, B. Luo, J. Guo, L. Zhang, & J. Xie. “The Potential and Challenges of Time-Resolved Single-Photon Detection Based on Current-Carrying Superconducting Nanowires.” *Journal of Physics D: Applied Physics* **2020**, 53 (1), 013001.
- [17] Y. M. Sigal, R. Zhou, & X. Zhuang. “Visualizing and Discovering Cellular Structures with Super-Resolution Microscopy.” *Science*. American Association for the Advancement of Science **2018**, 880–887.
- [18] A. Djourno & C. Eyries. “Auditory Prosthesis by Means of a Distant Electrical Stimulation of the Sensory Nerve with the Use of an Indwelt Coiling.” *La Presse medicale* **1957**, 65 (63), 1417.

- [19] L. Galvani. “D Viribus Electricitatis in Motu Musculari: Commentarius.” *Press of the Academy of Sciences* **1791**.
- [20] C. LeRoy. “Où l’on Rend Compte de Quelques Tentatives Que l’on a Faites Pour Guérir Plusieurs Maladies Par l’électricité.” *Hist Acad Roy Sciences, Mémoire Math Phys.* **1755**, 60, 87.
- [21] M. Piccolino. “Luigi Galvani and Animal Electricity: Two Centuries after the Foundation of Electrophysiology.” *Trends in Neurosciences* **1997**, 20 (10), 443–448.
- [22] G. S. Brindley & W. S. Lewin. “The Sensations Produced by Electrical Stimulation of the Visual Cortex.” *The Journal of Physiology* **1968**, 196 (2), 479–493.
- [23] J. Marshall, T. W. Cronin, & S. Kleinlogel. “Stomatopod Eye Structure and Function: A Review.” *Arthropod Structure and Development.* **2007**, 420–448.
- [24] C.-H. Sung & J.-Z. Chuang. “The Cell Biology of Vision.” *The Journal of cell biology* **2010**, 190 (6), 953–963.
- [25] R. M. Mirochnik & J. S. Pezaris. “Contemporary Approaches to Visual Prostheses;” **2019**.
- [26] E. Zrenner. “Fighting Blindness with Microelectronics.” *Science Translational Medicine* **2013**, 5 (210), 210ps16-210ps16.
- [27] H. Kolb. “Gross Anatomy of the Eye;” **1995**.
- [28] J. Hirsch & C. A. Curcio. “The Spatial Resolution Capacity of Human Foveal Retina.” *Vision Research* **1989**, 29 (9), 1095–1101.
- [29] S. Lambertus, N. M. Bax, A. Fakin, J. M. M. Groenewoud, B. J. Klevering, A. T. Moore, M. Michaelides, A. R. Webster, G. J. Van Der Wilt, & C. B. Hoyng. “Highly Sensitive Measurements of Disease Progression in Rare Disorders: Developing and Validating a Multimodal Model of Retinal Degeneration in Stargardt Disease.” *PLoS ONE* **2017**, 12 (3), e0174020.
- [30] H. Strasburger, I. Rentschler, & M. Jüttner. “Peripheral Vision and Pattern Recognition: A Review.” *Journal of Vision* **2011**, 11 (5).
- [31] C. Owsley & G. McGwin. “Bidirectionality of the Association of Vision Impairment with Depression and Anxiety.” *JAMA Ophthalmology* **2019**, 137 (7), 801.
- [32] WHO. “International Classification of Diseases.” **2019**, 11th Revis.
- [33] R. R. A. Bourne, S. R. Flaxman, T. Braithwaite, M. V. Cicinelli, A. Das, J. B. Jonas, J. Keeffe, J. H. Kempen, J. Leasher, H. Limburg, K. Naidoo, K. Pesudovs, S. Resnikoff, A. Silvester, G. A. Stevens, N. Tahhan, T. Y. Wong, & H. R. Taylor. “Magnitude, Temporal Trends, and Projections of the Global Prevalence of Blindness and Distance and near Vision Impairment: A Systematic Review and Meta-Analysis.” *The Lancet Global Health* **2017**, 5 (9), e888–e897.
- [34] R. R. A. Bourne, G. A. Stevens, R. A. White, J. L. Smith, S. R. Flaxman, H. Price, J. B. Jonas, J. Keeffe, J. Leasher, K. Naidoo, K. Pesudovs, S. Resnikoff, & H. R. Taylor. “Causes of Vision Loss Worldwide, 1990-2010: A Systematic Analysis.” *The Lancet Global Health* **2013**, 1 (6).
- [35] D. T. Hartong, E. L. Berson, & T. P. Dryja. “Retinitis Pigmentosa.” *The Lancet* **2006**, 368 (9549), 1795–1809.
- [36] L. S. Lim, P. Mitchell, J. M. Seddon, F. G. Holz, & T. Y. Wong. “Age-Related Macular Degeneration.” *Lancet (London, England)* **2012**, 379 (9827), 1728–1738.
- [37] H. P. N. Scholl, R. W. Strauss, M. S. Singh, D. Dalkara, B. Roska, S. Picaud, & J.-A. Sahel. “Emerging Therapies for Inherited Retinal Degeneration.” *Science Translational Medicine* **2016**, 8 (368), 368rv6-368rv6.
- [38] J. O. Mills, A. Jalil, & P. E. Stanga. “Electronic Retinal Implants and Artificial Vision: Journey and Present.” *Eye* **2017**, 31 (10), 1383–1398.
- [39] A. L. Hodgkin & A. F. Huxley. “A Quantitative Description of Membrane Current and Its Application to Conduction and Excitation in Nerve.” *The Journal of Physiology* **1952**, 117 (4), 500–544.
- [40] S. C. Chen, G. J. Suaning, J. W. Morley, & N. H. Lovell. “Simulating Prosthetic Vision: I. Visual Models of Phosphenes.” *Vision Research.* **2009**, 1493–1506.

- [41] N. C. Sinclair, M. N. Shivdasani, T. Perera, L. N. Gillespie, H. J. McDermott, L. N. Ayton, & P. J. Blamey. “The Appearance of Phosphenes Elicited Using a Suprachoroidal Retinal Prosthesis.” *Investigative Ophthalmology and Visual Science* **2016**, 57 (11), 4948–4961.
- [42] C. Hassler, T. Boretius, & T. Stieglitz. “Polymers for Neural Implants;” John Wiley & Sons, Ltd, **2011**; Vol. 49, 18–33.
- [43] B. Jones. Bionic implants – Jonesblog <https://prometheus.med.utah.edu/~bwjones/2009/08/bionic-implants/> (accessed **2020**).
- [44] P. Hickey & M. Stacy. “Deep Brain Stimulation: A Paradigm Shifting Approach to Treat Parkinson’s Disease.” *Frontiers in Neuroscience*. Frontiers Research Foundation **2016**.
- [45] K. T. Mullen, S. O. Dumoulin, & R. F. Hess. “Color Responses of the Human Lateral Geniculate Nucleus: Selective Amplification of S-Cone Signals between the Lateral Geniculate Nucleus and Primary Visual Cortex Measured with High-Field fMRI.” *European Journal of Neuroscience* **2008**, 28 (9), 1911–1923.
- [46] F. Panetsos, A. Sanchez-Jimenez, E. D. De Cerio, I. Diaz-Guemes, & F. M. Sanchez. “Consistent Phosphenes Generated by Electrical Microstimulation of the Visual Thalamus. An Experimental Approach for Thalamic Visual Neuroprostheses.” *Frontiers in Neuroscience* **2011**, 5 (JUL), 84.
- [47] A. Najarpour Foroushani, C. C. Pack, & M. Sawan. “Cortical Visual Prostheses: From Microstimulation to Functional Percept.” *Journal of Neural Engineering* **2018**, 15 (2).
- [48] C. I. Baker, D. D. Dilks, E. Peli, & N. Kanwisher. “Reorganization of Visual Processing in Macular Degeneration: Replication and Clues about the Role of Foveal Loss.” *Vision Research* **2008**, 48 (18), 1910–1919.
- [49] E. Fernandez. “Development of Visual Neuroprostheses: Trends and Challenges.” *Bioelectronic Medicine* **2018**, 4 (1).
- [50] R. A. Normann, E. M. Maynard, P. J. Rousche, & D. J. Warren. “A Neural Interface for a Cortical Vision Prosthesis.” *Vision Research* **1999**, 39 (15), 2577–2587.
- [51] E. Fernández, B. Greger, P. A. House, I. Aranda, C. Botella, J. Albiñá, C. Soto-Sánchez, A. Alfaro, & R. A. Normann. “Acute Human Brain Responses to Intracortical Microelectrode Arrays: Challenges and Future Prospects.” *Frontiers in Neuroengineering*. Frontiers Research Foundation **2014**.
- [52] M. Vaiman, R. Abuita, & I. Bekerman. “Optic Nerve Sheath Diameters in Healthy Adults Measured by Computer Tomography.” *International Journal of Ophthalmology* **2015**, 8 (6), 1240–1244.
- [53] C. Veraart, M.-C. Wanet-Defalque, B. Gérard, A. Vanlierde, & J. Delbeke. “Pattern Recognition with the Optic Nerve Visual Prosthesis.” *Artificial Organs* **2003**, 27 (11), 996–1004.
- [54] J. Badia, T. Boretius, D. Andreu, C. Azevedo-Coste, T. Stieglitz, & X. Navarro. “Comparative Analysis of Transverse Intrafascicular Multichannel, Longitudinal Intrafascicular and Multipolar Cuff Electrodes for the Selective Stimulation of Nerve Fascicles.” *Journal of Neural Engineering* **2011**, 8 (3).
- [55] S. Micera, J. Carpaneto, & S. Raspopovic. “Control of Hand Prostheses Using Peripheral Information.” *IEEE Reviews in Biomedical Engineering* **2010**, 3, 48–68.
- [56] E. H. Rijnbeek, N. Eleveld, & W. Olthuis. “Update on Peripheral Nerve Electrodes for Closed-Loop Neuroprosthetics.” *Frontiers in Neuroscience* **2018**, 12.
- [57] T. Boretius, J. Badia, A. Pascual-Font, M. Schuettler, X. Navarro, K. Yoshida, & T. Stieglitz. “A Transverse Intrafascicular Multichannel Electrode (TIME) to Interface with the Peripheral Nerve.” *Biosensors and Bioelectronics* **2010**, 26 (1), 62–69.
- [58] A. Cutrone, J. Del Valle, D. Santos, J. Badia, C. Filippeschi, S. Micera, X. Navarro, & S. Bossi. “A Three-Dimensional Self-Opening Intraneural Peripheral Interface (SELINe).” *Journal of Neural Engineering* **2015**, 12 (1), 016016.
- [59] V. Gaillet, A. Cutrone, F. Artoni, P. Vagni, A. Mega Pratiwi, S. A. Romero, D. Lipucci Di Paola, S. Micera, & D. Ghezzi. “Spatially Selective Activation of the Visual Cortex via Intraneural Stimulation of the Optic Nerve.” *Nature Biomedical Engineering* **2020**, 4 (2), 181–194.

- [60] H. Sakaguchi, M. Kamei, T. Fujikado, E. Yonezawa, M. Ozawa, C. Cecilia-Gonzalez, O. Ustariz-Gonzalez, H. Quiroz-Mercado, & Y. Tano. "Artificial Vision by Direct Optic Nerve Electrode (AV-DONE) Implantation in a Blind Patient with Retinitis Pigmentosa." *Journal of Artificial Organs* **2009**, 12 (3), 206–209.
- [61] H. Wassle & B. B. Boycott. "Functional Architecture of the Mammalian Retina." *Physiological Reviews*. **1991**, 447–480.
- [62] R. E. Marc, B. W. Jones, C. B. Watt, & E. Strettoi. "Neural Remodeling in Retinal Degeneration." *Progress in Retinal and Eye Research*. Elsevier Ltd **2003**, 607–655.
- [63] D. Ghezzi. "Retinal Prostheses: Progress toward the next Generation Implants." *Neural Technology* **2015**, 9, 290.
- [64] Y. H.-L. Luo & L. da Cruz. "The Argus® II Retinal Prosthesis System." *Progress in Retinal and Eye Research* **2016**, 50, 89–107.
- [65] K. Stingl, K. U. Bartz-Schmidt, D. Besch, C. K. Chee, C. L. Cottrill, F. Gekeler, M. Groppe, T. L. Jackson, R. E. MacLaren, A. Koitschev, A. Kusnyerik, J. Neffendorf, J. Nemeth, M. A. N. Naeem, T. Peters, J. D. Ramsden, H. Sachs, A. Simpson, M. S. Singh, B. Wilhelm, D. Wong, & E. Zrenner. "Subretinal Visual Implant Alpha IMS - Clinical Trial Interim Report." *Vision Research* **2015**, 111, 149–160.
- [66] E. Bloch, Y. Luo, L. da Cruz, & L. Cruz. "Advances in Retinal Prosthesis Systems." *Therapeutic advances in ophthalmology* **2019**, 11.
- [67] K. Stingl, R. Schippert, K. U. Bartz-Schmidt, D. Besch, C. L. Cottrill, T. L. Edwards, F. Gekeler, U. Greppmaier, K. Kiel, A. Koitschev, L. Kühlewein, R. E. MacLaren, J. D. Ramsden, J. Roeder, A. Rothermel, H. Sachs, G. S. Schröder, J. Tode, N. Troelenberg, & E. Zrenner. "Interim Results of a Multicenter Trial with the New Electronic Subretinal Implant Alpha AMS in 15 Patients Blind from Inherited Retinal Degenerations." *Frontiers in Neuroscience* **2017**, 11 (AUG), 445.
- [68] H. Lorach, G. Goetz, R. Smith, X. Lei, Y. Mandel, T. Kamins, K. Mathieson, P. Huie, J. Harris, A. Sher, & D. Palanker. "Photovoltaic Restoration of Sight with High Visual Acuity." *Nature Medicine* **2015**, 21 (5), 476–482.
- [69] Pixium Vision - Prima gearing up for a pivotal year | Edison <https://www.edisongroup.com/publication/prima-gearing-up-for-a-pivotal-year/23922/> (accessed **2020**).
- [70] K. Mathieson, J. Loudin, G. Goetz, P. Huie, L. Wang, T. I. Kamins, L. Galambos, R. Smith, J. S. Harris, A. Sher, & D. Palanker. "Photovoltaic Retinal Prosthesis with High Pixel Density." *Nature Photonics* **2012**, 6 (6), 391–397.
- [71] R. Daschner, A. Rothermel, R. Rudolf, S. Rudolf, & A. Stett. "Functionality and Performance of the Subretinal Implant Chip Alpha AMS." *Sensors and Materials* **2018**, 30 (2), 179–192.
- [72] L. N. Ayton, N. Barnes, G. Dagnelie, T. Fujikado, G. Goetz, R. Hornig, B. W. Jones, M. M. K. Muqit, D. L. Rathbun, K. Stingl, J. D. Weiland, & M. A. Petoe. "An Update on Retinal Prostheses." *Clinical Neurophysiology* **2019**.
- [73] C. Koch, W. Mokwa, M. Goertz, & P. Walter. "First Results of a Study on a Completely Implanted Retinal Prosthesis in Blind Humans." In *Proceedings of IEEE Sensors*; **2008**; 1237–1240.
- [74] P. Walter, Z. F. Kisvárdy, M. Görtz, N. Alteheld, G. Rossler, T. Stieglitz, & U. T. Eysel. "Cortical Activation via an Implanted Wireless Retinal Prosthesis." *Investigative Ophthalmology and Visual Science* **2005**, 46 (5), 1780–1785.
- [75] A. Y. Chow, V. Y. Chow, K. H. Packo, J. S. Pollack, G. A. Peyman, & R. Schuchard. "The Artificial Silicon Retina Microchip for the Treatment of Vision Loss from Retinitis Pigmentosa." *Archives of Ophthalmology* **2004**, 122 (4), 460–469.
- [76] C. J. Abbott, D. A. X. Nayagam, C. D. Luu, S. B. Epp, R. A. Williams, C. M. Salinas-LaRosa, J. Villalobos, C. McGowan, M. N. Shivdasani, O. Burns, J. Leavens, J. Yeoh, A. A. Brandli, P. C. Thien, J. Zhou, H. Feng, C. E. Williams, R. K. Shepherd, & P. J. Allen. "Safety Studies for a 44-Channel Suprachoroidal Retinal Prosthesis: A Chronic Passive Study." *Investigative Ophthalmology and Visual Science* **2018**, 59 (3), 1410–1424.

- [77] T. Fujikado, M. Kamei, H. Sakaguchi, H. Kanda, T. Endo, M. Hirota, T. Morimoto, K. Nishida, H. Kishima, Y. Terasawa, K. Oosawa, M. Ozawa, & K. Nishida. "One-Year Outcome of 49-Channel Suprachoroidal–Transretinal Stimulation Prosthesis in Patients with Advanced Retinitis Pigmentosa." *Investigative Ophthalmology and Visual Science* **2016**, 57 (14), 6147–6157.
- [78] F. S. Werblin & J. E. Dowling. "Organization of the Retina of the Mudpuppy, *Necturus Maculosus*. II. Intracellular Recording." *Journal of neurophysiology* **1969**, 32 (3), 339–355.
- [79] J. E. Dowling. "Retina: An Overview." In *Encyclopedia of Neuroscience*; Elsevier Ltd, **2009**; 159–169.
- [80] S. S. Patterson, M. Neitz, & J. Neitz. "Reconciling Color Vision Models With Midget Ganglion Cell Receptive Fields." *Frontiers in Neuroscience* **2019**, 13.
- [81] D. Boinagrov, S. Pangratz-Fuehrer, G. Goetz, & D. Palanker. "Selectivity of Direct and Network-Mediated Stimulation of the Retinal Ganglion Cells with Epi-, Sub- and Intraretinal Electrodes." *Journal of Neural Engineering* **2014**, 11 (2), 026008.
- [82] M. Eickenscheidt, M. Jenkner, R. Thewes, P. Fromherz, & G. Zeck. "Electrical Stimulation of Retinal Neurons in Epiretinal and Subretinal Configuration Using a Multicapacitor Array." *Journal of Neurophysiology* **2012**, 107 (10), 2742–2755.
- [83] D. Nanduri, I. Fine, A. Horsager, G. M. Boynton, M. S. Humayun, R. J. Greenberg, & J. D. Weiland. "Frequency and Amplitude Modulation Have Different Effects on the Percepts Elicited by Retinal Stimulation." *Investigative Ophthalmology and Visual Science* **2012**, 53 (1), 205–214.
- [84] E. Z. Blumenthal. "Glaucoma, the Requisites in Ophthalmology." *Journal of Glaucoma* **2000**, 9 (3), 280.
- [85] N. M. Jansonius, J. Nevalainen, B. Selig, L. M. Zangwill, P. A. Sample, W. M. Budde, J. B. Jonas, W. A. Lagrèze, P. J. Airaksinen, R. Vonthein, L. A. Levin, J. Paetzold, & U. Schiefer. "A Mathematical Description of Nerve Fiber Bundle Trajectories and Their Variability in the Human Retina." *Vision Research* **2009**, 49 (17), 2157–2163.
- [86] M. Beyeler, G. M. Boynton, I. Fine, & A. Rokem. "Pulse2percept: A Python-Based Simulation Framework for Bionic Vision." In *PROC. OF THE 16th PYTHON IN SCIENCE CONF.*; **2017**.
- [87] I. Fine & G. M. Boynton. "Pulse Trains to Percepts: The Challenge of Creating a Perceptually Intelligible World with Sight Recovery Technologies." *Philosophical Transactions of the Royal Society B: Biological Sciences* **2015**, 370 (1677).
- [88] A. K. Ahuja, J. Yeoh, J. D. Dorn, A. Caspi, V. Wuyyuru, M. J. McMahon, M. S. Humayun, R. J. Greenberg, L. daCruz, & Argus II Study Group. "Factors Affecting Perceptual Threshold in Argus II Retinal Prosthesis Subjects." *Translational Vision Science & Technology* **2013**, 2 (4), 1.
- [89] D. Palanker, A. Vankov, P. Huie, & S. Baccus. "Design of a High-Resolution Optoelectronic Retinal Prosthesis." *Journal of Neural Engineering* **2005**, 2 (1), S105.
- [90] K. Cha, K. W. Horch, & R. A. Normann. "Mobility Performance with a Pixelized Vision System." *Vision Research* **1992**, 32 (7).
- [91] G. Dagnelie, P. Keane, V. Narla, L. Yang, J. Weiland, & M. Humayun. "Real and Virtual Mobility Performance in Simulated Prosthetic Vision." *Journal of Neural Engineering* **2007**, 4 (1).
- [92] H. Ameri, T. Ratanapakorn, S. Ufer, H. Eckhardt, M. S. Humayun, & J. D. Weiland. "Toward a Wide-Field Retinal Prosthesis." *Journal of Neural Engineering* **2009**, 6 (3), 035002.
- [93] H. Kasi, W. Hasenkamp, G. Cosendai, A. Bertsch, & P. Renaud. "Simulation of Epiretinal Prostheses - Evaluation of Geometrical Factors Affecting Stimulation Thresholds." *Journal of NeuroEngineering and Rehabilitation* **2011**, 8 (1), 44.
- [94] F. Waschowski, S. Hesse, A. C. Rieck, T. Lohmann, C. Brockmann, T. Laube, N. Bornfeld, G. Thumann, P. Walter, W. Mokwa, S. Johnen, & G. Roessler. "Development of Very Large Electrode Arrays for Epiretinal Stimulation (VLARS)." *BioMedical Engineering Online* **2014**, 13 (1), 11.
- [95] The Lasker/IRRF Initiative for Innovation in Vision Science. "Restoring Vision to the Blind." *Translational Vision Science & Technology* **2014**, 3 (7), 1.

- [96] A. Pérez Fornos, J. Sommerhalder, B. Rappaz, A. B. Safran, & M. Pelizzone. “Simulation of Artificial Vision, III: Do the Spatial or Temporal Characteristics of Stimulus Pixelization Really Matter?” *Investigative Ophthalmology and Visual Science* **2005**, 46 (10), 3906–3912.
- [97] J.-H. H. Jung, D. Aloni, Y. Yitzhaky, & E. Peli. “Active Confocal Imaging for Visual Prostheses.” *Vision Research* **2015**, 111, 182–196.
- [98] L. Ferlauto, M. J. I. Airaghi Leccardi, N. A. L. Chenais, S. C. A. Gilliéron, P. Vagni, M. Bevilacqua, T. J. Wolfensberger, K. Sivula, & D. Ghezzi. “Design and Validation of a Foldable and Photovoltaic Wide-Field Epiretinal Prosthesis.” *Nature Communications* **2018**, 9 (1), 992.
- [99] G. Polino, C. Lubrano, G. Ciccone, & F. Santoro. “Photogenerated Electrical Fields for Biomedical Applications.” *Frontiers in bioengineering and biotechnology* **2018**, 6 (November), 167.
- [100] D. M. Bagnall & M. Boreland. “Photovoltaic Technologies.” *Energy Policy* **2008**, 36 (12), 4390–4396.
- [101] W. Shockley. “The Theory of P-n Junctions in Semiconductors and P-n Junction Transistors.” *Bell System Technical Journal* **1949**, 28 (3), 435–489.
- [102] M. T. Greiner & Z. H. Lu. “Thin-Film Metal Oxides in Organic Semiconductor Devices: Their Electronic Structures, Work Functions and Interfaces.” *NPG Asia Materials* **2013**, 5 (7).
- [103] B. J. Skromme. “Junctions and Barriers.” In *Encyclopedia of Materials: Science and Technology*; Elsevier, **2003**; 1–12.
- [104] F. Recart & A. Cuevas. “Application of Junction Capacitance Measurements to the Characterization of Solar Cells.” *IEEE Transactions on Electron Devices* **2006**, 53 (3), 442–448.
- [105] T. Flores, T. Huang, M. Bhuckory, E. Ho, Z. Chen, R. Dalal, L. Galambos, T. Kamins, K. Mathieson, & D. Palanker. “Honeycomb-Shaped Electro-Neural Interface Enables Cellular-Scale Pixels in Subretinal Prosthesis.” *Scientific Reports* **2019**, 9 (1).
- [106] A. Babayigit, A. Ethirajan, M. Muller, & B. Conings. “Toxicity of Organometal Halide Perovskite Solar Cells.” *Nature Materials* **2016**, 15 (3), 247–251.
- [107] K. A. Mazzi & C. K. Luscombe. “The Future of Organic Photovoltaics.” *Chemical Society Reviews*. Royal Society of Chemistry **2015**, 78–90.
- [108] D. Rand, M. Jakešová, G. Lubin, I. Věbřitě, M. David-pur, V. Ďerek, T. Cramer, N. S. Sariciftci, Y. Hanein, & E. D. Głowacki. “Direct Electrical Neurostimulation with Organic Pigment Photocapacitors.” *Advanced Materials* **2018**, 30 (25), 1707292.
- [109] G. Dennler, M. C. Scharber, & C. J. Brabec. “Polymer-Fullerene Bulk-Heterojunction Solar Cells.” *Advanced Materials* **2009**, 21 (13), 1323–1338.
- [110] V. Gautam, D. Rand, Y. Hanein, & K. S. Narayan. “A Polymer Optoelectronic Interface Provides Visual Cues to a Blind Retina.” *Advanced Materials* **2014**, 26 (11), 1751–1756.
- [111] J. F. Maya-Vetencourt, D. Ghezzi, M. R. Antognazza, E. Colombo, M. Mete, P. Feyen, A. Desii, A. Buschiazzi, M. Di Paolo, S. Di Marco, F. Ticconi, L. Emionite, D. Shmal, C. Marini, I. Donelli, G. Freddi, R. MacCarone, S. Bisti, G. Sambuceti, G. Pertile, G. Lanzani, & F. Benfenati. “A Fully Organic Retinal Prosthesis Restores Vision in a Rat Model of Degenerative Blindness.” *Nature Materials* **2017**, 16 (6), 681–689.
- [112] D. Ghezzi, M. R. Antognazza, R. MacCarone, S. Bellani, E. Lanzarini, N. Martino, M. Mete, G. Pertile, S. Bisti, G. Lanzani, & F. Benfenati. “A Polymer Optoelectronic Interface Restores Light Sensitivity in Blind Rat Retinas.” *Nature Photon* **2013**, 7 (5), 400–406.
- [113] S. M. McAfee, J. M. Topple, I. G. Hill, & G. C. Welch. “Key Components to the Recent Performance Increases of Solution Processed Non-Fullerene Small Molecule Acceptors.” *Journal of Materials Chemistry A* **2015**, 3 (32), 16393–16408.
- [114] F. Rattay. “The Basic Mechanism for the Electrical Stimulation of the Nervous System.” *Neuroscience* **1999**, 89 (2), 335–346.
- [115] Y. Park, V. Choong, Y. Gao, B. R. Hsieh, & C. W. Tang. “Work Function of Indium Tin Oxide Transparent Conductor Measured by Photoelectron Spectroscopy.” *Applied Physics Letters* **1996**, 68

- (19), 2699–2701.
- [116] A. W. Hains & T. J. Marks. “High-Efficiency Hole Extraction/Electron-Blocking Layer to Replace Poly(3,4-Ethylenedioxythiophene):Poly(Styrene Sulfonate) in Bulk-Heterojunction Polymer Solar Cells.” *Applied Physics Letters* **2008**, 92 (2).
- [117] S. Ahn, S.-H. Jeong, T.-H. Han, & T.-W. Lee. “Conducting Polymers as Anode Buffer Materials in Organic and Perovskite Optoelectronics.” *Advanced Optical Materials* **2017**, 5 (3), 1600512.
- [118] D. K. Freeman & S. I. Fried. “Multiple Components of Ganglion Cell Desensitization in Response to Prosthetic Stimulation.” *Journal of neural engineering* **2011**, 8 (1), 016008.
- [119] J. Davis, Y. H. Hsieh, & H. C. Lee. “Humans Perceive Flicker Artifacts at 500 Hz.” *Scientific Reports* **2015**, 5 (1), 7861.
- [120] F. C. Delori, R. H. Webb, & D. H. Sliney. “Maximum Permissible Exposures for Ocular Safety (ANSI 2000), with Emphasis on Ophthalmic Devices.” *Journal of the Optical Society of America A* **2007**, 24 (5), 1250.
- [121] D. Ghezzi, M. R. Antognazza, M. Dal Maschio, E. Lanzarini, F. Benfenati, & G. Lanzani. “A Hybrid Bioorganic Interface for Neuronal Photoactivation.” *Nature Communications* **2011**, 2 (1), 166.
- [122] M. R. Antognazza, M. Di Paolo, D. Ghezzi, M. Mete, S. Di Marco, J. F. Maya-Vetencourt, R. Maccarone, A. Desii, F. Di Fonzo, M. Bramini, A. Russo, L. Laudato, I. Donelli, M. Cilli, G. Freddi, G. Pertile, G. Lanzani, S. Bisti, & F. Benfenati. “Characterization of a Polymer-Based, Fully Organic Prosthesis for Implantation into the Subretinal Space of the Rat.” *Advanced Healthcare Materials* **2016**, 5 (17), 2271–2282.
- [123] D. Y. Lee, H. Lorach, P. Huie, & D. Palanker. “Implantation of Modular Photovoltaic Subretinal Prosthesis.” *Ophthalmic Surgery Lasers and Imaging Retina* **2016**, 47 (2), 171–174.
- [124] I. R. Minev, P. Musienko, A. Hirsch, Q. Barraud, N. Wenger, E. M. Moraud, J. Gandar, M. Capogrosso, T. Milekovic, L. Asboth, R. F. Torres, N. Vachicouras, Q. Liu, N. Pavlova, S. Duis, A. Larmagnac, J. Vörös, S. Micera, Z. Suo, G. Courtine, & S. P. Lacour. “Electronic Dura Mater for Long-Term Multimodal Neural Interfaces.” *Science* **2015**, 347 (6218), 159–163.
- [125] L. Baretke, N. Waiskopf, D. Rand, G. Lubin, M. David-Pur, J. Ben-Dov, S. Roy, C. Eleftheriou, E. Sernagor, O. Cheshnovsky, U. Banin, & Y. Hanein. “Semiconductor Nanorod-Carbon Nanotube Biomimetic Films for Wire-Free Photostimulation of Blind Retinas.” *Nano Letters* **2014**, 14 (11), 6685–6692.
- [126] S. F. Cogan. “Neural Stimulation and Recording Electrodes.” *Annual Review of Biomedical Engineering* **2008**, 10 (1), 275–309.
- [127] D. R. Merrill, M. Bikson, & J. G. R. R. Jefferys. “Electrical Stimulation of Excitable Tissue: Design of Efficacious and Safe Protocols.” *Journal of Neuroscience Methods* **2005**, 141 (2), 171–198.
- [128] W. Franks, I. Schenker, P. Schmutz, & A. Hierlemann. “Impedance Characterization and Modeling of Electrodes for Biomedical Applications.” *IEEE Transactions on Biomedical Engineering* **2005**, 52 (7), 1295–1302.
- [129] D. Boinagrov, X. Lei, G. Goetz, T. I. Kamins, K. Mathieson, L. Galambos, J. S. Harris, & D. Palanker. “Photovoltaic Pixels for Neural Stimulation: Circuit Models and Performance.” *IEEE Transactions on Biomedical Circuits and Systems* **2016**, 10 (1), 85–97.
- [130] B. Chang, N. L. Hawes, M. T. Pardue, A. M. German, R. E. Hurd, M. T. Davisson, S. Nusinowitz, K. Rengarajan, A. P. Boyd, S. S. Sidney, M. J. Phillips, R. E. Stewart, R. Chaudhury, J. M. Nickerson, J. R. Heckenlively, & J. H. Boatright. “Two Mouse Retinal Degenerations Caused by Missense Mutations in the β -Subunit of Rod CGMP Phosphodiesterase Gene.” *Vision Research* **2007**, 47 (5), 624–633.
- [131] B. Chang, N. L. Hawes, R. E. Hurd, M. T. Davisson, S. Nusinowitz, & J. R. Heckenlively. “Retinal Degeneration Mutants in the Mouse.” *Vision Research* **2002**, 42 (4), 517–525.
- [132] A. Stett, W. Barth, S. Weiss, H. Haemmerle, & E. Zrenner. “Electrical Multisite Stimulation of the Isolated Chicken Retina.” *Vision Research* **2000**, 40 (13), 1785–1795.
- [133] A. Romeo, Q. Liu, Z. Suo, & S. P. Lacour. “Elastomeric Substrates with Embedded Stiff Platforms

- for Stretchable Electronics.” *Applied Physics Letters* **2013**, 102 (13), 131904.
- [134] H. Lorach, J. Wang, D. Y. Lee, R. Dalal, P. Huie, & D. Palanker. “Retinal Safety of near Infrared Radiation in Photovoltaic Restoration of Sight.” *Biomedical Optics Express* **2016**, 7 (1), 13.
- [135] D. Van Norren & J. J. Vos. “Light Damage to the Retina: An Historical Approach.” *Eye (Basingstoke)*. Nature Publishing Group **2016**, 169–172.
- [136] A. Ahnood, H. Meffin, D. J. Garrett, K. Fox, K. Ganesan, A. Stacey, N. V. Apollo, Y. T. Wong, S. G. Lichter, W. Kentler, O. Kavehei, U. Greferath, K. A. Vessey, M. R. Ibbotson, E. L. Fletcher, A. N. Burkitt, & S. Praver. “Diamond Devices for High Acuity Prosthetic Vision.” *Advanced Biosystems* **2017**, 1 (1–2), 1600003.
- [137] J. R. Tumbleston, D. H. Ko, E. T. Samulski, & R. Lopez. “Analyzing Local Exciton Generation Profiles as a Means to Extract Transport Lengths in Organic Solar Cells.” *Physical Review B - Condensed Matter and Materials Physics* **2010**, 82 (20), 205325.
- [138] D. Gupta, M. Bag, & K. S. Narayan. “Area Dependent Efficiency of Organic Solar Cells.” *Applied Physics Letters* **2008**, 93 (16), 163301.
- [139] E. Zrenner, K. U. Bartz-Schmidt, H. Benav, D. Besch, A. Bruckmann, V.-P. P. V.-P. Gabel, F. Gekeler, U. Greppmaier, A. Harscher, S. Kibbel, J. Koch, A. Kusnyerik, T. Peters, K. Stingl, H. Sachs, A. Stett, P. Szurman, B. Wilhelm, R. Wilke, P. Szurma, B. Wilhelm, & R. Wilke. “Subretinal Electronic Chips Allow Blind Patients to Read Letters and Combine Them to Words.” *Proceedings of the Royal Society B: Biological Sciences* **2011**, 278 (1711), 1489–1497.
- [140] J. D. Dorn, A. K. Ahuja, A. Caspi, L. Da Cruz, G. Dagnelie, J. A. Sahel, R. J. Greenberg, & M. J. McMahon. “The Detection of Motion by Blind Subjects with the Epiretinal 60-Electrode (Argus II) Retinal Prosthesis.” *JAMA Ophthalmology* **2013**, 131 (2), 183–189.
- [141] A. P. Fornos, J. Sommerhalder, L. da Cruz, J. A. Sahel, S. Mohand-Said, F. Hafezi, & M. Pelizzone. “Temporal Properties of Visual Perception on Electrical Stimulation of the Retina.” *Investigative Ophthalmology and Visual Science* **2012**, 53 (6), 2720–2731.
- [142] A. C. Weitz, D. Nanduri, M. R. Behrend, A. Gonzalez-Calle, R. J. Greenberg, M. S. Humayun, R. H. Chow, & J. D. Weiland. “Improving the Spatial Resolution of Epiretinal Implants by Increasing Stimulus Pulse Duration.” *Science translational medicine* **2015**, 7 (318), 318ra203–318ra203.
- [143] L. Yue, P. Falabella, P. Christopher, V. Wuyyuru, J. Dorn, P. Schor, R. J. Greenberg, J. D. Weiland, & M. S. Humayun. “Ten-Year Follow-up of a Blind Patient Chronically Implanted with Epiretinal Prosthesis Argus I.” *Ophthalmology* **2015**, 122 (12), 2545-2552.e1.
- [144] R. J. Jensen & J. F. Rizzo. “Thresholds for Activation of Rabbit Retinal Ganglion Cells with a Subretinal Electrode.” *Experimental Eye Research* **2006**, 83 (2), 367–373.
- [145] M. R. Behrend, A. K. Ahuja, M. S. Humayun, R. H. Chow, & J. D. Weiland. “Resolution of the Epiretinal Prosthesis Is Not Limited by Electrode Size.” *IEEE Transactions on Neural Systems and Rehabilitation Engineering* **2011**, 19 (4), 436–442.
- [146] A. N. Kuo, P. K. Verkicharla, R. P. McNabb, C. Y. Cheung, S. Hilal, S. Farsiu, C. Chen, T. Y. Wong, M. Kamran Ikram, C. Y. Cheng, T. L. Young, S. M. Saw, & J. A. Izatt. “Posterior Eye Shape Measurement with Retinal OCT Compared to MRI.” *Investigative Ophthalmology and Visual Science* **2016**, 57 (9), 196–203.
- [147] Dellis Jean-Luc. Zfit - File Exchange - MATLAB Central <https://www.mathworks.com/matlabcentral/fileexchange/19460-zfit> (accessed **2020**).
- [148] X. Lei, S. Kane, S. Cogan, H. Lorach, L. Galambos, P. Huie, K. Mathieson, T. Kamins, J. Harris, & D. Palanker. “SiC Protective Coating for Photovoltaic Retinal Prosthesis.” *Journal of Neural Engineering* **2016**, 13 (4), 046016.
- [149] D. W. L. Hukins, A. Mahomed, & S. N. Kukureka. “Accelerated Aging for Testing Polymeric Biomaterials and Medical Devices.” *Medical Engineering and Physics* **2008**, 30 (10), 1270–1274.
- [150] R. Q. Quiroga, Z. Nadasdy, & Y. Ben-Shaul. “Unsupervised Spike Detection and Sorting with Wavelets and Superparamagnetic Clustering.” *Neural Computation* **2004**, 16 (8), 1661–1687.
- [151] M. Hammer, A. Roggan, D. Schweitzer, & G. Muller. “Optical Properties of Ocular Fundus Tissues-

- an in Vitro Study Using the Double-Integrating-Sphere Technique and Inverse Monte Carlo Simulation.” *Physics in Medicine and Biology* **1995**, 40 (6), 963–978.
- [152] P. B. Johnson & R. W. Christy. “Optical Constants of Transition Metals: Ti, V, Cr, Mn, Fe, Co, Ni, and Pd.” *Physical Review B* **1974**, 9 (12), 5056–5070.
- [153] J. S. Brown, D. I. Flitcroft, G. S. Ying, E. L. Francis, G. F. Schmid, G. E. Quinn, & R. A. Stone. “In Vivo Human Choroidal Thickness Measurements: Evidence for Diurnal Fluctuations.” *Investigative Ophthalmology and Visual Science* **2009**, 50 (1), 5–12.
- [154] N. E. Stankova, P. A. Atanasov, R. G. Nikov, R. G. Nikov, N. N. Nedyalkov, T. R. Stoyanov, N. Fukata, K. N. Kolev, E. I. Valova, J. S. Georgieva, & S. A. Armanov. “Optical Properties of Polydimethylsiloxane (PDMS) during Nanosecond Laser Processing.” *Applied Surface Science* **2016**, 374, 96–103.
- [155] J. Müllerová, M. Kaiser, V. Nádaždy, P. Šiffalovič, & E. Majková. “Optical Absorption Study of P3HT: PCBM Blend Photo-Oxidation for Bulk Heterojunction Solar Cells.” *Solar Energy* **2016**, 134, 294–301.
- [156] J. E. Mark. “Polymer Data Handbook;” Oxford University Press: New York, **1999**.
- [157] A. Narasimhan & K. K. Jha. “Bio-Heat Transfer Simulation of Square and Circular Array of Retinal Laser Irradiation.” *Frontiers in Heat and Mass Transfer* **2011**, 2 (3).
- [158] D. K. Sardar, B. G. Yust, F. J. Barrera, L. C. Mimun, & A. T. C. Tsin. “Optical Absorption and Scattering of Bovine Cornea, Lens and Retina in the Visible Region.” *Lasers in Medical Science* **2009**, 24 (6), 839–847.
- [159] S. A. Mirnezami, M. R. Jafarabadi, & M. Abrishami. “Temperature Distribution Simulation of the Human Eye Exposed to Laser Radiation.” *Journal of Lasers in Medical Sciences* **2013**, 4 (4), 175–181.
- [160] K. Gosalia, J. Weiland, M. Humayun, & G. Lazzi. “Thermal Elevation in the Human Eye and Head Due to the Operation of a Retinal Prosthesis.” *IEEE Transactions on Biomedical Engineering* **2004**, 51 (8), 1469–1477.
- [161] N. Martino, P. Feyen, M. Porro, C. Bossio, E. Zucchetti, D. Ghezzi, F. Benfenati, G. Lanzani, & M. R. Antognazza. “Photothermal Cellular Stimulation in Functional Bio-Polymer Interfaces.” *Scientific Reports* **2015**, 5 (1), 8911.
- [162] R. Sarnaik, H. Chen, X. Liu, & J. Cang. “Genetic Disruption of the On Visual Pathway Affects Cortical Orientation Selectivity and Contrast Sensitivity in Mice.” *Journal of Neurophysiology* **2014**, 111 (11), 2276–2286.
- [163] J. Liu, X. Wang, D. Li, N. E. Coates, R. A. Segalman, & D. G. Cahill. “Thermal Conductivity and Elastic Constants of PEDOT:PSS with High Electrical Conductivity.” *Macromolecules* **2015**, 48 (3), 585–591.
- [164] J. Wang, C. Sramek, Y. M. Paulus, D. Lavinsky, G. Schuele, D. Anderson, D. Dewey, & D. Palanker. “Retinal Safety of Near-Infrared Lasers in Cataract Surgery.” *Journal of Biomedical Optics* **2012**, 17 (9), 0950011.
- [165] N. A. L. Chenais, M. J. I. Airaghi Leccardi, & D. Ghezzi. “Capacitive-like Photovoltaic Epiretinal Stimulation Enhances and Narrows the Network-Mediated Activity of Retinal Ganglion Cells by Recruiting the Lateral Inhibitory Network.” *Journal of Neural Engineering* **2019**, 16 (6), 066009.
- [166] O. Vazquez-Mena, T. Sannomiya, M. Tosun, L. G. Villanueva, V. Savu, J. Voros, & J. Brugger. “High-Resolution Resistless Nanopatterning on Polymer and Flexible Substrates for Plasmonic Biosensing Using Stencil Masks.” *ACS Nano* **2012**, 6 (6), 5474–5481.
- [167] H. Ogawa, K. Suzuki, S. Kaneko, Y. Nakano, Y. Ishikawa, & T. Kitahara. “Tensile Testing of Microfabricated Thin Films;” Springer-Verlag, **1997**.
- [168] T. Tsuchiya, M. Hirata, & N. Chiba. “Young’s Modulus, Fracture Strain, and Tensile Strength of Sputtered Titanium Thin Films.” *Thin Solid Films* **2005**, 484, 245–250.
- [169] A. Norlin, J. Pan, & C. Leygraf. “Investigation of Interfacial Capacitance of Pt, Ti and TiN Coated Electrodes by Electrochemical Impedance Spectroscopy.” In *Biomolecular Engineering*; Elsevier,

- 2002; Vol. 19, 67–71.
- [170] Z. Chen & S. Diebels. “Nanoindentation of Soft Polymers: Modeling, Experiments and Parameter Identification.” *TECHNISCHE MECHANIK* **2014**, 34, 166–189.
- [171] S. Savagatrup, A. D. Printz, T. F. O’Connor, A. V. Zaretski, D. Rodriguez, E. J. Sawyer, K. M. Rajan, R. I. Acosta, S. E. Root, & D. J. Lipomi. “Mechanical Degradation and Stability of Organic Solar Cells: Molecular and Microstructural Determinants.” *Energy and Environmental Science*. Royal Society of Chemistry **2015**, 55–80.
- [172] U. Lang, N. Naujoks, & J. Dual. “Mechanical Characterization of PEDOT:PSS Thin Films.” *Synthetic Metals* **2009**, 159 (5–6), 473–479.
- [173] C. J. Robin, A. Vishnoi, & K. N. Jonnalagadda. “Mechanical Behavior and Anisotropy of Spin-Coated SU-8 Thin Films for MEMS.” *Journal of Microelectromechanical Systems* **2014**, 23 (1), 168–180.
- [174] W. Hasenkamp, D. Forchelet, K. Pataky, J. Villard, H. Van Lintel, A. Bertsch, Q. Wang, & P. Renaud. “Polyimide/SU-8 Catheter-Tip MEMS Gauge Pressure Sensor.” *Biomedical Microdevices* **2012**, 14 (5), 819–828.
- [175] T. Stieglitz. “Why Neurotechnologies? About the Purposes, Opportunities and Limitations of Neurotechnologies in Clinical Applications.” *Neuroethics* **2019**, 1–12.
- [176] P. Čvančara, T. Boretius, V. M. López-Álvarez, P. Maciejasz, D. Andreu, S. Raspopovic, F. Petrini, S. Micera, G. Granata, E. Fernandez, P. M. Rossini, K. Yoshida, W. Jensen, J.-L. Divoux, D. Guiraud, X. Navarro, & T. Stieglitz. “Stability of Thin-Film Metallization in Flexible Stimulation Electrodes: Analysis and Improvement of in Vivo Performance.” *bioRxiv* **2019**, 644914.
- [177] J. Pfau, D. Ganatra, A. Weltin, G. Urban, J. Kieninger, & T. Stieglitz. “Electrochemical Stability of Thin-Film Platinum as Suitable Material for Neural Stimulation Electrodes.” In *Proceedings of the Annual International Conference of the IEEE Engineering in Medicine and Biology Society, EMBS*; Institute of Electrical and Electronics Engineers Inc., **2019**; Vol. 2019, 3762–3765.
- [178] V. I. Madogni, B. Kounouhéwa, A. Akpo, M. Agbomahéna, S. A. Hounkpatin, & C. N. Awanou. “Comparison of Degradation Mechanisms in Organic Photovoltaic Devices upon Exposure to a Temperate and a Subequatorial Climate.” *Chemical Physics Letters* **2015**, 640, 201–214.
- [179] M. Schaer, F. Nüesch, D. Berner, W. Leo, & L. Zuppiroli. “Water Vapor and Oxygen Degradation Mechanisms in Organic Light Emitting Diodes.” *Advanced Functional Materials* **2001**, 11 (2), 116–121.
- [180] A. Weu, J. A. Kress, F. Paulus, D. Becker-Koch, V. Lami, A. A. Bakulin, & Y. Vaynzof. “Oxygen-Induced Doping as a Degradation Mechanism in Highly Efficient Organic Solar Cells.” *ACS Applied Energy Materials* **2019**, 2 (3), 1943–1950.
- [181] D. R. Bertschinger, E. Beknazar, M. Simonutti, A. B. Safran, J. A. Sahel, S. G. Rosolen, S. Picaud, & J. Salzmann. “A Review of in Vivo Animal Studies in Retinal Prosthesis Research.” *Graefe’s Archive for Clinical and Experimental Ophthalmology*. Springer **2008**, 1505–1517.
- [182] W. K. Noell. “The Effect of Iodoacetate on the Vertebrate Retina.” *Journal of Cellular and Comparative Physiology* **1951**, 37 (2), 283–307.
- [183] W. K. Noell. “Experimentally Induced Toxic Effects on Structure and Function of Visual Cells and Pigment Epithelium.” *American Journal of Ophthalmology* **1953**, 36 (6), 103–116.
- [184] N. Orzalesi, G. A. Calabria, & A. Grignolo. “Experimental Degeneration of the Rabbit Retina Induced by Iodoacetic Acid. A Study of the Ultrastructure, the Rhodopsin Cycle and the Uptake of ¹⁴C-Labeled Iodoacetic Acid.” *Experimental Eye Research* **1970**, 9 (2), 246–253.
- [185] L. Liang, Y. Katagiri, L. M. Franco, Y. Yamauchi, V. Enzmann, H. J. Kaplan, & J. H. Sandell. “Long-Term Cellular and Regional Specificity of the Photoreceptor Toxin, Iodoacetic Acid (IAA), in the Rabbit Retina.” *Visual Neuroscience* **2008**, 25 (2), 167–177.
- [186] P. A. Scott, H. J. Kaplan, & J. H. Sandell. “Anatomical Evidence of Photoreceptor Degeneration Induced by Iodoacetic Acid in the Porcine Eye.” *Experimental Eye Research* **2011**, 93 (4), 513–527.
- [187] J. M. Noel, J. P. Fernandez de Castro, P. J. DeMarco, L. M. Franco, W. Wang, E. V. Vukmanic, X. Peng, J. H. Sandell, P. A. Scott, H. J. Kaplan, & M. A. McCall. “Iodoacetic Acid, but Not Sodium

- Iodate, Creates an Inducible Swine Model of Photoreceptor Damage.” *Experimental Eye Research* **2012**, 97 (1), 137–147.
- [188] W. Wang, J. F. de Castro, E. Vukmanic, L. Zhou, D. Emery, P. J. DeMarco, H. J. Kaplan, & D. C. Dean. “Selective Rod Degeneration and Partial Cone Inactivation Characterize an Iodoacetic Acid Model of Swine Retinal Degeneration.” *Investigative Ophthalmology and Visual Science* **2011**, 52 (11), 7917–7923.
- [189] B. S. Winkler, M. W. Sauer, & C. A. Starnes. “Modulation of the Pasteur Effect in Retinal Cells: Implications for Understanding Compensatory Metabolic Mechanisms.” *Experimental Eye Research* **2003**, 76 (6), 715–723.
- [190] A. Hogg, S. Uhl, F. Feuvrier, Y. Girardet, B. Graf, T. Aellen, H. Keppner, Y. Tardy, & J. Burger. “Protective Multilayer Packaging for Long-Term Implantable Medical Devices.” *Surface and Coatings Technology* **2014**, 255, 124–129.
- [191] F. Selbmann, M. Baum, M. Wiemer, & T. Gessner. “Deposition of Parylene C and Characterization of Its Hermeticity for the Encapsulation of MEMS and Medical Devices.” In *2016 IEEE 11th Annual International Conference on Nano/Micro Engineered and Molecular Systems, NEMS 2016*; Institute of Electrical and Electronics Engineers Inc., **2016**; 427–432.
- [192] C. F. Carlborg, T. Haraldsson, K. Öberg, M. Malkoch, & W. Van Der Wijngaart. “Beyond PDMS: Off-Stoichiometry Thiol-Ene (OSTE) Based Soft Lithography for Rapid Prototyping of Microfluidic Devices.” *Lab on a Chip*. Royal Society of Chemistry **2011**, 3136–3147.
- [193] N. Sandström, R. Z. Shafagh, A. Vastesson, C. F. Carlborg, W. van der Wijngaart, & T. Haraldsson. “Reaction Injection Molding and Direct Covalent Bonding of OSTE+ Polymer Microfluidic Devices.” *Journal of Micromechanics and Microengineering* **2015**, 25 (7), 075002.
- [194] J. Hansson, J. M. Karlsson, C. F. Carlborg, W. Van Der Wijngaart, & T. Haraldsson. “Low Gas Permeable and Non-Absorbent Rubbery OSTE+ for Pneumatic Microvalves.” In *Proceedings of the IEEE International Conference on Micro Electro Mechanical Systems (MEMS)*; Institute of Electrical and Electronics Engineers Inc., **2014**; 987–990.
- [195] T. Haraldsson, C. F. Carlborg, & W. van der Wijngaart. “OSTE: A Novel Polymer System Developed for Lab-on-Chip.” In *Microfluidics, BioMEMS, and Medical Microsystems XII*; International Society for Optics and Photonics, **2014**; Vol. 8976, 897608.
- [196] A. Uji, T. Murakami, K. Nishijima, T. Akagi, T. Horii, N. Arakawa, Y. Muraoka, A. A. Ellabban, & N. Yoshimura. “Association between Hyperreflective Foci in the Outer Retina, Status of Photoreceptor Layer, and Visual Acuity in Diabetic Macular Edema.” *American Journal of Ophthalmology* **2012**, 153 (4), 710-717.e1.
- [197] L. J. Frishman & M. H. Wang. “Electroretinogram of Human, Monkey and Mouse.” In *Adler’s Physiology of the Eye*; Elsevier, **2011**; 480–501.
- [198] M. J. I. Airaghi Leccardi, N. A. L. Chenais, L. Ferlauto, M. Kawecki, E. G. Zollinger, & D. Ghezzi. “Photovoltaic Organic Interface for Neuronal Stimulation in the Near-Infrared.” *Communications Materials* **2020**, 1 (21), 1–13.
- [199] S. Gribi, S. du Bois de Dunilac, D. Ghezzi, & S. P. Lacour. “A Microfabricated Nerve-on-a-Chip Platform for Rapid Assessment of Neural Conduction in Explanted Peripheral Nerve Fibers.” *Nature Communications* **2018**, 9 (1), 1–10.
- [200] M. Jakešová, M. Silverå Ejneby, V. Ďerek, T. Schmidt, M. Gryszel, J. Brask, R. Schindl, D. T. Simon, M. Berggren, F. Elinder, & E. D. Głowacki. “Optoelectronic Control of Single Cells Using Organic Photocapacitors.” *Science advances* **2019**, 5 (4), eaav5265.
- [201] P. Feyen, E. Colombo, D. Endeman, M. Nova, L. Laudato, N. Martino, M. R. Antognazza, G. Lanzani, F. Benfenati, & D. Ghezzi. “Light-Evoked Hyperpolarization and Silencing of Neurons by Conjugated Polymers.” *Scientific Reports* **2016**, 6, 22718.
- [202] N. Martino, D. Ghezzi, F. Benfenati, G. Lanzani, & M. R. Antognazza. “Organic Semiconductors for Artificial Vision.” *Journal of Materials Chemistry B* **2013**, 1 (31), 3768.
- [203] C. Tortiglione, M. R. Antognazza, A. Tino, C. Bossio, V. Marchesano, A. Bauduin, M. Zangoli, S. V. Morata, & G. Lanzani. “Semiconducting Polymers Are Light Nanotransducers in Eyeless Animals.”

- Science Advances* **2017**, 3 (1), e1601699.
- [204] S. Vaquero, C. Bossio, S. Bellani, N. Martino, E. Zucchetti, G. Lanzani, M. R. Antognazza, M. Rosa, G. Lanzani, & M. R. Antognazza. “Conjugated Polymers for the Optical Control of the Electrical Activity of Living Cells.” *J. Mater. Chem. B* **2016**, 4 (31), 5272–5283.
- [205] O. S. Abdullaeva, F. Balzer, M. Schulz, J. Parisi, A. Lützen, K. Dedek, & M. Schiek. “Organic Photovoltaic Sensors for Photocapacitive Stimulation of Voltage-Gated Ion Channels in Neuroblastoma Cells.” *Advanced Functional Materials* **2018**, 1805177.
- [206] G. Lanzani, M. R. Antognazza, N. Martino, D. Ghezzi, & F. Benfenati. “Controlling Cell Functions by Light.” In *International IEEE/EMBS Conference on Neural Engineering, NER*; IEEE Computer Society, **2015**; Vol. 2015-July, 603–606.
- [207] M. R. Antognazza, N. Martino, D. Ghezzi, P. Feyen, E. Colombo, D. Endeman, F. Benfenati, & G. Lanzani. “Shedding Light on Living Cells.” *Advanced Materials* **2015**, 27 (46), 7662–7669.
- [208] F. Lodola, N. Martino, G. Tullii, G. Lanzani, & M. R. Antognazza. “Conjugated Polymers Mediate Effective Activation of the Mammalian Ion Channel Transient Receptor Potential Vanilloid 1.” *Scientific Reports* **2017**, 7 (1), 1–10.
- [209] J. K. Bowmaker & H. J. Dartnall. “Visual Pigments of Rods and Cones in a Human Retina.” *The Journal of Physiology* **1980**, 298 (1), 501–511.
- [210] G. Grancini, M. Maiuri, D. Fazzi, A. Petrozza, H. J. Egelhaaf, D. Brida, G. Cerullo, & G. Lanzani. “Hot Exciton Dissociation in Polymer Solar Cells.” *Nature Materials* **2013**, 12 (1), 29–33.
- [211] A. Håkansson, S. Han, S. Wang, J. Lu, S. Braun, M. Fahlman, M. Berggren, X. Crispin, & S. Fabiano. “Effect of (3-Glycidioxypropyl)Trimethoxysilane (GOPS) on the Electrical Properties of PEDOT:PSS Films.” *Journal of Polymer Science Part B: Polymer Physics* **2017**, 55 (10), 814–820.
- [212] M. ElMahmoudy, S. Inal, A. Charrier, I. Uguz, G. G. Malliaras, & S. Sanaur. “Tailoring the Electrochemical and Mechanical Properties of PEDOT:PSS Films for Bioelectronics.” *Macromolecular Materials and Engineering* **2017**, 302 (5), 1600497.
- [213] W. Kim, J. Choi, J.-H. Kim, T. Kim, C. Lee, S. Lee, M. Kim, B. J. Kim, & T.-S. Kim. “Comparative Study of the Mechanical Properties of All-Polymer and Fullerene–Polymer Solar Cells: The Importance of Polymer Acceptors for High Fracture Resistance.” *Chemistry of Materials* **2018**, 30 (6), 2102–2111.
- [214] C. Gargini, E. Terzibasi, F. Mazzoni, & E. Strettoi. “Retinal Organization in the Retinal Degeneration 10 (Rd10) Mutant Mouse: A Morphological and ERG Study.” *Journal of Comparative Neurology* **2007**, 500 (2), 222–238.
- [215] M. E. Pennesi, K. V. Michaels, S. S. Magee, A. Maricle, S. P. Davin, A. K. Garg, M. J. Gale, D. C. Tu, Y. Wen, L. R. Erker, & P. J. Francis. “Long-Term Characterization of Retinal Degeneration in Rd1 and Rd10 Mice Using Spectral Domain Optical Coherence Tomography.” *Investigative Ophthalmology and Visual Science* **2012**, 53 (8), 4644–4656.
- [216] D. J. Margolis & P. B. Detwiler. “Cellular Origin of Spontaneous Ganglion Cell Spike Activity in Animal Models of Retinitis Pigmentosa.” *Journal of Ophthalmology* **2011**, 507037.
- [217] G. Dagnelie, P. Christopher, A. Ardit, L. da Cruz, J. L. Duncan, A. C. Ho, L. C. Olmos de Koo, J. A. Sahel, P. E. Stanga, G. Thumann, Y. Wang, M. Arsiero, J. D. Dorn, & R. J. Greenberg. “Performance of Real-World Functional Vision Tasks by Blind Subjects Improves after Implantation with the Argus® II Retinal Prosthesis System.” *Clinical and Experimental Ophthalmology* **2017**, 45 (2), 152–159.
- [218] K. Stingl, K. U. Bartz-Schmidt, D. Besch, A. Braun, A. Bruckmann, F. Gekeler, U. Grepmaier, S. Hipp, G. Hortdorfer, C. Kernstock, A. Koitschev, A. Kusnyerik, H. Sachs, A. Schatz, T. Peters, B. Wilhelm, & E. Zrenner. “Artificial Vision with Wirelessly Powered Subretinal Electronic Implant Alpha-IMS.” *Proceedings of the Royal Society B: Biological Sciences* **2013**, 280 (1757), 20130077.
- [219] H. Christiaan Stronks, M. P. Barry, & G. Dagnelie. “Electrically Elicited Visual Evoked Potentials in Argus II Retinal Implant Wearers.” *Investigative Ophthalmology and Visual Science* **2013**, 54 (6), 3891–3901.

- [220] D. L. Rathbun, N. Ghorbani, H. Shabani, E. Zrenner, & Z. Hosseinzadeh. "Spike-Triggered Average Electrical Stimuli as Input Filters for Bionic Vision - A Perspective." *Journal of Neural Engineering* **2018**, 15 (6), 063002.
- [221] D. Freeman, J. Rizzo, & S. Fried. "Electric Stimulation with Sinusoids and White Noise for Neural Prostheses." *Frontiers in Neuroscience* **2010**, 4, 1.
- [222] Y. Mandel, G. Goetz, D. Lavinsky, P. Huie, K. Mathieson, L. Wang, T. Kamins, L. Galambos, R. Manivanh, J. Harris, & D. Palanker. "Cortical Responses Elicited by Photovoltaic Subretinal Prostheses Exhibit Similarities to Visually Evoked Potentials." *Nature Communications* **2013**, 4, 1980.
- [223] G. Simone, D. Di Carlo Rasi, X. De Vries, G. H. L. Heintges, S. C. J. Meskers, R. A. J. Janssen, & G. H. Gelinck. "Near-Infrared Tandem Organic Photodiodes for Future Application in Artificial Retinal Implants." *Advanced Materials* **2018**, 1804678.
- [224] T. J. T. P. Van Den Berg & H. Spekreijse. "Near Infrared Light Absorption in the Human Eye Media." *Vision Research* **1997**, 37 (2), 249–253.
- [225] G. Matsui & H. Kato. "Analysis of Thermal Diffusivity of Ti Thin Film by Thermoreflectance and Periodic Heating Technique." *Review of Scientific Instruments* **2011**, 82 (3), 034905.
- [226] X. Fan, W. Nie, H. Tsai, N. Wang, H. Huang, Y. Cheng, R. Wen, L. Ma, F. Yan, & Y. Xia. "PEDOT:PSS for Flexible and Stretchable Electronics: Modifications, Strategies, and Applications." *Advanced Science* **2019**, 6 (19), 1900813.
- [227] H. Chen, J. Peet, S. Hu, J. Azoulay, G. Bazan, & M. Dadmun. "The Role of Fullerene Mixing Behavior in the Performance of Organic Photovoltaics: PCBM in Low-Bandgap Polymers." *Advanced Functional Materials* **2014**, 24 (1), 140–150.
- [228] C. H. Henager & W. T. Pawlewicz. "Thermal Conductivities of Thin, Sputtered Optical Films." *Applied Optics* **1993**, 32 (1), 91.
- [229] C. J. M. Emmott, J. A. Röhr, M. Campoy-Quiles, T. Kirchartz, A. Urbina, N. J. Ekins-Daukes, & J. Nelson. "Organic Photovoltaic Greenhouses: A Unique Application for Semi-Transparent PV?" *Energy and Environmental Science* **2015**, 8 (4), 1317–1328.
- [230] Z. Guo, D. Lee, Y. Liu, F. Sun, A. Sliwinski, H. Gao, P. C. Burns, L. Huang, & T. Luo. "Tuning the Thermal Conductivity of Solar Cell Polymers through Side Chain Engineering." *Physical Chemistry Chemical Physics* **2014**, 16 (17), 7764–7771.
- [231] L. J. Guerin, M. Bossel, M. Demierre, S. Calmes, & P. Renaud. "Simple and Low Cost Fabrication of Embedded Micro-Channels by Using a New Thick-Film Photoplastic." In *International Conference on Solid-State Sensors and Actuators, Proceedings*; IEEE, **1997**; Vol. 2, 1419–1422.
- [232] C. W. Chen, S. Y. Hsiao, C. Y. Chen, H. W. Kang, Z. Y. Huang, & H. W. Lin. "Optical Properties of Organometal Halide Perovskite Thin Films and General Device Structure Design Rules for Perovskite Single and Tandem Solar Cells." *Journal of Materials Chemistry A* **2015**, 3 (17), 9152–9159.
- [233] S. Arscott, F. Garet, P. Mounaix, L. Duvillaret, J. L. Coutaz, & D. Lippens. "Terahertz Time-Domain Spectroscopy of Films Fabricated from SU-8." *Electronics Letters* **1999**, 35 (3), 243–244.
- [234] C. Markos, K. Vlachos, & G. Kakarantzas. "Guiding and Thermal Properties of a Hybrid Polymer-Infused Photonic Crystal Fiber." *Optical Materials Express* **2012**, 2 (7), 929.
- [235] D. Erickson, D. Sinton, & D. Li. "Joule Heating and Heat Transfer in Poly(Dimethylsiloxane) Microfluidic Systems." *Lab on a Chip* **2003**, 3 (3), 141–149.
- [236] J. Gasiorowski, R. Menon, K. Hingerl, M. Dachev, & N. S. Sariciftci. "Surface Morphology, Optical Properties and Conductivity Changes of Poly(3,4-Ethylenedioxythiophene):Poly(Styrenesulfonate) by Using Additives." *Thin Solid Films* **2013**, 536, 211–215.
- [237] M. Vuylsteke, J. Van Dorpe, J. Roelens, T. De Bo, & S. Mordon. "Endovenous Laser Treatment: A Morphological Study in an Animal Model." *Phlebology* **2009**, 24 (4), 166–175.
- [238] M. J. I. Airaghi Leccardi, P. Vagni, & D. Ghezzi. "Multilayer 3D Electrodes for Neural Implants." *Journal of Neural Engineering* **2019**, 16 (2), 026013.

-
- [239] Z. Liu, S. Shy Liow, S. Li Lai, A. Alli-Shaik, G. E. Holder, B. Harshad Parikh, S. Krishnakumar, Z. Li, M. Jin Tan, J. Gunaratne, V. Amutha Barathi, W. Hunziker, R. Lakshminarayanan, C. Woon Teck Tan, C. K. Chee, P. Zhao, G. Lingam, X. Jun Loh, & X. Su. “Retinal-Detachment Repair and Vitreous-like-Body Reformation via a Thermogelling Polymer Endotamponade.” *Nature Biomedical Engineering* **2019**, 3, 598–610.
- [240] T. Stieglitz. “Of Man and Mice: Translational Research in Neurotechnology.” *Neuron* **2020**, 105, 12–15.
- [241] C. K. Baker & J. G. Flannery. “Innovative Optogenetic Strategies for Vision Restoration.” *Frontiers in Cellular Neuroscience* **2018**, 12.
- [242] A. Auricchio, A. J. Smith, & R. R. Ali. “The Future Looks Brighter After 25 Years of Retinal Gene Therapy.” *Human Gene Therapy* **2017**, 28 (11), 982–987.
- [243] G. Lanzani. “Organic Electronics Meets Biology.” *Nature Materials* **2014**, 13 (8), 775–776.
- [244] M. Morana, M. Wegscheider, A. Bonanni, N. Kopidakis, S. Shaheen, M. Scharber, Z. Zhu, D. Waller, R. Gaudiana, C. Brabec, B. M. Morana, M. Wegscheider, A. Bonanni, N. Kopidakis, S. Shaheen, M. Scharber, Z. Zhu, D. Waller, R. Gaudiana, & C. Brabec. “Bipolar Charge Transport in PCPDTBT-PCBM Bulk-Heterojunctions for Photovoltaic Applications.” *Advanced Functional Materials* **2008**, 18 (12), 1757–1766.
- [245] R. Hooke. “Micrographia: Or Some Physiological Descriptions of Minute Bodies Made by Magnifying Glasses with Observations and Inquiries Thereupon;” The Royal Society: London, **1665**.

List of publications

Publications relevant for this thesis are highlighted by †.

Peer-reviewed journal articles

- N.A.L. Chenais, **M.J.I. Airaghi Leccardi**, and Diego Ghezzi, “Single-pixel and single receptive field epiretinal stimulation with a wide-field and high-density retinal prosthesis for artificial vision”, under review in *Nature Communications*, 2020. †
- **M.J.I. Airaghi Leccardi** and D. Ghezzi, “Organic electronics for neuroprosthetics”, under review in *Healthcare Technology Letters - Special Issue: Medical Bionics: From Emerging Technologies to Clinical Practice*, 2020.
- **M.J.I. Airaghi Leccardi**, N.A.L. Chenais, L. Ferlauto, M. Kawecki, E.G. Zollinger, and D. Ghezzi, “Polymeric, photovoltaic, and near-infrared-responsive neural prosthesis”, *Communications Materials* 1 (21), 2020. †
- N.A.L. Chenais, **M.J.I. Airaghi Leccardi**, and D. Ghezzi, “Capacitive-like photovoltaic epiretinal stimulation enhances and narrows the network-mediated activity of retinal ganglion cells by recruiting the lateral inhibitory network”, *Journal of Neural Engineering* 16 (6), 2019. †
- **M.J.I. Airaghi Leccardi**, P. Vagni, and D. Ghezzi “Multilayer 3D electrodes for neural implants”, *Journal of Neural Engineering* 16 (2), 026013, 2019.
- L. Ferlauto, A.N. D’Angelo, P. Vagni, **M.J.I. Airaghi Leccardi**, F.M. Mor, E.A. Cuttaz, M.O. Heuschkel, L. Stoppini, and D. Ghezzi, “Development and characterization of PEDOT: PSS/Alginate soft microelectrodes for application in neuroprosthetics”, *Frontiers in Neuroscience* 12, 648, 2018.
- L. Ferlauto*, **M.J.I. Airaghi Leccardi***, N.A.L. Chenais*, S.C.A. Gilliéron, P. Vagni, M. Bevilacqua, T.J. Wolfensberger, K. Sivula, and D. Ghezzi, “Design and validation of a foldable and photovoltaic wide-field epiretinal prosthesis”, *Nature Communications* 9 (1), 992, 2018. *equal contribution. †

Patents

- **M.J.I. Airaghi Leccardi**, L. Ferlauto, and D. Ghezzi, “Polymer-based optoelectronic interface and methods for its manufacture”, WO2018177547A1, 2017. †

- **M.J.I. Airaghi Leccardi** and D. Ghezzi, "Implantable electrode and method for manufacturing", WO2018103828A1, 2016.

Conference proceedings

- **M.J.I. Airaghi Leccardi**, N.A.L. Chenais, C.H. Vila, T.J. Wolfensberger, and D. Ghezzi, "Development of a Foldable and Photovoltaic Wide-Field Epiretinal Prosthesis", *Artificial Vision*, Aachen (DE), 2019.
- **M.J.I. Airaghi Leccardi**, N.A.L. Chenais, and D. Ghezzi, "Development of a large-area and spherical array of polymeric photovoltaic pixels for artificial vision", *microTAS*, Basel (CH), 2019.
- **M.J.I. Airaghi Leccardi**, N.A.L. Chenais, C.H. Vila, T.J. Wolfensberger, and D. Ghezzi, "Development of a Foldable and Photovoltaic Wide-Field Epiretinal Prosthesis", *NER*, San Francisco (CA, USA), 2019.
- **M.J.I. Airaghi Leccardi**, L. Ferlauto, N.A.L. Chenais, S. Gilliéron, T.J. Wolfensberger, K. Sivula, and D. Ghezzi, "Design and Validation of a Foldable and Photovoltaic Wide-Field Epiretinal Prosthesis", *GRC Neuroelectronic Interfaces*, Galveston (TX, USA), 2018.
- **M.J.I. Airaghi Leccardi**, L. Ferlauto, N.A.L. Chenais, M. Bevilacqua, T.J. Wolfensberger, K. Sivula, and D. Ghezzi, "Design and validation of a foldable and photovoltaic wide-field epiretinal prosthesis", *Artificial Vision*, Aachen (DE), 2017.
- **M.J.I. Airaghi Leccardi**, L. Ferlauto, K. Sivula and D. Ghezzi, "Injectable, Self-opening, and Freestanding Retinal Prosthesis for Fighting Blindness", *E-MRS*, Strasbourg (FR), Spring 2017.
- **M.J.I. Airaghi Leccardi**, V. Gaillet, B. Duckert, and D. Ghezzi, "3D multi-layer probe for application in neuroprosthetics", *E-MRS*, Strasbourg (FR), Spring 2017.
- **M.J.I. Airaghi Leccardi**, L. Ferlauto, M. Salari, and D. Ghezzi, "Injectable, Self-opening, and Freestanding Retinal Prosthesis for Fighting Blindness", *NanoBioTech Montreux*, Montreux (CH), 2016.

Curriculum Vitae

Marta Jole Ildelfonsa AIRAGHI LECCARDI



ADDRESS

Via San Jorio 3A
CH - 6512 Giubiasco
Switzerland



OFFICE

EPFL Campus Biotech
B3-03 243.134
Ch. Des Mines 9
CH – 1202 Geneva



PHONE

+41 79 961 47 84



EMAIL

airaghi.marta@gmail.com



DATE OF BIRTH

10th of March 1990



NATIONALITY

Swiss and Italian



GOOGLE SCHOLAR

Marta Airaghi Leccardi
EPFL PhD Student



ORCID

[https://orcid.org/
0000-0001-9646-5264](https://orcid.org/0000-0001-9646-5264)



LANGUAGES



REFERENCES

Prof. Diego Ghezzi
(diego.ghezzi@epfl.ch)

Prof. Markus Niederberger
(markus.niederberger@mat.ethz.ch)

EDUCATION

→ 10 / 2015 – ongoing (05 / 2020)

Ph.D. in Neuroprosthetics

Laboratory of Neuroengineering, Prof. D. Ghezzi
EPFL Microsystems and Microelectronics Doctoral School
– Lausanne, Switzerland



- ▶ Development of a wide-field and photovoltaic retinal prosthesis
- ▶ Microfabrication of flexible implants with high-density electrodes

→ 09 / 2009 – 04 / 2015

B.Sc. and M.Sc. in Materials Science

ETHZ Materials Science Department
– Zurich, Switzerland



- ▶ GPA: 5.5 / 6
- ▶ Master specialization: micro/nano/bio-technology and microfabrication
- ▶ Master thesis (ETHZ-EPFL): “Design, Fabrication, and Characterization of AFM Tips for Tensions Measurement and Manipulation of Fluid Interfaces.” Prof. J. Brügger and Prof. L. Isa
- ▶ Master semester Project II (EPFL): “3D Complex SU-8 Structures by Means of Microstereolithography.” Prof. J. Brügger
- ▶ Master semester Project I (ETHZ): “Nanoparticle-based Anatase Magnetite Composite Aerogels.” Prof. M. Niederberger
- ▶ Bachelor internship (Mawson Institute, UniSA Australia): “Oxidized Porous Silicon as a Drug Delivery Vehicle for the Antibody Infliximab.” Prof. N. Voelcker
- ▶ Bachelor Thesis (ETHZ): “Preparation of Nanoparticle-based Anatase Magnetite Aerogels.” Prof. M. Niederberger

WORK EXPERIENCES

- ▶ Doctoral assistant (10 / 2015 – ongoing). EPFL, Laboratory of Neuroengineering (LNE), Lausanne (CH). *Ph.D. thesis and teaching assistance*. Prof. D. Ghezzi
- ▶ Scientific assistant (05 – 07 / 2015). EPFL, Laboratory of Microsystems 1 (LMIS1), Lausanne. *Microfabrication of AFM tips*. Prof. J. Brügger and Prof. L. Isa
- ▶ Jr. scientific assistant (09 – 12 / 2013). ETH Zürich, D-MATL, Laboratory of Multifunctional Materials, Zürich (CH). *Preparation of anisotropic magnetic aerogels*. Prof. M. Niederberger
- ▶ Private lessons (09 / 2007 – 06 / 2012). MISE association (mise.ch), Bellinzona (CH). *High school level mathematics, physics, chemistry, and biology*. Direction: Stefano Peduzzi, Gabriel Speziga
- ▶ Assistant coach (09 / 2008 – 06 / 2009). SFG Locarno (CH). *Rhythmic gymnastics*. Claudia Rezzonico

Marta AIRAGHI LECCARDI

Skills

Materials Science
 Micro/NanoTechnology
 Biomedical Engineering
 Implantable/Soft Electronics
 Neuroprosthetics

MICROFABRICATION:

Cleanrooms
 Photolithography
 Wet and dry etching
 Sputtering, Evaporation
 Stencil lithography
 Supercritical drying
 Glovebox
 SEM, FIB, AFM / KPFM

MATERIALS:

Epoxies (SU8, OSTEmers)
 Elastomers (PDMS)
 Polyimide, Parylene-C
 Organic electronic materials,
 Bulk heterojunction organic
 photovoltaics
 Electrodes and coatings (Pt, Ti,
 TiN, SIROF, PEDOT:PSS, Pt black)
 Nanomaterials

COMPUTER:

MS-Office, Matlab, ImageJ,
 CleWin 5, SolidWorks,
 AutoCAD, Illustrator,
 Photoshop, Abaqus,
 Gwyddion, Origin, Comsol

INTERESTS



ADDITIONAL CERTIFICATIONS AND AWARDS

- ▶ RESAL module 1: Introductory Course in Laboratory Animal Science (theory and practice), small rodents.
- ▶ Zonta Club Lugano scholarship 2010. Several Swiss scholarships (2005 – 2015).
- ▶ Swiss absolute champion of rhythmic gymnastics (2006).
- ▶ Driving License: B. PADI Advanced Open Water Diver, Deep diver.

PUBLICATIONS

- ▶ N.A.L. Chenais, **M.J.I. Airaghi Leccardi**, and D. Ghezzi, "Single-pixel and single receptive field epiretinal stimulation with a wide-field and high-density retinal prosthesis for artificial vision", under review in *Nature Communications*, 2020.
- ▶ **M.J.I. Airaghi Leccardi** and D. Ghezzi, "Organic electronics for neuroprosthetics", under review in *Healthcare Technology Letters - Special Issue: Medical Bionics: From Emerging Technologies to Clinical Practice*.
- ▶ **M.J.I. Airaghi Leccardi**, N.A.L. Chenais, L. Ferlauto, M. Kawecki, E.G. Zollinger, and D. Ghezzi, "Polymeric, photovoltaic, and near-infrared-responsive neural prosthesis", *Communications Materials* 1 (21), 2020.
- ▶ N.A.L. Chenais, **M.J.I. Airaghi Leccardi**, and D. Ghezzi, "Capacitive-like photovoltaic epiretinal stimulation enhances and narrows the network-mediated activity of retinal ganglion cells by recruiting the lateral inhibitory network", *Journal of neural engineering* 16 (6), 2019.
- ▶ **M.J.I. Airaghi Leccardi**, P. Vagni, and D. Ghezzi, "Multilayer 3D electrodes for neural implants", *Journal of Neural Engineering* 16 (2), 026013, 2018.
- ▶ L. Ferlauto, A.N. D'Angelo, P. Vagni, **M.J.I. Airaghi Leccardi**, F.M. Mor, E.A. Cuttaz, M.O. Heuschkel, L. Stoppini, and D. Ghezzi, "Development and characterization of PEDOT: PSS/Alginate soft microelectrodes for application in neuroprosthetics", *Frontiers in Neuroscience* 12, 648, 2018.
- ▶ L. Ferlauto*, **M.J.I. Airaghi Leccardi***, N.A.L. Chenais*, S.C.A. Gilliéron, P. Vagni, M. Bevilacqua, T.J. Wolfensberger, K. Sivula, and D. Ghezzi, "Design and validation of a foldable and photovoltaic wide-field epiretinal prosthesis", *Nature Communications* 9 (1), 992, 2018. *equal contribution.
- ▶ S.J.P. McInnes, C.T. Turner, S.A. Al-Bataineh, **M.J.I. Airaghi Leccardi**, Y. Irani, K.A. Williams, A.J. Cowin, and N.H. Voelcker, "Surface engineering of porous silicon to optimise therapeutic antibody loading and release", *Materials Chemistry B* 3 (20), 4123, 2015.
- ▶ F.J. Heiligtag, **M.J.I. Airaghi Leccardi**, D. Erdem, M.J. Süess, and M. Niederberger, "Anisotropically structured magnetic aerogel monoliths", *Nanoscale* 6 (21), 13213, 2014.

PATENTS

- ▶ **M.J.I. Airaghi Leccardi**, L. Ferlauto, and D. Ghezzi, "Polymer-based optoelectronic interface and methods for its manufacture", WO2018177547A1, 2017.
- ▶ **M.J.I. Airaghi Leccardi** and D. Ghezzi, "Implantable electrode and method for manufacturing", WO2018103828A1, 2016.

Marta AIRAGHI LECCARDI

CONFERENCES

Talks

- ▶ Artificial Vision: the International Symposium on Visual Prosthetics, Aachen (DE), 2019.
- ▶ Translational Neurotechnology for Vision in Real Life: from Light to Sight, Lausanne (CH), 2019, *selected student pitch presentation*.
- ▶ Joint Symposium on Nanofabrication and Nanoengineering, Singapore, 2018, *invited speaker*.
- ▶ Artificial Vision: the International Symposium on Visual Prosthetics, Aachen (DE), 2017.

Posters

- ▶ μTAS, Basel (CH), 2019.
- ▶ NER, San Francisco (CA, USA), 2019.
- ▶ GRC, Galveston (TX, USA), 2018.
- ▶ E-MRS, Strasbourg (FR), Spring 2017.
- ▶ NanoBioTech, Montreux (CH), 2016. *Most wonderful poster award*.
- ▶ MaP Graduate Symposium, Zürich (CH), 2016.

“The next care to be taken, in respect of the Senses, is a supplying of their infirmities with instruments, and as it were, the adding of artificial organs to the natural ... and as glasses have highly promoted our seeing, so 'tis not improbable, but that there may be found many mechanical inventions to improve our other senses of hearing, smelling, tasting, and touching.”

Robert Hooke, 1665.²⁴⁵

English natural philosopher, discoverer and coiner of the cell